이학박사학위논문

Spectroscopic and Nanoscopic Studies of Anions, DNA, and Membranes

분광학과 나노스코피를 이용한 음이온, DNA, 지질막에 대한 연구

2014년 2월

서울대학교 대학원
화학부 물리화학전공
김 남 두

Ph. D. Dissertation

Spectroscopic and Nanoscopic Studies of Anions, DNA, and Membranes

A DISSERTATION

SUBMITTED TO THE DEPARTEMENT OF CHEMISTRY

OF SEOUL NATIONAL UNIVERSITY

FOR THE DEGREE OF DOCTOR OF PHILOSOPHY

February 2014

Supervisors:
Prof. Seong Keun Kim

Department of Chemistry

Seoul National University

Namdoo Kim

Abstract

Spectroscopic and Nanoscopic Studies of Anions, DNA, and Membranes

Namdoo Kim
Major in Physical Chemistry
Department of Chemistry
Seoul National University

Spectroscopy, the study of the change in light signal upon the interaction with the objects of interest, and microscopy, the study of the objects by directly imaging them with microscope have been widely used from elementary particle physics to bioscience. Numerous efforts have been made to combine these two fields to develop new observation tools even though they were usually used independently. Fluorescence microscopy made us to observe living species in real time without invasion through labeling of the fluorescent molecules. However, there is an intrinsic optical diffraction limit in far-field optical microscopy. Recently, super-resolution microscopy techniques have developed that overcome the diffraction limit using the photophysical properties like absorption and emission of the molecules. As a result, one can observe small objects such as organelles, proteins, DNAs that have smaller size than diffraction limit.

A combination of dynamic molecular combing and STED nanoscopy was demonstrated to accurately and precisely measure the lengths of DNA ranging widely in size from 117 bp to 23,130 bp. A size difference of as small as 100 bp could be discriminated, fostering the prospect of this method being used in detecting copy number variation.

With the combination of STED nanoscopy and alternating laser excitation (ALEX)-FRET single-molecule spectroscopy, we were able to detect a single molecule in a tightly confined volume that is 50-times smaller than the diffraction-limited confocal volume. We demonstrated the feasibility of this new technique for a dsDNA (20 bp) labeled by ATTO647N and DY-510XL. FRET between two dyes was acquired under both confocal and STED conditions. With this new technique, we were able to observe a single diffusing DNA molecule at up to 5 nM concentration, which is 100 times higher than the condition of typical single-molecule measurements.

Model lipid membranes such as GUVs and tethered free-standing bilayers are excellent systems for studying trans-membrane proteins free from any surface interactions. However, membrane proteins in such systems are not very well studied because of the difficulty of incorporating proteins into GUVs or tethered membranes while still maintaining protein function. Inspired by previous work on DNA-mediated membrane fusion, we have applied this DNA-machinery to mediate fusion of small proteoliposomes containing the photosynthetic reaction center to either GUVs or DNA-tethered lipid membrane patches formed by GUV rupture

onto DNA coated glass surfaces. The diffusion behavior of the delivered proteins was measured and compared with the diffusion of those in glass-supported bilayers. Also, the protein activity and orientation before and after fusion was analysed.

We investigated electron attachment to three dihalobenzene molecules, bromochlorobenzene (BCB), bromoiodobenzene (BIB) and chloroiodobenzene (CIB) by molecular beam photoelectron spectroscopy (PES). The most prominent product of electron attachment in the anion mass spectra was the atomic fragment of the less electronegative halogen of the two, i.e., Br^- for BCB and I^- for BIB and CIB. Photoelectron spectroscopy and *ab initio* calculations suggested that the approaching electron prefers to attack the less electronegative atom, a seemingly counterintuitive finding but consistent with the mass spectrometric result. For the iodine-containing species BIB and CIB, the photoelectron spectrum consists of bands from both the molecular anion and atomic I^-, the latter of which is produced by photodissociation of the former. Molecular orbital analysis revealed that a large degree of orbital energy reordering takes place upon electron attachment. These phenomena were shown to be readily explained by simple molecular orbital theory and the electronegativity of the halogen atoms.

Hetero-dimer anions of naphthalene (Np), anthracene (An), phenanthrene (Ph) and pyrene (Py) were investigated by time-of-flight mass spectrometer (TOF-MS), anion photoelectron spectroscopy and theoretical calculation. Two possible geometries exist with their electron affinity (EA) difference, parallel displaced (PD) and T-shaped. Dispersion force plays a key role in PD structure with the formation

of new anionic core while π-hydrogen interaction plays a key role in T-shaped structure with the monomer anionic core. Their optimized structures and charge distributions can be simply explained by the relative difference of EA.

Key words: Super-resolution STED nanoscopy, Dynamic molecular combing, Single-molecule spectroscopy, DNA-mediated vesicle fusion, Negative ion photoelectron spectroscopy, *Ab initio* calculation

Student number: 2006-20356

Contents

Chapter 1. Introduction

1.1 Far-field optical nanoscopy

The development of optical microscopy has led to numerous advances in many scientific fields, especially within the natural science. The naked human eyes cannot observe and distinguish between objects that are smaller than ~50 μm. However, Antony van Leeuwenhoek (1632-1723) was able to observe insects, sewer water, human hair, sperm and other extremely small objects with the help of the microscopes. The most advantageous feature of an optical microscope is its non-invasiveness and high resolving power.[1,2] By fluorescently tagging targets with fluorophores, we can observe the inside of a cell without violating or damaging it.[3,4] With recent advances in fluorescence microscopy, we can even obtain images of living cells in real time.[5] Objective lenses with high magnification and high numerical aperture (NA) have also accelerated the advance of microscopy. Even with the high NA-oil immersion objective lens, though, there is an intrinsic limit to the spatial resolution obtainable via a microscope due to optical diffraction. Ernst Abbe first discussed this optical diffraction limit in microscope system and formulated it as following:

$$\Delta r \approx \frac{\lambda}{2nsin\theta} = \frac{\lambda}{2NA} \qquad (1.1)$$

where Δr is the resolution, n is the refractive index of the medium, θ is the semi-aperture angle and λ is the wavelength of the light used.[6] Typically, it is not possible to distinguish between two objects that are nearby each other within 200 nm laterally and 500 nm axially when visible light is used.

Intensive efforts were made to overcome this diffraction limit. Some people used UV[7] or x-ray[8] since the wavelength of such light is shorter than that of visible light. However, the optics required when using such light source becomes complicated, in addition, UV and x-ray cannot be used to observe living specimens due to their high levels of photon energy. Electron microscopy provides sub-nanometer resolution.[9] However, sample preparation and imaging conditions have many constraints that disallow its use in physiological condition. Two-photon microscopy also confines the focal volume below the diffraction limit.[10] 4-Pi[11] and I^2M[12] use two opposing objective lenses to enhance the axial resolution. In total internal reflection microscopy, the axial resolution can be increased by using an evanescent wave with a very shallow penetration depth (~100 nm).[13] Material with a negative refractive index can also be used to make a hyperlens system.[14] Structured illumination microscopy has also explored the use of beam engineering to modulate the shape of the light that can be used to increase the spatial resolution.[15]

Several other types of super-resolution microscopy that utilize single-molecule localization methods have been developed recently. PALM,[16] STORM[17] and dSTORM[18] take advantage of the photoswitching property of fluorophores. Low-power excitation light only switches on a small number of molecules simultaneously. They are localized and then switched off, a cycle is repeated stochastically and recorded with a CCD camera. However, none of these techniques were fundamentally able to break diffraction limit.

In 1994, Stefan W. Hell first reported the notion of super-resolution microscopy

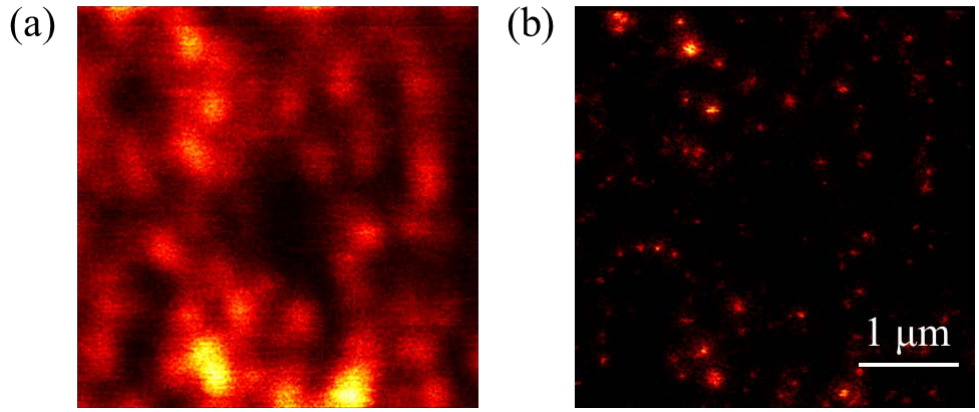

Figure 1.1 (a) Confocal and (b) STED images of 20 nm fluorescent beads coated with fluorescent dye. Excitation: 635 nm, STED: 780 nm. Image size: 4 μm x 4 μm, 256 x 256 pixels. Scale bar: 1 μm.

using stimulated emission[19], which was first demonstrated experimentally in 1999.[20] Stimulated emission depletion (STED) nanoscopy is a confocal-based technique that scans the sample in order to obtain an image. It uses the optical electronic transition between S_0 and S_1 to confine the effective fluorescent volume. It has unlimited resolution in principle. Most frequently uses organic dyes and fluorescent proteins as fluorophores (Figure 1.1). STED can be combined with other techniques such as fluorescence correlation spectroscopy (FCS),[21] 4Pi-microscopy,[22] lithography[23] and fluorescence lifetime imaging (FLIM).[24] In addition, STED can be performed using various types of lasers including Ti:Sapphire femtosecond lasers,[25] picosecond diode lasers,[26] continuous lasers,[27] stimulated Raman scattering from fibers[28] and supercontinuum lasers.[29]

Over the last 10 years, STED nanoscopy has undergone an outstanding evolution, for example, three dimensional (3D) STED with a π–phase modulator,[30] multi-color STED combined with FLIM,[31] two-photon STED[32] and isotropic STED.[33] Numerous biological samples have been imaged with STED nanoscopy, for example, microtubules,[34] actin filaments,[35] vimentin filaments,[36] pre-synaptic active zones,[37] the fate of synaptic vesicles,[38] olfactory neurons,[39] amyloid precursor protein,[40] mitochondria,[41] endoplasmic reticulum[42] and many receptors,[43] channels.[37] Of particular note, the endoplasmic reticulum and dendritic spines of living cells were imaged, as was the brain of a live mouse.[44,45] Fast imaging (video rate) has also recently become possible due to mirror scanning.[46]

1.2 Fluorescence resonance energy transfer (FRET)

A molecule undergoes vibronic transition from S_0 to S_1 under irradiation at proper wavelength. A vibrationally excited molecule rapidly moves to the ground state of S_1 by vibrational relaxation. It, then returns to S_0 by a radiative (fluorescence) or non-radiative process. Since it undergoes vibrational relaxation before it fluoresces, the fluorescence wavelength is usually red-shifted from the absorbed wavelength. However, if there is another molecule with an absorption spectrum that overlaps the emission spectrum of the first molecule, the energy can be transferred from the first molecule (donor) to the second molecule (acceptor) via a dipole-dipole interaction (Figure 1.2). The rate of the fluorescence resonance energy transfer or Förster resonance energy transfer (FRET) depends on R^6 as seen in the following equation.[47]

$$k_T = \frac{9(ln10)\Phi_D \kappa^2 J(\nu)}{128\pi^5 N_A n^4 R^6 \tau_D} \qquad (1.2)$$

In the above equation, k_T is the rate of energy transfer, Φ_D is the quantum yield of the donor, κ is the orientation factor of the dipole coupling, $J(\nu)$ is the spectral overlap integral, N_A is Avogadro's number, n is the refractive index of the medium, R is the distance between two dipoles, and τ_D is the lifetime of donor. $J(\nu)$, the spectral overlap integral, can be expressed as:

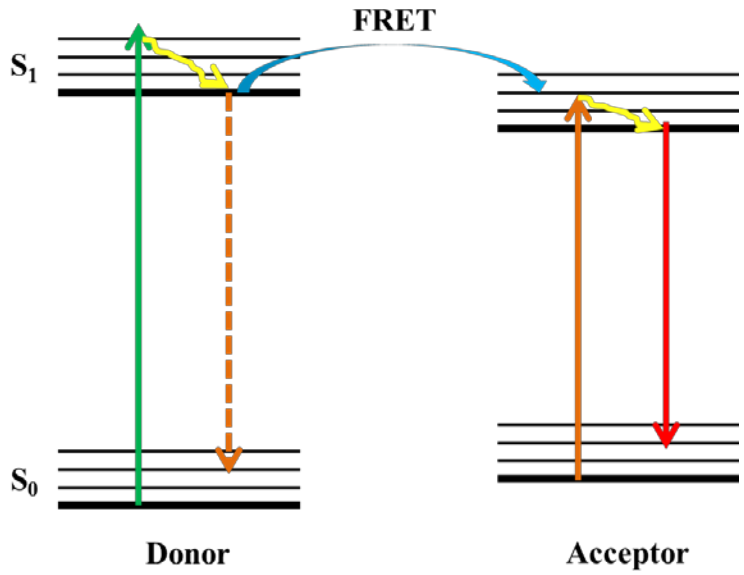

Figure 1.2 Schematic representation of FRET. Energy can be transferred from one molecule (donor) to the other molecule (acceptor) via dipole-dipole interaction. Resulting fluorescence is much red-shifted than incident excitation light.

$$J(\nu) = \int_0^\infty (\varepsilon^A(\nu)\emptyset(\nu)/\nu^4)d\nu \qquad (1.3)$$

where $\varepsilon^A(\nu)$ is the molar absorbance of the acceptor, $\emptyset(\nu)$ is the normalized fluorescence of the donor at wavenumber ν. In equation 1.2, k_T can be simplified by adopting a new constant R_0 so that:

$$k_T = \frac{9(ln10)\Phi_D\kappa^2 J(\nu)}{128\pi^5 N_A n^4 R^6 \tau_D} = k_D \left(\frac{R_0}{R}\right)^6 \qquad (1.4)$$

where $R_0^6 = (8.785 \times 10^{-25})\ \Phi_D\ \kappa^2\ n^{-4} J(\nu) cm^6$ and $k_D = 1/\tau_D$. The relationship between FRET efficiency E and the energy transfer rate, k_T is expressed as:

$$E = \frac{k_T}{k_D + k_T} = \frac{k_D(R_0/R)^6}{k_D + k_D(R_0/R)^6} = \frac{1}{1+(R/R_0)^6} \qquad (1.5)$$

From the above equation, we can measure the distance between two fluorophores from FRET efficiency, which is very sensitive to the distance. This is why FRET is often called as "spectroscopic ruler".[48] Experimentally, the E value is obtained by detecting the fluorescence emissions from both the donor and acceptor:

$$E = \frac{F_D^A}{F_D^A + \gamma F_D^D} \qquad (1.6)$$

where F_D^A and F_D^D are the fluorescence of the acceptor and donor at donor excitation respectively and, γ is a normalizing factor that reflects the quantum yield of the fluorophores and the detection efficiency of the detector at a specific

wavelength:

$$\gamma = \frac{\Phi_A \eta_A}{\Phi_D \eta_D} \qquad (1.7)$$

where Φ_A and Φ_D are the quantum yield of acceptor and donor, respectively, and η_A and η_D are the detection efficiency of the detector at each emission range.

1.3 Total internal reflection (TIR)

Light undergoes refraction when it passes through media with a different refractive index like water-air. The relationship between the incident angle (θ_1) and the refracted angle (θ_2) is given by Snell's law:

$$\frac{n_2}{n_1} = \frac{\sin\theta_1}{\sin\theta_2} \qquad (1.8)$$

When light travels from a medium with a higher refractive index into a medium with a lower refractive index medium, the refracted angle becomes larger than the incident angle. As a result, no light can pass through the medium with the higher refractive index at a certain incident angle and be reflected onto the original medium (Figure 1.3). We call this angle the critical angle and this phenomenon total internal reflection (TIR). If we use a coverglass with a refractive index of 1.515 and an aqueous solution with a refractive index of 1.33, the critical angle becomes 61.39°. The TIR generates an evanescent wave at the interface, and resulting

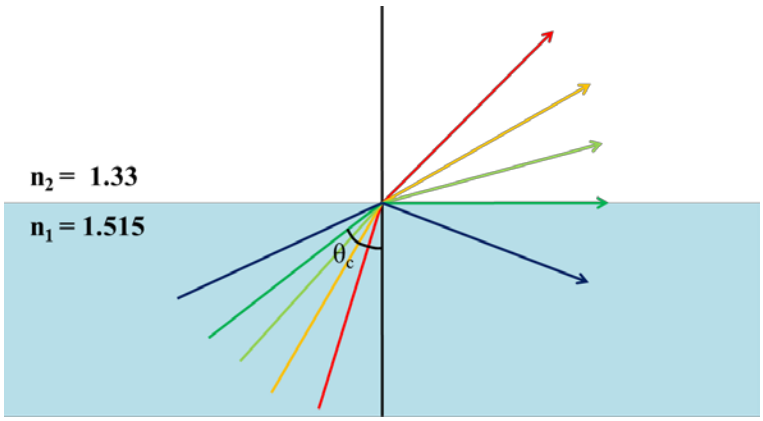

Figure 1.3 Total internal reflection occurs when light travels from the medium with a higher refractive index to the medium with a smaller refractive index. At specific angle, critical angle (θ_c), no light can propagate to the medium with a smaller refractive index (green line).

evanescent wave propagates axially along the medium with a lower refractive index. However, the intensity of an evanescent wave decays exponentially, thus, its penetration depth is only about 100~200 nm from the interface. This is a very valuable property since only the molecules near the interface can be excited by an evanescent wave, giving an excellent signal-to-noise (S/N) ratio with a greatly reduced background.

1.4 Anion clusters

Anion clusters have not attracted as much attention as neutral and cationic clusters due to their instability and a lack of appropriate investigative tools for examining them. The development of new techniques such as the time-of-flight mass spectrometer (TOF-MS)[49] and negative ion photoelectron spectrometer[50] has made possible the study of molecular anions and their clusters in the gas phase. Advances in quantum calculations and simulations have also helped support the experimental results of researchers.

There are few ways to generate negatively charged anions (Figure 1.4). One way is to solvate electrons using polar solvents such as water or ammonia.[51] Due to the stabilization effect of the polar solvent, the electrons can have a stable cage structure surrounded by solvents with characteristic absorption in the infrared (IR) region. The second way is to capture an electron within a molecule's dipolar electric field.[52] Unlike in normal anions where an electron occupies the molecular orbital, a

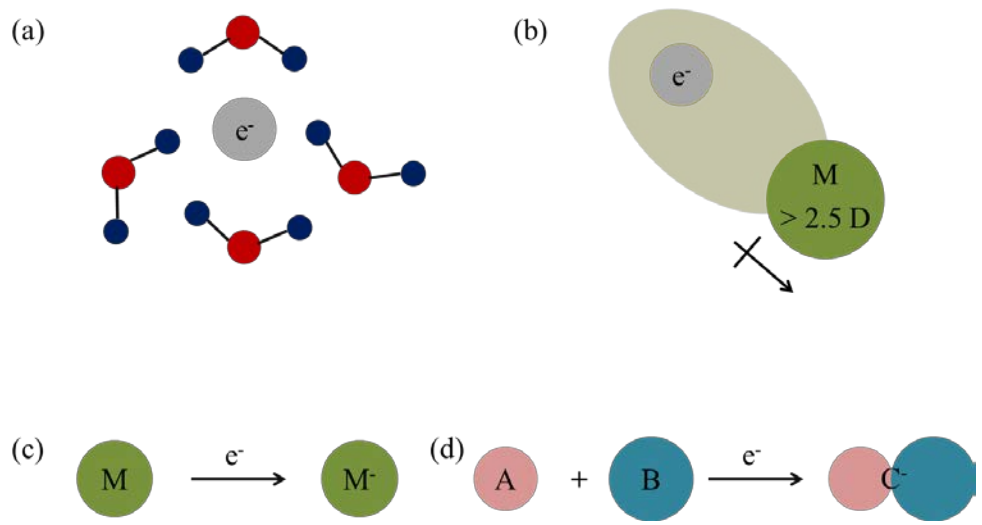

Figure 1.4 Schematic representations of (a) solvated electron, (b) dipole-bound anion and (c) valence anion with a monomeric ion core and (d) valence anion with a new ion core.

dipole-bound electron occupies an extremely diffusive orbital apart from the core (10~100 Å) with an *s*-like orbital character. Molecules with a high dipole moment (> 2.5 D) can form dipole-bound anions. Since this electron does not affect the molecular orbital or molecular structure, its molecular core is nearly identical to that of a neutral molecule. The most prominent features of a dipole-bound anion are the small electron binding energy (EBE) (< 100 meV) and very sharp peak in the photoelectron spectrum due to the favorable Franck-Condon overlap. The last means of generating negatively charged anion is valence anions where an electron occupies the molecular orbital of the neutral species. When a molecule has a positive electron affinity (EA), an electron enters its lowest unoccupied molecular orbital (LUMO) to become a stable valence anion. Orbital rearrangement would follow upon electron attachment due to the changes in electron configuration.

Clusters are generated when the unit species form an aggregate. In general, the size of the molecular clusters are in the range of Å~nm, which lies between molecule and bulk systems. Anion clusters stabilize themselves or are stabilized by the solvation of solvent molecules. Neutral clusters are stabilized by a dispersion force like van der Waals interaction; however, a charge-dipole interaction which is more powerful than the dispersion force stabilizes anion clusters.

1.5 Negative ion photoelectron spectroscopy

The photoelectric effect explains the electron ejection from the metal upon the irradiation.[53] When the light irradiates the metal, photoelectrons are ejected with a

certain amount of kinetic energy (EKE) that matches the difference between the incident photon energy and the work function of the metal (Φ).

$$\mathrm{EKE} = h\nu_0 - \Phi \qquad (1.9)$$

Similarly, an electron is ejected from the orbital of the anion when the anion interacts with light. An electron from a singly occupied molecular orbital (SOMO) of the anion is ejected with the kinetic energy that matches the difference between the incident photon energy and the EBE.

$$\mathrm{EKE} = h\nu_0 - \mathrm{EBE} \qquad (1.10)$$

Negative ion photoelectron spectroscopy (PES) measure the EKE of the ejected electrons. Even though operates based on the same basic principles as a conventional neutral PES, negative ion PES has intrinsic properties that differs from those of a neutral PES. Leaving electron feels weak electric field since remaining moiety is a neutral species that opposite to the neutral PES that leaving electron feels strong Coulombic attraction from cationic core. Furthermore, the direct detachment channel is dominant since there is no Rydberg state in the anions. Unlike with anions, there are many Rydberg states above and near the ionization threshold which may cause the competitive autoionization via Rydberg state.

Since an anion is well defined at its vibronic ground state, we can obtain information of neutral states from PES. Following the Franck-Condon principle and Koopmans' theorem, we can indirectly deduce information regarding an anionic state. The peak intensity is proportional to the transition probability, and this is governed by the Franck-Condon factor that is determined by the overlap between

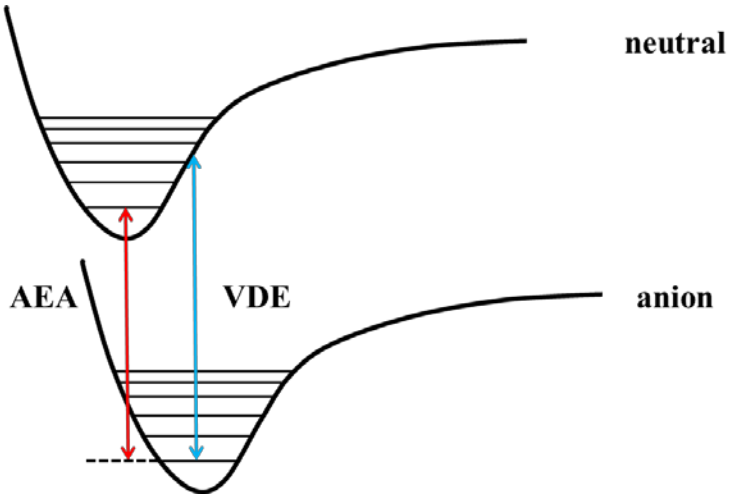

Figure 1.5 Potential energy surface diagram that represents the adiabatic electron affinity (AEA) and vertical detachment energy (VDE)

the vibrational wave functions of both states since electronic transition is a vertical transition. Koopmans' theorem states that the ionization energy equals the negative value of the highest occupied molecular orbital (HOMO) in a closed-shell. This theorem assumes that the electron has no effect on any other electrons during any process. Although the attachment and detachment of the electron do in reality affect the remaining electrons, Koopmans' theorem is still useful for approximation.

Electron affinity (EA) is generally inferred from adiabatic electron affinity (AEA) which is the difference of the energy between a neutral molecule and anion in its optimized structure. However, it is very difficult to obtain the AEA experimentally since electronic transition is too faster than the nuclear motion. Thus, we evaluate the vertical detachment energy (VDE) in place of the AEA which is a difference of the energy between the anion and the neutral molecule with an anionic structure (Figure 1.5).

Chapter 2. Experimental Sections

2.1 Stimulated emission depletion (STED) nanoscopy

2.1.1 Basic photophysics of STED

A fluorescent molecule is excited to the S_1 state when it absorbs light of the proper wavelength (vibronic transition). After fast vibrational relaxation (~ps), it returns to the S_0 state via a radiative (fluorescence) or non-radiative transition. However, if we apply an additional beam of energy which is similar to the difference between the vibrationally excited state of the S_0 and the vibrationally ground state of the S_1 before emission of fluorescence, the population at the S_1 is depleted to the S_0 through stimulated emission (Figure 2.1a). The stimulated emission depletion wavelength is generally red-shifted far from the excitation wavelength (> 100 nm). The relation between excitation, detection and STED wavelength for ATTO647N dye is depicted in Figure 2.1b.

A STED beam usually follows a short excitation beam after ~150 ps delay to ensure that most of the excited molecules undergo vibrational relaxation to the ground state of the S_1. The use of a short excitation pulse makes the excited state population build up quickly during each cycle (Figure 2.2). In reality, however, the two pulses partially overlap due to the Gaussian temporal profile of the beams. Assuming that a rectangular-shaped STED beam with a pulse width τ_s is turned on at t = 0, depletion of the excited state population (k_{STED}) begins and competes with spontaneous emission (k_r) and non-radiative decay (k_{nr}).

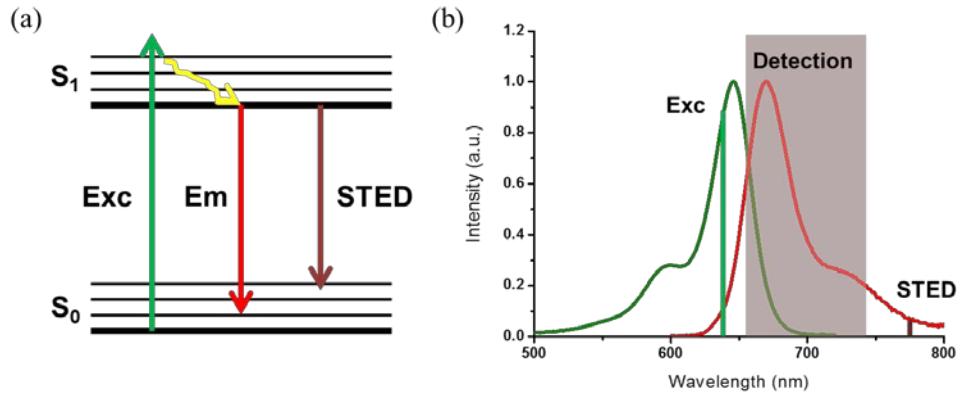

Figure 2.1 (a) Simple two-level Jablonski diagram of common organic dye depicts the molecular transition involved in STED nanoscopy. (b) Relation between the excitation, detection and STED wavelengths for ATTO647N dye.

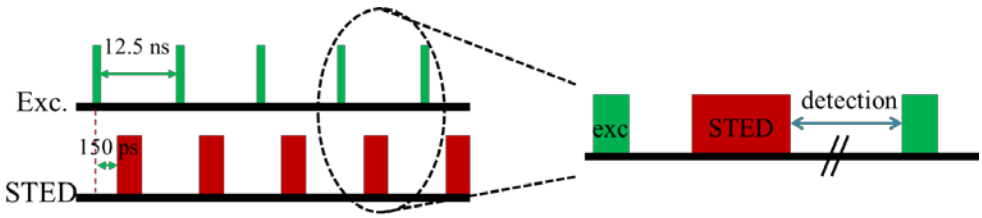

Figure 2.2 Pulse sequences in pulse-pulse STED system. Ideally, there is a 150 ps time gap between excitation and STED pulses, however, there is an overlap due to the Gaussian-shaped temporal profile.

We can thus derive the equation for normalized population probability (n_1):

$$\begin{aligned} \frac{dn_1(t)}{dt} &= -\left(k_f + k_{STED}\right)n_1(t) \qquad 0 \le t \le \tau_s \\ \frac{dn_1(t)}{dt} &= -k_f n_1(t) \qquad\qquad\qquad t > \tau_s \end{aligned} \tag{2.1}$$

where k_f is the spontaneous decay rate ($k_f = k_r + k_{nr}$). If we solve the above equation, we can obtain the probability of finding molecules in S_1.

$$\begin{aligned} n_1(t) &= n_1(0) \times \exp\left[-\left(k_f + k_{STED}\right)t\right] \qquad 0 \le t \le \tau_s \\ n_1(t) &= n_1(\tau_s) \times \exp\left[-k_f(\tau - \tau_s)\right] \qquad\qquad t \ge \tau_s \end{aligned} \tag{2.2}$$

Thus, the probability to find molecules in S_1 decays exponentially with lifetime of $(k_f + k_{STED})^{-1}$ and k_f^{-1}. The time averaged population of the S_1 (ρ_1^{avg}) is important since all that measured are detected photons during certain time intervals. ρ_1^{avg} can be approximated by means of the following equation:

$$\begin{aligned} \rho_1^{avg} &= \left(\frac{1}{jT}\right) \times \left[\int_0^T n_1(t)dt + \int_T^{2T} n_1(t)dt + \cdots + \int_{(j-1)T}^{jT} n_1(t)dt\right] \\ &\approx \left(\frac{1}{jT}\right) \times \left(j \times \int_0^T n_1(t)dt\right) = \frac{1}{T} \times \int_0^T n_1(t)dt \approx \frac{1}{T} \times \int_0^\infty n_1(t)dt \end{aligned} \tag{2.3}$$

Where T is an inverse of the frequency of the light and j is a dwell time. The average photon count (N) without the STED beam (fluorescence) is

$$N(k_{STED} = 0) = \frac{\zeta k_r}{T} n_1(0) \left(\frac{1 - exp(-k_f \tau_s)}{k_f} + \frac{exp(-k_f \tau_s)}{k_f}\right) \tag{2.4}$$

and the average photon count (N) with the STED beam is

$$N(k_{STED}) = \frac{\zeta k_r}{T}\left(n_1(0)\int_0^{\tau_s}\exp\left(-\left(k_f + k_{STED}\right)t\right)dt + n_1(\tau_s)\int_{\tau_s}^{\infty}\exp\left(-k_f(t-\tau_s)\right)dt\right)$$
$$= \frac{\zeta k_r}{T}n_1(0)\left(\frac{1-exp\left(-(k_f+k_{STED})\tau_s\right)}{k_f + k_{STED}} + \frac{exp\left(-(k_f+k_{STED})\tau_s\right)}{k_f}\right) \quad (2.5)$$

where ζ is the detection efficiency. We can also obtain the fluorescence suppression factor (η) by STED beam as follow:

$$\eta(t \geq \tau_s) = \frac{N(k_{STED})}{N(k_{STED}=0)} = \exp(-k_{STED}\tau_s) = \exp(-\sigma_s\gamma_s\tau_s I_{STED}) \quad (2.6)$$

In above equation, σ_s is a stimulated emission cross section at λ_s, γ_s is an inverse of the photon energy (λ_s/hc) and I_{STED} is the intensity of the STED beam that defines the I_s, the saturation intensity where half of the fluorescence is suppressed.

$$I_s = \frac{ln2}{\sigma_s\gamma_s\tau_s} \quad (2.7)$$

A continuous wave (CW) laser can also be used as a STED beam like Figure 2.3. It does not need any complex optics (discussed in chapter 3) and is inexpensive relative to the cost of femtosecond pulsed laser.

To obtain a higher resolution, the I_{STED} has to be increased which may cause other pathways to compete with the STED process (Figure 2.4). Re-excitation or direct excitation by a strong STED beam may lower the depletion efficiency.[19,26] In addition, transient absorption or excited state absorption followed by an intersystem crossing to the triplet state also lowers the STED efficiency.[54] Lastly, transition from S_1 to S_n may cause permanent photobleaching of the dye.[55] However, this is rare for

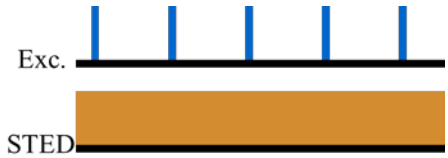

Figure 2.3 A Pulse-CW STED system. Since STED beam comes from CW laser, no synchronization between two beams is necessary.

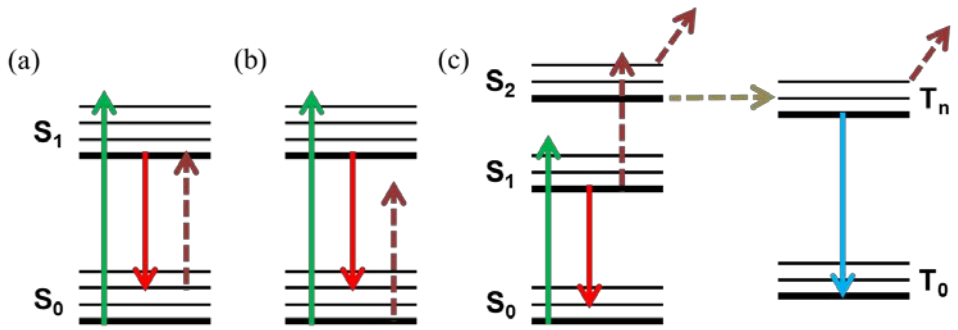

Figure 2.4 (a) Re-excitation, (b) direct excitation, and (c) transient absorption and photobleaching by strong STED beam that may lower the STED efficiency.

most commonly used dyes.[56]

2.1.2 Resolution

In the absence of a STED beam, an excitation beam has a diffraction limited point spread function (PSF) with a ~λ/2NA lateral resolution which cannot be smaller than 200 nm in full width at half maximum (FWHM) with confocal microscopy (Figure 2.5a). The overlap of another doughnut-shaped STED beam (Figure 2.5b) with an excitation beam effectively suppresses the fluorescence except in the narrow center region (Figure 2.5c). In principle, there is no limit to the lateral resolution in STED nanoscopy since the higher the STED beam power is, the higher the resolution that can be achieved.[57] Our STED system routinely achieves 20 nm resolution in two dimensions (Figure 2.6).

We can evaluate the PSF of confocal microscopy with the following approximation:

$$h_c(r) \cong exp\left(-\frac{4ln2r^2}{d_c^2}\right) \qquad (2.8)$$

where d_c is a FHWM of the confocal PSF. We can also evaluate the effective PSF of STED nanoscopy with $H_{STED}(r) = h_c(r) \times \eta(I_{STED}(r))$, where $I_{STED}(r)$ is the intensity distribution of the STED beam which is a product of a quadratic function and a Gaussian function that describe the central zero and the crest of the STED beam, respectively with the maximum intensity (I_m) at the doughnut crest (r_m).

$$I_{STED}(r) \cong \left(\frac{eI_m}{r_m^2}\right) r^2 \times exp\left(-\frac{r^2}{r_m^2}\right) \qquad (2.9)$$

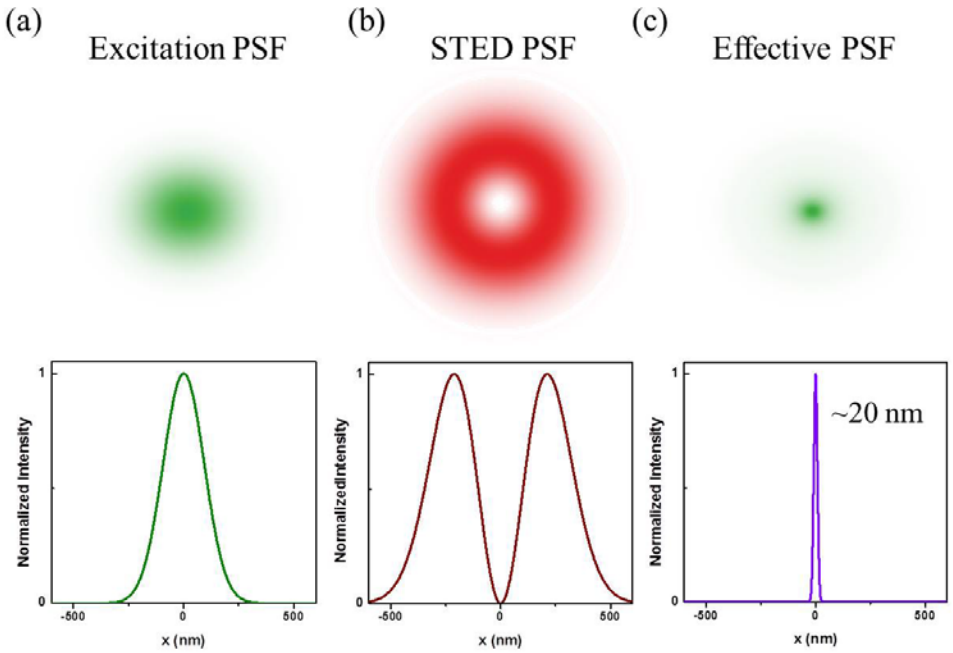

Figure 2.5 xy cross-section images and line profiles of (a) excitation beam, (b) STED beam, and (c) effective focal spot.

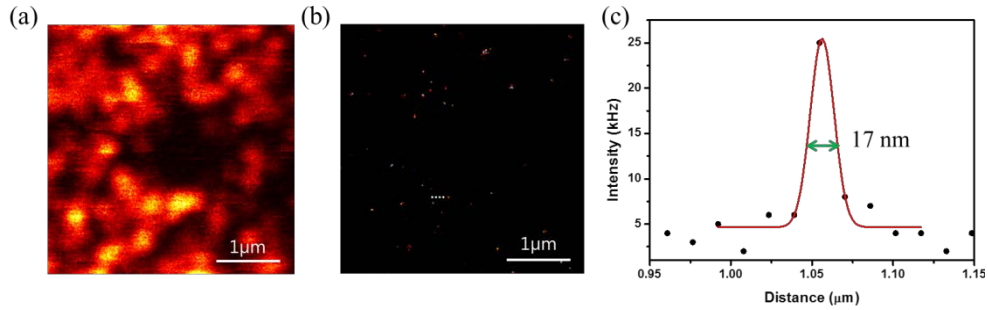

Figure 2.6 (a) confocal and (b) STED images of 20 nm fluorescent beads. (c): line profile of white dotted line in (b).

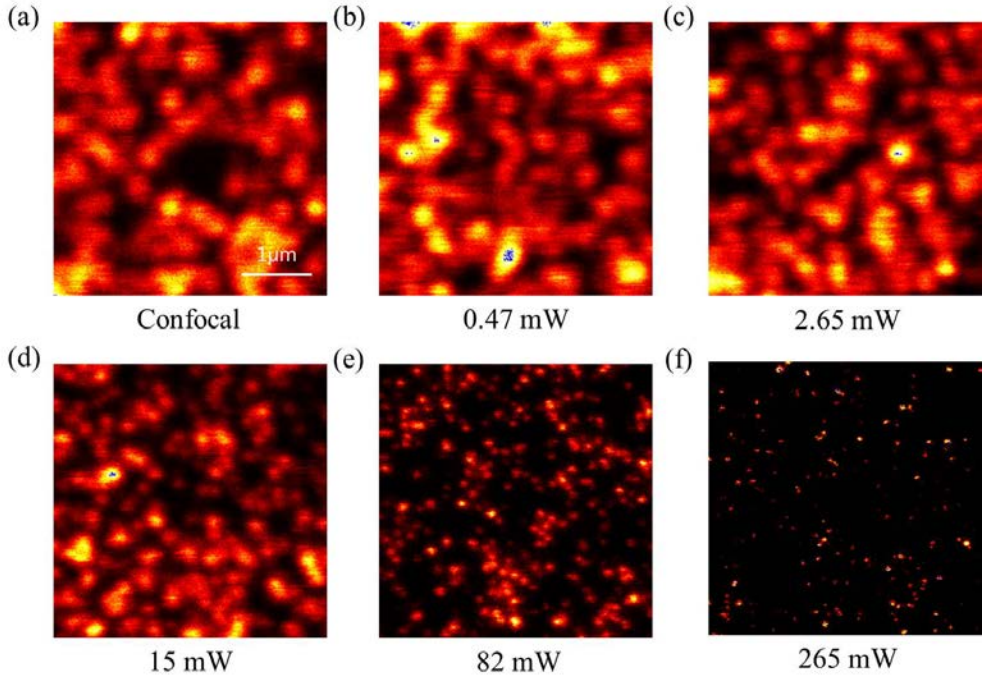

Figure 2.7 Effect of the STED beam intensity on lateral resolution probed by 20 nm fluorescent beads.

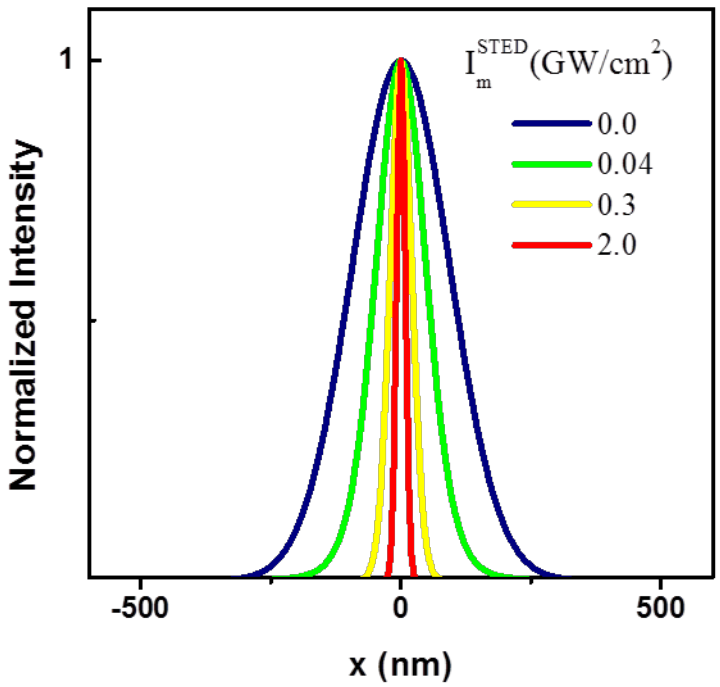

Figure 2.8 Line profile of the doughnut center region as the STED beam intensity increasing

Inserting equation 2.9 into $I_{STED}(r)$ gives the effective PSF of STED nanoscopy.

$$\begin{aligned} h_{STED}(r) &= h_c(r) \times exp\left(-\frac{ln2 I_{STED}(r)}{I_s}\right) \\ &\cong \exp\left(-\frac{4ln2r^2}{d_c^2}\right) \times exp\left(-\frac{4ln2\beta I_m r^2}{I_s}\right) \\ &= \exp\left(-4ln2\left(\frac{1}{d_c^2}+\frac{\beta I_m}{I_s}\right)r^2\right) \end{aligned} \qquad (2.10)$$

Thus, the resolution of STED nanoscopy can be formulated as the following equation:

$$\Delta r \cong \frac{d_c}{\sqrt{1+\beta d_c^2 I_m/I_s}} \qquad (2.11)$$

Since the resolution is proportional to the inverse square root of the STED beam intensity, one has to increase the STED beam intensity four times to achieve twice the desired resolution enhancement. The effect of the STED beam intensity on lateral resolution was visualized in Figure 2.7 with 20 nm fluorescent beads under various STED beam intensities. In addition, the line profile of the center region is depicted as the STED beam intensity increased (Figure 2.8).

2.1.3 Experimental setup

Our detailed pulse-pulse STED nanoscopy setup is represented in Figure 2.9. A femtosecond pulsed Ti:Sapphire laser (< 100 fs, 80 MHz, 690 nm~1040 nm, Mai Tai HP, Spectra-Physics) is used as a light source for both the excitation and the

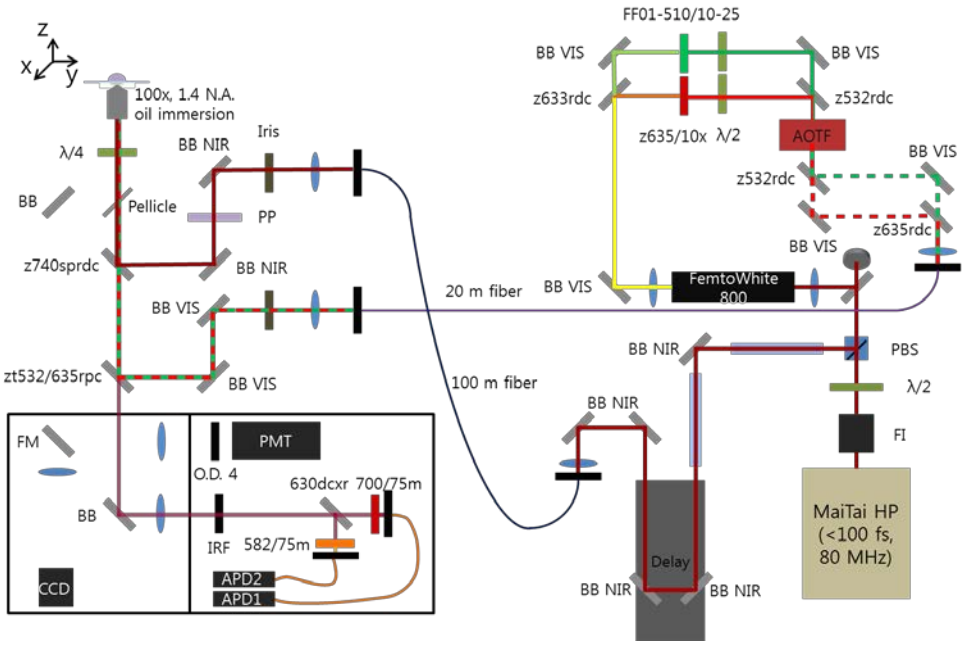

Figure 2.9 Schematic of STED nanoscopy: PBS: polarizing beam splitter, BB: broad band mirror, AOTF: acousto-optic tunable filter, PP: phase plate, λ/2: half-waveplate, λ/4: quarter-waveplate, FM: flip-mirror, PMT: photomultiplier tube, APD: avalanche photodiode, IRF: IR-blocking filter, CCD: charge-coupled device.

STED beam. For excitation, *p*-polarized 780 nm light is focused into a photonic crystal fiber (FemtoWhite800, NKT Photonics) to generate a supercontinuum. Two kinds of filters (z635/10x and z532/5x, Chroma) are used to select the excitation wavelengths. Alternatively, acousto-optic tunable filter (AOTFnC-VIS, AA Opto-Electronic) is used to filter the resonant wavelength into an acoustic wave. A 20 m-long polarization-maintaining single mode fiber (PM460-HP, Thorlabs) filters and guides the excitation beam to microscope body. *s*-polarized 780 nm light passes through two glass rods (ROD-12-12-200-FDS90-600-900, CVI) and is stretched to ~5 ps to prevent spectral broadening. This beam is further stretched to 280 ps by a 100 m-long polarization-maintaining single mode fiber (PMJ-A3HPC-3S-633-4/125-3-100-1-SP, OZ Optics). Two beams are collimated by f = 40 mm achromatic lenses and reflected by dichroic mirrors (z740sprdc for STED beam and zt532/635rpc for excitation beam, Chroma). The polarizations of the two beams are made circularly using an achromatic half-waveplate and an achromatic quarter-waveplate to obtain nearly zero intensity at doughnut minimum. A two-dimensional (2D) doughnut shape is made by inserting a phase plate (VPP-1a, RPC Photonics) in the middle of the beam path. Due to the sequential phase shifting from 0 to 2π, destructive interference makes the central part of the STED beam vanishes after being focused by an objective lens. Both beams are focused by an oil immersion objective lens (HCX PL APO 100X, 1.4 NA, Leica). For fine alignment and to establish the overlap of the two beams, scattered photons from the 80 nm gold bead are detected by photomultiplier tube (PMT, MP962, Perkin

Elmer) in non-confocal mode.

The fluorescence signal from the sample passes through the emission filter and IR-blocking filter, and further spatially being filtered by multimode fiber (62.5 μm diameter M31L01, Thorlabs) which serves as a confocal pinhole. Photons are detected by avalanche photodiode (APD, SPCM-AQR-14-FC, Perkin Elmer). For time-correlated single photon counting (TCSPS), we use another APD (PFCCTC-FCAPC, MPD) with a short instrumental response function. A multi-channel analyzer (P77782, FAST ComTec) or TCSPC module (SPC-150, Becker & Hickle) performs further processes to make images. The sample is placed on the piezo stage (NanoMax-TS, Thorlabs) and scanned three dimensionally. The piezo stage is controlled by an analog output board (PCI-6731, National Instrument). The images are visualized and further processed using the Imspector program kindly supported by Andreas Schönle of the Max-Planck Institute.

A CW laser can also be used as a STED beam as seen in Figure 2.3. However, to do so one has to increase the intensity of the STED beam to achieve the same resolution obtained in a pulse-pulse STED system by about a factor of $\Gamma = \delta/[\tau ln2]$, where δ denotes the interval of the laser pulse.

2.2 Total internal reflection fluorescence microscopy (TIRFM)

The entire experimental setup is depicted in Figure 2.10. Three kinds of lasers and the lamp are used as light sources. 633 nm (25-LHP-928-249, Melles Griot), 532

nm (85-GCA-020, Melles Griot), and 488 nm (85-BCD-030-115, Melles Griot) light is allowed to enter the inverted microscope (TE-300, Nikon) by a mechanical shutter (VMM-D3, Uniblitz) to illuminate the sample through a high-NA objective lens. The position of the sample is controlled using motorized sample stage that can be operated via joystick. Wide-field images are obtained with a mercury lamp when we observe only the supported lipid bilayer or fluorescence recovery after photobleaching (FRAP) experiment. By tilting one of the broad band mirrors, the TIR condition is produced to observe the membrane patches near the surface while eliminating the background signal from floating vesicles. Fluorescence from the sample is collected using the same objective lens and recorded using a CCD camera (iXon 897, Andor) after passing through an emission filter and are further processed using the MetaMorph program (Figure 2.11).

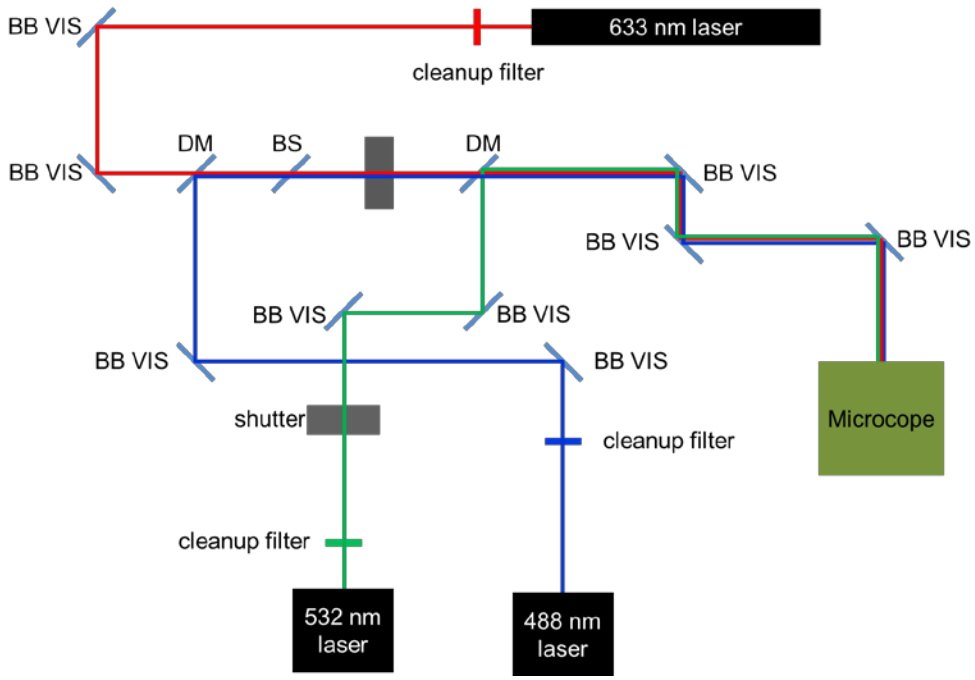

Figure 2.10 An entire experimental setup for TIRF experiment.

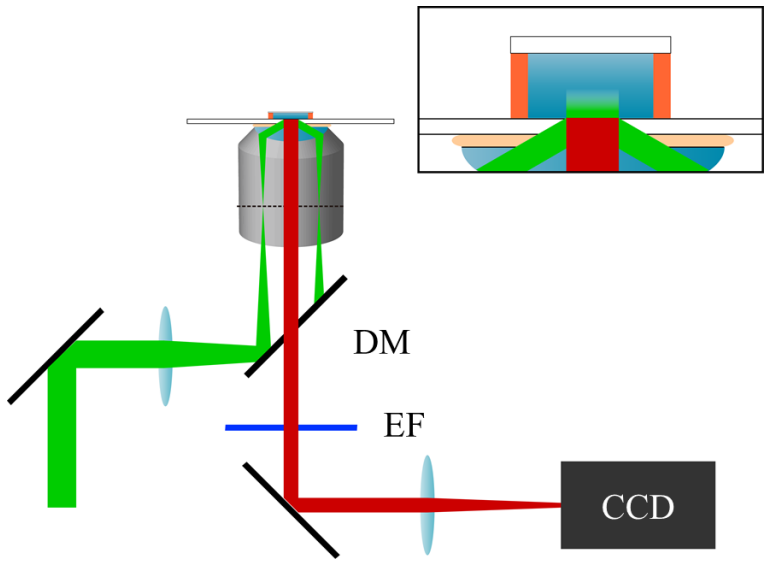

Figure 2.11 Detailed representation of the TIRFM setup near the microscope. Excitation beam is focused at back focal plane of the objective lens. Fluorescence from the sample is collected by same objective and detected by CCD camera. Inset: enlarged view of the glass-water interface where TIR phenomenon occurs to generate evanescent wave.

2.3 Negative ion photoelectron spectroscopy

2.3.1 General information about apparatus

Our molecular beam chamber combined with mass spectrometer and photoelectron spectrometer is represented in Figure 2.12. Two diffusion pumps (DP, 2400 L/s and 1800 L/s, Varian) and two turbo molecular pumps (TMP, 150 L/s, 400 L/s, Alcatel) are used to produce vacuum in four independent chambers differentially. A gate valve is used to isolate the TMP-pumped chambers from DP-pumped chambers. Pressure is maintained at 3 x 10^{-5} torr and 1 x 10^{-7} torr in the first and fourth chambers during the operation with 5 bar of Ar gas.

The first chamber contains a molecular beam source and extraction electrodes. Anions are generated by thermal expansion with Ar carrier gas followed by electron impact. The anion source is floated on a -1,000 V voltage isolated from the ground voltage.

The second chamber has two einzel lenses and two perpendicular deflectors to focus and guide the anions. Ion optics are made of brass because of its high conductivity. To prevent the formation of local charge due to the collision of the anions, the surface of the ion optics is coated with Aerodag G graphite spray. The second and third chambers serve as a Wiley-McLaren type TOF-MS[49] to select the anions by their mass before entering the fourth chamber. The mass of the anions is detected by a microchannel plate (MCP) assembly of 25 mm active diameter (Galileo Electro Optics) and analyzed by oscilloscope. The FWHM of the M/ΔM is

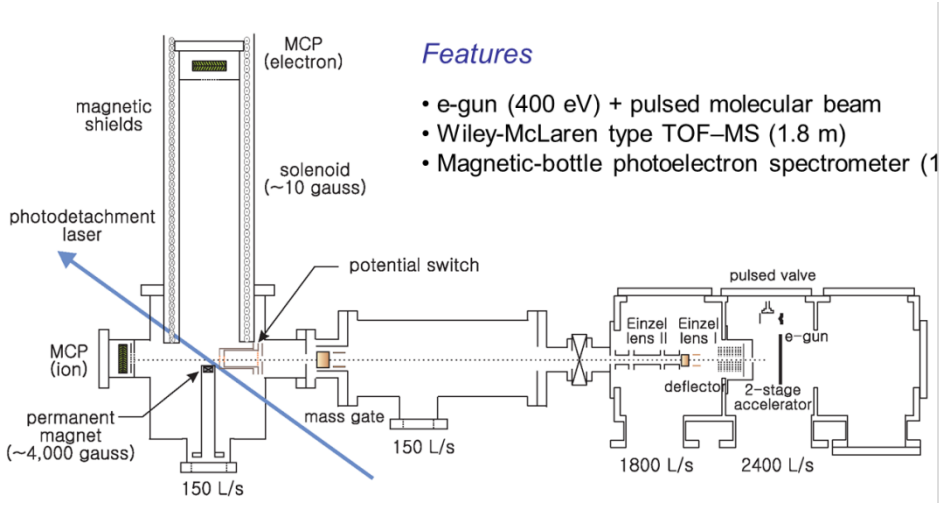

Figure 2.12 Schematic diagram of anion photoelectron spectroscopy chamber assembly.

about 200 at 300 amu.

The fourth chamber is a photodetachment chamber where photoelectrons are ejected by irradiation of the laser. The photoelectrons are ejected in all directions (4π radian), making it impractical to collect enough photoelectrons with one MCP detector due to time considerations. Thus, we adopt a magnetic-bottle type photoelectron spectrometer which uses a magnetic field to collect nearly 100% of the photoelectrons.[58,59] Instead, there is a broadening of the photoelectron spectrum that lowers the energy resolution. Photoelectrons are detected by a MCP assembly of 25 mm active diameter, amplified by a pre-amplifier (SR 240, Stanford Research System) and stored in a PC through a GPIB cable connected to the multichannel scaler (SR 430, Stanford Research System).

Photons from the output of the pulsed Nd:YAG laser (Surelite I-20, Continuum) are used to detach electrons from the anions. Fundamental (1,064 nm, 1.164 eV), second harmonics (532 nm, 2.329 eV), third harmonics (355 nm, 3.496 eV), and various wavelengths from Nd:YAG-pumped dye laser (SCANMATE, Lambda-Physik) are used. The photoelectron spectrum (PES) is calibrated with that of O_2^-. Timing and triggering are controlled by delay generator (DG 535, Stanford Research System) as depicted in Figure 2.13.

2.3.2 Molecular beam source

There are many methods by which one can generate an anion, including electron impact, laser ablation, electric discharge, and electron attachment. Our molecular

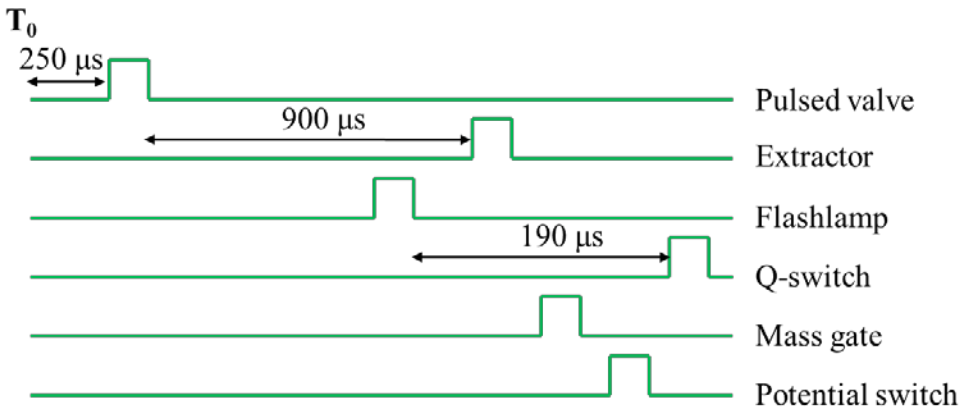

Figure 2.13 Example of the pulse sequences in DG 535 that synchronizes electronics to obtain photoelectron spectrum.

beam utilizes the slow electron attachment to jet-cooled molecules. When molecules expand through a very small nozzle with high pressure of noble carrier gas, they undergo many collisions and are cooled. The electron impact method first ionizes the Ar gas and produces secondary low-kinetic energy electrons. These electrons are attached to neutral molecules with positive electron affinity (EA).

$$Ar + e^- (400\ eV) \rightarrow Ar^+ + e^- (< 400\ eV) + e^- (\sim 0\ eV) \qquad (2.12)$$

$$M + e^- (\sim 0\ eV) \rightarrow M^- \qquad (2.13)$$

Figure 2.14 shows our anion source in detail. A pulsed solenoid valve operates at 10 or 20 Hz according to the wavelength of the laser. The original coil is replaced with a Teflon-coated one capable of performing at high temperatures up to 250 °C. Thermally emitted electrons from a home-made electron emitter (ES-020, Kimball Physics) are accelerated with 400 eV energy.

2.3.3 Wiley-McLaren type TOF-MS

To obtain the whole mass spectrum in a single measurement, we use a TOF-MS. Ions of different masses are accelerated by the same kinetic energy, resulting in different arrival times at a MCP detector. The ions can thus be distinguished by their velocity. There is a severe problem in using only one accelerating stage since a small difference in the initial position may results in a broadening of the mass spectrum. A Wiley-McLaren type TOF-MS uses two sequential accelerating stages (weak field to strong field, Figure 2.15) to reduce the spectral broadening.[49]

The focusing point of an ion is independent of its mass and depends on the

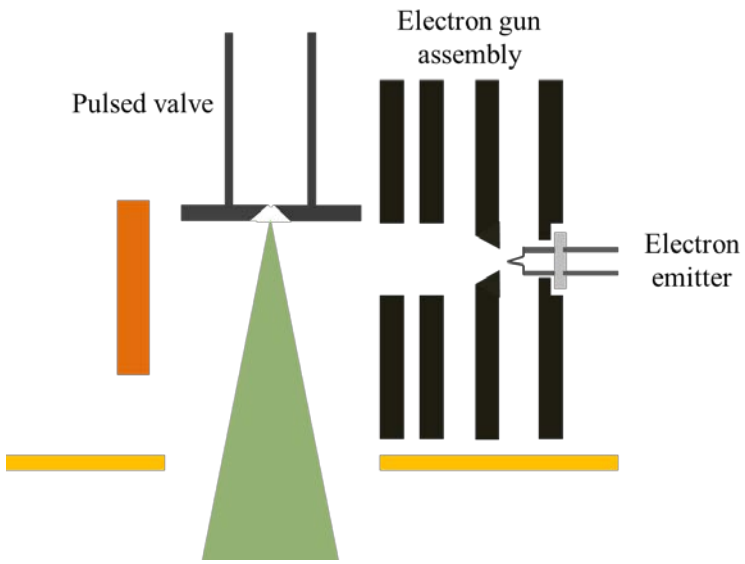

Figure 2.14 The anion source is composed of the pulsed solenoid valve, an electron emitter and several electrodes.

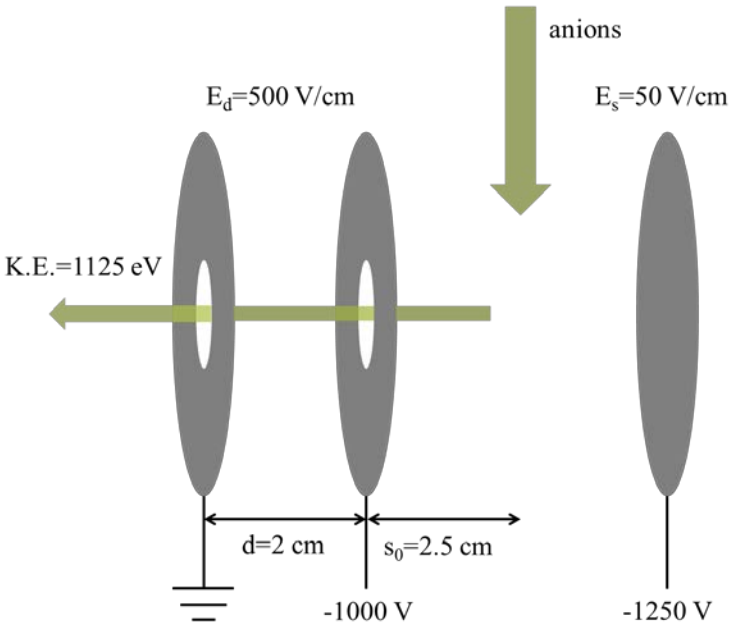

Figure 2.15 Details of Wiley-McLaren type TOF-MS. Acceleration of anions is achieved in two steps with different electric fields.

extraction and acceleration electric fields. If ion has an energy of 1,100 eV, s_0 = 2.5 cm, d = 2 cm and D = 1.8 m, spatial focusing is achieved with E_s = 40 V/cm and E_d = 500 V/cm at MCP. In the real experiment, condition is modified to E_s = 50 V/cm and E_d = 500 V/cm due to the ion optics in the flight tube.

2.3.4 Mass gate

There are numerous anions of different masses in a molecular beam out of which specific anions must be selected. This is done using a mass gate that uses a pulsed electric field to cut off the anions by their flight time. The mass gate system consists of three electrodes and two perpendicular deflectors (Figure 2.16). Two mass gates are used to discard the anions which are lighter and heavier than the ones of interest. An electrical pulse is applied to mass gate 1 before the anions of interest pass through deflector, with the lighter anions being deflected to the electrode and discarded. Likewise, an electrical pulse is applied to mass gate 2 after the anions of interest pass through the deflector, with the heavier anions being deflected to the electrode and discarded.

2.3.5 Potential switch

In a magnetic-bottle type photoelectron spectrometer, the energy resolution is affected by Doppler broadening due to the efforts made to have high collection efficiency. To minimize Doppler broadening, deceleration of the anions is essential.

$$\Delta E = 4\left(\frac{m_e}{m_i}E_e E_i\right)^{1/2} \qquad (2.14)$$

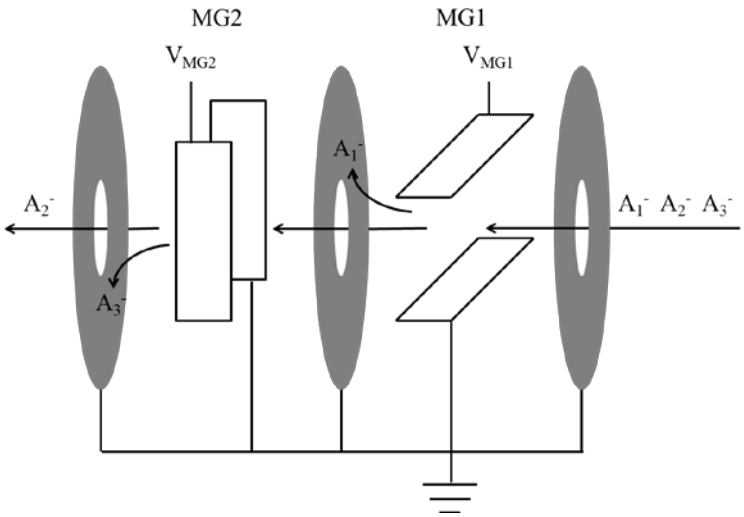

Figure 2.16 Mass gates with two deflectors. MG1 deflects the lighter anions while MG2 deflects the heavier ions than the anions of interest.

where E_e and E_i are the kinetic energy of photoelectron and its parent anion, respectively, and m_e and m_i are their mass. According to equation 2.14, the energy resolution enhanced nine times when the photoelectron has a kinetic energy of 1 eV from the anions (300 amu) , and the kinetic energy of the anion is reduced from 1,100 eV to 20 eV.

A potential switch plays a role as a decelerator prior to photodetachment. It consists of two cylindrical tubes (Figure 2.17). When anions enter the inner tube, a high voltage is applied to the inner tube, where anions do not feel the change of potential in the inner tube. The anions are decelerated when they come out of the inner tube due to the difference between ground potential and high potential in the inner tube.

2.3.6 Magnetic-bottle type photoelectron spectrometer

A field-free TOF photoelectron spectrometer is useful for investigating the angular distributions of photoelectrons with high energy resolution. However, it is not suitable for anions with a very small photodetachment cross-section. In order to increase the collection efficiency, Kriut and Read developed a magnetic-bottle type photoelectron spectrometer. A rare-earth magnet (~4,000 G, 10 mm thickness and 10 mm diameter) is used to generate strong magnetic field in the direction of the MCP detector to guide photoelectrons. A long solenoid coil (1 m long and 15 cm in diameter) is used to generate a weak magnetic field (10 G) with a 0.8 A current. To mitigate the effect of unwanted external magnetic fields such as the earth's magnetic

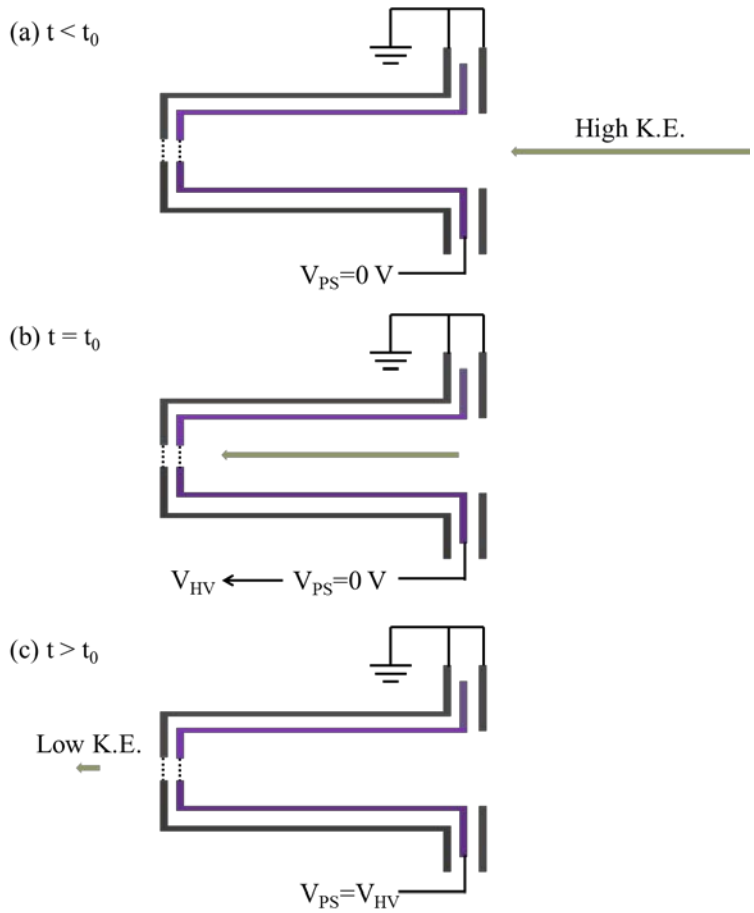

Figure 2.17 The action of potential switch. (a) $t < t_0$, anions with high kinetic energy (1,120 V) enter the inner tube. (b) $t = t_0$, 1,100 V is applied to the inner tube. (c) $t > t_0$, anions feel a deceleration due to the difference of the voltage between ground and the inner tube.

field, the magnetic bottle is wrapped in several sheets of μ-metal.

The EBE is calculated from the results obtained from the photoelectron spectrum with a few additional parameters.

$$EKE = \frac{1}{2} m_e \frac{L^2}{(t - t_0)} + V_c \qquad (2.15)$$

In the above equation, t_0 is a time-zero correction factor and V_c is a contact potential (typically ~0.1 eV). However, the raw data of photoelectron spectrum is a function of time, *I*(t), which is converted by multiplying it by the Jacobian factor.

$$|I(E)| = \left| I(t) \frac{dt}{dE} \right| = \left| I(t) \left(\frac{L^3}{m_e L^2} \right) \right| \qquad (2.16)$$

As seen in Figure 2.18, the raw spectrum of O_2^- is converted by Jacobian factor. EBE is then, obtained by subtracting EKE from incident photon energy.

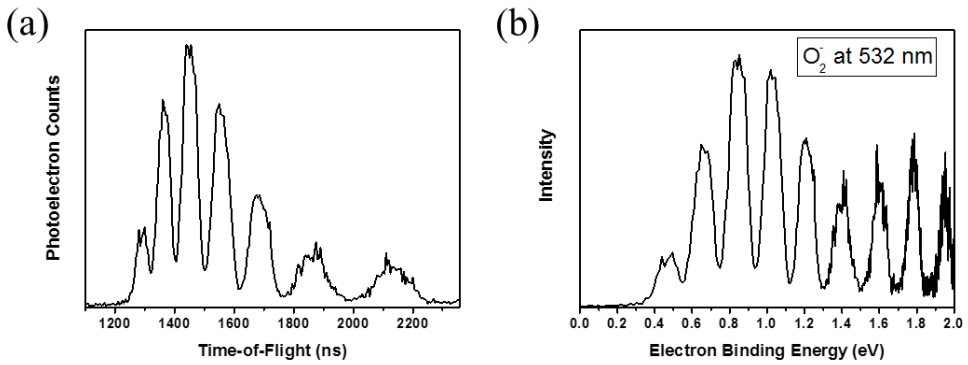

Figure 2.18 (a) The raw photoelectron spectrum and (b) converted photoelectron spectrum of O_2^-.

Chapter 3. Direct and precise length measurement of single, stretched DNA fragments by dynamic molecular combing and STED nanoscopy

3.1 Introduction

Deoxyribonucleic acid (DNA) is an essential molecule for life in our planet with rich chemistry surrounding its structure and reactions. While mostly forming genes that carry genetic information,[60,61] certain DNAs have structural,[62] regulatory,[63] and enzymatic[64,65] properties. X-ray diffraction, electron microscopy, and scanning probe microscopy were used to study the structures of DNA, but imaging of a single DNA in biological environment remains far too challenging a goal to date. Optical microscopy was deemed unsuitable to observe an object less than in size the optical diffraction limit, $\lambda/2NA$ ~200 nm (λ: wavelength of visible light, NA: numerical aperture), for over a century until the advent of super-resolution nanoscopy since the middle of the 1990's.[19] Recently, stimulated emission depletion (STED) nanoscopy and its variant ground state depletion (GSD) nanoscopy were respectively demonstrated to achieve a lateral resolution of ~6 nm and 12 nm for a single color center in fluorescent nanodiamonds,[66,67] STED nanoscopy was also employed to image the intact form of λDNA on a poly-L-lysine coated coverslip with a spatial resolution of 45 nm, which is comparable to the persistence length of DNA.[68]

Agarose gel electrophoresis has been widely used in biochemistry to measure the size distribution of DNA molecules by separating them by their electrostatic charge upon applying an electric potential.[69,70] Despite its popularity and usefulness, it requires determination of agarose concentration and use of a ladder DNA to

compare the size of sample DNAs. The upper limit of DNA size measurable with this technique is ~10 kbp at a reasonable resolution, which is too short to identify longer DNAs such as λDNA or chromosomal DNA. Finally, one can only observe bands of an ensemble of DNA, but not single DNA molecules.

On the other hand, fluorescence has been effectively used to measure the size of single DNA molecules. Goodwin *et al*. utilized flow cytometry to detect the fluorescence signal from individual fragments of flowing DNA.[71] Foquet *et al*. also measured the fluorescence burst from single DNA fragments using a microfluidic channel.[72] Laib *et al*. deduced the length of certain DNA fragments by comparing the brightness of the fluorescence signal assuming that it is proportional to the length of DNA.[73] Although these methods generally allow quick measurements, they are indirect in nature and often fraught with large standard deviations. In contrast, we use direct optical imaging by STED nanoscopy in this work to measure the length of individual DNA molecules linearly stretched on a coverslip.

DNAs can be stretched by using capillary force,[74,75] force flow, [75] and dynamic molecular combing (DMC).[76-78] DMC is simple and gives superior reproducibility. Short DNAs as well as longer ones such as chromosomal DNA can be easily stretched. AFM was also used to image the combed DNA on various substrates.[79-81]

In this work, we report a new method to quickly measure the length of individual DNA fragments by the combined method of DMC and STED nanoscopy. This new method is shown to be highly accurate and precise.

3.2 Experiment

3.2.1 Sample preparation

Initially, we tested the feasibility of dynamic molecular combing with a full sequence λDNA (48,502 bp, N3011S, New England Biolabs). A λDNA stock was diluted to 800 pM with TE buffer (10 mM Tris, 1 mM EDTA, 20 mM $MgCl_2$, 100 mM NaCl, pH 7.4). 10 μL of diluted sample was incubated at 75°C for 15 min to prevent the adhesive ends of DNA from sticking to each other. The sample was then transferred to ice and incubated for 40 min with the addition of YOYO-1 (13 μM in TE buffer) to achieve the ratio of 1 dye per 5 base pairs. The brightness of the dye increased greatly (over 500 fold) upon binding to DNA.[82] After incubation, the sample was loaded in Teflon chamber to which 1.5 mL of TE buffer (10 mM Tris, 1 mM EDTA, 20 mM $MgCl_2$, 100 mM NaCl, pH 7.4) was further added.

λDNA fragments (N3012S and N3014S, New England Biolabs) were diluted with TE buffer (10 mM Tris, 1 mM EDTA, 20 mM $MgCl_2$, 100 mM NaCl, pH 7.4) by a factor of 20. 10 μL of the sample DNA was mixed with 3 μL of YOYO-1 and left at room temperature for 40 min. After 40 min at room temperature, the mixture was added to 1.5 mL of TE buffer (10 mM Tris, 1 mM EDTA, 20 mM $MgCl_2$, 100 mM NaCl, pH 7.4) and loaded in Teflon chamber.

Since we did not know the exact concentration of the fragments, we went through many trials to determine the optimal amount of dye. An excess amount of dye resulted in a low S/N ratio due to the adhesion of free dyes on coverslip that

appeared as background. On the other hand, an insufficient amount of dye yielded poor image quality with many dark spots along the DNA strands. In our experiment, we predicted that a DNA intercalating dimeric cyanine dye YOYO-1 would be added to *Bst*EII or *Hin*dIII-treated λDNA at the similar dye per base pair ratio as in the full sequence λDNA experiment. These results accurately correspond to that of Persson *et al.*[68] YOYO-1 dye is known to bind to a single-stranded as well as double-stranded DNA. Therefore, although the sticky ends have a length of about 12 bps for whole λDNA, 5 bps for *Bst*EII-treated λDNA, and 4 bps for *Hin*dIII-treated λDNA, they can be observed in the images.

3.2.2 Silanization of coverslips

A coverslip was washed with acetone, transferred into a beaker, sonicated for 20 min in 1:1 mixture of deionized water and methanol, and sonicated again in chloroform for another 20 min. To clean the surface of coverslip, it was treated with piranha solution (a 7:3 mixture of 98 % sulfuric acid and 35% hydrogen peroxide, Sigma) for at least 2 hours in a water bath kept at 65°C until all bubbles disappeared. The coverslip was then transferred to a clean beaker with Teflon tweezers, where it was alternately sonicated in chloroform and deionized water. The final treatment was done in chloroform to keep the hydrophobic surface intact. The coverslip was transferred to a new beaker containing 100 mL of *n*-heptane, where 100 μL of trimethoxy(7-octen-1-yl)silane (Sigma) was added and incubated overnight while moisture was removed with Drierite (Sigma). The coverslip was recovered and

sonicated in *n*-heptane, deionized water and chloroform, sequentially for 5 min, and stored in a dry jar with Drierite.

3.2.3 Dynamic molecular combing

A silanized coverslip was immersed in the Teflon chamber containing the sample DNA. After 5 min, the coverslip was constantly pulled up at a speed of 200 μm/sec (Figure 3.1) using a glass extraction system, that is transformed from syringe pump, to control the pull-up speed mechanically. A longer incubation time in Teflon chamber resulted in the sticking of both adhesive ends of DNA to coverslip, hampering the normal combing process. The pulling speed also affects the quality of DNA stretching (Figure 3.2). After the pulling up step, the coverslip was placed on a slide glass and mounted with 97% 2, 2'-Thiodiethanol (Sigma). Nail polish was used to prevent leakage of TDE. Specifically, mercaptoethanolamine and trolox were added to reduce photobleaching and photoblinking.

3.2.4 STED nanoscopy

Our pulsed-CW STED nanoscopy system is schematically shown in Figure 3.3. A super-continuum light was generated from the 800 nm output of a Ti-Sapphire laser (<100 fs, 80 MHz, Mai Tai HP, Spectra-Physics) by a photonic crystal finer (FemtoWhite800, NKT Photonics). An excitation filter (FL488-10, Thorlabs) was used to select light at 488 nm, which was used as an excitation source (2 μW at focal plane to minimize photobleaching by the excitation beam). For stimulated emission depletion, we used the strong CW output (120 mW at focal plane) of a 592

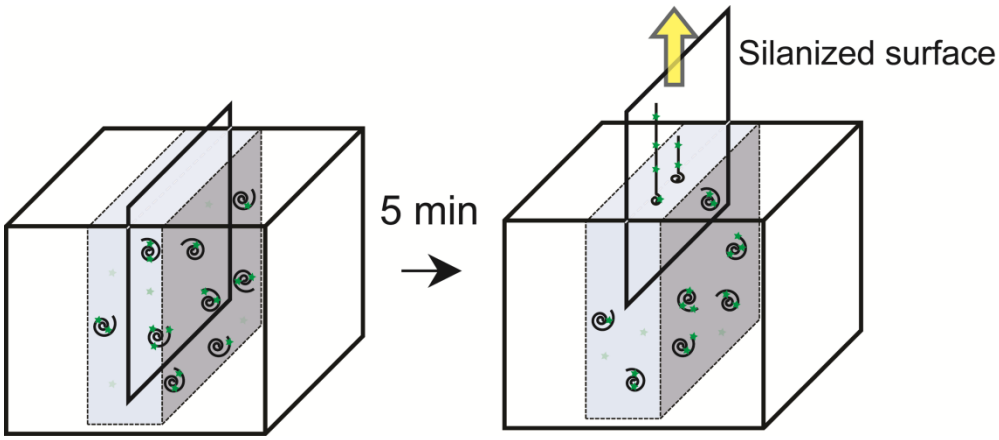

Figure 3.1 Schematic representation of dynamic molecular combing. A solution containing DNA labeled with YOYO-1 was transferred to a Teflon chamber. A silanized coverslip was immersed in the solution and left there for 5 min. The coverslip was then pulled up at a speed of 200 μm/sec to yield linearly stretched DNA on the coverslip.

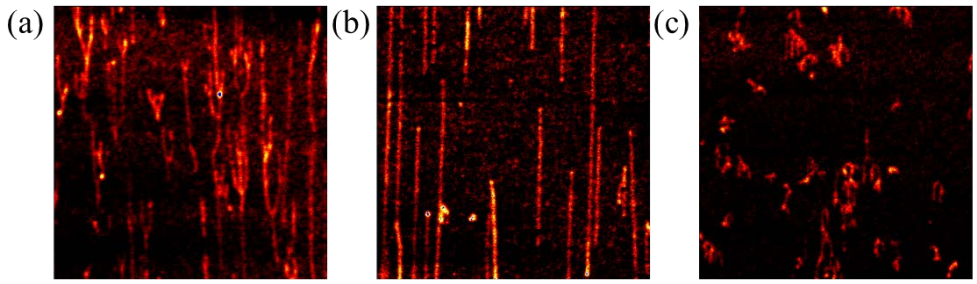

Figure 3.2 The difference in linearity of combed λDNA with pull-up speed. (a) 20 μm/sec, (b) 200 μm/sec, and (c) 1,000 μm/sec

nm laser (2RU-VFL-P-1500-592, MPB Communications). The two beams propagated collinearly after reflection at dichroic mirrors and became circularly polarized by half- and quarter-waveplate in view of the random orientation of the dipole of the dyes. The STED beam passed through a phase mask (VPP-1a, RPC Photonics) and became a doughnut shape at focal plane. The excitation beam was made to overlap with the doughnut-shaped STED beam at the focal point. No synchronization was necessary since we used a CW STED beam. An oil immersion type objective (HCX PL APO, 100X, 1.4 NA, Leica) was used to focus the two beams and to collect fluorescence through a home-built inverted confocal fluorescence microscope. The sample area was scanned by a piezo stage (NanoMax-TS, Thorlabs) and the fluorescence signal was detected by an avalanche photodiode detector (SPCM-AQR-14-FC, Perkin Elmer) after passing through an emission filter (FF01-530/55-25, Semrock). We obtained images repeatedly at the same position and found that each object appeared at exactly the same position, which indicates that spatial drifting due to the piezo stage was negligible. The strong CW STED beam was blocked by a 594 nm notch filter (NF03-594E-25, Semrock). The imaging acquisition time for an area of 18 μm x 18 μm was less than 30 s. Imaging and post-imaging processes were performed with the software programs *Imspector* and *Image J*. Line profiles of DNA strands were obtained from the image and the end-to-end length based on the point spread function of our STED scheme is automatically calculated.

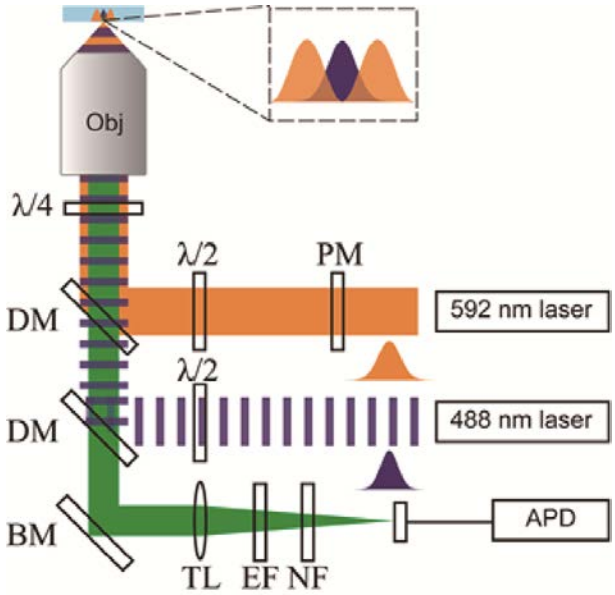

Figure 3.3 Schematic of our pulsed-CW STED nanoscopy system. PM: phase mask, λ/2: half-waveplate, λ/4: quarter-waveplate, DM: dichroic mirror, BM: broadband mirror, Obj: objective lens, TL: tube lens, EF: emission filter, NF: notch filter, APD: avalanche photodiode.

3.3 Results and discussion

The top panel of Figure 3.4 shows whole-area confocal and STED images of the *Bst*EII-treated λDNA fragments linearly stretched, while the bottom panel compares the same images in a more densely populated region of DNA fragments. With the STED beam on, the fluorescence from YOYO-1 was almost completely depleted except in the central part where the STED beam intensity was nearly zero. No spatial drifting induced by piezo stage was detected. The FWHM width of our STED images was enhanced by 5 times to ~47 nm from that of confocal images (~240 nm, Figure 3.5). Some of the very closely placed DNA fragments that are not fully resolved by confocal imaging can be readily distinguished by STED imaging (white boxes in the bottom panel of Figure 3.4).

The density of the combed DNA showed strong dependence on pH and salt concentration. In our case, DNA fragments were most densely combed at pH 7.4 and salt concentration of 20 mM $MgCl_2$ and 100 mM NaCl (Figure 3.6 and 3.7). Most of DNA fragments were well-stretched linearly by DMC, but we also found a small number of fragments that were U-shaped or crooked. The U-shaped fragments result from those which stick to the surface of the coverslip at two ends before pulling, while the crooked ones appear to be formed during the combing process as the hydrophobic interaction of DNA base with the silanized surface of coverslip changes as DNA is pulled.

The concentration of YOYO-1 also affects the quality of the image (Figure 3.8).

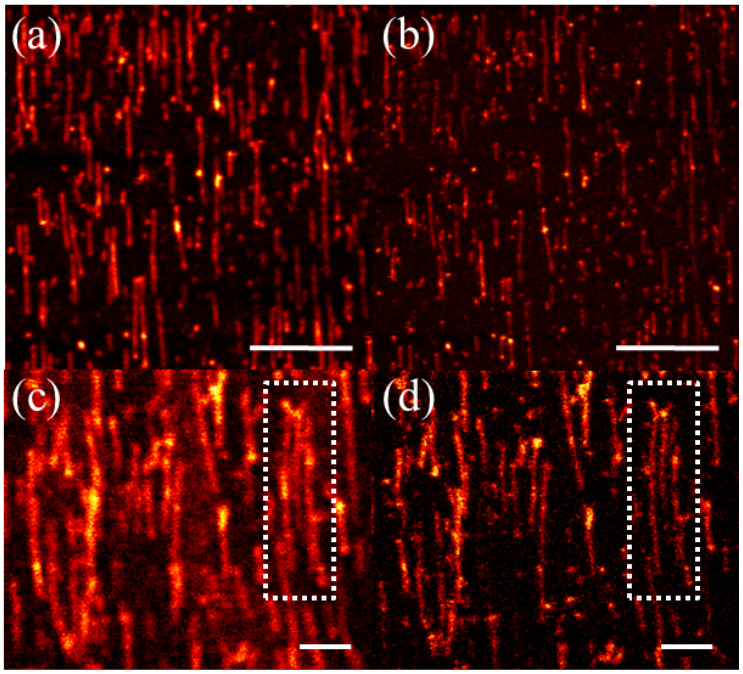

Figure 3.4 Top: Whole-area (a) confocal and (b) STED images of combed λDNA fragments digested with *Bst*EII restriction enzyme. λDNA fragments were stained with YOYO-1, an intercalating dye, and stretched on a coverslip by dynamic molecular combing. Image size: 18 μm x 18 μm. Scale bar: 5 μm. Bottom: (c) confocal and (d) STED images of a more densely populated region of DNA fragments. The 3 strands in the white box are shown to be clearly resolved in the STED image. Scale bar: 1 μm.

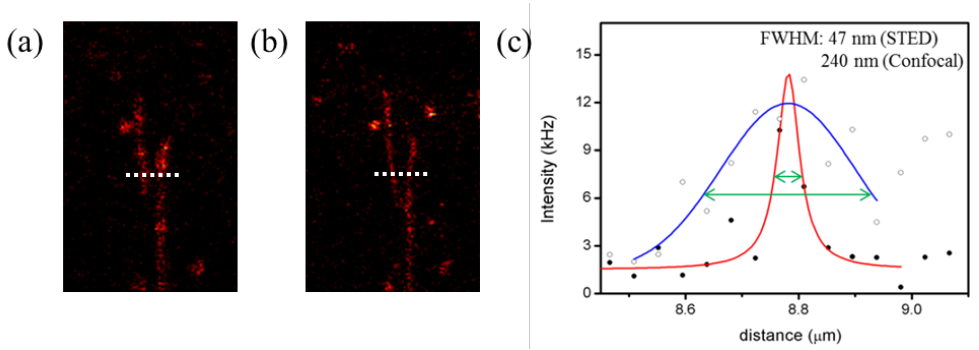

Figure 3.5 FWHM lateral width of (a) confocal vs. (b) STED images, with (c) their line profiles along the white dashed lines fitted by Gaussian (confocal) and Lorentzian (STED) curve. Because of the low spatial resolution of the confocal image, the signal intensity to the right side of the peak (at distance > ~8.8 μm) is due to a nearby fragment.

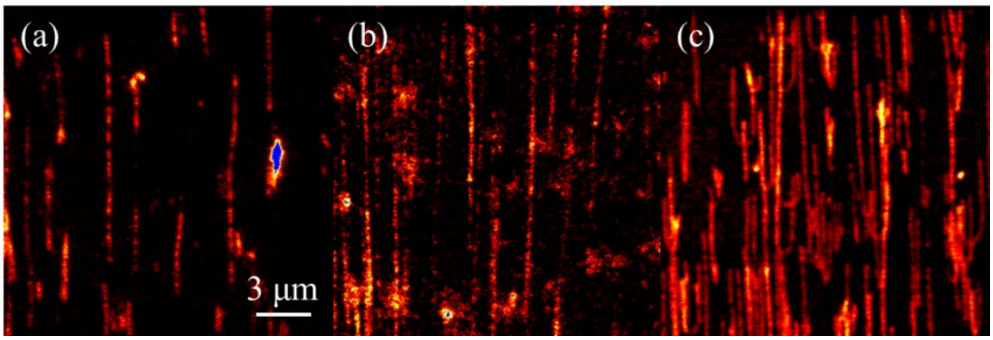

Figure 3.6 The difference in density of combed λDNA with pH of the buffer. (a) MES buffer at pH 4.5, (b) MES buffer at pH 5.5, and (c) TE buffer at pH 7.4

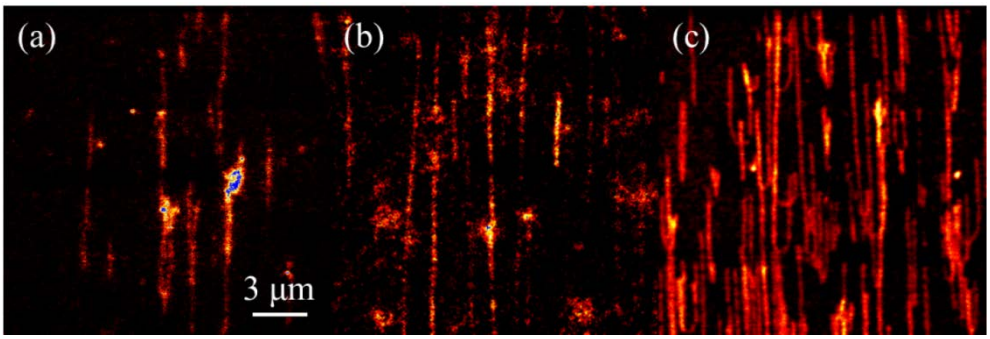

Figure 3.7 The difference in density of combed λDNA with salt concentration of the TE buffer. (a) without salt, (b) 100 mM NaCl, and (c) 20 mM $MgCl_2$ and 100 mM NaCl.

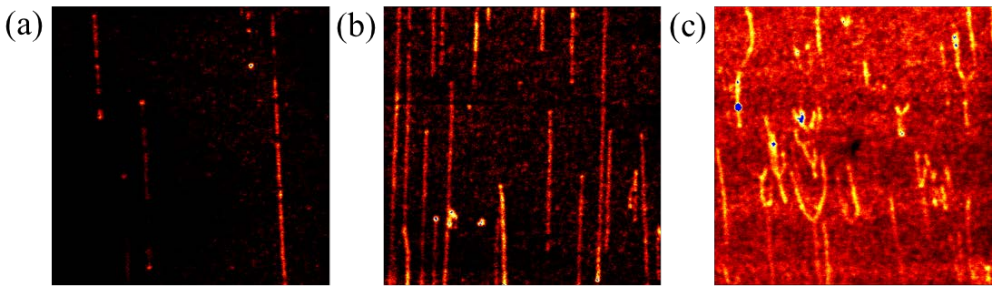

Figure 3.8 The brightness difference of combed λDNAs depends on the ratio of dye per base pairs in the MES buffer. (a) 1:30, (b) 1:5, and (c) 1:1.

At a low concentration, a large number of dark regions appear along strands, which makes it difficult to identify intact fragments. At high concentrations, the signal-to-noise (S/N) ratio suffers, but the concentration of YOYO-1 little affects the spatial resolution itself.

Since the pulse-CW STED scheme generally has low depletion efficiency due to the unintended temporal overlap of the two beams and the continuous irradiation of the STED beam, a strong intensity of the latter is needed to achieve a similar performance to the pulse-pulse scheme. A possible danger with using a strong STED beam is the photobleaching of YOYO-1, which would lead to a disrupted image of DNA along its strand. In order to avoid this problem, the average power of the STED beam was adjusted to 120 mW at focal plane and the dwell time per pixel never exceeded 100 μs and mainly remained at 75 μs, to obtain a typical photon count of about 30~50 per pixel. A shorter dwell time may be used to completely avoid photobleaching at the expense of a low S/N ratio. Of course, another alternative would be to use a pulsed STED beam, which requires synchronization with the excitation beam but would definitely improve the resolution without much risk of photobleaching. We also used a minimum power of the excitation beam (2 μW) as it affected the degree of photobleaching. When we obtain confocal and STED images from the same region for comparison, we always obtain the confocal image first to avoid photobleaching by the STED beam.

Figure 3.9 and 3.10 show the size distribution of DNA fragments treated with *Bst*EII and *Hin*dIII, respectively. It is known that the distance between two adjacent

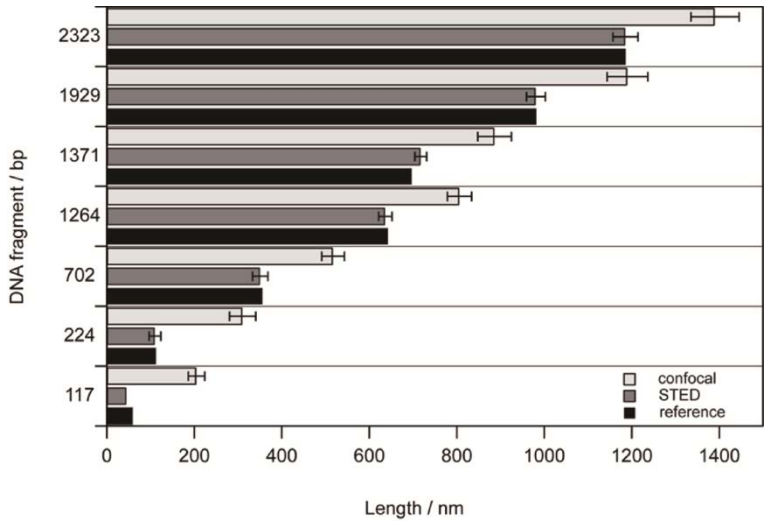

Figure 3.9 Histogram for the size distribution of *Bst*EII-treated λDNA fragments. Each horizontal panel gives the length of a DNA fragment measured by confocal microscopy (top, light gray bar) and STED nanoscopy (middle, gray bar) along with the reference value provided by the manufacturer (bottom, black bar). An excellent agreement between the STED and reference values are consistently seen, whereas the confocal values tend to be far off, relatively more so for shorter fragments. For each fragment, 20 DNA strands were analysed and averaged for the length measurement.

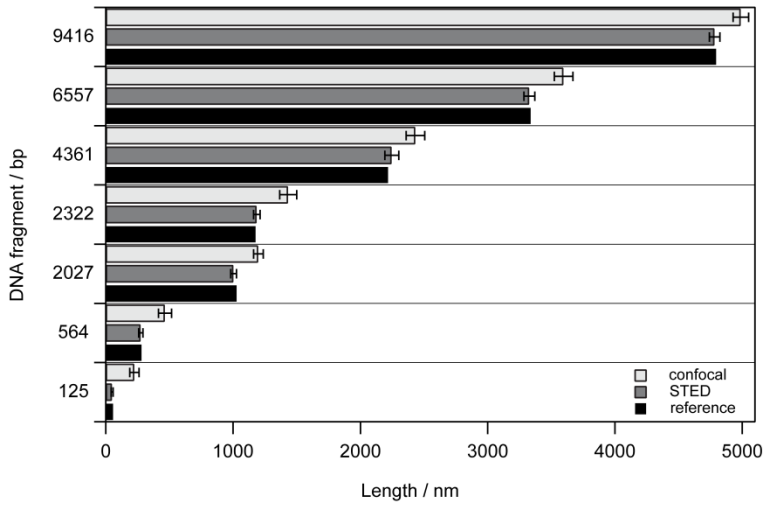

Figure 3.10 Histogram for the size distribution of *Hin*dIII-treated λDNA fragments. Each horizontal panel gives the length of a DNA fragment measured by confocal microscopy (top, light gray bar) and STED nanoscopy (middle, gray bar) along with the reference value provided by the manufacturer (bottom, black bar). An excellent agreement between the STED and reference values are consistently seen, whereas the confocal values tend to be far off, relatively more so for shorter fragments.

base pairs is considerably increased with DMC by a factor of up to ~2 depending on various experimental conditions such as the substrate for DMC, shear strength of the adsorbed DNA, and adhesion energy at the DNA-surface interface.[78] In our case, this elongation factor is estimated to be ~1.5 by an analytical approximation,[83] yielding an interpair distance of ~0.5 nm. When we converted the measured lengths of DNA fragments into the number of base pairs using this value, the result was in excellent agreement, perhaps fortuitously but at least consistently, with the reference values provided by the manufacturer of our sample (Table 3.1 and 3.2). The result in Figure 3.9 and 3.10 represent that a combination of dynamic molecular combing and STED nanoscopy was demonstrated to accurately and precisely analyze the lengths of DNA widely ranging in size from 117 bp to 23,130 bp. Moreover, distinguishing 1,264 bp from 1,371 bp as well as 117 bp from 224 bp is a sufficient evidence to prove the feasibility of the new method to copy number variation assay.

To make the length determination more consistent, we also performed tapping mode AFM measurements for both intact λDNA and fragmented λDNA on identical coverslip surface. We found that the lengths from AFM measurement agree very well with the reference values as well as our STED measurement (Figure 3.11, 3.12 and Table 3.2). Compared with STED, AFM has much longer acquisition time and can damage the stretched DNAs on a coverslip due to the direct interaction between AFM tip and the stretched DNAs. Actually, some stretched DNAs were broken while AFM measured the morphology of fixed DNAs on a coverslip.

Confocal (in nm) (standard deviation)	4,988 (121)	3,597 (146)	2,433 (147)	1,433 (135)	1,200 (76)	466 (102)	225 (72)
STED (in nm) (standard deviation)	4,784 (82)	3,327 (86)	2,247 (110)	1,187 (51)	1,004 (46)	275 (34)	50 (14)
Reference (in nm) (in bp)	4,802 (9,416)	3,344 (6,557)	2,224 (4,361)	1,184 (2,322)	1,034 (2,027)	288 (564)	64 (125)
STED/Reference ratio (in %)	99.63	99.49	101.03	100.25	97.10	95.49	78.13

Table 3.1 Comparison of the lengths of *Hin*dIII-treated λDNA fragments experimentally measured by confocal microscopy (top row) and STED nanoscopy (second row) along with the reference values provided by the manufacturer (third row). The STED results are much more accurate (closer to the reference values, shown by the excellent STED/Reference ratios given in the bottom row) and precise (with smaller standard deviations) than the confocal values. DNA fragments as short as 50 nm (~100 bp) can be easily measured and discriminated in size by STED nanoscopy, in strong contrast to confocal microscopy.

AFM (in nm)	1,187	972	700	639	358	123	58
(standard deviation)	(60)	(52)	(33)	(16)	(29)	(13)	(10)
STED (in nm)	1,186	981	718	637	351	110	45
(standard deviation)	(57)	(43)	(27)	(30)	(35)	(27)	(0)
Reference (in nm)	1,188	984	699	645	358	114	60
(in bp)	(2,323)	(1,929)	(1,371)	(1,264)	(702)	(224)	(117)

Table 3.2 Comparison of the lengths of *Bst*EII-treated λDNA fragments experimentally measured by AFM (first row) and STED nanoscopy (second row) along with the reference values provided by the manufacturer (third row). The lengths from AFM measurement agree very well with the reference values as well as our STED measurement.

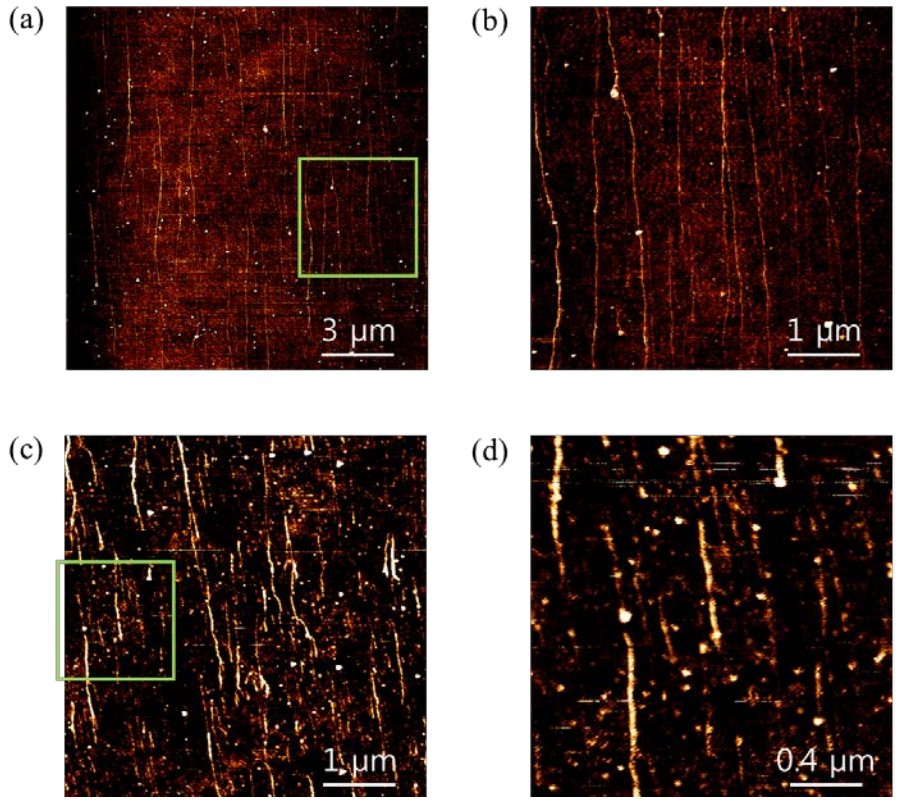

Figure 3.11 Tapping mode AFM images of (a) combed λDNA (15 µm x 15 µm) and (b) enlarged image of green-boxed region of (a). AFM images of (c) combed λDNA fragments digested with *Bst*EII restriction enzyme and (d) enlarged image of green-boxed region of (c).

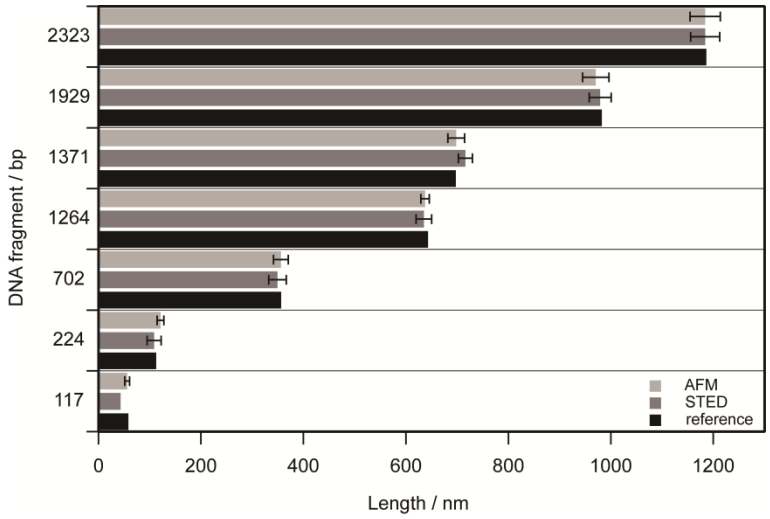

Figure 3.12 Histogram for the size distribution of *Bst*EII-treated λDNA fragments. Each horizontal panel gives the length of a DNA fragment measured by AFM (top, light gray bar) and STED nanoscopy (middle, gray bar) along with the reference value provided by the manufacturer (bottom, black bar). An excellent agreement among AFM, STED and reference values is consistently seen.

We note that the STED results are not only much more “accurate” (closer to the reference values) but also more “precise” (with smaller standard deviations) than the confocal values. Point spread function of our STED system is ~50 nm, which may contribute to the discrepancy between the STED-measured vs. actual length. For DNA fragments longer than ~1,000 bp, the ratio of the STED vs. reference values ranges from 99.49% to 101.03%. DNA fragments ranging widely in size from 117 bp to 23,130 bp could be stretched and identified at once in a single image.

Determination of the size of DNA can be utilized in the diagnosis of the genetic disorder caused by copy number variation (CNV). Unlike single nucleotide polymorphism (SNP) caused by alterations of a single base in the genome sequence, CNV results from certain fractions of the sequence entirely missing or duplicated. Recently, Baday *et al*. designed a CNV detection scheme using two-color SHRImP and SHREC.[84] They were able to resolve two probes 32 nm apart from each other, but had to modify their DNA to covalently conjugate additional dye molecules (TAMRA, Cy3 and Cy5) outside the DNA backbone, which itself was stained with YOYO-1. By comparison, our method does not need such DNA modification or fluorophore conjugation since we measure directly the size of DNA, not the distance between the single probes.

3.4 Conclusion

In summary, by using the combined method of DMC and STED nanoscopy, we demonstrated the feasibility of measuring the length of individual DNA fragments

linearly stretched on a coverslip. With this method, the lengths of DNA fragments widely ranging size could be measured accurately and precisely by super-resolution imaging, with no need for elaborate covalent conjugation steps for the dye since the intercalating dye we used can fluorescently stain DNA simply by mixing with them. Possible applications in CNV detection and diagnosis of trinucleotide disorder are anticipated.

Chapter 4. Observation of a single diffusing molecule in a sub-diffraction-limit volume by ALEX-FRET and STED nanoscopy

4.1 Introduction

Observation of a single molecule is important for biochemists and biophysicists since one can obtain information such as conformational change, interaction with other molecules from individual molecules that are possibly averaged out in ensemble condition.[85,86] To observe a single molecule with fluorescence technique, we have to reduce the focal volume or lower the concentration of the sample. Confocal microscopy offers the smallest focal volume among ever developed conventional microscope techniques.[87] Even with confocal microscope, however, one has to dilute the sample down to tens of pM to ensure there is only one molecule per observation time. In this case, we cannot obtain exact information of the interaction or kinetics of the enzyme that has a dissociation constant larger than ~nM.

Various methods have been developed to observe a single molecule in high concentration. Total internal reflection enabled us to elevate the concentration by confining axial resolution to ~100 nm with evanescent wave.[88] Zero-mode waveguide, of which diameter is much smaller than the wavelength of the light used, was utilized to generate evanescent field of which penetration depth is tens of nm.[89] Convex Lens Induced Confinement (CLIC) was carried out near the contact point of a plano-convex lens and coverglass, which confine z-axis down to 5 nm.[90] Concentration-independent single molecule spectroscopy (ciSMS) used UV and visible light for reversible photo-switching of fluorophore in high concentration of

fluorescent protein.[91] Many of them were applied to immobilized fluorophores in the presence of high level of background.

Fluorescence Resonance Energy Transfer (FRET) has been widely used to study biomolecules due to its capability of measuring short distance (1~10 Å).[92] Most intermolecular and intramolecular interactions occurring *in vivo* fall within this range. FRET efficiency (*E*) depends on R^{-6} (R: distance between two fluorophores), thus one can simply obtain information about distance and the conformational changes along the reaction. However, conventional single molecule FRET experiment cannot tell us about stoichiometry of the samples.

Alternating laser excitation (ALEX)-FRET single-molecule spectroscopy was developed to overcome the limitation of conventional smFRET experiments.[93] By adding another laser to excite acceptor molecules and alternating two excitation lasers, we can evaluate additional parameter *S* (stoichiometry) which tells us the composition of the fluorophores in the sample. By plotting *E* versus *S* in 2D, we can obtain both compositional and conformational information. In addition, ALEX-FRET technique can be extended to study 3D conformational changes by adding another proper dye.[94]

Since 1990's, many groups have tried to overcome the optical diffraction limit in far-field optical microscopy (~λ/2NA, λ: wavelength of the light used, NA: numerical aperture). Stimulated emission was applied to conventional confocal microscopy to switch-off the molecules in excited state to prevent them from emitting fluorescence.[95] Doughnut-shaped STED beam effectively depleted the

fluorescence resulting in tiny focal volume where fluorescence can be emitted. With such a method, lateral resolution was greatly enhanced down to 6 nm with single nitrogen vacancy center in fluorescent nanodiamonds.[66] In this work, we demonstrate a novel method to observe a single diffusing molecule in highly concentrated solution by combination of ALEX-FRET and STED nanoscopy (ALFRED). A single diffusing DNA strand could be observed in up to 5 nM with this method due to the sub-diffraction-limit focal volume.

4.2 Experiment

4.2.1 Sample preparation

Three kinds of single stranded DNA (20 bp) were amino-modified to be conjugated with NHS ester form of the dyes. 5' of poly T sequence was conjugated with ATTO 647N NHS ester, and 3' and 5' of each poly A sequence were conjugated with DY-510XL NHS ester to make high- and low-FRET samples. Reaction mixture was further purified with HPLC. Resulting ssDNA samples were annealed to make high- and low-FRET samples. To dilute these samples down to 5 nM, we used 30% and 40% PEG 8000 solution with quite amount of trolox as a triplet state quencher. We chose the PEG 8000 solution because of the high viscosity of the PEG solution in order to slow the diffusion of the samples. It is important to reduce a diffusion rate since an observation volume would decrease by 50 times which accompanies a shorter observation time. To obtain maximum photon counts in a short time, we increased the viscosity of the solvent. In addition to this, DNA samples would

undergo many collisions during diffusion due to the large PEG 8000 molecules which is a similar environment in the cytosol where the molecules experience the collision with several other molecules and organelles.

4.2.2 ALFRED setup

Our experimental apparatus is briefly schematized in Figure 4.1. A supercontinuum light was generated with photonic crystal fiber (FemtoWhite800, NKT Photonics) and 635 nm and 510 nm light were selected by an acousto-optic tunable filter (AOTF, AOTFnC-VIS, AA Opto-Electronic). Two beams propagated alternatingly (50 μs alternating time) after AOFT to excite ATTO647N and DY-510XL independently. To avoid the temporal cross-talk, on-time of the AOTF was adjusted to 46 μs, and 4 μs remained as off-time. 780 nm STED beam from Mai Tai HP (80 MHz, < 100 fs, Spectra-Physics) was initially stretched by two glass rods and further stretched to 280 ps by 100 m-long polarization maintaining single mode fiber (OZ Optics). The excitation beam and the STED beam were circularly polarized to ensure the effective depletion of randomly oriented dipoles of fluorophores. Phase plate (VPP-1a, RPC Photonics) modulated the phase of the STED beam to become a doughnut-shaped at focal plane. Irradiation of excitation beam followed by STED beam with 150 ps time delay suppressed fluorescence except tiny volume at the center where the destructive interference made the intensity of STED beam zero. Resulting fluorescence were divided by dichroic mirror (630dcxr, Chroma) and detected by two APDs (SPCM-AQR-14-FC, Perkin

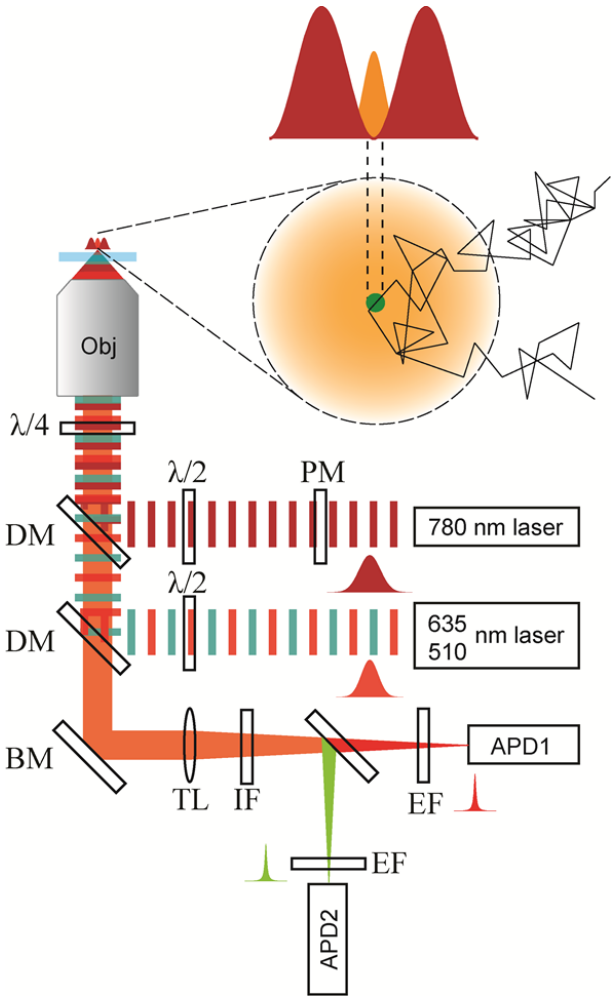

Figure 4.1 Schematic of ALEX-FRET-STED (ALFRED). Two excitation beams (635 nm, 510 nm) irradiate sample alternatingly with 50 μs alternating time. 780 nm STED beam confines the focal volume 50 times smaller than the diffraction-limited confocal volume. Thus, a single-diffusing molecule can be observed in much higher concentration. PM: phase mask, DM: dichroic mirror, BM: broadband mirror, TL: tube lens, IF: IR blocking filter, EF: emission filter.

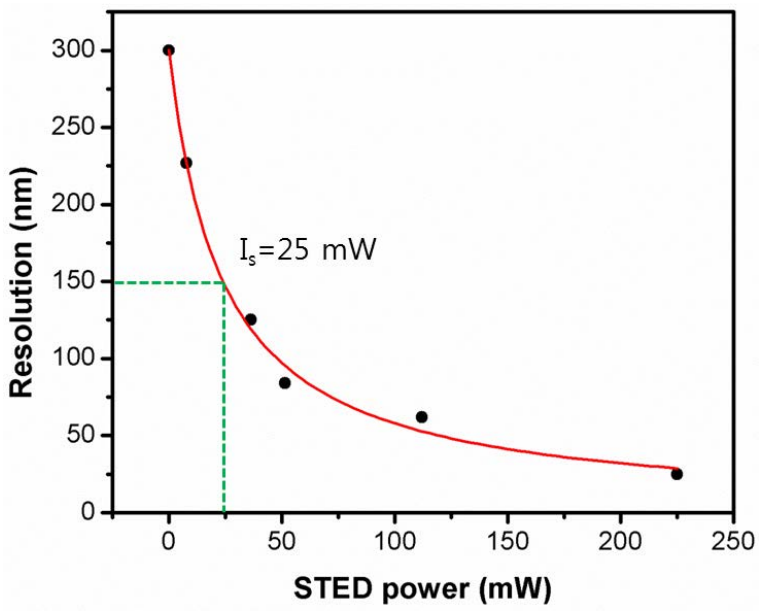

Figure 4.2 STED beam power versus resolution. Resolution was obtained from the full-width at half maximum (FWHM) value of the STED image of 20 nm fluorescent Crimson beads (Invitrogen) mounted in water. Red curve is a result of the polynomial fitting. Saturation intensity (I_s) is 25 mW at focal plane.

Elmer) after passing through band pass filters (FF01-582/75-25, Semrock and ET655LP, Chroma) and IR blocking filter (FF01-720/SP-25, Semrock). We made a reference curve for the FWHM and the STED beam power (Figure 4.2). FCS data was obtained with the correlator (Flex02-01D, Correlator.com).

4.2.3 FCS data analysis

Fluorescence correlation spectroscopy (FCS) was introduced to measure the diffusion time of the DNA samples in 30% and 40% PEG 8000 solution, which determines the binning time used in data analysis process of ALFRED. The fluctuations of the fluorescence signal in the small focal volume is occurred due to various reasons such as diffusion, triplet state, *etc*., and we can quantify these fluctuations by temporally autocorrelating the recorded fluorescence intensities. The autocorrelation function $G(\tau)$ is defined as

$$G(\tau) = \frac{< F(t) \cdot F(t+\tau) >}{< F(t) >^2} = 1 + \frac{< \delta F(t) \cdot \delta F(t+\tau) >}{< F(t) >^2} \qquad (4.1)$$

where $F(t)$ and $\delta F(t)$ mean the fluorescence signal and its fluctuation, respectively. If the fluorescence fluctuations come only from the translational diffusion of fluorescent molecules, the autocorrelation can be rewrote as following form.

$$G(\tau) = 1 + \frac{1}{N}\left(1 + \frac{\tau}{\tau_D}\right)^{-1}\left(1 + \frac{\tau}{k^2\tau_D}\right)^{-\frac{1}{2}} \qquad (4.2)$$

Here, N, τ_D and k are the average number of molecules in the focal volume, the diffusion time of the sample and the aspect ratio of the focal volume, respectively. Because the diffusion time is directly related to the diffusion coefficient of the sample, we can calculate the diffusion coefficient of the DNA samples from this analysis. Furthermore, the diffusion time also highly depends on the viscosity of the solvent, we can measure the viscosity of the 30% and 40% PEG 8000 solution using Stokes-Einstein relation.

Conventional organic fluorophores usually have additional fluctuations from other sources such as triplet state. In the case of triplet blinking, the fluorescence fluctuation can be expressed as a function of the kinetic constants describing the transition between singlet and triplet states. As a result, the autocorrelation function can be expressed as

$$G(\tau) = 1 + \left[\frac{1}{N}\left(1 + \frac{\tau}{\tau_D}\right)^{-1}\left(1 + \frac{\tau}{k^2\tau_D}\right)^{-\frac{1}{2}}\right] \cdot \left[1 + \frac{F_T}{1 - F_T}\exp\left(-\frac{\tau}{\tau_T}\right)\right] \qquad (4.3)$$

with F_T and τ_T are the fraction of the molecules in triplet state and triplet state relaxation time, respectively.

Before we analyze the FCS results, we calibrated our STED-FCS setup to confirm the focal volume and to enhance the precision of fitting process by fixing the parameter related to the focal volume, *k*. For this calibration process, we used a conventional organic dye, Cy5, whose diffusion coefficient has been well studied by previous researches. We measured the autocorrelation curve of the fluorescence

intensity from Cy5 solution (10 s acquisition, 10 times repeat), and fitted the results by using multi-curve & multi-parameter fitting algorithm. In this case, slightly modified autocorrelation function was used to fit the FCS data, which can be expressed as following equation.

$$G(\tau) = 1 + \frac{1}{N}(1 + \frac{4D\tau}{r^2})^{-1}(1 + \frac{4D\tau}{k^2 r^2})^{-\frac{1}{2}} \qquad (4.4)$$

Here *D* means the diffusion coefficient of the fluorescent molecule and *r* is the lateral $1/e^2$ dimension of focal volume where the fluorescence intensity has dropped by the factor of e^2 compared with its peak value. Through the calibration process, we can measure the volume of focal spot and can fix the spatial parameters, *r* and *k*, to accurately analyze the autocorrelation curves.

In order to measure the diffusion time of the DNA samples in the PEG solution, we obtained the autocorrelation curve for 120 s and fitted this curve by equation 4.3. All measurements were repeated 10 times and each result was fitted independently giving the average values and the standard errors to increase the reliability.

4.2.4 ALFRED data analysis

Collected fluorescence signals were saved as a photon counts per binning time. Then, they were modified to the arrays of photon counts per alternating time. With this process, we could classify the detected photons with the excitation wavelengths and emission detector (donor emission and acceptor emission from donor excitation,

and those from acceptor excitation). Direct excitation and emission leakage to other channel were negligible. Background level also checked for the case of excitation only, STED-only and both beams without the sample. We made a histogram of photon counts versus number of event. As a result, the background signal was appeared as a large peak at the lower photon counts region, and the larger value than the higher edge was chosen as a background level. With the reconstructed emission arrays, we calculated *E* and *S* values for each set of photon bursts according to the ref. 93. 2D histogram for the distribution of *E* and *S* value gave us the information about the conformation and composition.

4.3 Results and discussion

First, we demonstrated the number of molecules per focal volume in 5 nM solution with Poisson distribution, and the results were consistent with the experiment that confirmed the observation of a single molecule in concentrations we chose (Figure 4.3 (a)). Then, we acquired the FCS curve of Cy5 dye molecule to evaluate the viscosity of 30% and 40% PEG 8000 solution (Figure 4.3 (b)). Viscosity of 30% and 40% PEG 8000 solution were found to be 11.4 mPa·s and 20.4 mPa·s that are much larger than water (1.002 mPa·s at 20 °C). Thus diffusion time would increase in those solutions compared with that in water since diffusion constant greatly reduced in ALFRED condition. The diffusion time for both confocal ALEX and ALFRED was obtained by fitting FCS curve shown in Figure 4.3 (c), (d). Diffusion time reduced due to the reduced focal volume. Figure 4.4 shows the photon traces

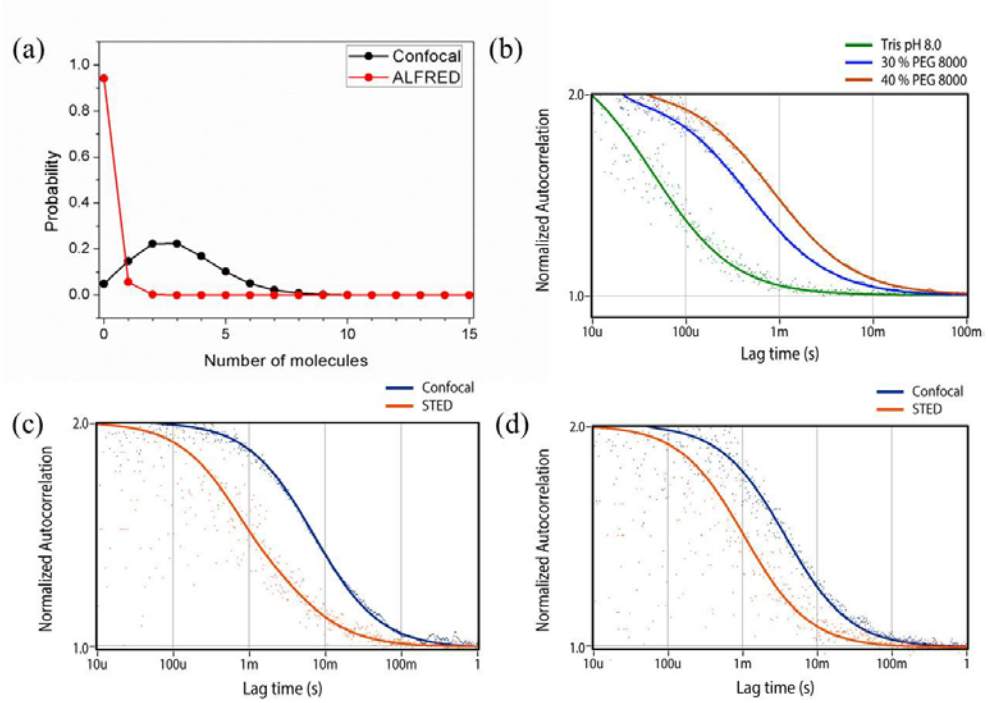

Figure 4.3 (a) Demonstrated Poisson distribution of the number of molecules in a focal volume of 5 nM solution (black: confocal, red: ALFRED), (b) FCS curve of Cy5 in Tris (green dots), 30% PEG 8000 solution (blue dots), and 40% PEG 8000 solution (orange dots). They were normalized and fitted by autocorrelation function (lines in each graph). FCS curves of dsDNA samples in confocal (blue dots) and STED condition (orange dots) in (c) 30 % and (d) 40% PEG 8000 solution. They were fitted by autocorrelation function (lines in each graph).

of 5 nM dsDNA labelled with ATTO647N and DY-510XL in 30% PEG 8000 solution (a) and 40% PEG 8000 solution (b). In this concentration, there were too many molecules in confocal volume (left graphs in each trace) whereas no or only one molecule existed in ALFRED condition (right graphs in each trace).

E and *S* values were calculated from the photon traces with following equations where $\gamma = (\Phi_A\eta_A/\Phi_D\eta_D)$, Φ is a quantum yield of the dye and η is a detection efficiency of the detector.

$$E = \frac{F_{D_{exc}}^{A_{em}}}{(F_{D_{exc}}^{A_{em}} + \gamma F_{D_{exc}}^{D_{em}})}$$

$$S = \frac{F_{D_{exc}}}{(F_{D_{exc}} + F_{A_{exc}})}$$

$$F_{D_{exc}} = F_{D_{exc}}^{A_{em}} + \gamma F_{D_{exc}}^{D_{em}}$$

$$F_{A_{exc}} = F_{A_{exc}}^{A_{em}} + F_{A_{exc}}^{D_{em}}$$

2D plot of *E*-*S* values for 5 nM samples in 30% and 40% PEG 8000 solutions were given in Figure 4.5 and 4.6 (details of data analysis were given in ref. 94). Binning times for confocal ALEX and for ALFRED were chosen on the basis of fore-mentioned FCS data (3.4 ms (confocal), 1.0 ms (ALFRED) for 30% PEG 8000 and 6.6 ms (confocal), 1.8 ms (ALFRED for 40% PEG 8000). Distributions are very different between confocal and ALFRED in 5 nM samples. Donor-only sample (red circle) and high-FRET sample (green circle) are clearly resolved in ALFRED 2D plots while there was only one broad, featureless distribution in confocal ALEX 2D

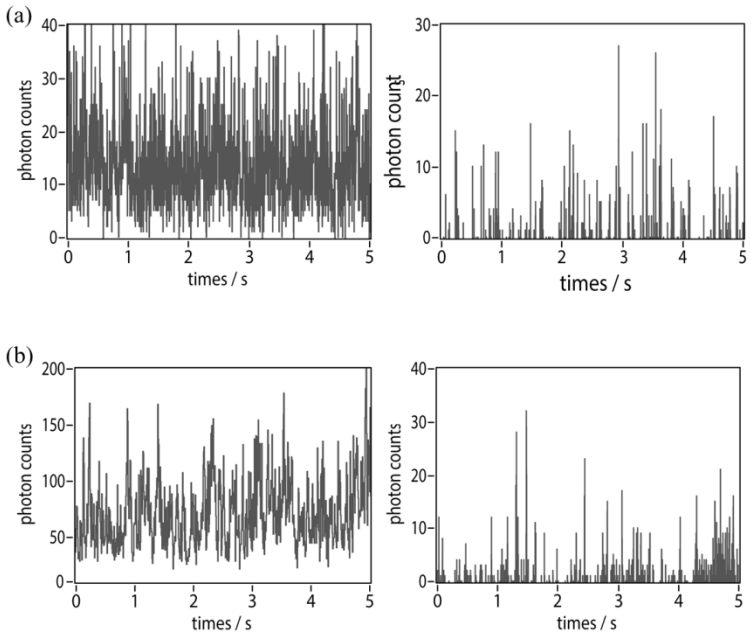

Figure 4.4 Sum of the photon trace of 5 nM dsDNA labeled with ATTO647N and DY-510XL in (a) 30% and (b) 40% PEG 8000 solution. Bursts from a single molecule are observed in ALFRED condition (right graphs in each trace), but not in confocal condition (left graphs in each trace) due to the existence of too many molecules in the large focal volume.

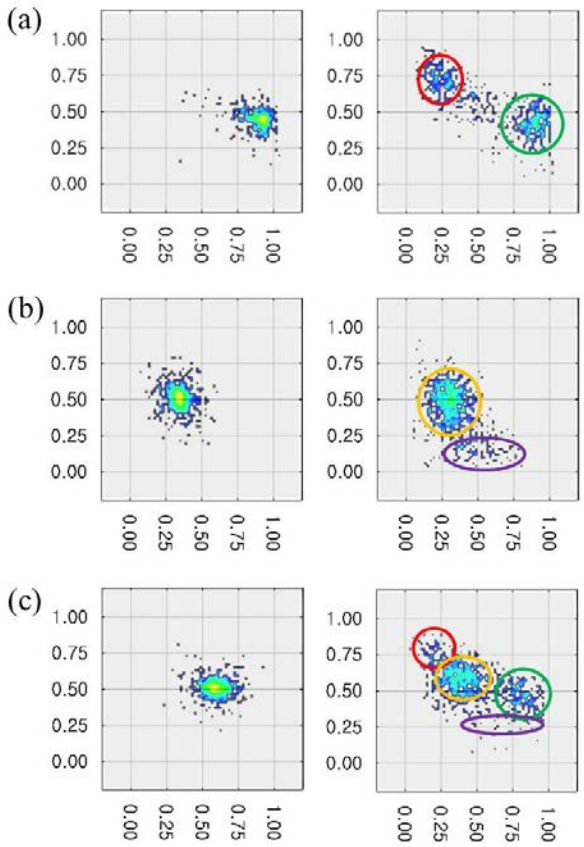

Figure 4.5 *E-S* 2D-plot of 5 nM dual labelled dsDNA (20 bp) in 30% PEG 8000 solution. (a): confocal ALEX (left) and ALFRED (right) 2D plot for high-FRET sample, (b): confocal ALEX (left) and ALFRED (right) 2D plot for low-FRET sample, and (c): confocal ALEX (left) and ALFRED (right) 2D plot for mixed sample. In these concentrations, too many molecules exist in confocal volume to give broad, featureless ensemble distribution. However, there is only one diffusing molecule in ALFRED condition due to the confined focal volume. Donor-only (red circle) and accept-only (purple circle) and normal sample (yellow and green circle) can be resolved in ALFRED data.

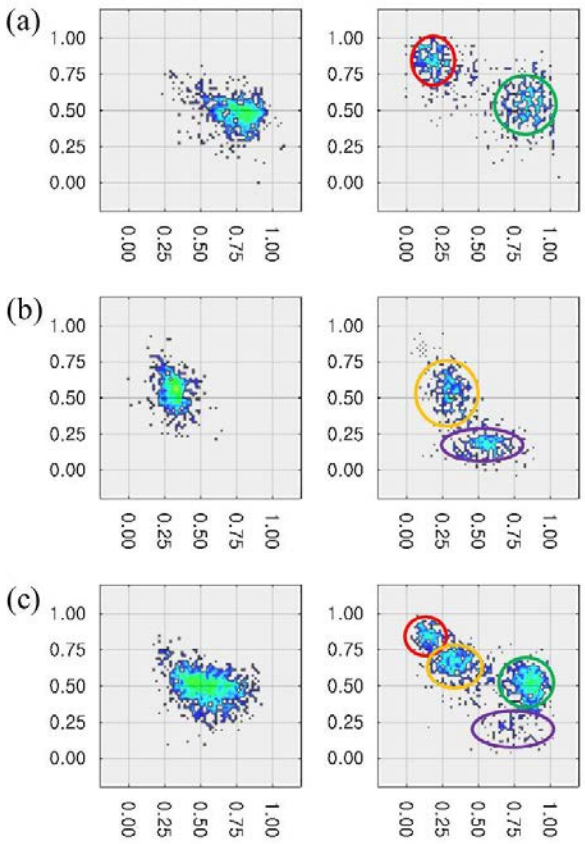

Figure 4.6 *E-S* 2D-plot of 5 nM dual labelled dsDNA (20 bp) in 40% PEG 8000 solution. (a): confocal ALEX (left) and ALFRED (right) 2D plot for high-FRET sample, (b): confocal ALEX (left) and ALFRED (right) 2D plot for low-FRET sample, and (c): confocal ALEX (left) and ALFRED (right) 2D plot for mixed sample. In these concentrations, too many molecules exist in confocal volume to give broad, featureless ensemble distribution. However, there is only one diffusing molecule in ALFRED condition due to the confined focal volume. Donor-only (red circle) and accept-only (purple circle) and normal sample (yellow and green circle) can be resolved in ALFRED data.

plot because of ensemble condition ((a) in Figure 4.5 and 4.6). As shown in Figure 4.3 (a), there could be up to 10 molecules in confocal volume during observation time, which resulted in the feature like that. In contrast to this, there was no chance that two or more molecules were observed at the same time in ALFRED condition. Acceptor-only sample (purple circle) and low-FRET sample (yellow circle) are also clearly resolved in ALFRED 2D plots while there was only one broad, featureless distribution in confocal ALEX 2D plots ((b) in Figure 4.5 and 4.6). We mixed both high-FRET and low-FRET samples to be 5 nM concentration in 30% and 40% PEG 8000 solutions to investigated the feasibility of our ALFRED technique whether high-FRET and low-FRET sample can be discriminated from each other and from donor-only and acceptor-only samples. As shown in (c) in Figure 4.5 and 4.6, four kinds of samples are clearly resolved in ALFRED condition in contrast to confocal ALEX.

The area near $S = 0.5$, $E = 0.85$ and $S = 0.5$, $E = 0.3$ became broad in ALFRED 2D plot than confocal ALEX in low concentration because of its reduced focal volume. This can be interpreted as a combination of two factors. First, STED beam used to reduce the focal volume was quite strong to bleach dyes during diffusion. Some of them could emit fluorescence until they escaped from the focal volume while others could not. Those bleached dyes were not able to emit sufficient photons as we expected. Also, reduced focal volume limited the observation time resulted in reduction of total photon number. In confocal ALEX, small variation in

photon number does not affect *E* and *S* values. However, that might significantly affect *E* and *S* values when photon counts are relatively small. Usually, photon count reduces nearly six times in STED condition compared to the confocal condition. Therefore, the distribution of the data point in ALFRED 2D plot would be broader than that in confocal ALEX.

4.4 Conclusion

In conclusion, we combined ALEX-FRET single molecule spectroscopy and super-resolution STED nanoscopy to confine the focal volume, much smaller than the diffraction limited confocal volume. With this new technique, we could observe a single diffusing molecule at up to 5 nM, which is 100-times increased concentration than that in conventional confocal ALEX. This concentration is comparable with the dissociation constant of many enzymes.

Chapter 5. Programmed transfer of lipids and integral membrane proteins between membranes using DNA-lipid-conjugate mediated fusion

This work was done at Stanford University from April to September, 2010.

(Advisor: Prof. Steven G. Boxer)

5.1 Introduction

Integral membrane proteins are often difficult to study in their natural environment due to the complexity of cell membranes, and this has driven efforts to create reliable model membrane systems in which membrane proteins can be studied. Small unilamellar vesicles (SUVs), typically tens to hundreds of nm in diameter, are the most common system with membrane proteins typically reconstituted by detergent dialysis.[96] While methods have been developed to tether SUVs and proteoliposomes[97] to surfaces to study their dynamics and interactions[98], this geometry limits the application of surface-sensitive analytical methods. Free-standing model lipid membranes such as tethered lipid bilayers and giant unilamellar vesicles (GUVs) are a promising alternative as the lipid bilayer is free from surface interactions; however, these systems have only been used infrequently due to the difficulty of incorporating membrane proteins into either GUVs or tethered membranes while still maintaining protein function. In this work we demonstrate a general method for transferring integral membrane proteins in a programmed fashion from SUVs to GUVs or tethered bilayers using synthetic DNA-lipid conjugates. This approach should prove useful for many applications and also provides important insight into the membrane fusion mechanism itself.

Several important examples of protein incorporation into GUVs have been described. Manneville and co-workers reconstituted an integral membrane protein into GUVs using an electroformation technique[99], but this method requires the

membrane protein be exposed to organic solvents and undergo dehydration while in a lipid film, a procedure which will likely denature many membrane proteins. Girard *et al*. addressed this limitation by using partially dried proteoliposomes to form GUVs with membrane proteins[100], a considerable improvement, though the membrane proteins must endure a long drying and electroformation process. Kahya *et al*. reported a different approach in which bacteriorhodopsin was reconstituted into preformed GUVs by the fusion of small proteoliposomes to the GUVs, where fusion was mediated by a fusogenic peptide[101]. This procedure circumvented the need for membrane proteins to be present during the dehydration and electroformation steps commonly used to form GUVs, but the undefined nature of the fusogenic peptide, which presumably remains in the GUV following membrane fusion, limited the approach in this case. Recently, Varnier *et al*. reported that they observed transfer of membrane protein or membrane dye from proteoliposomes to GUVs simply by mixing proteoliposomes with concentrated GUVs,[102] without detergents or a dehydration step or fusion peptides. However, the plausible mechanism should be further studied to understand the transfer process. This suggests that well-defined and reliable fusion machinery might provide a more general solution.

We have developed a membrane fusion system that exploits DNA hybridization, where the DNA is anchored to a lipid-like molecule at the 5' and 3' ends on the respective membrane partners, and have demonstrated both lipid and content mixing

that is sequence specific between SUVs.[103,104] This system mimics the geometry of the natural SNARE-mediated fusion system[105] and can be systematically modified to optimize and program fusion. A related system has been developed by Stengel *et al*. using cholesterol anchors.[106] Given the specificity (due to DNA sequence), and gentleness (integral membrane proteins are always in a nearly native environment), this DNA fusion machinery can be used to deliver integral membrane proteins from small proteoliposomes into either tethered GUVs or free-standing tethered lipid membrane patches, both of which are illustrated schematically in Figure 5.1A.[107] DNA-lipid conjugates are also used to create these architectures, where the DNA is anchored at its 5' end to the glass surface and the complementary sequence, also anchored at its 5' end (the yellow strands), tethers the GUVs or bilayer patches at a precisely controlled distance from the surface. As illustrated in Figure 5.1B, the target membrane also displays a different DNA sequence, also anchored to the lipid at its 5' end (the blue strand), that can hybridize with its complementary sequence displayed on an incoming SUV or proteoliposome where the DNA is anchored to the lipid at its 3' end. As shown in the following, membrane fusion can either deliver membrane-associated lipids to target membranes, thereby "staining" them in the programmed fashion, or can deliver integral membrane proteins. The application of this system to content transfer across a membrane is described in a separate paper.[108] In addition to demonstrating protein delivery, we ascertain the orientation of the protein before and after delivery, which information sheds light on the mechanism of membrane fusion mediated by DNA-lipids.

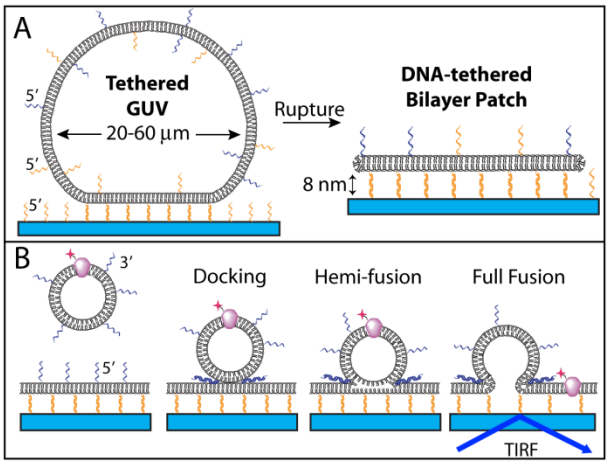

Figure 5.1 A: DNA-tethered lipid bilayer patch formation by GUV rupture onto DNA-immobilized on a glass substrate. The GUV membrane contains two orthogonal 5' coupled lipid-DNA conjugates, one for tethering to the anti-sense strand immobilized on the surface and creating the architecture (the yellow strands), the other for fusion (the blue strand). The GUV binds and ruptures to form a DNA-tethered bilayer patch, held at the distance specified by the DNA-duplex (8 nm for a 24 mer). B: Schematic diagram of membrane protein transferred to a tethered patch by DNA-mediated fusion (the protein is a cartoon representation of a dye labeled RC). An SUV displaying the blue anti-sense strand, which is anchored to the lipid at its 3' end, docks and subsequently fuses to the patch by DNA hybridization, transferring a dye-labeled membrane protein into the patch. Note: figures are not drawn to scale and the blue 5' anchored fusion strand on target patch is expected to be on both the lower and upper surface, but only the latter is draw for clarity.

5.2 Materials and methods

5.2.1 Materials and reagents

Egg phosphatidylcholine (EggPC), 1,2-dioleoyl-*sn*-glycero-3-phosphocholine (DOPC), 1,2-dioleoyl-*sn*-glycero-3-phosphoethanol-amine (DOPE) and cholesterol were purchased from Avanti polar lipids, Inc. Dithiothreitol (DTT) and horse heart cytochrome c were purchased from Sigma-Aldrich. Alexa633-C_5-maleimide, Oregon Green 488 1,2-dihexadecanoyl-*sn*-glycero-3-phosphoethanolamine (OG-DHPE), Texas Red 1,2-dihexadecanoyl-*sn*-glycero-3-phosphoethanolamine (TR-DHPE), and QSY®-21 carboxylic acid succinimidyl ester, a fluorescence quencher for Alexa633, were purchased from Invitrogen. The amine-reactive QSY®-21 dissolved in 50% DMSO is deactivated before use by incubating in pH 10.0 for at least 2 hr.

5.2.2 Reaction centers and dye labeling

His-tagged bacterial reaction centers (RCs) were extracted and purified from *Rhodobacter capsulatus* as described previously.[109] Since all native cysteine residues are buried in the interior of the RC, a solvent-exposed leucine was mutated to a cysteine, forming the (M)L189C mutant,[110]; this residue is close to the special pair or P, illustrated schematically in the inset to Figure 5.2A, and we will refer to this side of the RC as the P side. Purified (M)L189C RCs in a buffer of 10 mM Tris pH 7.4 and 0.05 wt% deriphat were mixed with a 100-fold molar excess of DTT and incubated at 4°C for 30 min while stirring to reduce the surface cysteine. A PD-10

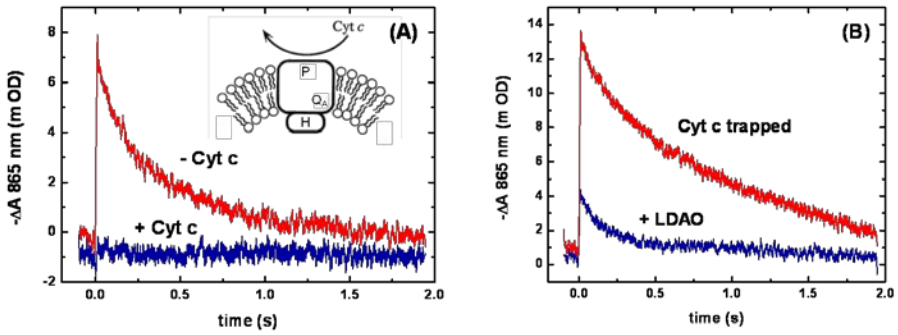

Figure 5.2 (A) P^+Q^- recombination kinetics of RCs in proteoliposomes in the absence and presence of cytochrome c measured by nanosecond transient absorption. The concentrations of RCs and cytochrome c are 324 nM and 20 μM, respectively. 256 spectra were averaged for each graph. These data verify that the orientation of RCs in proteoliposomes with P-site facing outward (inset) and that protein functions is maintained as well. (B) P^+Q^- recombination kinetics of RCs in cytochrome c containing proteoliposomes in the absence and presence of 0.01% LDAO. The concentration of RCs and cytochrome c are the same as (A). Cytochrome c inside of the proteoliposome appears to only interact with the P-site of RCs after LDAO disrupts the SUVs.

desalting column (GE healthcare) was used to remove DTT after reduction. It was essential to remove all of the DTT after reduction since DTT has a higher reactivity toward the Alexa633-C_5-maleimide than cysteine. After the DTT was removed, a 5-fold molar excess of Alexa633-C_5-maleimide (λ_{abs}: 633 nm, λ_{em}: 647 nm) dissolved in DMSO (1mg/mL) was added to the reduced RCs and incubated at room temperature for 2 hr. The mixture was then loaded onto a Ni:NTA column and washed with a buffer containing 10 mM Tris, 300 mM NaCl, 0.05 % deriphat and 5 mM imidazole, pH 7.4 to remove the unconjugated dye. Alexa633-RC conjugates were then eluted with 300mM imidazole in the above buffer, and further purified by FPLC. The isolated Alexa633-RC solution in a buffer containing 10 mM Tris pH 7.4 and 0.05 % deriphat was then concentrated and stored at -80°C. The dye labeling efficiency was estimated to be > 90%, as determined by UV-Vis absorption using the extinction coefficient of 288,000 $M^{-1}cm^{-1}$ for the RC at 800 nm and 159,000 $M^{-1}cm^{-1}$ for Alexa633 at 633 nm (Figure 5.3).

5.2.3 Preparation of vesicles

Two kinds of SUVs were used in this study: SUVs used to form supported lipid bilayers (SLBs) were composed of EggPC, while SUVs used for bilayer fusion were composed of a 2:1:1 molar ratio of DOPC:DOPE:cholesterol. To visualize the SUVs or the resulting bilayer, 1 mol% of OG-DHPE was included in both SUV compositions. For the case where a tethered patch is stained by a lipid dye, 5 mol% TR-DHPE was included in the SUVs rather than 1 mol% OG-DHPE. The lipid

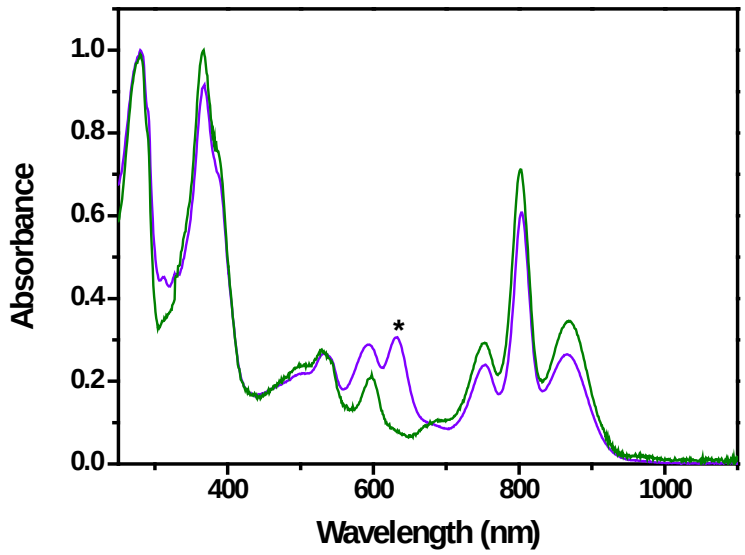

Figure 5.3 UV-Vis spectrum of a solution of the unlabeled RC (green), and the Alexa633-RC conjugate (violet). The two spectra are normalized at 280 nm. In order to calculate the labeling efficiency of the Alexa633 conjugation, we used an extinction coefficient for the RCs of 288,000 $M^{-1}cm^{-1}$ at 800nm and an extinction coefficient for Alexa633 dye of 159,000 $M^{-1}cm^{-1}$ at 633 nm (asterisk). Assuming that the Alexa633 only conjugated with the surface cysteine (i.e. one Alexa633 per RC), the conjugation efficiency is ~93 % in this case.

mixture for each batch of SUVs was made in HPLC-grade chloroform and dried to form lipid films in a vacuum desiccator for more than 2 hrs. The dried mixture was re-suspended in buffer (10 mM Tris and 250 mM NaCl, pH 8.0), and then extruded through a 100 nm pore membrane using an Avanti mini-extruder. If the SUVs were to be used in a membrane fusion experiment, DNA-lipid conjugates (sequences given below) were added to the solution of the SUVs, where they spontaneously insert. The resulting solution of SUVs was stored at 4°C in the dark to allow for incorporation of the DNA-lipids into the SUVs.

5.2.4 Preparation and characterization of proteoliposomes

Alexa633-RCs were incorporated into SUVs by detergent dialysis.[111] A solution of RCs in a buffer containing 10 mM Tris pH 7.4 and 0.05 % deriphat was mixed with SUVs composed of either EggPC or the DOPC:DOPE:cholesterol mixture (molar ratio of RC:lipid = 1:500), and to the resulting solution was added detergent-containing buffer (1% *n*-octyl *p*-D–glucopyranoside, 50 mM HEPES, 100 mM NaCl and 0.5% glycerol, pH 7.4). We found that the final concentration of octyl glucopyranoside should be less than 1% for efficient dialysis. This solution was incubated with gentle shaking at room temperature for 30 min. After incubation, the solution was dialyzed against 50 mM HEPES, 100 mM NaCl and 0.5% glycerol at pH 7.4 with Bio-beads SM-2 (1g/L) outside. Dialysis was performed three consecutive times while stirring for 1hr, 2hrs, and then overnight with the buffer replaced each time. Proteoliposomes were isolated from unincorporated RCs using a

Sepharose CL-4B size exclusion column (Sigma Aldrich). The RC:lipid ratio can be estimated by UV-Vis absorption (Figure 5.4) using the extinction coefficient of OG-DHPE added to the membrane (85,000 $M^{-1}cm^{-1}$ at 504 nm) and RC (288,000 $M^{-1}cm^{-1}$ at 800 nm)[112]. The ratio varied between 1:500 ~ 1:3,000 for each batch of dialysis carried out.

The RC orientation in proteoliposomes was investigated by $P^+Q_A^-$ recombination kinetics in proteoliposomes (Figure 5.2) and by quenching the fluorescence from the covalently attached Alexa633 dye on the P-side of the RC by a nonfluorescent FRET acceptor, QSY®-21.[113] Intrinsic $P^+Q_A^-$ recombination kinetics, an assay for function, were measured by transient absorption spectroscopy as previously described.[110] A frequency-doubled pulsed Nd:YAG laser (532 nm) was used to excite the RCs and a continuous tungsten lamp fitted with a monochromator was used to probe the absorbance change at 865 nm. An electrical shutter made excitation light getting to the detector at 0.5 Hz. The detection system consisted of two photodiodes with response time of 1 ms, one diode was for the reference and the other for the sample. Cyt. c was reduced by sodium dithionite and then was run down a PD-10 column to remove excess reductant. For some measurements, cyt. c was trapped inside the vesicles by rehydrating the dried lipid film with buffer containing 8 mM cyt. c before extruding the SUVs; uncaptured cyt. c were separated from the SUVs by size exclusion chromatography (Sepharose CL-4B column). Transient absorption kinetics were obtained for the RC proteoliposomes prepared as described in Materials and Methods (0.2 g lipid/L, 0.5 μM RCs) with

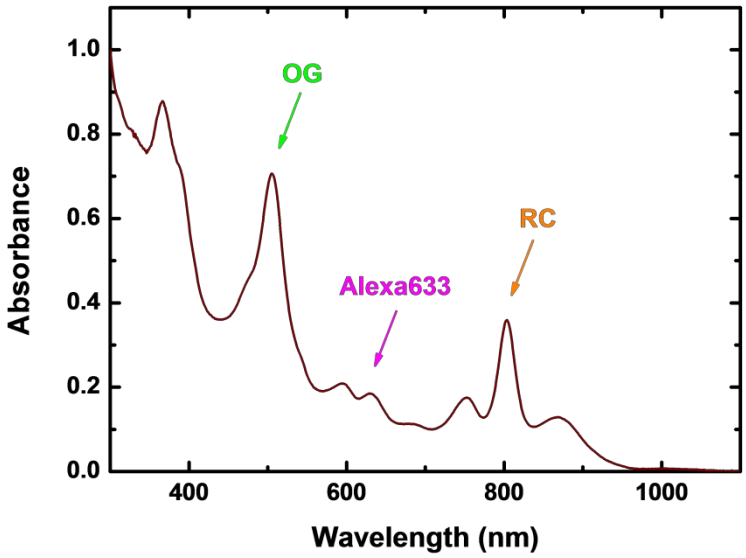

Figure 5.4 Absorption spectrum of RC-containing proteoliposomes at room temperature. The lipid contains 1 mol% OG-DHPE whose absorption maximum occurs at 504 nm. Comparing the value of this peak with the 800 nm peak of the RC, the RC:lipid ratio can be calculated.

and without external cyt. c (2 ~ 3 μM), and for proteoliposomes with trapped cyt. c, before and after the addition of LDAO which disrupts the integrity of the membranes (Figure 5.2). Without external cyt. c, control proteoliposomes show normal $P^+Q_A^-$ recombination kinetics with a single exponential decay. However, such kinetics were not observed when cyt. c was added externally to the control proteoliposomes since P^+ is reduced by cyt. c very quickly and this traps Q_A^- so further $P^+Q_A^-$ recombination is not observed. Proteoliposomes with trapped cyt. c show the same recombination kinetics as control proteoliposomes without cyt. c indicating that the internal cyt. c cannot reduce P^+. Only after addition of LDAO, was $P^+Q_A^-$ recombination observed as P^+ is then reduced by cyt. c. These measurements agree with those reported earlier,[110] and demonstrate that the surface of the RCs where cyt. c binds, near the special pair P and near where the Alexa633 is bound, is facing outward on the proteoliposome (inset, Figure 5.2A), consistent with much earlier work. This experiment also demonstrated that the RCs remained functional in the proteoliposomes. After the proteoliposomes were suspended in 50 mM HEPES, 100 mM NaCl and 0.5% glycerol, pH 7.4 (dialysis buffer) to a final concentration of 0.1 g lipid/L (0.2 μM Alexa633-RCs), the fluorescence intensity of Alexa633 at 647 nm was analyzed in a fluorometer (Perkin Elmer LS-55) using 633nm excitation light before and after addition of 25 μM QSY®-21 quencher. The 0.2 μM of Alexa633-maleimide in the same buffer was used to estimate the quenching efficiency and compare with that of Alexa633-RCs in proteoliposomes. The orientation of Alexa633-labeled RCs in SLBs formed from proteoliposomes

(EggPC)[114] was analyzed by monitoring the fluorescence using a 633 nm HeNe laser in TIRF mode before and after quenching by QSY®-21 (25 μM final concentration). As a control experiment, the quenching behavior of a SLB composed of EggPC containing 1mol% TR-DHPE was tested in the same manner.

5.2.5 DNA-hybridization-mediated fusion to DNA-tethered lipid bilayer patches and GUVs

DNA-tethered lipid bilayer patches were formed by giant vesicle rupture on DNA-immobilized surface as described previously[107] and illustrated in Figure 5.1A. GUVs were prepared by the electroformation method.[115] The lipid mixture for the GUVs[116] was composed of 2:1:1 molar ratio of DOPC:DOPE:cholesterol, 0.2 mol% OG-DHPE, and 0.5 mol% each of two orthogonal DNA-lipid conjugates[103]:5'-coupled lipid-polyT 24 mer for fusion (the blue strand in Figure 5.1), and 5'-lipid-TAGTATTCAACATTTCCGTGTCGA 24 mer for tethering to the anti-sense strand which is immobilized on the surface (the yellow strands in Figure 5.1). This lipid mixture was dissolved in methanol and coated on Pt electrodes to form a dried lipid film. The container surrounding the electrodes was filled with 0.5 M sucrose solution, and then an AC electric field of 2.5 V and 10 Hz was applied for 2 hr.

DNA-coated glass surfaces were prepared by attaching DNA covalently to the glass surface by click chemistry.[106] Following vapor-deposition of azidosilane monolayers on a glass coverslip (VWR), the azide-covered glass surfaces were exposed to a solution of a 5' alkynyl modified oligonucleotide (alkynyl-C_6-

TCGACACGGAAATGTTGAATACTA, the yellow strand on the surface, Figure 5.1) in the presence of copper catalyst. The remaining unreacted azides on the surface were passivated by ethynylphosphonic acid, which effectively repels vesicles and GUVs. When GUVs displaying the anti-sense DNA-lipid conjugate were added to the solution above the DNA-functionalized surface and allowed to bind, the GUVs either ruptured to form tethered bilayer patches if the DNA coverage on the surface was high enough (more than 5 nmoles/m^2 surface density), or they stayed as a dome-shaped bound GUV with a flat contact region if the DNA coverage is low (about 0.26~2.6 nmoles/m^2 surface density).[107,117]

Hybridization between a 5' coupled DNA-lipid in the GUV and a 5' attached anti-sense DNA-alkyne on the surface tethers the membrane to the surface and creates an ~8 nm spacer between the lower leaflet of the bilayer patch or tethered GUV and the solid support; this distance can be adjusted simply and precisely by varying the length of the DNA sequence.[107] On the other hand, hybridization between DNA-lipids on different membrane surfaces, one coupled at the 5' end and the other at the 3' end, brings the two membranes into close proximity and induces membrane fusion.[103,104] In this study, 3'-lipid-polyA (24 mer) displayed on the SUVs and 5'-lipid-polyT (24 mer) displayed on the target membrane were used to induce vesicle fusion to planar tethered bilayers or GUVs (illustrated schematically in Figure 5.1B and 5.5). For incorporation of DNA-lipids into SUVs or proteoliposomes, the DNA-lipid in a micellar suspension in H_2O was added to the SUVs or proteoliposomes (both composed of the DOPC:DOPE:cholesterol mixture) to yield a final

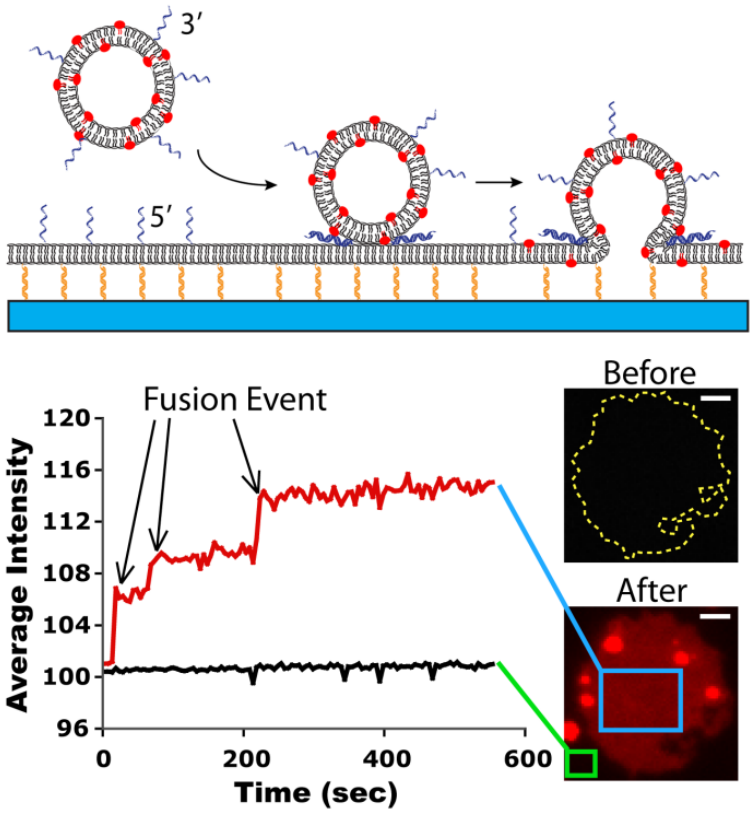

Figure 5.5 DNA-mediated lipid membrane fusion is monitored by lipid-dye transfer from docked vesicles (~100 nm diameter) to the tethered bilayer patch (30~50 μm). When small vesicles containing TR-labeled lipids dock and fuse to a tethered patch, TR-lipids diffuse, and the patch is stained as in the schematic. Jumps of TR intensity corresponding to fusion event are monitored in patch area (blue square) and background (green square) by total internal reflection. The bright spots of after-fusion image are docked vesicles since not all docked vesicles undergo fusion.

concentration of 0.4 mol% (with regard to the lipid),[103] and incubated overnight at 4°C in order to allow the DNA-lipid to partition entirely into the membrane.

After tethered bilayer patches or GUVs were formed on a DNA-functionalized glass surface, a small amount (typically 1 μL of a 0.5 g/L SUV solution into 80 μL of solution in a well) of SUVs or proteoliposomes displaying the anti-sense DNA sequence were added and allowed to dock and fuse to the target membrane. In the case of the dye-labeled lipid staining experiments, SUVs with 5 mol% TR-DHPE were introduced and the fusion process was monitored by measuring the increase of red fluorescence in the bilayer patch area as the TR membrane-dye diffuses and stains the patch. By using TIRF only fluorescence signals from the patch near the surface are observed effectively eliminating background from floating vesicles in the solution. In the case of the RC transfer experiments, Alexa633-RC proteoliposomes with 1 mol% OG-DHPE, which does not overlap spectrally with Alexa633, were used. The OG signal was used to monitor membrane fusion, while membrane protein transfer was monitored by Alexa633 fluorescence using a 633 nm HeNe laser for excitation. After a target patch or GUV was selected and located on an inverted fluorescence microscope (Nikon TE300), proteoliposomes were added, and immediately a video stream with 56 ms/frame time resolution (Andor iXon 897 CCD camera) was acquired using the 633 nm laser excitation in TIRF mode.

The orientation of transferred RCs to tethered GUVs was probed by adding the QSY®-21 fluorescence quencher. After tethered GUVs were formed on a DNA-immobilized surface, a small amount of proteoliposomes displaying the 3'-anchored

anti-sense DNA were added to deliver RCs into GUV lipid membranes (*vida infra*). The transfer of RCs was confirmed and a suitable tethered GUV with transferred RCs was selected. Images before and after QSY®-21 addition (final concentration of 20 mg/L) were taken by TIRF microscopy with 633 nm excitation. To test for the possible leakiness of tethered GUVs, the fluorescence quenching behavior was measured for the TR lipid dye in a tethered GUV located side-by-side on the surface with an adjacent tethered patch.

5.2.6 RC mobility by single particle tracking

The mobility of membrane proteins incorporated into lipid bilayers can be used as an indicator for proper incorporation and to study clustering behavior and protein-lipid interactions.[118] We quantitatively measured the mobility of individual RCs in the target membrane by single particle tracking (SPT) of the Alexa633 emission, using methods previously described.[119] SPT analysis cannot be done properly with crowded objects, hence, proteoliposomes containing low numbers of Alexa633 labeled RCs (less than 1:2,000 RC:lipid ratio) were used for RC delivery to achieve collision-free conditions. The exposure time and frame rate of the CCD camera (Andor iXon 897) was chosen to be 50 ms and 17.8 frames/s. Image recording and single particle tracking were performed using the Metamorph imaging software. The mean-square displacement (MSD) for individual Alexa633-labeled RCs was calculated as a function of time lag t, as described previously.[120,121] For Brownian diffusion, the MSD is a linear function vs. time and the lateral diffusion coefficient

D can be obtained by fitting the MSD to the equation, MSD = 4*Dt*.

5.3 Results and discussion

5.3.1 Membrane dye transfer by vesicle fusion to a planar bilayer patch

As an initial step toward demonstrating delivery of a transmembrane protein from proteoliposomes to a GUV or tethered lipid patch, we first demonstrated that the DNA fusion machinery could be used to deliver a dye-labeled lipid from an SUV to a DNA-tethered membrane patch via membrane fusion. As shown in Figure 5.5, after a suitable tethered patch was located by observing a small amount of OG-DHPE, a dilute suspension of SUVs labeled with 5% Texas Red (TR)-lipids and displaying 3' coupled DNA-lipid conjugate that is complementary to the 5' coupled DNA-lipid conjugate on the patch was manually pipetted into the solution above a patch of interest. As these SUVs encountered the patch by diffusion, hybridization between the 3' coupled DNA-lipids on the SUV and the complementary 5' coupled DNA-lipids on the membrane patch resulted in docking and fusion of the SUVs to the patch, both of which were observed by video fluorescence microscopy. Individual SUV docking is readily observed as the appearance of a diffraction-limited spot on the patch. Interestingly, these docked SUVs are immobile at the DNA-lipid concentrations used in these experiments.[122] Fusion was observed as a sudden decrease in the TR fluorescence intensity in the docked SUV and a concomitant stepwise increase in the TR intensity in the patch area, indicating

discrete lipid transfer events (Figure 5.5).[123] The different sizes of the jumps in fluorescence on the patch are likely due to fusion of SUVs of slightly different size to the patch. Although transfer of the membrane dye can occur via hemi-fusion, this can be clearly distinguished from full fusion because the bright spot due to the docked vesicle completely disappears in the case of full fusion, implying that both leaflets become continuous with the patch bilayer. As discussed elsewhere, this process is accompanied by the transfer of an aqueous content dye from the SUV to the gap underneath the membrane patch or to the interior of a surface-tethered GUV.[108] We note that this method of DNA-programmed staining of individual membranes may be useful for imaging of biological samples, and this will also be described elsewhere.[124]

5.3.2 Membrane protein transfer by vesicle fusion

We used the photosynthetic RC as a model membrane protein for demonstrating integral membrane protein transfer because we have extensive experience working with this protein, its orientation and function can be probed using well-established assays, and we used the RC in early work from our laboratory on the preparation of SLBs from proteoliposomes.[112] In that work as here, RC containing proteoliposomes were formed, and the cyt. c reduction of P^+ assay (Figure 5.2)[112,125] was used to demonstrate that nearly all RCs had inserted into SUVs with the cyt. c binding site on the P-side exposed; this result agreed with earlier work from other labs.[126] Supported bilayers were formed from these proteoliposomes (EggPC and 1

% TR-DHPE), and it was demonstrated that the RCs were functional in the SLB based on $P^+Q_A^-$ recombination kinetics measured by stacking many slides with SLBs on both sides.[112] Interestingly, the cyt. c binding face of the RC in the SLB remained accessible in a large fraction of the RCs in the SLB, contrary to what might be expected if a vesicle fuses to the surface and opens to expose its interior, in which case the P-face of the RC would be towards the glass, inaccessible to cyt. c. Furthermore, based on FRAP measurements of Rhodamine-labeled RCs, the RCs were found to be immobile. These results could be rationalized by noting that the H-subunit, which is on the opposite side of the membrane from the P-side (see inset in Figure 5.2A), protrudes from the membrane surface and bears a number of positive charges that could interact with the negatively charged glass surface inhibiting lateral mobility. Although this interaction might alter the structure of the H-subunit, it has been demonstrated that the H-subunit is not required for function.[127] Given that observation, we thought this would be a good test case for the DNA-tethered membrane patch and GUV systems, both to demonstrate the possibility of transferring an integral membrane protein and to measure the mobility when the bilayer is held away from the solid support.

As described in detail and methods, RC proteins were isolated as described earlier[112] with minor, but possibly significant modifications and labeled with the Alexa633 dye. The RC:lipid mole ratio for these proteoliposomes was calculated to be between 1:500 and 1:1,000, as determined by UV-Vis absorption spectroscopy

(Figure 5.4) of the ratio of the lipid-dye OG-DHPE and the Alexa633-RC. 3' DNA-lipid conjugates were added to these proteoliposomes in order to mediate membrane fusion to the target GUV or tethered patch. As in the TR lipid-dye transfer experiment, the Alexa633-RC proteoliposomes displaying the 3' DNA-lipid conjugates were pipetted into the solution above a tethered bilayer patch displaying the complementary 5' anchored DNA-lipid conjugates as shown schematically in Figure 5.6A. The proteoliposomes and the patch were both visualized by OG fluorescence, and RC transfer was monitored by Alexa633 fluorescence. As the proteoliposomes docked and fused to the membrane patch, the patch displayed a number of rapidly moving, diffraction limited spots observed only in the Alexa633 channel (Figure 5.6B). This was only observed when the complementary DNA strands were included and when proteoliposomes containing the Alexa633 labeled RCs were present in the SUVs (data not shown). Since docked SUVs on the patch were observed to be immobile by visualizing the OG-DHPE lipid dye (as for the docked TR-DHPE containing SUVs discussed in detail above), the presence of these highly mobile spots whose emission corresponds to Alexa633 suggests that they are Alexa633-RCs that have been transferred to the patch. As shown in Figure 5.7, these spots undergo single-step photobleaching, consistent with their being single Alexa633 RCs.

The DNA fusion machinery can also be used to transfer Alexa633-RCs to tethered GUVs by fusion of proteoliposomes (Figure 5.6C). Tethered GUVs, instead of tethered membrane patches, can be formed by sufficiently lowering the

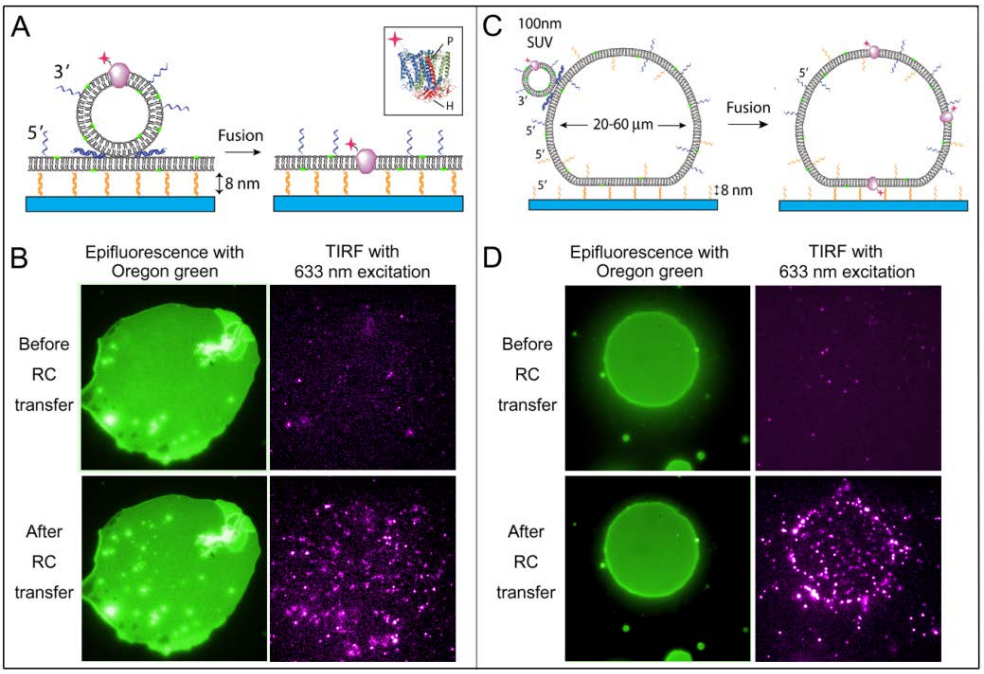

Figure 5.6 RC transfer by DNA-mediated fusion. A: RCs in proteoliposomes are transferred to a tethered bilayer patch. The actual structure of RC, and position of dye, P special pair and H subunit is shown in inset. B: The patch containing OG-lipids are observed by epi-fluorescence microscopy and Alexa633 labeled RCs are probed by TIRF with 633 nm excitation. The 40 µm patch is populated by transferred RCs appear as bright moving dots after fusion of proteoliposomes. Some proteoliposomes do not undergo fusion even after docking and remain fixed dots visualized by OG. C: RCs in proteoliposomes are transferred to a tethered GUV. D: The transferred RCs are detected in bottom membrane of a flattened GUV, where ~100 nm SUVs cannot reach into the 8 nm gap with 24 mer DNA. In both cases, the gap can be adjusted to 16 nm or 24 nm with 48 mer or 72 mer DNA, respectively.

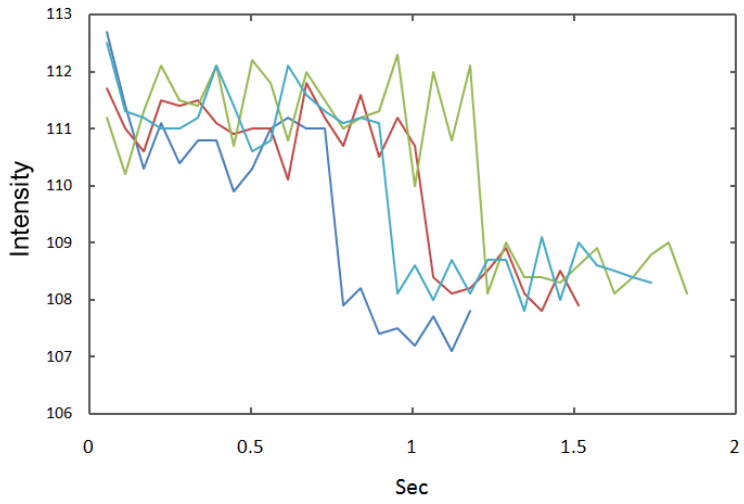

Figure 5.7 Representative photobleaching time traces of Alexa633-RCs in a tethered bilayer. To estimate the number of dyes in each of the dots in a tethered patch or GUV, the Alexa633 fluorescence intensity of each moving spot in a video stream was recorded and traced by single particle tracking. From the center of a dot, the average intensity inside of 3-pixel-radius circular region was recorded. We observed that most of the mobile spots were bleached in a few seconds and for each of the 50 dots sampled, the one-step bleaching patterns are clearly observed over the noise. The intensity is in arbitrary units and the background value is not subtracted because the relative intensity change is enough to show bleaching behavior.

density of immobilized DNAs on the glass surface so that enough DNA tethers are formed to create a flattened contact region on the surface, but not enough to cause rupture leading to membrane patch formation.[107] This strategy holds the GUV on the surface for convenient analysis either by wide-field fluorescence or TIRF, but retains the integrity of the GUV, keeping its contents separated from the outside solution. As with the tethered patch, the gap between the membrane forming the contact region of the GUV and the glass substrate is about 8 nm with 24 mer DNA hybrids. When Alexa633-RC-containing proteoliposomes were allowed to fuse with a tethered GUV by hybridization of complementary DNA-lipid conjugates (3' coupled on the SUV, 5' on the target GUV), the small, bright Alexa633-RC dots were observed in the flattened contact region at the bottom of the tethered GUV which we exclusively detect by TIRF microscopy. Since the gap between the membrane forming the contact region and the substrate is too small to admit an SUV, there is no chance that the mobile spots are due to small SUVs diffusing along the plane of the membrane.[122] Rather, these dots are presumed to represent Alexa633-labeled RCs, which were transferred to the upper dome of the tethered GUV by DNA-mediated fusion and then freely migrated by diffusion in the membrane to the lower planar contact region. Thus, we conclude that the bright, highly mobile spots in both the experiments of Figure 5.6 must be the Alexa633-labeled RCs which have been delivered to the target membrane by the DNA fusion machinery.

5.3.3 Mobility of RCs in SLBs and tethered bilayer patches

As described in the previous section, in earlier work when proteoliposomes containing RCs were used to make SLBs, the RCs were found to be functional, but immobile by FRAP measurements.[112] Repeating these measurements with the current system, we were surprised to observe that ~95% of the RCs were mobile in the SLBs, as roughly estimated by FRAP and by single particle tracking discussed below. We do not know the origin of the difference, but there are differences in details: the original RCs were not His-tagged (the His-tag is on the P-face); the original work used Rhodamine instead of Alexa633; a different detergent and protein reconstitution method were used; SUVs and proteoliposomes were prepared by different methods; and many lab techniques have been evolved such as protein purification, surface cleaning and preparation methods.

The diffusion coefficient of the RCs in SLBs and tethered membrane patches or GUVs were measured by single particle tracking, and compared with lipid mobility measured by FRAP. A video of Alexa633-RCs incorporated into tethered patches or GUVs at a low density was taken with 56 ms time resolution, and the trajectories of individual RCs were traced for SPT analysis. The diffusion coefficient of each individual RC was calculated from a plot of its MSD vs. time, and the distribution of diffusion coefficients for all RCs analyzed is shown in Figure 5.8. Because the distribution of diffusion coefficients of Alexa633-RCs in tethered patches and GUVs was indistinguishable, we combined both sets of data into one, and obtained

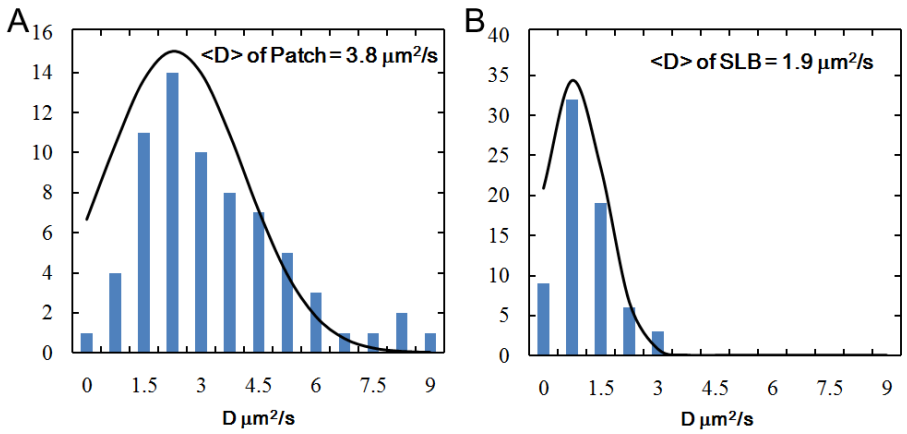

Figure 5.8 Histograms plot of independent diffusion coefficient of RCs in A. tethered bilayer patches (N = 68) or B. SLBs (N = 69). The average diffusion coefficient is indicated. Black traces are the expected statistical spread of diffusion coefficients given by equation 5.2. Bin width is 0.75.

an average diffusion coefficient of 3.8 ± 1.8 $\mu m^2\ s^{-1}$, while RCs in SLBs had an average diffusion coefficient of 1.9 ± 0.8 $\mu m^2\ s^{-1}$. The average lipid mobility measured by FRAP of OG-DHPE membrane dye was 5.9 ± 0.9 $\mu m^2\ s^{-1}$ for tethered patches and 3.2 ± 0.4 $\mu m^2\ s^{-1}$ for SLBs. While the lipid mobility in these tethered patches is greater than that in SLBs and similar to that obtained in an entirely free-standing GUV, the ratio of the lipid to protein mobility (~1.6) is similar in the two formats. Distributions generally tailed toward larger diffusion coefficients, consistent with previous measurements.[119,128] The standard deviation of each distribution of diffusion coefficients, which is 0.8 $\mu m^2\ s^{-1}$ for SLBs and 1.8 $\mu m^2\ s^{-1}$ for patches, agree with the theoretical standard deviation, , (0.9 $\mu m^2\ s^{-1}$ for SLBs and 1.8 $\mu m^2\ s^{-1}$) deduced by equation 5. 1:[120,121]

$$\sigma = \mathrm{D}\left[\frac{2N_D}{3(N_T - N_D)}\right]^{1/2} \qquad (5.1)$$

where N_T is the total number of steps observed (in our case typically 40) and N_D is the number of time intervals used for the least-squares fit to the data (typically 10).

The mobility of an integral membrane protein or peptide can be roughly predicted using the Saffman and Delbrück model of a cylinder diffusing laterally in a membrane (Equation 5.2):[118]

$$D_T = \frac{k_B T}{4\pi\mu h}\left(log\,\frac{\mu h}{\mu' a} - 0.5772\right) \qquad (5.2)$$

where k_B is the Boltzmann constant, T is the temperature, μ and μ' are the viscosity of the membrane and of the surrounding aqueous medium, respectively, h is the

membrane thickness, and *a* is the radius of the particle. Although not all reported diffusion coefficients of mobile membrane proteins (in the range of 1~5 $\mu m^2\ s^{-1}$)[129] agree well with this model,[130] we found that the Saffman-Delbrück modeled diffusion coefficient (4.5 $\mu m^2\ s^{-1}$, using h = 40 Å , μ = 2.94 P and μ' = 1 cP) of the Alexa633-RCs (a = 5 nm)[131] in the tethered patches was similar to the experimentally determined value.

5.3.4 Orientation of RCs in SLBs, tethered bilayer patches and GUVs

In our original work on RCs in SLBs, the orientation of RCs was monitored by using the P-side specific and functionally relevant blockage of $P^+Q_A^-$ recombination in the presence of reduced cyt. c.[112] While this could be used to probe the orientation in proteoliposomes, which confirmed that nearly all RCs have their P-side on the outside (Figure 5.2A), the cyt. c binding assay for planar membranes required the assembly of large area SLBs on multiple stacked glass slides to achieve a large enough absorption, and this is not possible with the finite area DNA-tethered bilayer patches or GUVs, which are inherently designed for single object microscopy experiments. Alexa633 is an exceptionally bright and stable dye, ideal for the single RC measurements described above, but the conventional fluorescence quenchers, e.g. Co^{2+} used to quench rhodamine-type dyes,[132] are ineffective with Alexa633. A class of non-fluorescent, FRET-based quenchers has been developed, and QSY®-21 is effective with Alexa633, though the concentrations of QSY®-21

that can be achieved are substantially less than for ions like Co^{2+} and QSY®-21 is rather large and has sufficient hydrophobic regions that might partition into membranes. In order to test the utility of this method of analysis, we first observed the bulk quenching behavior of Alexa633-RCs in proteoliposomes when the QSY®-21 quencher was added to the external solution. This was compared to the quenching behavior of a control solution of Alexa633 (0.2 μM in the same buffer of proteoliposomes) with approximately the same initial Alexa633 fluorescence intensity as the proteoliposome solution (0.1 g/L). After QSY®-21 was added to both solutions (final concentration of 25 μM), the fluorescence intensity at 647 nm of both solutions decreased to ~30% of the initial intensity. Furthermore, we observed that the fluorescence intensity of Alexa633-RC in an SLB also decreased to ~30% of the initial intensity when the QSY®-21 quencher (25 μM) was added to the solution above the SLB (Figure 5.9). Since the free Alexa633 dyes and those reconstituted into proteoliposomes and SLBs show the same behavior in the presence of quencher, we concluded that this method of analysis corresponded directly to the cyt. c binding assay and could be used to determine the orientation of the RCs in our tethered GUVs.

The orientation of RCs transferred to tethered membrane patches cannot be estimated by fluorescence quenching because both sides of the lipid membrane are exposed to the solution and hence readily accessible to the quencher. However, since the inside of a tethered GUV is isolated from the bulk solution, we were able

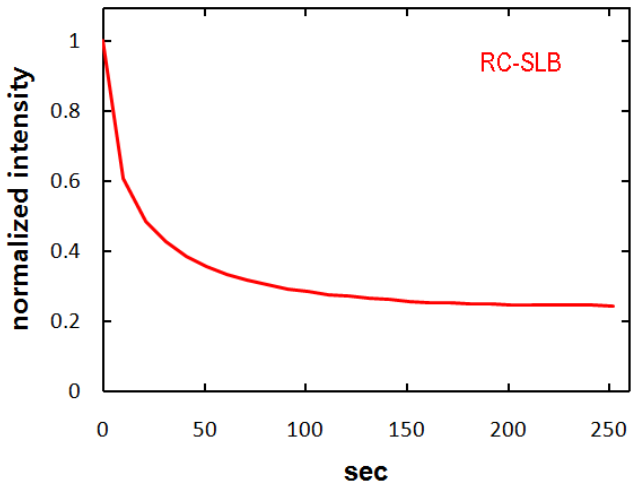

Figure 5.9 QSY®-21 quenching behavior of an Alexa633-RCs containing SLB. RC SLB is formed on a cover glass by Alexa633-RCs containing EggPC proteoliposomes. The average intensity of fluorescence microscopy images was monitored upon addition of QSY®-21. The fluorescence is quenched to some extent shortly after addition of QSY®-21 quencher to the bulk solution above the SLB, and gradually decreased to 0.24 of initial intensity. This gradual decrease is not due to mixing and diffusion of QSY®-21 since QSY®-21 is mixed vigorously after addition. Because the QSY®-21 seems to be inserted into lipid membrane, we speculate that the gradual accumulation of QSY®-21 in the lipid membrane caused the further decay of fluorescence after the initial introduction of quencher. This can be interpreted that most RCs are oriented in the way that Alexa binding site is exposed to the bulk solution, agreed with cyt. c binding experiment of Salafsky *et al.*

to use the fluorescence quenching assay to determine the orientation of RCs transferred to tethered GUVs. In this experiment, Alexa633-RCs were first transferred from proteoliposomes to a tethered GUV membrane by DNA-mediated fusion as described earlier, detected by the appearance of the characteristic bright mobile spots in the Alexa633 channel (as seen in Figure 5.6B, D and again in Figure 5.10B). The QSY®-21 quencher was then added to the solution outside the GUV and the bright spots were observed to disappear (Figure 5.10C), indicating that almost all of the Alexa633-RCs in the tethered GUV were oriented with their P-face exposed to the external solution, as shown schematically in Figure 5.6 and consistent with the retention of orientation upon fusion illustrated in Figure 5.1B and 5.6A. Because the tethered and flattened hemispherical GUVs are under tension, and since transient holes in GUVs have been reported[133], the tethered GUVs might be leaky. However, we have no evidence for leakiness – if holes are formed, the tethered GUV will start to rupture and become a patch; the fluorescence dye inside of GUVs was not observed to be leaked out.[108] Since the quenching of RCs was observed within a few minutes of addition of QSY®-21, we expect that the QSY®-21 quencher could not diffuse into the inside of the GUVs during this short interval even if GUVs are slightly leaky.[134]

5.4 Conclusion

The retention of RC orientation during protein and lipid transfer to a tethered GUV provides insight into the mechanism of DNA-mediated fusion, suggesting that the

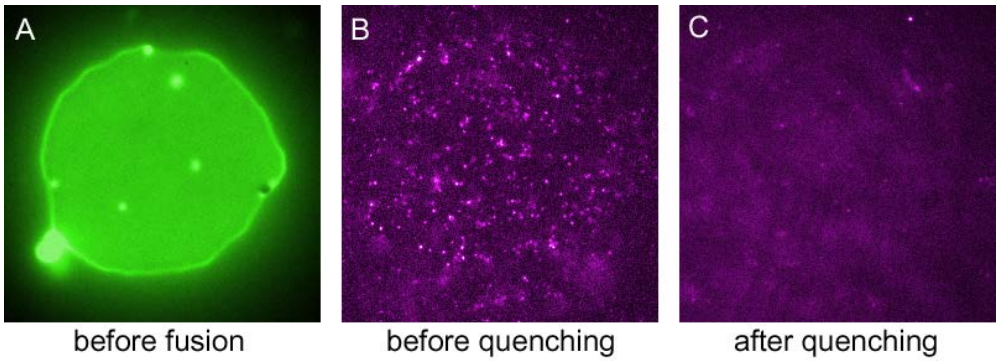

Figure 5.10 Fluorescence quenching experiment for Alexa633-labled RCs transferred to a GUV. A: A tethered GUV is visualized by a small amount of OG-DHPE lipid dye, B: bright dots of Alexa633-RCs appear as a result of fusion and are visualized by TIRF (λ_{ex} = 633 nm, λ_{em}= 650-675 nm), C: the dots become dim after the QSY-21 quencher is added.

proteoliposomes are able to fully fuse into the target membrane in a manner analogous to what is believed to occur[135] during full collapse fusion of synaptic vesicles to the pre-synaptic membrane of a nerve terminal. Indeed, the ability to reliably monitor the transfer of an integral membrane protein during vesicle fusion and to assay its resulting orientation in the target membrane afterward is both unusual and potentially highly informative for mechanistic studies of membrane fusion. A variety of research groups interested, often studying synaptic vesicle recycling at the nerve terminals of cultured neurons, have been able to monitor the transfer of integral membrane proteins from vesicles to the target plasma membrane by means of GFP-fusion proteins[135-139] or immunofluorescence, but these are difficult studies and the noise inherent to these realistic biological systems makes the analysis of their results in terms of mechanistic insight not simple. In model membrane fusion systems, which are designed to simplify the complicated biological picture and focus on the underlying principles and mechanism of membrane fusion, the study of integral protein transfer and orientation during fusion is often not possible or is not performed, and the more easily accessible indicator of membrane fusion-lipid mixing-is the most widely used. In this light, we anticipate that our model membrane architectures (the DNA-tethered membrane patch and tethered GUV) can serve as promising alternatives to conventional model membrane fusion systems, as they easily permit observation of lipid, content, and protein transfer during vesicle fusion events.

Chapter 6. Atomic selectivity in dissociative electron attachment to dihalobenzenes

6.1 Introduction

Chemical selectivity is often used in organic synthesis to effectively produce and purify specific molecules of interest.[140-142] Living organisms commonly utilize selectivity to recognize, to uptake, to synthesize, to secrete, and to transport specific molecules or ions in physiological systems.[143-145] At the molecular level, different types of atom-selective reactions have been studied with molecular beams. McDonald *et al.* found that the D + ICl reactive collision selectively yields DI + Cl rather than DCl + I, although the latter is the more exothermic reaction.[146] It was suggested that the electron in the D atom enters the empty molecular orbital of ICl that resembles the atomic I orbital, thus leading to the DI product. The atomic selectivity that results from asymmetric participation of a molecular orbital in a reactive collision was aptly (and whimsically) named "orbital asymmetry". Taking this notion further, Liu *et al.* found that the collision of ICl with the Si (111)-(7x7) surface predominantly (~82%) leads to the I-end-first collision to form a Si–I–Cl transition state, followed by breaking of the I–Cl bond and the rejection of the Cl atom back into the gas phase,[147] despite this being the least exothermic of all possible reactions.

The simple diatomic case of orbital asymmetry needs to be revised when the diatomic molecular orbital mixes with another orbital, especially when the latter is the likes of a diffuse, delocalized orbital of a benzene ring that lies between the diatom. The goal of the present study is to address, by investigating the direct

electron attachment to dihalobenzene species such as bromochlorobenzene (BCB), bromoiodobenzene (BIB) and chloroiodobenzene (CIB), (1) how well the principle of orbital asymmetry is preserved in the aromatic dihalogens; (2) whether the effect depends on the relative position of the substitution sites of the halogen atoms; and (3) how the relevant molecular orbitals change in energy upon electron attachment.

6.2 Experiment

The details of our experimental scheme have been described elsewhere.[148,149] Briefly, we first generated a molecular beam of dihalobenzene molecules by expanding a thermally evaporated sample seeded in 4 bar of Ar carrier gas through a pulsed nozzle. Electron impact by an electron gun (400 eV, 200 μA) produced low-energy secondary electrons, whose attachment to neutral molecules turned them into anions. These anions were extracted into a Wiley-McLaren type time-of-flight mass spectrometer, where they were mass-selected by a mass gate before entering a magnetic-bottle type photoelectron spectrometer. Irradiation of anions by the third harmonic output (355 nm) of a pulsed Nd:YAG laser ejected photoelectrons whose kinetic energy was measured to yield the photoelectron spectrum by subtracting the electron kinetic energy from the incident photon energy.

6.3 Computational details

Gaussian 03 revision C.02 was used for theoretical calculations.[152] We used a split-valence basis set for both MP2 and B3LYP methods in the case of BCB. For the

iodine-containing molecules BIB and CIB, however, we adopted the LanL2DZ basis set for both MP2 and B3LYP methods since a split-valence basis set is not applicable to heavy atoms. (According to the Gaussian user's reference, we note that split-valence basis sets can be applied only to hydrogen up to krypton.) We also note that the 6-311 basis set is not defined for iodine, while the LanL2DZ basis set was successfully used to calculate iodine-containing molecules. Radical anions were calculated with unrestricted methods. All results given here were verified by vibrational frequency analysis to ensure energy minima. Atomic charges in all our figures were obtained from Mulliken charge analysis. The calculated vertical detachment energy was obtained by subtracting the energy of the anionic ground state from that of the neutral species at the anionic geometry. Potential energy curve was obtained with the relaxed potential energy surface scan.

6.4 Results and discussion

6.4.1 Atomic selectivity in electron attachment to bromochlorobenzene (BCB)

Figure 6.1 shows the anion mass spectrum obtained with *p*-bromochlorobenzene (4-BCB), which exhibits a series of mass peaks for the clusters of 4-BCB as well as a prominent mass peak for a major fragment, Br^-, which must have come from dissociative electron attachment (DEA) during electron impact as has been suggested by Rosa *et al.*[150] This is supported by the fact that the intensity ratio of Br^-/BCB^- increases with the kinetic energy of the electron beam. It is noteworthy

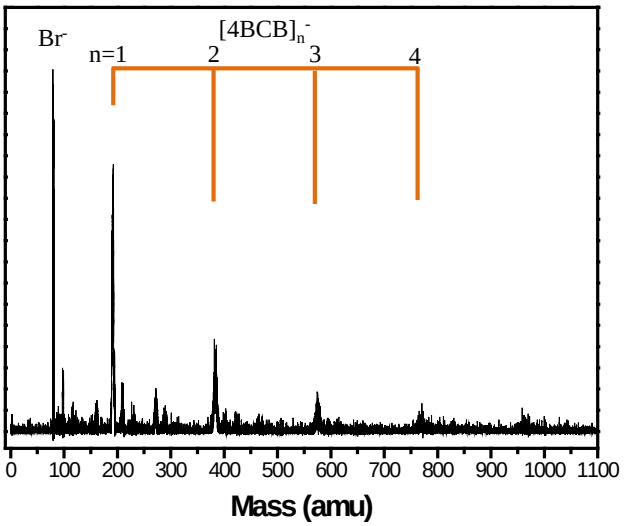

Figure 6.1 Mass spectrum of the cluster anions of 4-BCB. The most intense peak is due to the fragmentation product Br^-. Among the homogeneous anion clusters, the monomer anion is the predominant species. Heavier clusters were observed up to hexamer, at much weaker intensities.

that the other possible fragment, Cl^-, is nearly absent from the mass spectrum, which is quite consistent with the results of previous studies.[150] The overall mass distribution is much the same for the other two isomers of BCB (2- and 3-BCB for *o*- and *m*-BCB, respectively), which indicates that these molecules all undergo nearly identical DEA processes regardless of the relative positions of the Br and Cl atoms, yielding Br^- but not Cl^-.

When a free electron is captured by a neutral BCB molecule in the gas phase, it forms a transient negative ion BCB^{-}*, from which two possible pathways lead to fragment and intact anions respectively:

$$BCB^{-}* \rightarrow Br^- + C_6H_4Cl\cdot \qquad (6.1)$$

$$\rightarrow BCB^- + \text{excess energy} \qquad (6.2)$$

The first of these represents the DEA channel that produces Br^- and a radical, while the second channel yields a relaxed valence anion of BCB. The fact that the mass peaks of Br^- and BCB^- in Figure 6.1 are of comparable intensity may indicate that a considerable amount of BCB undergoes DEA upon electron attachment, possibly because the vertical transition from BCB to BCB^- leads the system to land on the highly repulsive part of the latter's potential energy surface, in a similar way as with SF_6 and other cases.[151]

The cluster mass peaks show a rapidly decreasing intensity at larger cluster size and we only observed clusters up to $(BCB)_6^-$. Other species such as $[(BCB)_m(H_2O)_n]^-$ from trace amount of residual water in our apparatus and

$[(BCB)_mBr_n]^-$ from recombination with the dissociated Br^- were observed in weak intensity.

Figure 6.2 shows the photoelectron spectra of the three isomeric BCB monomer anions obtained at 355 nm (= 3.496 eV). All of these spectra appear to be mainly composed of a small number of component bands, and we found that they can be rather solidly represented by two common Gaussian bands centered at ~2.4 and ~ 2.8 eV. The vertical detachment energies (VDEs) of these three isomers of BCB are estimated to be nearly identical too: 2.33, 2.36, and 2.40 eV for 2-, 3-, and 4-BCB, respectively, which are in reasonable agreement with the theoretical values (Table 6.1) calculated with the Gaussian package.[152] It appears that the relative positions of Br and Cl in the BCB isomers play little role in the overall electron attachment process. Interestingly, no sign of the photoelectron band for Br^- (EA = 3.36 eV)[153] was detected in Figure 6.2, even considering the large scattering noise in the relevant spectral region. This suggests that Br^- in Figure 6.1 comes only from DEA that occurs before the free flight, which means the two Gaussian component bands of Figure 6.2 are genuinely due to the BCB monomeric anion. According to our potential energy surface scan calculations, there occur curve-crossings involving three anion states (Figure 6.3). Two of these states (of $^2A_2$ and $^2B_1$ symmetry) are closely-lying in energy with a minimum at 1.9 Å along C-Br bond distance. The third anion state (of $^2A_1$ symmetry) has a higher energy than the other two states at a distance shorter than 1.9 Å, but it becomes the lowest-energy state at distance

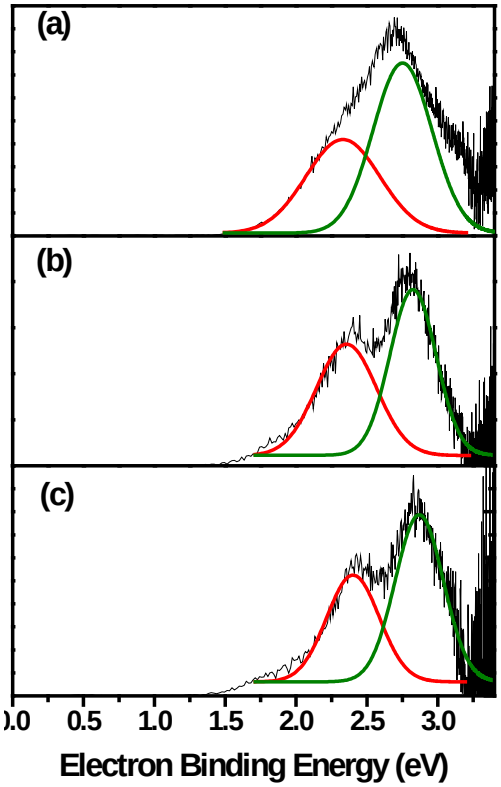

Figure 6.2 Photoelectron spectra of (a) 2-BCB, (b) 3-BCB and (c) 4-BCB monomeric anions. No trace of Br^- photoelectron band was observed, indicating that the Br^- anion detected in the mass spectrum does not come from dissociative electron attachment during the time-of-flight. All three isomers yield similar values of VDE, while their spectra are all deconvoluted into two Gaussian bands that are ~0.45 eV apart. Experimental data above 3.4 eV is omitted due to the scattering noise of electrons.

	MP2/aug-cc-pVDZ	B3LYP/6-311++G**	Experiment
2-BCB	2.91	2.84	2.33
3-BCB	2.23	2.76	2.36
4-BCB	2.33	2.80	2.40

Table 6.1 Calculated and experimentally measured vertical detachment energies (VDEs, in eV) of the three isomers of bromochlorobenzene (BCB). Calculated energies were obtained at the MP2/aug-cc-pVDZ and B3LYP/6-311++G** levels, while the experimental values were obtained from anion photoelectron spectroscopy.

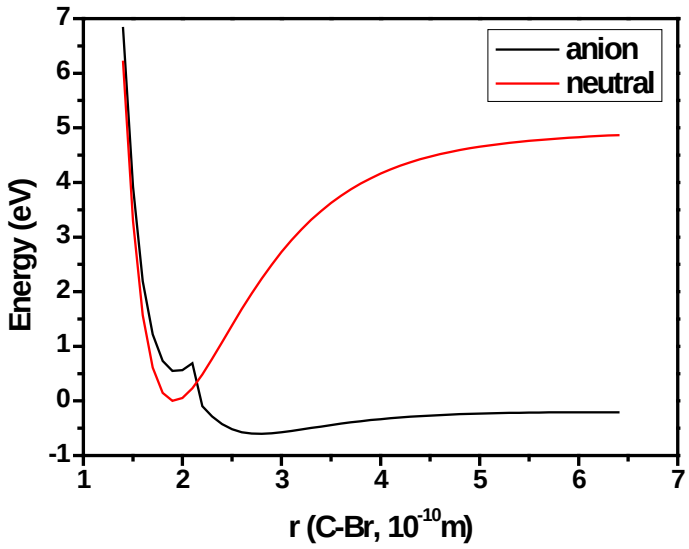

Figure 6.3 Calculated potential energy curves of the 4-BCB. The energies were calculated as the C-Br distance varies from 1.4 Å to 6.4 Å. There is a curve-crossing in the anion potential energy curve near 2.0 Å. The anionic ground state has A_1 symmetry which shows very steep repulsive curve at short distance (< 2.0 Å). At that distance, another two closely-lying anionic states with A_2 and B_1 symmetry are more stable than the state with A_1 symmetry. Calculations were carried out using Gaussian 03, revision C.02 at the B3LYP/6-311++G** level.

greater than 1.9 Å, with a shallow minimum at 2.5 Å. According to our higher-level CASSCF calculation, the origin of the first band in the photoelectron spectra is the transition from the anionic $^2A_1$ state to neutral $^3A_1$ state, while that of the second band is the transition from the anionic $^2A_1$ state to neutral $^3B_1$ state for 4-BCB. The calculated VDE values for the two bands are 2.84 and 3.23 eV, whose difference (0.39 eV) is in good agreement with the experimental one (2.86 – 2.40 eV = 0.46 eV). These assignment only apply to 4-BCB with C_{2v} symmetry but not to 2- and 3-BCB that have C_s symmetry. According to our calculation, there are six neutral states of $^1A_1$, $^1A_2$, $^1B_1$, $^3A_1$, $^3A_2$ and $^3B_1$ symmetry but three of them ($^1B_1$, $^3A_2$, and $^1A_2$) are located more than 4 eV above the anionic ground state. We note that the photoelectron spectrum of 2-BCB is not completely deconvoluted with two component bands. Although its symmetry is different from that of 4-BCB, a possible third band at ~3.15 eV may be due to a transition to neutral ground state ($^1A_1$), whose energy increase steeply as the C-Br distance increases, from even below the anionic ground state ($^2A_1$) at short C-Br distance to above the two neutral triplet states (calculated VDE of 3.48 eV vs. 2.84 eV for $^3A_1$ and 3.23 eV for $^3B_1$) at the CASSCF C-Br distance of 2.64 Å. The neutral ground state ($^1A_1$) has C_{2v} symmetry for all three *p*-substituted dihalobenzenes and C_s symmetry for all six *o*- and *m*-substituted dihalobenzenes.

6.4.2 Molecular orbitals of BCB and BCB$^-$

To understand the observed DEA and its preferential atomic selectivity for Br^-, we

carried out *ab initio* calculations for the electronic structures of BCB and BCB^- at the level of MP2/aug-cc-pVDZ and B3LYP/6-311++G** for all three isomers. The most significant change in molecular structure when going from BCB to BCB^- is the elongation of the C–Br bond (1.9 to 2.5 Å, Figure 6.4), with an indication that the singly occupied molecular orbital (SOMO) of the monomeric anion is anti-bonding in nature, notably in the C–Br region. In contrast, only insignificant changes were observed in the C–Cl bond length and structural parameters of the benzene ring. The calculated electrostatic charge indicates that the negative charge of the electron to turn BCB into BCB^- is almost entirely (-0.95 e~-0.98 e) invested on the *less* electronegative Br atom, whereas the more electronegative Cl atom gains little negative charge.

A localized core of electrostatic charge such as found in BCB^- is likely to be prone to a large solvation effect. Figure 6.5 compares the photoelectron spectrum of 3-BCB^- and its monohydrated complex, $[(3\text{-BCB})_1(H_2O)_1]^-$. Although they both have the same Gaussian component bands mentioned earlier, those of the latter are blue-shifted by about 0.2 eV, apparently due to the stabilization effect of the water molecule. The magnitude of the blue shift is comparable to that found for the monomeric anion core of naphthalene stabilized by the water molecule.[154] Since the majority of the anionic charge is on the Br^- atom in BCB^-, we expect that water selectively hydrates it when it makes a 1:1 complex with BCB^-, which is supported by our *ab initio* calculation that finds the C–Br distance is further elongated to 2.76

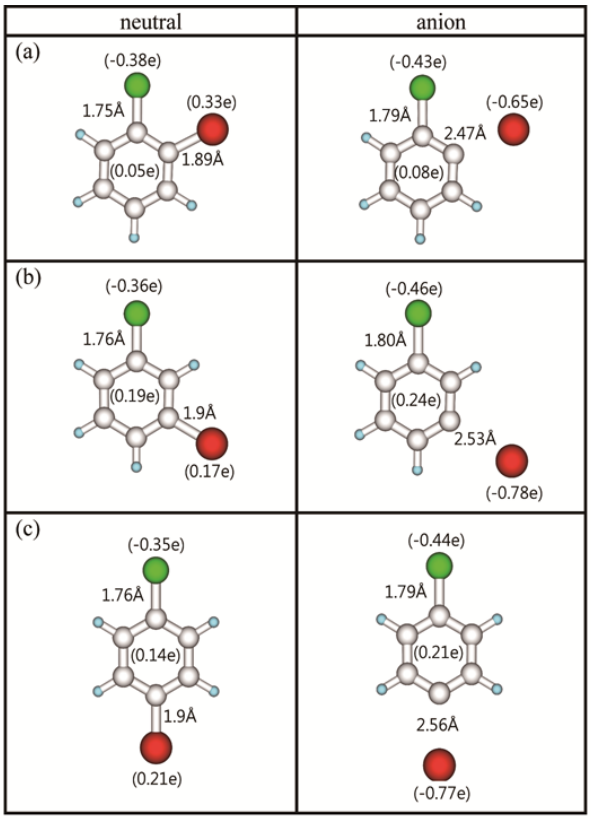

Figure 6.4 Optimized geometries for all three isomers of neutral and anionic BCB obtained with B3LYP functional. The Cl and Br atoms are colored green and red, respectively. The C–Br bond length increases from 1.9 Å to 2.5 Å upon electron attachment, indicating that the approaching electron enters an anti-bonding orbital. In neutral BCB, Br has a partial positive charge whereas Cl has a partial negative charge, in accord with the higher electronegativity of the Cl atom. In anionic BCB^{-}, most (95~98%) of the extra charge newly added goes to the Br atom, leaving the Mulliken charge of Cl and the benzene ring largely unaffected.

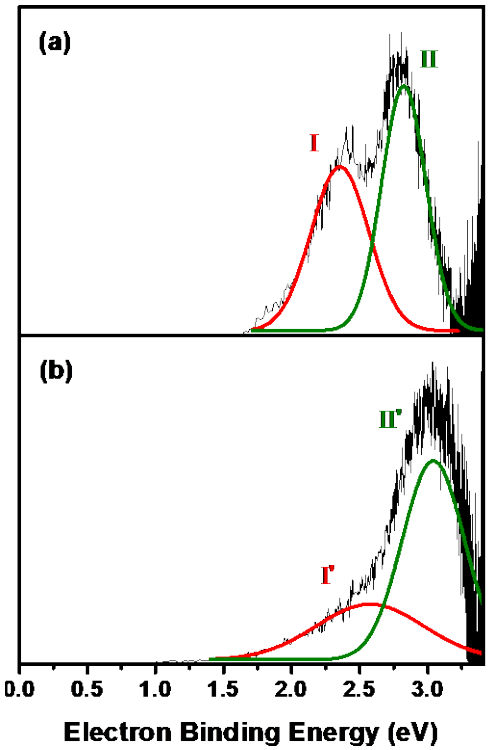

Figure 6.5 Photoelectron spectra of (a) $[3\text{-BCB}]^-$ and (b) $[(3\text{-BCB})_1(H_2O)_1]^-$ taken at 355 nm. Both spectra are deconvoluted into two Gaussian bands with nearly the same energy difference. Water acts as a solvent to stabilize $[3\text{-BCB}]^-$ by about 0.2 eV, with its H atom interacting with Br that has a partial negative charge.

Å in $[(3\text{-BCB})_1(H_2O)_1]^-$ from 2.53 Å in 3-BCB$^-$, with little changes in all other parameters of molecular geometry (Figure 6.6 for 2-BCB) and the overall characteristics of the molecular orbitals (Figure 6.7).

Atom-selective electron attachment itself is quite interesting for this aromatic species but what is even more surprising is that the electron is attached to the *less* electronegative atom, Br, not to the more electronegative one, Cl. We note that the "orbital asymmetry" model originally developed by Herschbach[155] to explain the overwhelming disparity of the D + ICl product formation in a counterintuitive way (electron of the D atom attacking the *less* electronegative I atom to produce DI predominantly)[146] should also apply to the current case of BCB. The original model based on the simple frontier orbital theory[156,157] predicted that the empty orbital of ICl subject to the incoming D atom is its LUMO, which resembles the higher-lying atomic I orbital rather than the more stable Cl orbital, fostering the DI product. The model also predicted that reactions of Br, O, and CH_3 with ICl occur through the I-end collision first, in the same way as with D + ICl. From their extensive studies, Herschbach *et al.* proposed the "electronegativity ordering rule" that identifies the preferred arrangement of atoms in triatomic reactants, the least electronegative atom being the prime target of the incoming atom.[158]

Despite the clear insight and success of the above model, the present target molecule BCB may not obey the rule since its diffuse, delocalized electron cloud of the benzene ring between Br and Cl could cause significant deviation from the

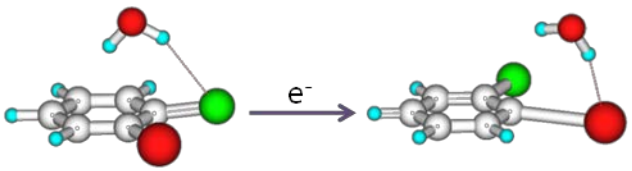

Figure 6.6 Optimized structures of $[(2\text{-BCB})_1\text{-}(H_2O)_1]$ and $[(2\text{-BCB})_1\text{-}(H_2O)_1]^-$. In the neutral state, an H atom of water directly interacts with Cl, which is the only negatively charged moiety in 2-BCB. In the anionic state, water moves toward the Br atom for a more preferential interaction, with its H atom forming a tighter bond with Br, which accommodates most of the negative charge in electron attachment. Note the C–Br bond is significantly elongated in BCB^-.

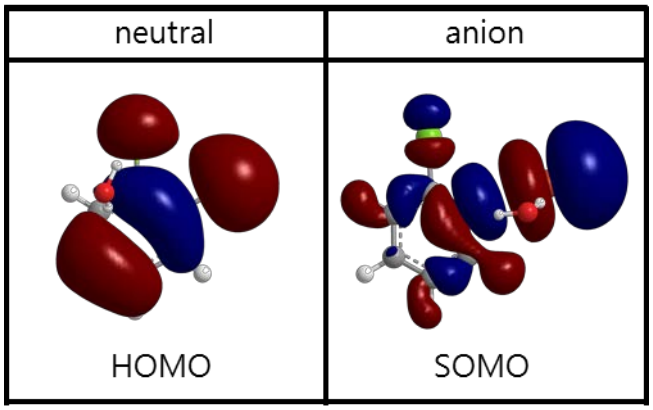

Figure 6.7 Neutral HOMO and anionic SOMO of $[(2\text{-BCB})_1\text{-}(H_2O)_1]^-$. Cl and Br are colored green and red, respectively. Water interacts directly with Cl in the neutral but switches to a preferential interaction with the Br-end in the anion. Calculations were carried out using Gaussian 03, revision C.02 with B3LYP/6-311++G**.

simple diatomic-based model. Therefore, we find the high degree of atomic selectivity observed in our electron attachment rather unexpected and temptingly akin to that found in the original atom + diatom reaction. To address the origin of the atomic selectivity in our experiment with BCB, a full scale molecular orbital scheme was carried out.

Figure 6.8 shows the HOMO of 4-BCB and the SOMO of 4-BCB$^-$, the latter of which has an anti-bonding character with an electron density predominantly localized on the Br atom. (See also Figure 6.9 for the similar cases of 2-BCB and 3-BCB.) Since the bonding orbital involving the Cl atom lies well below the non-bonding orbital and Br is more polarizable than Cl, the approaching electron is guided to the Br-end and enters what becomes the SOMO of the anion localized on the C–Br bond, leading to its dissociation. Furthermore, the approaching electron induces what may be called "orbital energy reordering". Figure 6.10 shows that the LUMO and LUMO+1 of neutral 4-BCB undergo great destabilization by neatly 4 eV upon electron attachment to become the LUMO+1 and LUMO+4 of the anion, respectively. On the other hand, the LUMO+2 of the neutral that represents the σ^*(C–Br) orbital is stabilized and becomes the SOMO of the anion. The vacant MO representing the Cl-benzene locates at 0.92 eV higher energy than that of Br-benzene in neutral. Thus, it is unlikely to attract the excess electron. Mulliken charge analysis also supports our experimental results based on the estimation of atomic charges on Br and Cl in the neutral and anionic states (Table 6.2). In the

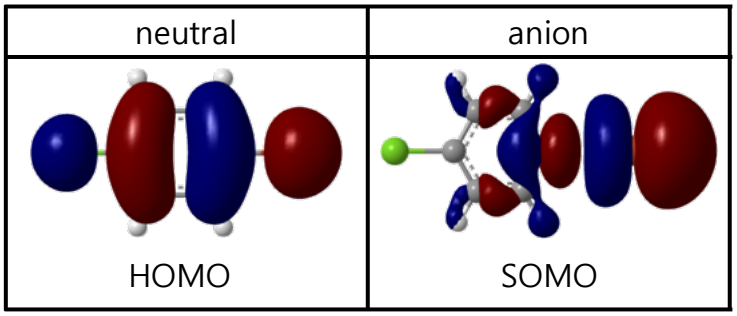

Figure 6.8 Relevant molecular orbitals of neutral and anionic 4-BCB obtained with B3LYP functional. Upon electron attachment, the newly added negative charge that goes into an anti-bonding orbital is mostly localized on the *less* electronegative Br atom. The same trend is observed for 2-BCB and 3-BCB.

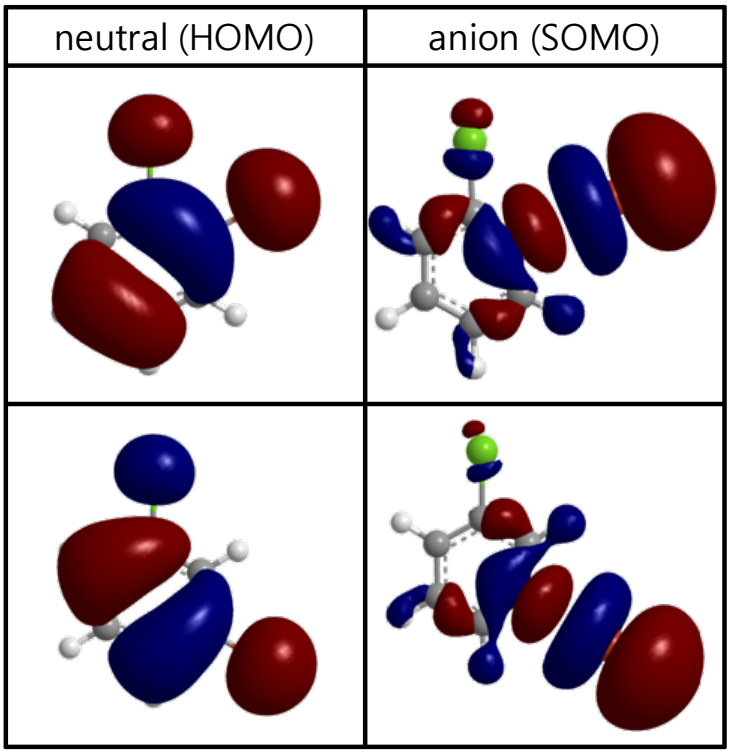

Figure 6.9 Neutral HOMO and anionic SOMO of 2-BCB (top) and 3-BCB (bottom). Cl and Br are colored green and red, respectively. The HOMO of the neutral molecule is a non-bonding orbital, with a node between C and Br. The SOMO of the anion is highly developed around the Br moiety, as in the case of 4-BCB (Figure 6.8). Calculations were carried out using Gaussian 03, revision C.02 at the MP2/aug-cc-pVDZ level.

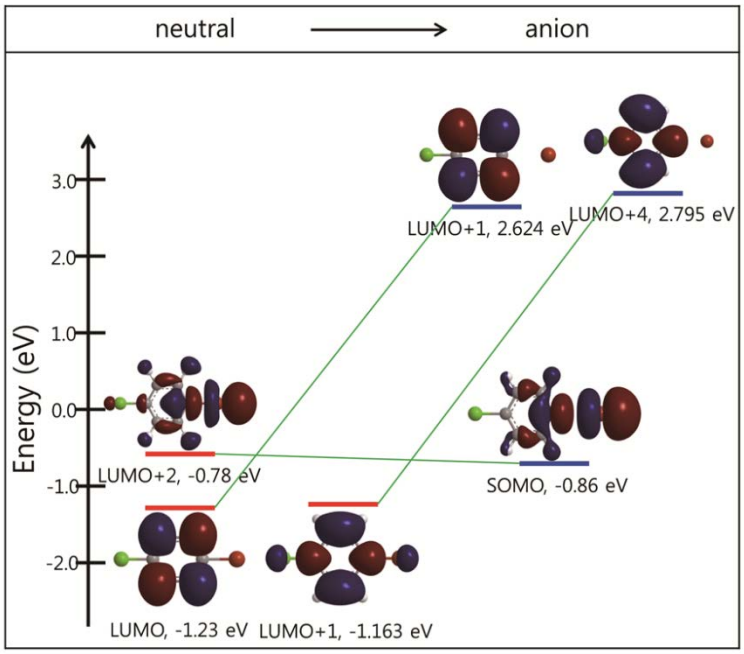

Figure 6.10 Orbital energy reordering for 4-BCB following electron attachment obtained with B3LYP functional. The LUMO and LUMO+1 of neutral 4-BCB are greatly destabilized by nearly 4 eV upon electron attachment and become the LUMO+1 and LUMO+4 of the anion, respectively. On the other hand, the LUMO+2 of neutral 4-BCB remains at nearly the same energy to become the SOMO of the anion.

		Cl	Ring	Br
2-BCB	neutral	-0.375	0.046	0.329
	anion	-0.429	0.078	-0.649
3-BCB	neutral	-0.364	0.192	0.172
	anion	-0.458	0.234	-0.776
4-BCB	neutral	-0.353	0.140	0.213
	anion	-0.437	0.210	-0.773

Table 6.2 Mulliken atomic charges for the three isomers of BCB calculated at the MP2/aug-cc-pVDZ level. Most of the negative charge (-0.95 e~-0.98 e) is invested on the *less* electronegative Br atom upon electron attachment, which undergoes a drastic change from a positively charged moiety in the neutral to the strongest negatively charged one in the anion.

neutral state of all three isomers, Cl has a partial negative charge and Br has a partial positive charge since Cl is more electronegative than Br. In the anionic state, however, Br takes up most of the negative charge (-0.7 e~-0.8 e) while the charge on Cl remains nearly the same as in the neutral, indicating that nearly a whole electronic charge goes to the Br-end exclusively.

6.4.3 Atomic selectivity in electron attachment to bromoiodobenzene (BIB) and chloroiodobenzene (CIB)

In order to see if and how rigorously the atomic selectivity of electron attachment holds for other dihalobenzene species, we carried out the same mass spectrometry and photoelectron spectroscopy experiments for BIB and CIB. Figure 6.11 shows the mass distribution of the anion clusters of 4-BIB, which is much the same with those of 2- and 3-BIB as well as 2-, 3-, and 4-CIB (Figure 6.12), again reconfirming that these members of the dihalobenzene family undergo very similar DEA processes regardless of the relative positions of their two halogen atoms. For both BIB and CIB, the most abundant species in the mass spectra are the anion of the *less* electronegative halogen atom, I^-, in full compliance with the orbital asymmetry model. We again confirm that I^- results from DEA by observing that the ratios of I^-/BIB^- and I^-/CIB^- increase with the kinetic energy of electron impact. No sign of the *more* electronegative atoms, Br^- or Cl^-, was detected. As in the case of BCB, the photoelectron spectra of BIB and CIB can also be deconvoluted into two Gaussian component bands separated by ~0.5 eV (Figure 6.13 and 6.14). Their experimental

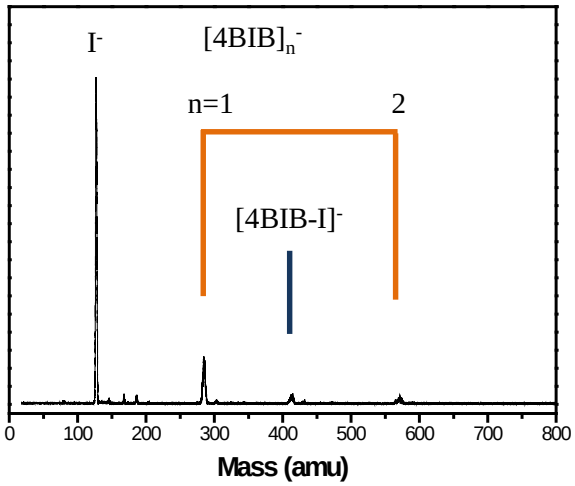

Figure 6.11 Mass spectrum of the cluster anions of 4-BIB. The most intense peak is due to the fragmentation product I^-. Among the homogeneous anion clusters, only the monomer anion shows a significant intensity, while clusters larger than dimer have negligible intensities.

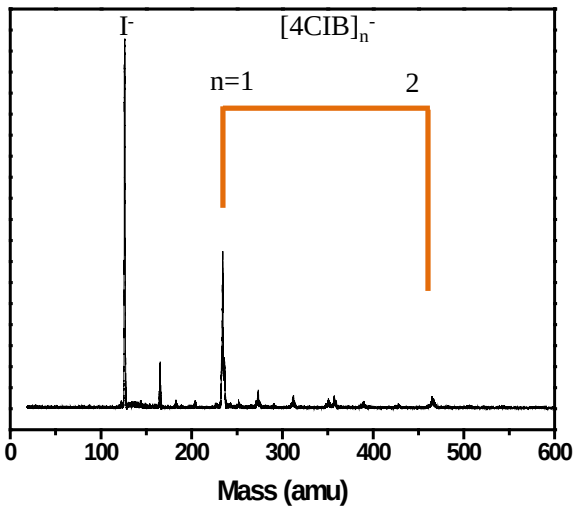

Figure 6.12 Mass spectrum of 4-CIB cluster anions. The most intense peak is due to I^-, with the cluster anions trailing in intensity in a rapidly decreasing manner.

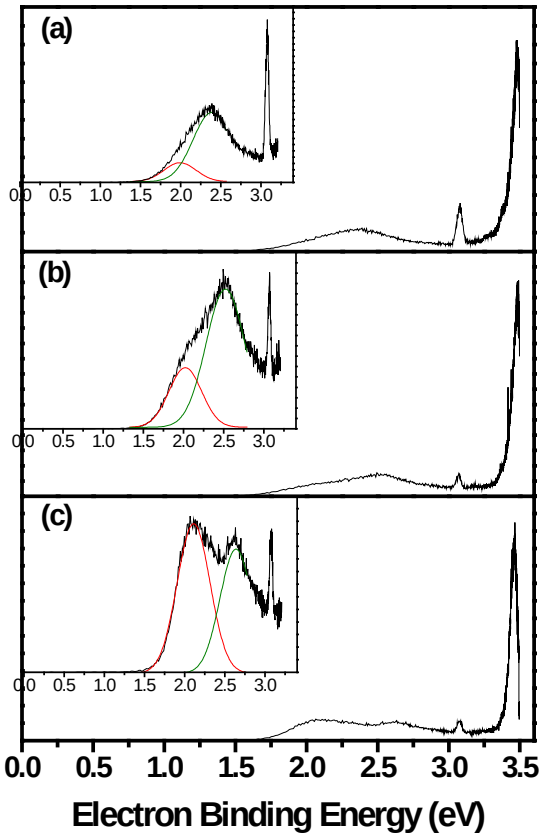

Figure 6.13 Photoelectron spectra of (a) 2-BIB, (b) 3-BIB and (c) 4-BIB monomer anions. The sharp band in all three insets at 3.06 eV is due to I^-, which results from photodissociation followed by photodetachment. As with BCB, the spectra from 1.5 to 3.0 eV for all three isomers can be deconvoluted into two Gaussian bands that are ~0.5 eV apart.

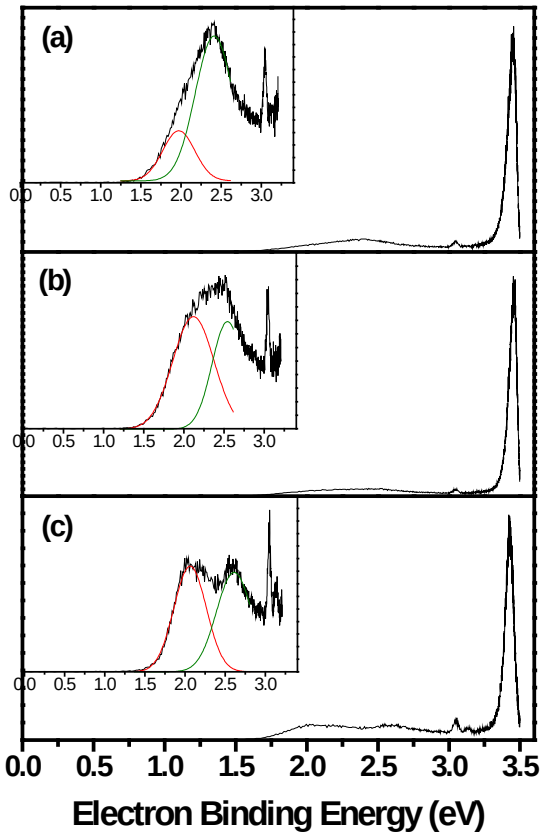

Figure 6.14 Photoelectron spectrum of (a) 2-CIB, (b) 3-CIB and (c) 4-CIB monomer anions. The sharp atomic photoelectron band of I^- at 3.06 eV is due to a two-photon process involving photodissociation followed by photodetachment. As in the case of BCB, the broad photoelectron spectrum from 1.5 to 3.0 eV can be deconvoluted into two Gaussian bands separated by ~0.5 eV.

VDE values do not exactly match the theoretical ones in isomer-dependent trend but are in reasonable agreement overall (Table 6.3). We also performed theoretical calculations for both BIB and CIB to compare with the results for BCB. We carried out calculations for the same six neutral states and three anion states, and found that the anionic ground state is always $^2A_1$ as in the case of BCB. Likewise, the major two photoelectron bands are due to the transition $^3A_1 \leftarrow {}^2A_1$ and $^3B_1 \leftarrow {}^2A_1$, just as in the case of BCB.

An additional feature was found for all six isomers of BIB and CIB, however, in the form of a sharp photoelectron peak at 3.06 eV. The FWHM of this peak is 40 meV, indicating its atomic (as opposed to molecular) origin, and the electron binding energy corresponds to the known electron affinity of I^-.[159] To investigate the origin of this I^- peak, we carried out laser power dependent experiments. Since the photoelectron spectra of Figure 6.13 and 6.14 were taken at the mass of dihalobenzene monomer anion, there may be the following two mechanisms for the generation of I^-: I^- dissociating from an activated monomer anion during its free flight vs. I^- generated by photon in the photodetachment region at the end of flight. We expect that the photoelectron signal from I^- is linearly proportional to the power of the laser beam if I^- is automatically generated from dissociation during time-of-flight, whereas a quadratic dependence is expected if I^- is generated by photodissociation in the photodetachment region. Figure 6.15 shows the plot of photoelectron yield versus the power of the photodetachment laser, whose slope is

	MP2/LanL2DZ	B3LYP/LanL2DZ	Experiment
2-BIB	2.28	2.49	1.99
3-BIB	2.48	2.44	2.03
4-BIB	2.16	2.51	2.11
2-CIB	2.13	2.58	1.97
3-CIB	2.13	2.51	2.12
4-CIB	2.19	2.52	2.06

Table 6.3 Calculated and experimentally measured vertical detachment energies (VDEs, in eV) of the three isomers of bromochlorobenzene (BIB) and chloroiodobenzene (CIB). Calculated energies were obtained at the MP2/LanL2DZ and B3LYP/LanL2DZ levels, while the experimental values were obtained from anion photoelectron spectroscopy.

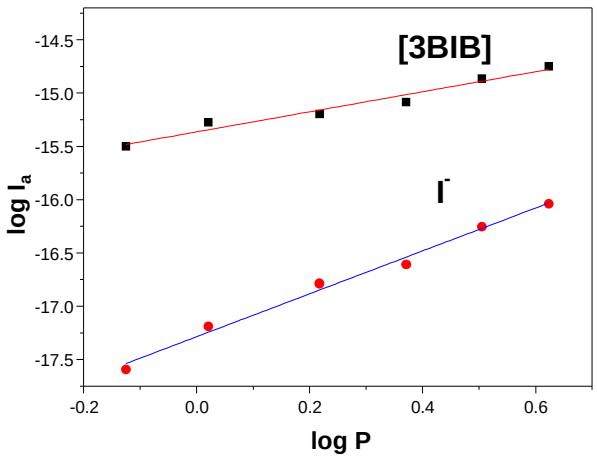

Figure 6.15 A log-log plot of I_a (anion intensity) vs. P (laser power) for I^- and $[3\text{-BIB}]^-$. The slope is 0.94 for BIB^- and 2.0 for I^-, indicating that the electron detachment from BIB^- is a one-photon process, whereas that from I^- is a two-photon process.

0.94 for $[3\text{-BIB}]^-$ and 2.0 for I^-, suggesting that the sharp I^- peak in the photoelectron spectrum comes from a two-photon process.

Therefore, there exist two distinct origins of photoelectron signal from BIB^- or CIB^-. The molecular anion may undergo one-photon detachment of electron (process (6.3) below) or a two-photon process where the first photon dissociates the molecular anion to generate I^- (process (6.4a)), whose electron is then removed by the second photon (process (6.4b)):

$$BIB^- \text{ (or } CIB^-) + h\nu \rightarrow BIB \text{ (or CIB)} + e^- \qquad (6.3)$$

$$\rightarrow C_6H_4Br\cdot \text{ (or } C_6H_4Cl\cdot) + I^- \qquad (6.4a)$$

$$I^- + h\nu \rightarrow I + e^- \qquad (6.4b)$$

We carried out *ab initio* calculations at the level of MP2/LanL2DZ and B3LYP/LanL2DZ for all six anions and their neutral counterparts. Here again, the most significant structural change upon electron attachment is the elongation of the C–I bond (from 2.2 to 2.7 Å, Figures 6.16 and 6.17) with little change in the C–Br or C–Cl bond length and structural parameters of the benzene ring.

Just as in the case of BCB, the bonding orbital of BIB and CIB resembles the atomic orbital of Br and Cl, respectively, since they are more electronegative than I, whereas the anti-bonding orbital takes up the character of the less electronegative I atom (Figure 6.18, 6.19 and 6.20). Orbital energy reordering very much like that occurring in BCB is also found in BIB and CIB. On the other hand, unlike in BCB where Cl had a partial negative charge in the neutral state, both halogen atoms Br and

I of neutral BIB are found to have partial positive charges while the benzene ring takes up the balancing negative charge (Table 6.4). In the BIB^- anion, the I atom takes up most of the excess charge (about -0.9 e) to turn from a positively charged moiety to a strongly negatively charged one (-0.68 e~-0.76 e). In the case of CIB, Cl is negatively charged in the neutral state but at a much lesser degree than in BCB, leaving the benzene ring apparently with more negative charge (Table 6.4). The negative charges on Cl and the benzene ring are only slightly increased in the anion, however, with most of the negative charge (-0.60 e~-0.68 e) moving to the I atom.

We find the negative charge on the benzene ring in BIB and CIB quite intriguing in the presence of the halogen atoms, which in BCB make the ring positively charged. For BIB in particular, the ring is the only positively charged moiety, whereas the Cl atom is the only negatively charged moiety in BCB. If we were to draw a primitive conclusion on the electronegative scale of halogen atoms and the benzene ring from these limited results, it would be Cl > benzene ring > Br ≥ I in decreasing order.

6.5 Conclusion

We found strong atomic selectivity in the DEA of the three dihalobenzene species, BCB, BIB, and CIB. Despite the vastly different electronic structure of these dihalobenzenes from that of simple diatomic halogens, the atomic selectivity is surprisingly akin to that found many years ago in the reactive collision of D + ICl in that the (free or hydrogenic) electron attacks the *less* electronegative end of the target molecule. This seemingly counterintuitive result is in accord with the “orbital

asymmetry" model of Herschbach that dictates the incoming electron to enter the empty orbital resembling the atomic orbital of the *less* electronegative atom. We found that the relative positions of halogen substitution play little role and that some of the molecular orbitals undergo drastic energy reordering upon electron attachment. We also explained the DEA of BCB anion into Br^- and the two-photon process that yields atomic I^- peak in the photoelectron spectra of BIB and CIB.

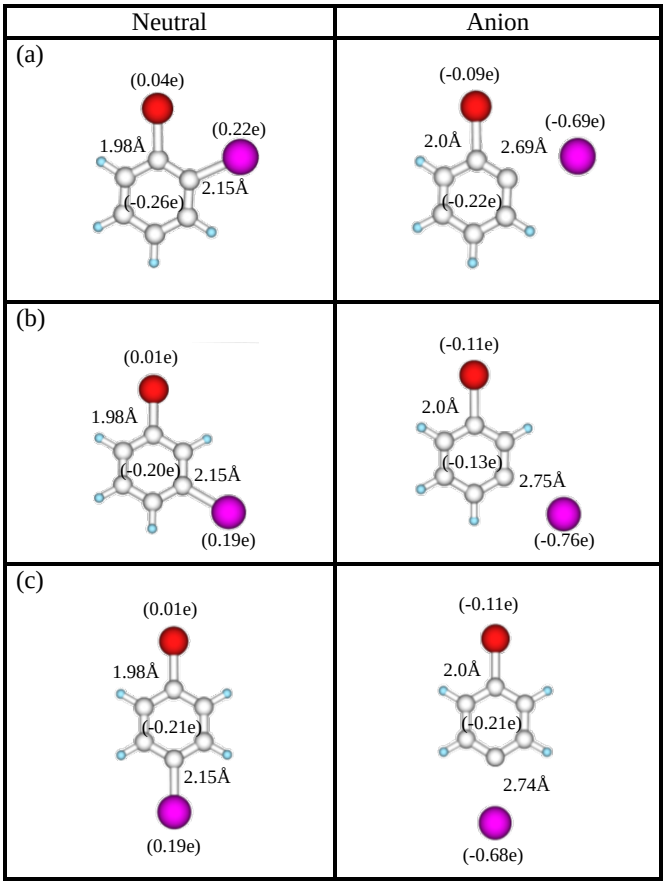

Figure 6.16 Optimized geometries for the three isomers of neutral and anionic BIB. Br and I are colored red and purple, respectively. The C–Br bond length increases drastically from 2.2 to 2.7 Å upon electron attachment, indicating the anti-bonding nature of the SOMO localized around the C–Br bond. Most of the approaching electron's charge (87~95%) goes to the I atom. Note that neither halogen atom has a negative charge in neutral BIB.

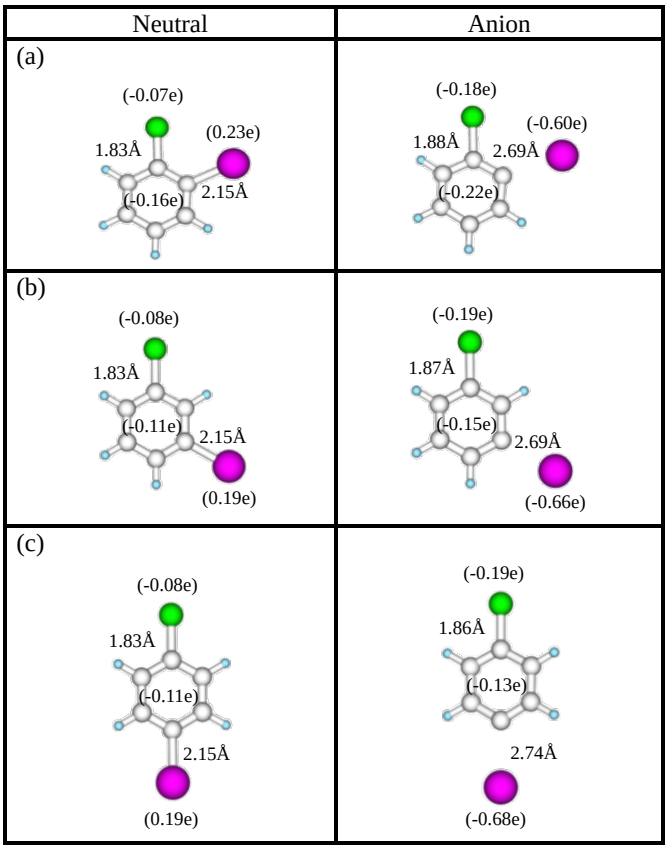

Figure 6.17 Optimized geometries for the three isomers of neutral and anionic CIB. Cl and I are colored green and purple, respectively. As with BIB, the C–I bond length increases drastically from 2.2 to 2.7 Å upon electron attachment, and most of the approaching electron's charge (83~87%) goes to the I atom.

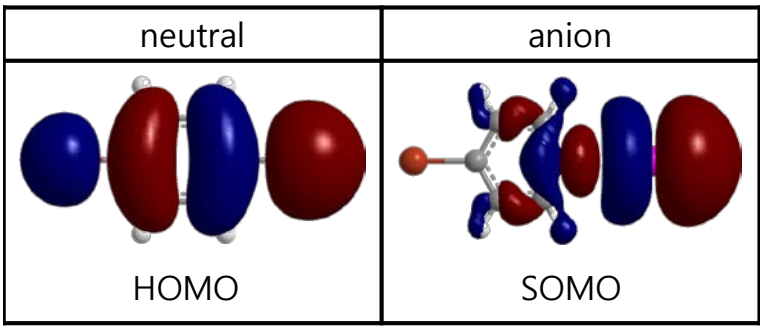

Figure 6.18 Relevant molecular orbitals of neutral and anionic 4-BIB obtained with B3LYP functional. Upon electron attachment, the newly added negative charge is mostly localized on the *less* electronegative I atom, as in the case of 4-BCB (Figure 6.8). The same trend is observed for 2-BIB and 3-BIB.

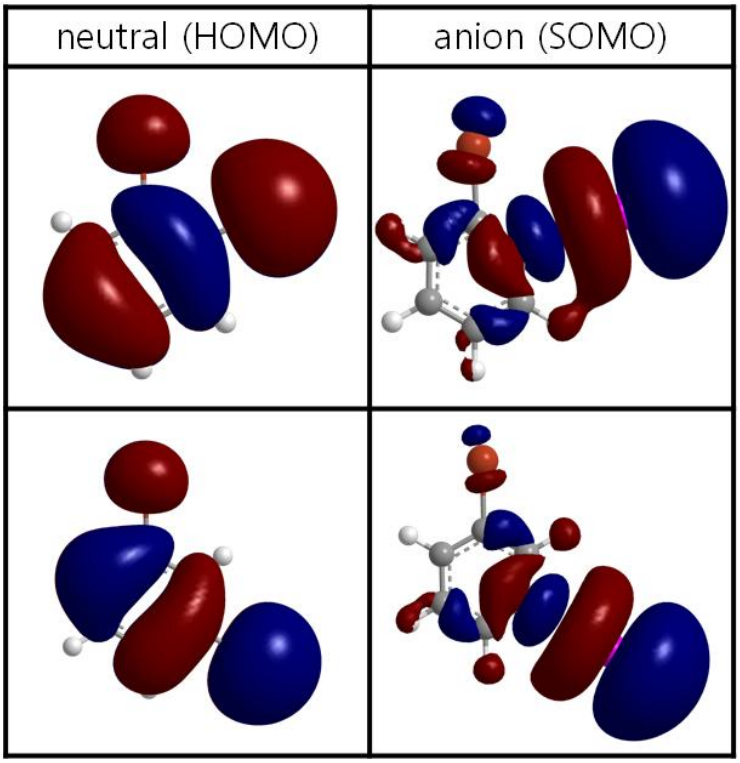

Figure 6.19 Neutral HOMO and anionic SOMO of 2-BIB (top) and 3-BIB (bottom). Br and I are colored red and purple, respectively. The HOMO of the neutral molecule is a non-bonding orbital, with a node between C and I. The SOMO of the anion is highly developed around the I moiety. Calculations were carried out using Gaussian 03, revision C.02 at the MP2/LanL2DZ level.

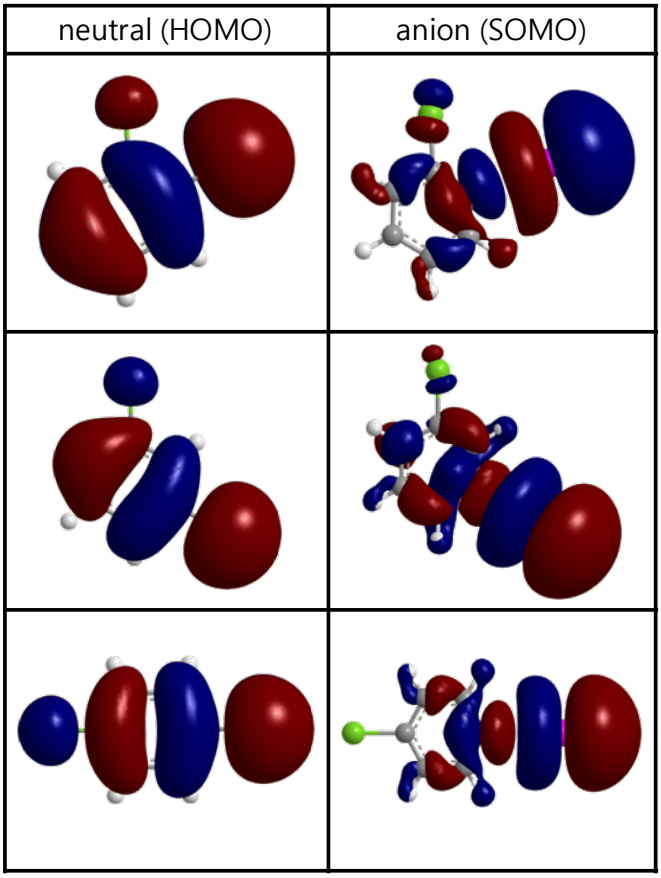

Figure 6.20 Neutral HOMO and anionic SOMO of 2-CIB (top), 3-CIB (middle), and 4-CIB (bottom). Cl and I are colored green and purple, respectively. The HOMO of the neutral molecule is a non-bonding orbital, with a node between C and I. The SOMO of the anion is highly developed around the I moiety. Calculations were carried out using Gaussian 03, revision C.02 at the MP2/LanL2DZ level.

		Br	Ring	I
2-BIB	neutral	0.036	-0.258	0.222
	anion	-0.090	-0.220	-0.690
3-BIB	neutral	0.013	-0.205	0.192
	anion	-0.106	-0.136	-0.758
4-BIB	neutral	0.014	-0.206	0.192
	anion	-0.105	-0.212	-0.683
		Cl	Ring	I
2-CIB	neutral	-0.067	-0.164	0.231
	anion	-0.181	-0.224	-0.5954
3-CIB	neutral	-0.086	-0.110	0.196
	anion	-0.186	-0.156	-0.658
4-CIB	neutral	-0.083	-0.112	0.195
	anion	-0.184	-0.133	-0.683

Table 6.4 Mulliken atomic charges of the three isomers of BIB and CIB calculated at the MP2/LanL2DZ level. Here, it is the I atom, again the *least* electronegative moiety, that undergoes the most drastic change in atomic charge upon electron attachment.

Chapter 7. Anion photoelectron spectroscopy and theoretical calculation of the hetero-dimers of polycyclic aromatic hydrocarbons

7.1 Introduction

Small aromatic hydrocarbons like benzene (Bz) and naphthalene (Np) do not make stable monomer anion upon the attachment of an extra electron in the gas phase since they have negative EA. Incoming electron feels strong repulsion due to the rich π-electron in the small area.[160,161] Only short-lived anionic species can exist in the gas phase for a very short time. The long-lived monomer anion was observed in the condensed phase.[162,163] For example, Np^- can exist in solution because of the stabilization effect of the solvent and the counterion. Thus, their EA was estimated indirectly through the electron transmission spectrum or by extrapolation of the higher clusters' EA.[164] However, stable monomer anion can be formed if the size of the molecule becomes bigger than naphthalene. The smallest stable monomer anion among polycyclic aromatic hydrocarbon (PAH) is a phenanthrene anion with the vertical detachment energy (VDE) of 0.13 eV measured by our photoelectron spectroscopy apparatus.[165] Otherwise, an unstable monomer anion becomes a stable cluster anion by making a complex with themselves (homo-cluster) or with other PAH molecules (hetero-cluster).

Structures of small homo-cluster cations and neutral counterparts were studied by theoretical calculation.[166] They found that charge resonance phenomenon in cation was important to have a stacking structure. The charge resonance band of the PAH anion was also observed and theoretically calculated by T. Shida and S. Iwata.[167] Homo-dimer anions of PAH larger than naphthalene all have parallel-displaced (PD)

structure, so that the excess negative charge is delocalized between two molecules.[168-170] In this case, the chromophore of the higher cluster anion is completely different from that of the monomer anion. Therefore, a new anionic core is generated upon electron attachment. An electrostatic interaction like dispersion force acts as a key role in this stacking structure that stabilizes the repulsion from an excess electron. On the other hands, Np_2^- is thought to have T-shaped structure due to high repulsion between the π electron and excess negative charge.[164]

$[Bz\text{-}Np]^-$ is the smallest stable hetero-dimer anion and its VDE was found to be 0.03 eV by PES.[171] Since the ring size of the benzene is not large enough to delocalize the excess negative charge, this complex adopts the T-shaped structure with a naphthalene monomer anionic core. Due to the solvation effect of the benzene molecule (~0.2 eV), a naphthalene monomer that has a negative EA (-0.19 eV) can form a stable valence anion complex. Two hydrogens in benzene are perpendicular to the naphthalene ring in order to have π-hydrogen interaction. However, there is no result that has been described on the large hetero-dimer anions. In this work, we report the TOF-MS, PES and theoretical calculation of hetero-dimer anions of PAH to reveal the optimized structures, charge distribution and anionic cores of each complex with a rather simple EA concept.

7.2 Experiment

The details of our experimental scheme have been described elsewhere.[149] Briefly, we generated a molecular beam of mixed clusters by expanding a thermally

evaporated sample seeded in 5 bar of Ar carrier gas through a pulsed solenoid valve that can be heated up to 200 °C. Since the melting points of four molecules are all different from each other, we never elevated the temperature of the sample mixture above the lower melting point. High-energy electron from an electron gun (400 eV, 200 μA) produced low-energy secondary electrons, whose attachment to neutral molecules turned them into anions. These anions were extracted into a Wiley-McLaren type time-of-flight mass spectrometer, where they were mass-selected by a mass gate before entering a magnetic-bottle type photoelectron spectrometer. The irradiation of anions by the second harmonic output (532 nm) of a pulsed Nd:YAG laser or 508 nm laser from 355 nm pumped dye laser ejected photoelectrons whose kinetic energy was measured to yield the photoelectron spectrum by subtracting the electron kinetic energy from the incident photon energy.

7.3 Results and discussion

7.3.1 PES of hetero-dimer anion of PAH

Figure 7.1 shows the mass spectrum of the mixture of An and Py, where the molar mass of An and Py are 178 and 202, respectively. There are two prominent peaks that correspond to the monomer anion of each molecule and two small peaks that correspond to homo-dimer anions. The intensities of these homo-dimer anions are 30 times smaller than that of the monomer anion. Besides homogeneous clusters, a 1:1 cluster appears between the peaks of homo-dimers that correspond to the hetero-dimer anion.

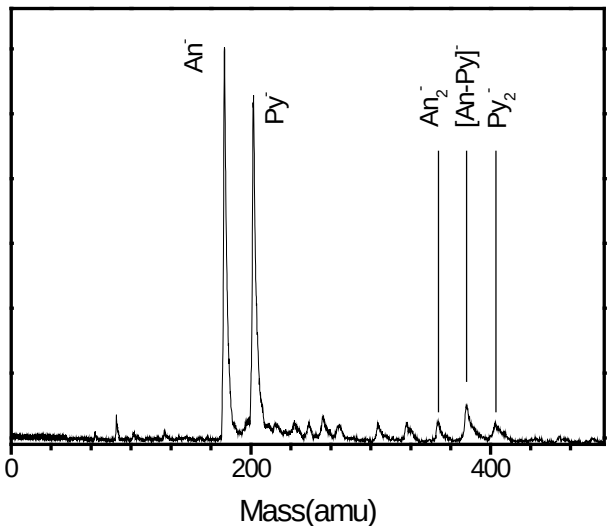

Figure 7.1 Mass spectrum of a mixed cluster of anthracene (An) and pyrene (Py). The most prominent species is monomer anion of each molecule. There are homo-dimer anions with smaller intensities. In addition to this, hetero-dimer anion is observed with significant intensity.

Figure 7.2 shows the PES of (a) An^-, (b) $[Np\text{-}An]^-$, (c) Py^-, (d) $[Ph\text{-}Py]^-$, and (e) $[Np\text{-}Py]^-$. The PES shape of $[Np\text{-}An]^-$ is similar to that of An^- except for the VDE (0.53 eV for An^- and 0.80 eV for $[Np\text{-}An]^-$). Symmetric vibration mode of An, ν_6 (1,408 cm^{-1} = 0.17 eV) also appeared in both PES. Furthermore, a broad and featureless peak exists at the high electron binding energy (EBE). This peak does not come from direct electron detachment since it does not appear in the specific wavelengths of photodetachment photon. If we plot the electron kinetic energy (EKE) versus photoelectron intensity, this peak always appears at the same position regardless of the photon energy used. Thus, its origin is an autodetachment where the electron detachment occurs via some short-lived excited states. If the anion is excited to the highly-excited state with the same spin multiplicity, internal vibrational relaxation occurs before the ejection of the photoelectron. The resulting anion mostly undergoes photodetachment at the second excited state due to the selection rule. Therefore, the EKE is independent of the photon energy used (details are in ref.149). The shape of the PES tells us the origin of the ion core. $[Np\text{-}(H_2O)_1]^-$ and $[Np\text{-}Bz]^-$ have same PES shapes, and the T-shaped geometries indicate they have a common Np^- monomer core.[164,171] The PES of $[Np\text{-}An]^-$ is similar to that of An^-, however, neither $[Np\text{-}(H_2O)_1]^-$ nor $[Np\text{-}Bz]^-$ show similar spectra. Consequently, we can deduce that the anionic core of $[Np\text{-}An]^-$ is An^-. The role of a naphthalene molecule is a solvation of anthracene anion core to stabilize it about 0.27 eV. The same results were obtained in $[Np\text{-}Py]^-$ and $[Ph\text{-}Py]^-$, The PES of $[Np\text{-}Py]^-$ and $[Ph\text{-}Py]^-$ are similar to that of Py^-. Therefore, they have a common Py^-

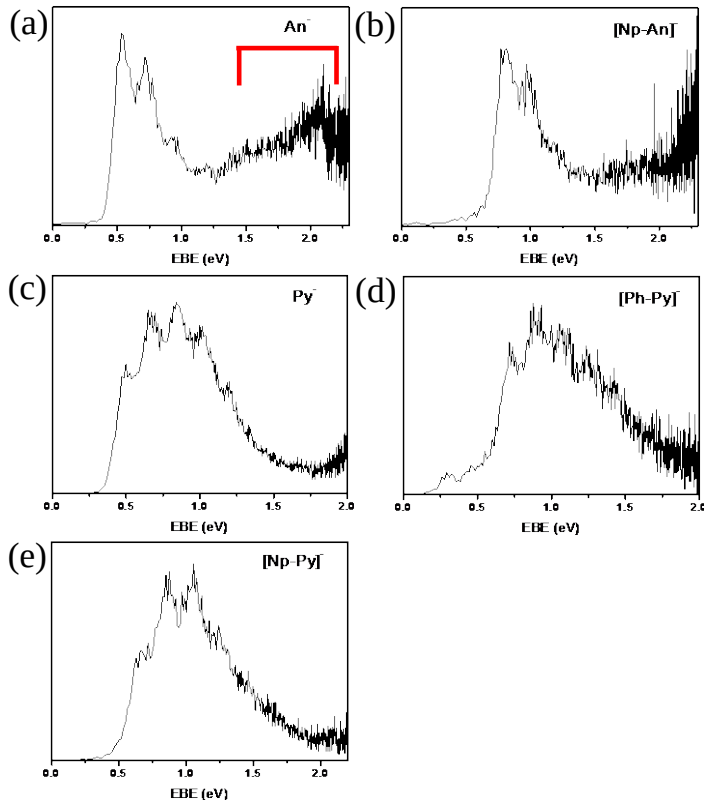

Figure 7.2 Photoelectron spectra of (a) anthracene monomer anion, (b) hetero-dimer anion of naphthalene-anthracene, (c) pyrene monomer anion, (d) hetero-dimer anion of phenanthrene-pyrene, and (e) hetero-dimer anion of naphthalene-pyrene. The PES shape in (b) is similar to that in (a), and those of (d) and (e) are similar to that in (c) indicating they have a monomer anionic core. Less electronegative naphthalene and phenanthrene act as a solvent to stabilize a monomer anionic core of more electronegative anthracene and pyrene. Red region in (a) denotes the photoelectron signals by autodetachment.

monomer core in the same context with $[Np\text{-}An]^-$.

Figure 7.3 shows the opposite to the case in Figure 7.2. The PES of (a) Py^- and (b) $[An\text{-}Py]^-$ are obtained at 532 nm (2.33 eV). At a glance, the shape of the PES (b) is much more different from that of Py^-. First, there are many vibrational progressions in (a) while no exist in (b). Second, the width of the band in (a) is much broader than that of (b). However, the PES shape of $[An\text{-}Py]^-$ is similar to that of An^- except for the absence of the vibrational progressions. We deconvoluted the PES with Gaussian functions for the comparison, and found that the intervals between peaks are not consistent with those in the PES of An^-. Thus, PES of (b) comes from a totally new anionic core rather than from Py^- or An^-. Further evidence for the generation of a new ionic core will be discussed in the next theoretical calculation section.

7.3.2 Theoretical calculation of the optimized structure and charge distribution of hetero-dimer anion of PAH

To obtain the optimized structure and charge distribution of each hetero-dimer anion, we carried out a theoretical calculation with the density functional B3LYP method at the 6-31++G** level using Gaussian 03 package.[152] Geometries were fully optimized and the frequencies checked to confirm that the obtained structure is lying on the global minimum point in the potential energy surface. VDE values were calculated to be compared with the experimentally obtained VDE values. Theoretical VDE for $[Np\text{-}An]^-$, $[Np\text{-}Py]^-$, $[An\text{-}Py]^-$ and $[Ph\text{-}Py]^-$ are 0.80 eV, 0.69

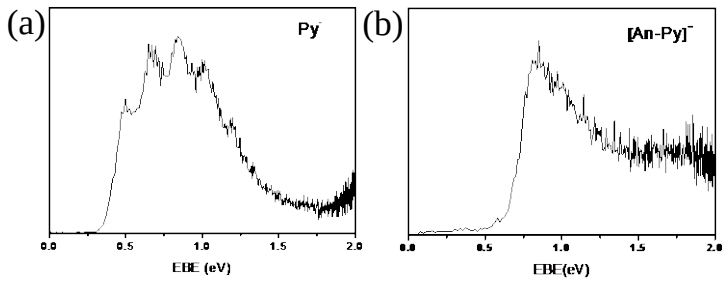

Figure 7.3 Photoelectron spectra of (a) pyrene monomer anion and (b) hetero-dimer anion of pyrene-anthracene at 532 nm. The shape of the PES in (b) is differs from that in (a) and (a) in Figure 7.2 indicating new anion core is formed.

eV, 0.94 eV and 0.72 eV, respectively, which agree well with the experimental values.

Figure 7.4 represents the theoretically obtained structures for hetero-dimer anions. There are three anions with T-shaped structure and one with parallel-displaced structure. These numbers coincide with the results of PES. There are three hetero-dimer anions that have the same shapes with one of the monomer anions ($[Np\text{-}An]^-$, $[Np\text{-}Py]^-$ and $[Ph\text{-}Py]^-$), and there is a hetero-dimer anion that form a totally different anionic core ($[An\text{-}Py]^-$). The three hetero-dimer anions that adopted a T-shaped structure have monomeric anion cores (An^- in $[Np\text{-}An]^-$, Py^- in $[Np\text{-}Py]^-$ and $[Ph\text{-}Py]^-$) while the other molecule stabilizes the ion core (Np^- in $[Np\text{-}An]^-$ and $[Np\text{-}Py]^-$, Ph^- in $[Ph\text{-}Py]^-$). In the T-shaped structure, hydrogen atoms in the less electronegative molecule are perpendicular to the face of the more electronegative anion core, which results in stabilization by π - hydrogen interaction like $[Bz\text{-}Np]^-$. The distance between these hydrogens and the anion core molecule ranges 2.7 Å~3.0 Å. Most excess negative charge is localized to the more electronegative molecule. This tendency becomes obvious with the increase of the difference in EA value (-0.19 eV for Np, 0.13 eV for Ph, 0.53 eV for An and 0.45 eV for Py). Our molecular orbital (MO) calculation revealed that the singly occupied molecular orbital (SOMO) of these hetero-dimers are the same as those of anionic core, which verifies the results of PES, T-shaped structure and charge localization.

On the other hand, two molecules lie together in a dislocated position to be

	[Np–An]⁻	[Np–Py]⁻
Geometry	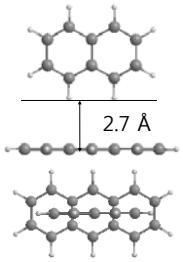	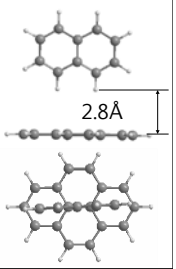
Charge	Np : −0.01 An : −0.99	Np : −0.22 Py : −0.78
	[An–Py]⁻	[Ph–Py]⁻
Geometry	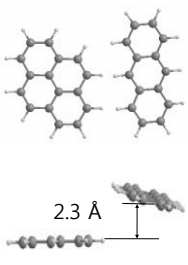	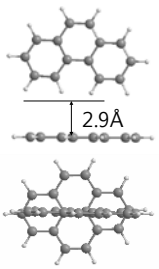
Charge	An : −0.56 Py : −0.44	Ph : −0.25 Py : −0.75

Figure 7.4 Optimized geometries and charge distributions of four hetero-dimer anions. The complex that has small differences in electron affinity shows PD structure ($[An\text{-}Py]^{-}$) and shares nearly half of the excess negative charge. However, those that have large differences in electron affinity show T-shaped structure ($[Np\text{-}An]^{-}$, $[Np\text{-}Py]^{-}$, and $[Ph\text{-}Py]^{-}$) and the excess negative charge is localized to the more electronegative molecule.

stabilized by dispersion forces like anthracene dimer anion.[168] Since the two molecules (An and Py) have similar EA value, excess negative charge is almost evenly delocalized between the two molecules in $[An\text{-}Py]^-$. There might be local minimums with T-shaped structures. Thus, we applied several T-shaped structures to obtain local minimum structures. However, we could not find any local minimum, and every T-shaped structure finally converged to PD structure. Thus, there is no local minimum with T-shaped structure. In MO calculation, the singly occupied molecular orbital (SOMO) of these hetero-dimers are different from those of any parent molecule and are evenly distributed over the complex which also verifies the results of PES, PD structure and charge delocalization.

7.4 Conclusion

In conclusion, the nature of the hetero-dimer of PAH anions was investigated by mass-selected anion photoelectron spectroscopy and theoretical calculation. A complex between molecules with comparable electron affinity becomes a parallel-displaced structure due to the electrostatic interaction like dispersion force between two moieties with the delocalized negative charge distribution. In contrast, the T-shaped structure with a monomer anionic core is dominant when the electron affinity of the two molecules differs from each other. In this case, the π-hydrogen interaction becomes more important and the excess negative charge is localized to the more electronegative molecule.

References

(1) Stephens, D. J.; Allan, V. J. *Science* **2003**, *300*, 82.

(2) Lichtman, J. W.; Conchello, J. A. *Nat. Methods* **2005**, *2*, 910.

(3) Haugland, R. P. *The Handbook: A Guide to fluorescence probes and labeling technologies*, 2005.

(4) Lippincott-Schwartz, J.; Snapp, E.; Kenworthy, A. *Nat. Rev. Mol. Cell. Bio.* **2001**, *2*, 444.

(5) Yamauchi, K.; Yang, M.; Jiang, P.; Xu, M. X.; Yamamoto, N.; Tsuchiya, H.; Tomita, K.; Moossa, A. R.; Bouvet, M.; Hoffman, R. M. *Cancer Res.* **2006**, *66*, 4208.

(6) Abbe, E. *Archiv für mikroskopische Anatomie* **1873**, *9*, 413.

(7) Fukazawa, K. In *Methods lignin chemistry*; Springer: 1992, p110.

(8) Schmahl, G. *Röntgen Centennial: X-rays in Natural and Life Sciences* **1997**, 261.

(9) Browning, N.; Chisholm, M.; Pennycook, S. *Nature* **1993**, *366*, 143.

(10) Denk, W.; Strickler, J. H.; Webb, W. W. *Science* **1990**, *248*, 73.

(11) Schrader, M.; Hell, S. *J. Microsc.* **1996**, *183*, 110.

(12) Gustafsson, M. G. L.; Agard, D. A.; Sedat, J. W. *J. Microsc-Oxford* **1999**, *195*, 10.

(13) Axelrod, D. *J. Cell. Bio.* **1981**, *89*, 141.

(14) Liu, Z. W.; Lee, H.; Xiong, Y.; Sun, C.; Zhang, X. *Science* **2007**, *315*, 1686.

(15) Gustafsson, M. G. *Proc. Natl. Acad. Sci.* **2005**, *102*, 13081.

(16) Hess, S. T.; Girirajan, T. P.; Mason, M. D. *Biophys. J.* **2006**, *91*, 4258.

(17) Rust, M. J.; Bates, M.; Zhuang, X. *Nat. Methods* **2006**, *3*, 793.

(18) van de Linde, S.; Löschberger, A.; Klein, T.; Heidbreder, M.; Wolter, S.; Heilemann, M.; Sauer, M. *Nat. Protoc.* **2011**, *6*, 991.

(19) Hell, S. W.; Wichmann, J. *Opt. Lett.* **1994**, *19*, 780.

(20) Klar, T. A.; Hell, S. W. *Opt. Lett.* **1999**, *24*, 954.

(21) Kastrup, L.; Blom, H.; Eggeling, C.; Hell, S. W. *Phys. Rev. Lett.* **2005**, *94*, 178104.

(22) Dyba, M.; Hell, S. W. *Phys. Rev. Lett.* **2002**, *88*, 163901.

(23) Fischer, J.; von Freymann, G.; Wegener, M. *Adv. Mater.* **2010**, *22*, 3578.

(24) Lenz, M.; Brown, A.; Auksorius, E.; Davis, D.; Dunsby, C.; Neil, M.; French, P. In *SPIE BiOS*; International Society for Optics and Photonics: 2011, p 79032D.

(25) Klar, T. A.; Jakobs, S.; Dyba, M.; Egner, A.; Hell, S. W. *Proc. Natl. Acad. Sci.* **2000**, *97*, 8206.

(26) Westphal, V.; Blanca, C. M.; Dyba, M.; Kastrup, L.; Hell, S. W. *Appl. Phys. Lett.* **2003**, *82*, 3125.

(27) Willig, K. I.; Harke, B.; Medda, R.; Hell, S. W. *Nat. Methods* **2007**, *4*, 915.

(28) Rankin, B. R.; Kellner, R. R.; Hell, S. W. *Opt. Lett.* **2008**, *33*, 2491.

(29) Wildanger, D.; Rittweger, E.; Kastrup, L.; Hell, S. W. *Opt. Express* **2008**, *16*, 9614.

(30) Harke, B.;Ullal, C. K.; Keller, J.; & Hell, S. W. *Nano Lett.* **2008** *8*, 1309.

(31) Bückers, J.; Wildanger, D.; Vicidomini, G.; Kastrup, L.; Hell, S. W. *Opt. Express* **2011**, *19*, 3130.

(32) Moneron, G.; Hell, S. W. *Opt. Express* **2009**, *17*, 14567.

(33) Schmidt, R.; Wurm, C. A.; Punge, A.; Egner, A.; Jakobs, S.; Hell, S. W. *Nano Lett.* **2009**, *9*, 2508.

(34) Vicidomini, G.; Moneron, G.; Eggeling, C.; Rittweger, E.; Hell, S. W. *Opt. Express* **2012**, *20*, 5225.

(35) Mace, E. M.; Orange, J. S. *Commun. Integr. Biol.* **2012**, *5*, 184.

(36) Rankin, B. R.; Hell, S. W. *Opt. Express* **2009**, *17*, 15679.

(37) Kittel, R. J.; Wichmann, C.; Rasse, T. M.; Fouquet, W.; Schmidt, M.; Schmid, A.; Wagh, D. A.; Pawlu, C.; Kellner, R. R.; Willig, K. I. *Sci. Signal.* **2006**, *312*, 1051.

(38) Willig, K. I.; Rizzoli, S. O.; Westphal, V.; Jahn, R.; Hell, S. W. *Nature* **2006**, *440*, 935.

(39) Lin, W.; Margolskee, R.; Donnert, G.; Hell, S. W.; Restrepo, D. *Proc. Natl. Acad. Sci.* **2007**, *104*, 2471.

(40) Schneider, A.; Rajendran, L.; Honsho, M.; Gralle, M.; Donnert, G.; Wouters, F.; Hell, S. W.; Simons, M. *J. Neurosci.* **2008**, *28*, 2874.

(41) Donnert, G.; Keller, J.; Wurm, C. A.; Rizzoli, S. O.; Westphal, V.; Schönle, A.; Jahn, R.; Jakobs, S.; Eggeling, C.; Hell, S. W. *Biophys. J.* **2007**, *92*, L67.

(42) Hein, B.; Willig, K. I.; Hell, S. W. *Proc. Natl. Acad. Sci.* **2008**, *105*, 14271.

(43) Blom, H.; RöNnlund, D.; Scott, L.; Spicarova, Z.; Rantanen, V.; Widengren, J.; Aperia, A.; Brismar, H. *Microsc. Res. Techniq.* **2012**, *75*, 220.

(44) Berning, S.; Willig, K. I.; Steffens, H.; Dibaj, P.; Hell, S. W. *Science* **2012**, *335*, 551.

(45) Urban, N. T.; Willig, K. I.; Hell, S. W.; Nägerl, U. V. *Biophys. J.* **2011**, *101*, 1277.

(46) Westphal, V.; Rizzoli, S. O.; Lauterbach, M. A.; Kamin, D.; Jahn, R.; Hell, S. W. *Science* **2008**, *320*, 246.

(47) Förster, T. *Annalen der physik* **1948**, *437*, 55.

(48) Stryer, L.; Haugland, R. P. *Proc. Natl. Acad. Sci.* **1967**, *58*, 719.

(49) Wiley, W.; McLaren, I. H. *Rev. Sci. Instrum.* **1955**, *26*, 1150.

(50) Ervin, K.; Lineberger, W.; JAI Press: Greenwich: 1992; Vol. 1, p 121.

(51) STEIN, G. *Advan. Chem. Ser.* **1965**, 230.

(52) Bailey, C. G.; Dessent, C. E.; Johnson, M. A.; Bowen Jr, K. H. *J. Chem. Phys.* **1996**, *104*, 6976.

(53) Einstein, A. *Annalen der Phy-sik, Wiley-VCH Verlag GmbH & Co. KgaA, Berlin* **1905**.

(54) Hotta, J. I.; Fron, E.; Dedecker, P.; Janssen, K. P. F.; Li, C.; Mullen, K.; Harke, B.; Buckers, J.; Hell, S. W.; Hofkens, J. *J. Am. Chem. Soc.* **2010**, *132*, 5021.

(55) Eggeling, C.; Widengren, J.; Rigler, R.; Seidel, C. A. M. *Anal. Chem.* **1998**, *70*, 2651.

(56) Rittweger, E.; Rankin, B. R.; Westphal, V.; Hell, S. W. *Chem. Phys. Lett.* **2007**, *442*, 483.

(57) Donnert, G.; Keller, J.; Medda, R.; Andrei, M. A.; Rizzoli, S. O.; Luhrmann, R.; Jahn, R.; Eggeling, C.; Hell, S. W. *Proc. Natl. Acad. Sci.* **2006**, *103*, 11440.

(58) Kruit, P.; Read, F. *J. Phys. E: Sci. Instrum.* **1983**, *16*, 313.

(59) Cheshnovsky, O.; Yang, S.; Pettiette, C.; Craycraft, M.; Smalley, R. *Rev. Sci. Instrum.* **1987**, *58*, 2131.

(60) Crick, F. H. **1958**, *12*, p 138.

(61) Crick, F. *Nature* **1970**, *227*, 561.

(62) Marmorstein, L. Y.; Kinev, A. V.; Chan, G. K. T.; Bochar, D. A.; Beniya, H.; Epstein, J. A.; Yen, T. J.; Shiekhattar, R. *Cell* **2001**, *104*, 247.

(63) Preston, C. M.; Frame, M. C.; Campbell, M. *Cell* **1988**, *52*, 425.

(64) Sen, D.; Geyer, C. R. *Curr.Opin. Chem. Biol.* **1998**, *2*, 680.

(65) Silverman, S. K. *Nucleic Acids Res.* **2005**, *33*, 6151.

(66) Rittweger, E.; Han, K. Y.; Irvine, S. E.; Eggeling, C.; Hell, S. W. *Nat. Photonics* **2009**, *3*, 144.

(67) Han, K. Y.; Kim, S. K.; Eggeling, C.; Hell, S. W. *Nano Lett.* **2010**, *10*, 3199.

(68) Persson, F.; Bingen, P.; Staudt, T.; Engelhardt, J.; Tegenfeldt, J.; Hell, S. W. *Angew. Chem. Int. Ed.* **2011**, *50*, 5581.

(69) Kryndushkin, D. S.; Alexandrov, I. M.; Ter-Avanesyan, M. D.; Kushnirov, V. V. *J. Biol. Chem.* **2003**, *278*, 49636.

(70) Sambrook, J.; Russell, D. W. *Molecular cloning: a laboratory manual*; CSHL press, **2001**; Vol. *2*.

(71) Goodwin, P. M.; Johnson, M. E.; Martin, J. C.; Ambrose, W. P.; Marrone, B. L.; Jett, J. H.; Keller, R. A. *Nucleic Acids Res.* **1993**, *21*, 803.

(72) Foquet, M.; Korlach, J.; Zipfel, W.; Webb, W. W.; Craighead, H. G. *Anal. Chem.* **2002**, *74*, 1415.

(73) Laib, S.; Rankl, M.; Ruckstuhl, T.; Seeger, S. *Nucleic Acids Res.* **2003**, *31*, e138.

(74) Otobe, K.; Ohtani, T. *Nucleic Acids Res.* **2001**, *29*, e109.

(75) Chan, T. F.; Ha, C.; Phong, A.; Cai, D.; Wan, E.; Leung, L.; Kwok, P. Y.; Xiao, M. *Nucleic Acids Res.* **2006**, *34*, e113.

(76) Michalet, X.; Ekong, R.; Fougerousse, F.; Rousseaux, S.; Schurra, C.; Hornigold, N.; Slegtenhorst, M.; Wolfe, J.; Povey, S.; Beckmann, J. S. *Science* **1997**, *277*, 1518.

(77) Gueroui, Z.; Freyssingeas, E.; Berge, B. *Proc. Natl. Acad. Sci.* **2002**, *99*, 6005.

(78) Benke, A.; Mertig, M.; Pompe, W. *Nanotechnology* **2011**, *22*, 035304.

(79) Hu, J.; Wang, M.; Weier, H. U. G.; Frantz, P.; Kolbe, W.; Ogletree, D. F.; Salmeron, M. *Langmuir* **1996**, *12*, 1697.

(80) Deng, Z. X.; Mao, C. D. *Nano Lett.* **2003**, *3*, 1545.

(81) Hu, J.; Zhang, Y.; Gao, H. B.; Li, M. Q.; Hartmann, U. *Nano Lett.* **2002**, *2*, 55.

(82) Figeys, D.; Arriaga, E.; Renborg, A.; Dovichi, N. J. *J. Chromatogr. A* **1994**, *669*, 205.

(83) Bensimon, D.; Simon, A.; Croquette, V.; Bensimon, A. *Phys. Rev. Lett.* **1995**, *74*, 4754.

(84) Baday, M.; Cravens, A.; Hastie, A.; Kim, H.; Kudeki, D. E.; Kwok, P. Y.; Xiao, M.; Selvin, P. R. *Nano Lett.* **2012**, *12*, 3861.

(85) Haarer, D.; Kador, L. *Angew. Chem. Int. Ed.* **1991**, *30*, 540.

(86) Moerner, W. E.; Kador, L. *Phys. Rev. Lett.* **1989**, *62*, 2535.

(87) Minsky, M. *Scanning* **1988**, *10*, 128.

(88) Ambrose, E. J. *Nature* **1956**, *178*, 1194.

(89) Levene, M. J.; Korlach, J.; Turner, S. W.; Foquet, M.; Craighead, H. G.; Webb, W. W. *Science* **2003**, *299*, 682.

(90) Leslie, S. R.; Fields, A. P.; Cohen, A. E. *Anal. Chem.* **2010**, *82*, 6224.

(91) Eggeling, C.; Hilbert, M.; Bock, H.; Ringemann, C.; Hofmann, M.; Stiel, A. C.; Andresen, M.; Jakobs, S.; Egner, A.; Schonle, A.; Hell, S. W. *Microsc. Res. Techniq.* **2007**, *70*, 1003.

(92) Forster, T. *Ann. Phys.-Berlin* **1948**, *2*, 55.

(93) Kapanidis, A. N.; Lee, N. K.; Laurence, T. A.; Doose, S.; Margeat, E.; Weiss, S. *Proc. Natl. Acad. Sci.* **2004**, *101*, 8936.

(94) Lee, N. K.; Kapanidis, A. N.; Koh, H. R.; Korlann, Y.; Ho, S. O.; Kim, Y.; Gassman, N.; Kim, S. K.; Weiss, S. *Biophys. J.* **2007**, *92*, 303.

(95) Hell, S. W.; Wichmann, J. *Opt. Lett.* **1994**, *19*, 780.

(96) Rigaud, J. L.; Levy, D. *Method. Enzymol.* **2003**, *372*, 65.

(97) Chuang, J. I., Stanford University, **2007**.

(98) Chan, Y. H. M.; Lenz, P.; Boxer, S. G. *Proc. Natl. Acad. Sci.* **2007**, *104*, 18913.

(99) Manneville, J. B.; Bassereau, P.; Ramaswamy, S.; Prost, J. *Phys. Rev. E.* **2001**, *64*.

(100) Girard, P.; Pecreaux, J.; Lenoir, G.; Falson, P.; Rigaud, J. L.; Bassereau, P. *Biophys. J.* **2004**, *87*, 2098.

(101) Kahya, N.; Pecheur, E. I.; de Boeij, W. P.; Wiersma, D. A.; Hoekstra, D. *Biophys. J.* **2001**, *81*, 1464.

(102) Varnier, A.; Kermarrec, F.; Blesneac, I.; Moreau, C.; Liguori, L.; Lenormand, J. L.; Picollet-D'hahan, N. *J. Membrane Biol.* **2010**, *233*, 85.

(103) Chan, Y. H. M.; van Lengerich, B.; Boxer, S. G. *Biointerphases* **2008**, *3*, Fa17.

(104) Chan, Y. H. M.; van Lengerich, B.; Boxer, S. G. *Proc. Natl. Acad. Sci.* **2009**, *106*, 979.

(105) Chen, Y. A.; Scheller, R. H. *Nat. Rev. Mol. Cell. Bio.* **2001**, *2*, 98.

(106) Stengel, G.; Zahn, R.; Hook, F. *J. Am. Chem. Soc.* **2007**, *129*, 9584.

(107) Chung, M.; Lowe, R. D.; Chan, Y. H. M.; Ganesan, P. V.; Boxer, S. G. *J Struct. Biol.* **2009**, *168*, 190.

(108) Rawle, R. J.; van Lengerich, B.; Chung, M.; Bendix, P. M.; Boxer, S. G. *Biophys. J.* **2011**, *101*, L37.

(109) Chuang, J. I.; Boxer, S. G.; Holten, D.; Kirmaier, C. *J. Phys. Chem. B.* **2008**, *112*, 5487.

(110) S. G. Boxer, J. S., S. Franzen, J. Salafsky *AIP Conf. Proc.* **1992**, *262*, 226.

(111) Xu, Y. B.; Zhang, F.; Su, Z. L.; McNew, J. A.; Shin, Y. K. *Nat. Struct. Mol. Biol.* **2005**, *12*, 417.

(112) Salafsky, J.; Groves, J. T.; Boxer, S. G. *Biochemistry* **1996**, *35*, 14773.

(113) Marras, S. A. E.; Kramer, F. R.; Tyagi, S. *Nucleic Acids Res.* **2002**, *30*.

(114) SUVs with fusogenic lipid mixture do not form a uniform SLB.

(115) Longo, M. L.; Ly, H. V. In *Methods in Membrane Lipids*; Springer: 2007, p 421.

(116) Chung, M.; Boxer, S. G. *Langmuir* **2011**, *27*, 5492.

(117) The DNA coverage on the surface is controlled by concentration of alkynyl-DNA and incubation time.

(118) Saffman, P. G.; Delbruck, M. *Proc. Natl. Acad. Sci.* **1975**, *72*, 3111.

(119) Yoshina-Ishii, C.; Chan, Y. H. M.; Johnson, J. M.; Kung, L. A.; Lenz, P.; Boxer, S. G. *Langmuir* **2006**, *22*, 5682.

(120) Qian, H.; Sheetz, M. P.; Elson, E. L. *Biophys. J.* **1991**, *60*, 910.

(121) Saxton, M. J. *Biophys. J.* **1997**, *72*, 1744.

(122) We have observed that SUVs docked prior to fusion on DNA-tethered patches are immobile, while docked SUVs on GUVs are mobile under otherwise identical conditions. The origin of this difference is not clear, but it is likely due to the difference in membrane tension between the tethered patch (low) and tethered GUV (high).

(123) Though it may take several seconds for TR dye to diffuse out over the patch, it appears as instantaneous increase due to infrequent (5 sec interval) image acquisition, to prevent bleaching.

(124) J. Leong, T. C. a. S. G. B. *in preparation*.

(125) Overfield, R.; Wraight, C. *Biochemistry* **1980**, *19*, 3322.

(126) Pachence, J. M.; Dutton, P. L.; Blasie, J. K. *BBA-Bioenergetics* **1979**, *548*, 348.

(127) Debus, R.; Feher, G.; Okamura, M. *Biochemistry* **1986**, *25*, 2276.

(128) van Lengerich, B.; Rawle, R. J.; Boxer, S. G. *Langmuir : the ACS journal of surfaces and colloids* **2010**, *26*, 8666.

(129) Ramadurai, S.; Holt, A.; Krasnikov, V.; van den Bogaart, G.; Killian, J. A.; Poolman, B. *J. Am. Chem. Soc.* **2009**, *131*, 12650.

(130) Gambin, Y.; Lopez-Esparza, R.; Reffay, M.; Sierecki, E.; Gov, N. S.; Genest, M.; Hodges, R. S.; Urbach, W. *Proc. Natl. Acad. Sci.* **2006**, *103*, 2098.

(131) Fotiadis, D.; Qian, P.; Philippsen, A.; Bullough, P. A.; Engel, A.; Hunter, C. N. *J. Biol. Chem.* **2004**, *279*, 2063.

(132) Ajo-Franklin, C. M.; Yoshina-Ishii, C.; Boxer, S. G. *Langmuir* **2005**, *21*, 4976.

(133) Rodriguez, N.; Heuvingh, J.; Pincet, F.; Cribier, S. *BBa-Gen. Subjects* **2005**, *1724*, 281.

(134) This negligible leakiness of tethered GUVs is also tested by the fluorescence quenching behavior of TR lipid dyes that are present in both inner and outer leaflet of tethered GUVs.

(135) Harata, N. C.; Aravanis, A. M.; Tsien, R. W. *J. Neurochem.* **2006**, *97*, 1546.

(136) Sankaranarayanan, S.; Ryan, T. A. *Nat. Cell. Biol.* **2000**, *2*, 197.

(137) Fernandez-Alfonso, T.; Kwan, R.; Ryan, T. A. *Neuron* **2006**, *51*, 179.

(138) Gandhi, S. P.; Stevens, C. F. *Nature* **2003**, *423*, 607.

(139) Ngatchou, A. N.; Kisler, K.; Fang, Q. H.; Walter, A. M.; Zhao, Y.; Bruns, D.; Sorensen, J. B.; Lindau, M. *Proc. Natl. Acad. Sci.* **2010**, *107*, 18463.

(140) Trost, B. M. *Science* **1983**, *219*, 245.

(141) Mikami, K.; Matsukawa, S. *Nature* **1997**, *385*, 613.

(142) Trasarti, A. F.; Marchi, A. J.; Apesteguia, C. R. *J. Catal.* **2004**, *224*, 484.

(143) MacKinnon, R. *Angew. Chem. Int. Ed.* **2004**, *43*, 4265.

(144) Konno, K.; Okada, S.; Hirayama, C. *J. Insect Physiol.* **2001**, *47*, 1451.

(145) Feinberg, H.; Mitchell, D. A.; Drickamer, K.; Weis, W. I. *Science* **2001**, *294*, 2163.

(146) Mcdonald, J. D.; Herschba.Dr; Lebreton, P. R.; Lee, Y. T. *J. Chem. Phys.* **1972**, *56*, 769.

(147) Liu, Y.; Masson, D. P.; Kummel, A. C. *Science* **1997**, *276*, 1681.

(148) Han, S. Y.; Song, J. K.; Kim, J. H.; Oh, H. B.; Kim, S. K. *J. Chem. Phys.* **1999**, *111*, 4041.

(149) Song, J. K.; Lee, N. K.; Kim, J. H.; Han, S. Y.; Kim, S. K. *J. Chem. Phys.*

2003, *119*, 3071.

(150) Rosa, A.; Barszczewska, W.; Nandi, D.; Ashok, V.; Kumar, S. V. K.; Krishnakumar, E.; Bruning, F.; Illenberger, E. *Chem. Phys. Lett.* **2001**, *342*, 536.

(151) Oster, T.; Kuhn, A.; Illenberger, E. *Int. J. Mass Spectrom. Ion Process.* **1989**, *89*, 1.

(152) Frisch, M. J.; Trucks, G. W.; Schlegel, H. B.; G. E. Scuseria; Robb, M. A.; Cheeseman, J. R.; J. A. Montgomery, J.; T. Vreven; Kudin, K. N.; Burant, J. C.; Millam, J. M.; Iyengar, S. S.; Tomasi, J.; Barone, V.; Mennucci, B.; Cossi, M.; Scalmani, G.; Rega, N.; Petersson, G. A.; Nakatsuji, H.; Hada, M.; Ehara, M.; Toyota, K.; Fukuda, R.; Hasegawa, J.; Ishida, M.; Nakajima, T.; Honda, Y.; Kitao, O.; Nakai, H.; Klene, M.; Li, X.; Knox, J. E.; Hratchian, H. P.; Cross, J. B.; Adamo, C.; Jaramillo, J.; Gomperts, R.; Stratmann, R. E.; Yazyev, O.; Austin, A. J.; Cammi, R.; Pomelli, C.; Ochterski, J. W.; Ayala, P. Y.; Morokuma, K.; Voth, G. A.; Salvador, P.; Dannenberg, J. J.; Zakrzewski, V. G.; Dapprich, S.; Daniels, A. D.; Strain, M. C.; Farkas, O.; Malick, D. K.; Rabuck, A. D.; Raghavachari, K.; Foresman, J. B.; Ortiz, J. V.; Cui, Q.; Baboul, A. G.; Clifford, S.; Cioslowski, J.; Stefanov, B. B.; Liu, G.; Liashenko, A.; Piskorz, P.; Komaromi, I.; Martin, R. L.; Fox, D. J.; Keith, T.; Al-Laham, M. A.; Peng, C. Y.; Nanayakkara, A.; Challacombe, M.; Gill, P. M. W.; Johnson, B.; Chen, W.; Wong, M. W.; Gonzalez, C.; Pople, J. A., Gaussian 03, Revision C.02; Gaussian, *Inc*: *Wallingford CT*, **2004** .

(153) Hotop, H.; Lineberger, W. C. *J. Phys. Chem. Ref. Data* **1985**, *14*, 731.

(154) Song, J. K.; Han, S. Y.; Chu, I. H.; Kim, J. H.; Kim, S. K.; Lyapustina, S. A.; Xu, S. J.; Nilles, J. M.; Bowen, K. H. *J. Chem. Phys.* **2002**, *116*, 4477.

(155) Herschbach, D. R. *Angew. Chem. Int. Ed*. **1987**, *26*, 1221.

(156) Fukui, K.; Yonezawa, T.; Shingu, H. *J. Chem. Phys.* **1952**, *20*, 722.

(157) Inagaki, S.; Fujimoto, H.; Fukui, K. *J. Am. Chem. Soc.* **1976**, *98*, 4054.

(158) Parrish, D. D.; Herschbach, D. R. *J. Am. Chem. Soc.* **1973**, *95*, 6133.

(159) Hanstorp, D.; Gustafsson, M. *J. Phys. B At. Mol. Opt.* **1992**, *25*, 1773.

(160) Jordan, K. D.; Burrow, P. D. *Accounts Chem. Res.* **1978**, *11*, 341.

(161) Jordan, K. D.; Burrow, P. D. *Chem. Rev.* **1987**, *87*, 557.

(162) Carrington, A.; Dravnieks, F.; Symons, M. C. R. *J. Chem. Soc.* **1959**, 947.

(163) Paul, D. E.; Lipkin, D.; Weissman, S. *J. Am. Chem. Soc.* **1956**, *78*, 116.

(164) Song, J. K.; Han, S. Y.; Chu, I.; Kim, J. H.; Kim, S. K.; Lyapustina, S. A.; Xu, S.; Nilles, J. M.; Bowen, K. H. *J. Chem. Phys.* **2002**, *116*, 4477.

(165) Lee, S. H.; Kim, N.; Ha, D. G.; Song, J. K. *RSC Adv*. **2013**, *3*, 17143.

(166) Bouvier, B.; Brenner, V.; Millie, P.; Soudan, J. M. *J. Phys. Chem. A.* **2002**, *106*, 10326.

(167) Shida, T.; Iwata, S. *J. Am. Chem. Soc*. **1973**, *95*, 3473.

(168) Song, J. K.; Lee, N. K.; Kim, S. K. *Angew. Chem. Int. Ed.* **2003**, *42*, 213.

(169) Ando, N.; Kokubo, S.; Mitsui, M.; Nakajima, A. *Chem. Phys. Lett.* **2004**, *389*, 279.

(170) Kim, J. H.; Lee, S. H.; Song, J. K. *J. Chem. Phys.* **2009**, *130*, 124321.

(171) Song, J. K.; Lee, N. K.; Han, S. Y.; Kim, S. K. *J. Chem. Phys.* **2002**, *117*, 9973.

Appendix A. Non-toxic fluorescent compounds and nanoparticles for bio-imaging

A.1 Introduction

Since the invention of light microscope, various optical imaging techniques have been developed and utilized for many applications in molecular biology and cell biology. With these optical imaging techniques, non-invasive, real-time *in vivo* imaging came to be realized to extend their use to tissue and organism.[1-3] Moreover, the recent development of various super-resolution microscopy techniques overcomes the intrinsic optical resolution limit of conventional microscopy methods due to the light diffraction property to maximize the spatial resolution about few nm.[4,5] Among the optical microscopic techniques, fluorescence microscopy has been widely used to achieve an exquisite sensitivity and resolution. The development of different categories of fluorophores such as organic dyes, quantum dots (QDs), nanoparticles, and fluorescent proteins makes the fluorescence microscopy perhaps to be the most powerful imaging tools that ever exist. Organic dyes have been most frequently used since the development of fluorescence microscopy and have various advantages including facile modification with functional groups, small size and broad range of absorption/emission spectra. The applications are however constrained by several limitations. Those include the susceptibility of photobleaching[6] and photoblinking[7,8] upon irradiation of light, and low quantum yield. The development of fluorophores possessing better properties has thus become of great importance in order to eliminate such problems and ultimately to increase the sensitivity of optical measurement. Moreover, it allows us

to monitor single biomolecules of a target system by detecting and tracking them, one of main topics of bio-imaging to understand the underlying biological mechanism of such molecules at the levels of cell, tissue, and organism. Semiconductor nanoparticles, quantum dots (QDs), has gained a great attention to enable the intended biological applications due to their photostability and brightness.[9,10] Their potential use spans from *in vitro* assay and cell imaging even to imaging in small animals.[11] Nevertheless, there are major drawbacks of their properties. The most important problem may be their potential *in vivo* cytotoxicity due to the toxic heavy metal ingredients such as cadmium, selenium, and tellurium. Thus, it is necessary to utilize better substitutes for the toxic quantum dots in the case of *in vivo* applications. The fluorophores for the biological applications have to satisfy following conditions: excellent photophysical properties including brightness and stability; biocompatibility in order to minimize the toxicity and clearance problem; facile functionalization scheme for the conjugation to biomolecule of interest.

As described, the development of relevant researches using various types of fluorescent materials continues to be improved in conjunction with the development of nanotechnology for various fields such as cell biology, drug delivery, *in vivo* imaging, diagnostics, and other types of bio-engineering technology. Thus, establishment and utilization of such materials are considered valuable, and there are numerous reports and progresses during last decade. In this work, we focus on

relatively or potentially non-toxic versions of fluorescent nanoparticles and an organic fluorophore, and describe their properties and applications.

A.2 Examples of non-toxic fluorophores

A.2.1 Fluorescent silicon nanoparticles

Strong red emission is observed when the bulk silicon undergoes electrochemical etching which results in the formation of mesoporous silicon layer.[12] Since this observation, many researchers have investigated the fabrication methods, optical and physical properties of mesoporous silicon layers.[13,14] The attention moved to the silicon nanocrystals which have similar luminescent properties. Besides the single exciton production from a photon, one exciton multi-photons and multi-excitons from one photon have been reported.[15,16] Various methods have been developed to generate various-sized silicon nanoparticles which emit different types of luminescence (Table A.1).

Porous silicon nanoparticles and microparticles have been used in various fields as fluorescent markers and tools for *in vivo* imaging and medical applications.[17-21] In the case of drug delivery, a main idea is the encapsulation of drugs with biocompatible polymer at a level of nanoparticle size. The main obstacle was, however, the fact that many organic molecules occasionally induce cytotoxic effects and the fluorescent labelling, an additional modification, is inevitable to obtain fluorescence image to monitor the particles.[22,23] The development of uniformly sized silicon nanoparticle production is considered as an option to circumvent this

Methods	Reactions	Properties
Electrochemical etching		nm~μm sized
Pyrolysis of silane	• Laser heating • Microdischarge • Microwave • Plasma treatment	Different sized
Laser ablation of silicon	• With unsaturated 1-alkene	1~10 nm, UV/blue luminescent
Thermal vaporization of silicon	• Hydrogen passivating	1~5 nm
Wet chemistry approach	• Sodium naphthalenide reduction of silicon halides • Sodium silicide and ammonium bromide • Br_2 and Mg_2Si powder	UV/blue colloidal nanoparticles
Solution-phase approach	• Reduction of $SiCl_4$ with $LiAlH_4$ or with sodium naphthalenide in inverse micelles	1~10 nm, UV/blue colloidal nanoparticles
Thermal degradation	• Degradation of diphenylsilane	1.5~4 nm, UV-blue-green
Ultrasound-assisted electrochemical approach	• Octyltrichlorosilane reduction	< 5 nm, blue luminescent octane-terminated Si nanocrystals
High-energy mechanical ball milling	• In either alkene or alkyne	< 4 nm, blue luminescent alkyl/alkenyl-passivated Si crystallites

Table A.1 Various methods to generate luminescent silicon nanoparticles

problem. Silicon nanoparticles have large surface area compared to the spherical size due to the presence of numerous pores that can carry small drugs for delivery. Small silicon nanoparticles less than 10 nm emit visible or near IR fluorescence (400 nm~1000 nm) upon the irradiation of UV (< 400 nm) or visible light (400 nm~600 nm). They show strong resistance to photobleaching and photoblinking relative to organic dyes. In addition, they are not scrutinized easily by renal system during circulation in the body. Many research groups have produced and modified various kinds of fluorescent silicon nanoparticles. Recently, water-dispersible fluorescent silicon nanoparticle was synthesized using microwave.[24] The size distributions of resulting nanoparticle measured by High-Resolution Transmission Electron Microscopy (HRTEM) and Dynamic Light Scattering (DLS) are in a range of 3~4 nm. Fluorescence intensity did not change significantly upon the change of the pH from 1 to 10 and by a continuous irradiation of 450 W xenon lamp for 120 min. It absorbs a broad wavelength range within 300~750 nm and emits a narrow wavelength range of 600 nm~750 nm.[24] Another water-dispersible fluorescent silicon nanoparticle was synthesized and their spectroscopic characterizations (Si-CH_2 vibration, Si-C component in Si 2*p* and C 1*s* levels) were confirmed by Fourier Transform Infrared Spectroscopy (FT-IR) and X-ray photoelectron spectroscopy.[25] Dual emission fluorescent silicon nanoparticle was synthesized by conjugating the organic dyes on the surface of the nanoparticles. The dyes undergo quenching in the presence of Cu^{2+} ion that can be used to the fast detection of cooper ion.[26]

For the *in vivo* applications of silicon nanoparticles, it is important to assess their

cytotoxicity and biocompatibility. In addition, nanoparticles need to be excreted after the completion of monitoring, thereby preventing production of any potential toxic material or accumulation in the body. S. P. Low *et al.*[27] measured the cytotoxicity of non-treated silicon microparticles and thermally-oxidized silicon microparticles using indirect cell viability assay (MTT assay[28]). Although human lens epithelial cells with non-treated microparticles did not survive at all, there was no significant change in the cell viability with thermally oxidized particles indicating that non-treated particles appear to be toxic in the cell. It was found that in the non-treated case, toxic reactive oxygen species (ROS) was produced after the introduction of the particles. To test the thermally oxidized case, thermally hydrocarbonized porous silicon (THCPSi) nanoparticles were introduced into both epithelial and macrophage cell.[29] The result showed that the nanoparticle also did not cause any noticeable cytotoxicity, oxidative stress, and immunogenicity. To track the pathway of the nanoparticles, radioactive ^{18}F-labeled THCPSi particles were introduced through both orally and intravenously to rat (Figure A.1). The particles moved intact through the gastrointestinal tract in the case of oral administration, whereas particles were mainly localized to the liver and spleen in the case of intravenous injection. J. Choi *et al.*[30] tested the cytotoxicity/cell viability and inflammatory response of 3 nm fluorescent silicon nanoparticle with 0.1~2 μm microparticles by injecting them into macrophage cells. There was almost no cytotoxicity and no inflammatory response in the case of nanoparticles whose concentration is less than 20 mg/ml--small nanoparticles can be accumulated up to

10,000 particles in a cell. In addition, biodegradability of the silicon nanoparticle was measured *in vivo* using a mouse model system.[31] Using near-infrared-emitting nanoparticles carrying a drug (doxorubicin, DOX), it was found that the nanoparticles were nearly degraded within 4 hours after injection and the amount of the released DOX increased over time. The product of degradation is silicic acid that can be excreted via the urine. Bare nanoparticles and dextran-coated nanoparticles were also tested using the mouse model and the fluorescence image showed that the nanoparticles were cleared within a short period of time. Thus, those demonstrate that the silicon-based nanoparticle is a good material of choice to be utilized as a relatively safe and biodegradable nanoparticle. The effect of fluorescent silicon nanoparticles on the hatching of larvae was studied with *Oryzias latipes* embryos. Hatching was not affected by the injection of nanoparticles up to 100 mg/L. However, abnormality increased about three times in the case of using sonicated nanoparticle suspension.[32]

An unusual property of silicon nanoparticle was recently reported.[33] Through specific physical and chemical treatment, the particle gains a magnetic moment as well as luminescence. The fluorescent magnetic silicon nanoparticles were synthesized by laser pyrolysis of silane followed by treatment of MeOH + HF + $FeCl_3$. This dual functionality of the nanoparticle has a potential to be served as a combined optical and magnetic tool (magneto-optical tool) in bio-imaging and medical treatment.

The surface chemistry of silicon nanoparticle is important because its proper

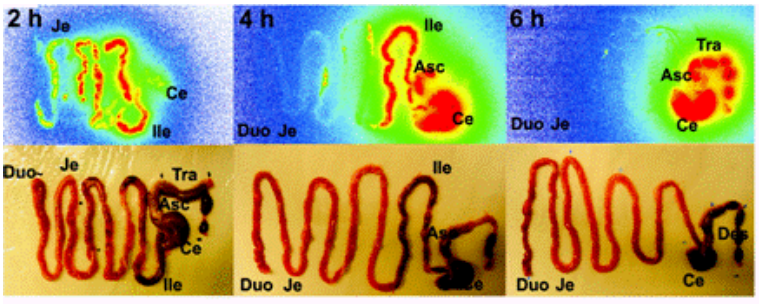

Figure A.1 Autoradiographs (upper) and photographs (lower) of the gastrointestinal tracts of rats 2, 4, and 6 hours after oral administration of ^{18}F-labeled THCPSi nanoparticles. Abbreviations: Duo, duodenum; Je, jejunum;Ile, ileum; Ce, cecum; Asc, ascendens; Tra, transversum; and Des, descendens. Copied from L. M. Bimbo *et al*. 2010.

modification enables the attachment of biomolecule to be monitored fluorescently. To functionalize the surface to covalently conjugate DNA molecules, 1~2 nm sized nanoparticles were conjugated with 5′ amino-modified DNA through the formation of carboxylamide bond by two sequential photoreactions.[34] Another type of surface functionalization involves hydrosilylation with undecylenic acid followed by carbodiimide chemistry to attached primary amine-containing biomolecules on the surface of particles. The covalently conjugated biomolecules were lysine, folate, antimesothelin and transferrin, and the derivatized silicon nanoparticles were successfully applied to monitor a cancer cell, demonstrating their feasibility as a bio-imaging probe for cancer study (Figure A.2).[35] Polyacrylic acid-grafted silicon nanoparticle was reported as a choice of modification and was prepared by grafting acrylic acid with the surface of silicon nanoparticle through UV-induced graft polymerization.[36] Such particles were well-dispersed in the solution by the water-soluble polymer and were suitable for cell imaging. Moreover, polyacrylic acid enhanced the luminescent intensity of the nanoparticles and increased the stability of nanoparticles. Allylamine and poly(acrylic acid) covered silicon nanoparticles also showed the water-solubility.[37,38] It should be noted that the fluorescent silicon nanoparticles have long lifetime (10~100 μs). Autofluorescence, one of major problems of cell imaging, can be ignored by time gating with regard to the lifetime of the autofluorescence (~5 ns) and that of the nanoparticles.[39]

In summary, the silicon nanoparticles are considered as an excellent alternative to quantum dots due to their relatively non-toxic attributes. The small-sized silicon

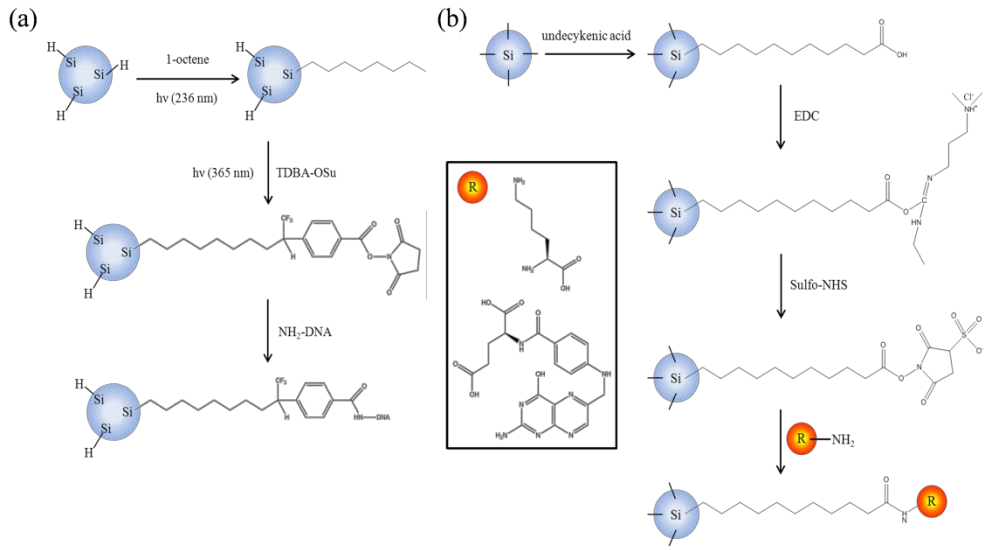

Figure A.2 (a) A schematic representation of the three successive reactions for DNA-conjugated silicon nanoparticle. 1-Octene was conjugated first to the SI-H bond followed by the addition of carbine. Adopted from L. Wang *et al*. 2004. (b) A schematic representation of the four successive reactions for bioconjugation. Silicon nanoparticels undergo hydrosilylation with undecylenic acid, reaction with EDC, formation of NHS-ester, and bioconjugation. Adopted from F. Erogbogbo *et al*. 2011.

nanoparticles have luminescent property ranging from visible to near IR. Thermally-oxidized particles do not have any significant cytotoxicity in living cells and are degraded immediately after the applications. Multiple surface chemistries enable the production of biomolecule-conjugated nanoprobes and they are successfully applied as imaging agents, suggesting that the future perspectives include a various type of biological and medical fields such as diagnostics and clinical *in vivo* imaging.

A.2.2 Fluorescent nanodiamond (FND)

Nanodiamond (ND) is one of the most promising nanomaterials to be applied for biomedical fields due to its unique physicochemical properties (reviewed in [40] and [41]). Biocompatible nature of the nanoparticle is due to its low toxicity ([42-44] and references therein) and facile surface functionalization[45,46] for the attachment of biomolecules of interest. In the case of fluorescence nanodiamond (FND), one or more electrons can be trapped within defect sites in the crystal when anionic vacancies are generated. Such electrons can absorb and emit visible range of light. The representative case is a F-center (*Farbe* in German is analogous to color in English.) in NaCl.[47] Those defect sites are called 'color center' since transparent crystals get color when exposed to light. Color center is often found in naturally occurring diamond because of nitrogen impurities in the jewel, which make nitrogen vacancies (N-V) and categorize such diamond as type I. The nitrogen vacancy can be artificially generated by the collision of nitrogen-containing

diamond by electrons, protons, neutrons and helium ions, and a heat treatment followed by annealing step finalizes the creation of nitrogen-vacancy center.[46,48-51]

N-V centers created in type Ib diamond can be excited by 450 nm~650 nm light, and emit far red-shifted fluorescence (600 nm~800 nm). The most important feature of this type is its superior photophysical nature to the quantum dot because it is intrinsically photoblinking-free[52] while excited by light (while the QD photoblinks upon irradiation) and possesses a comparable brightness[46] to the one of QD. The fluorescence quantum yield is nearly 0.99 and the fluorescence lifetime is ~12 nanoseconds.[53] In ground state, electronic spin angular momentum of N-V center is 1(S=1), that indicates triplet state.[54] According to the group theory, ground state was assigned as ^{3}A with C_{3v} symmetry, and first excited state is ^{3}E. These properties permit us to obtain a long time trajectory of fluorescence images or to fluorescently monitor the identical nanoparticle nearly endless times. The fluorescence intensity from FND is not decreased after 400 minutes of observation whereas emission from fluorescent polystyrene nanosphere carrying organic dyes drops to zero even before 100 minutes excitation.[42,46] Thus, these properties make FND very attractive to be utilized as a suitable candidate for a long-time observation without losing the valuable emission signature. Additionally, a strong Raman signal (1,332 cm^{-1}) from FND enables to produce confocal Raman-based cell imaging of the distribution of FND in A549 cell and to observe the interaction between FND-lysozyme complex and *E. coli*.[55] As mentioned, FND has a great potential for biological applications because, in addition to the properties described, it is possible to introduce several

different functional groups by surface modification.[44,56]

FND can be used as a Fluorescence Resonance Energy Transfer (FRET) donor and transfers the acquired energy to an acceptor when a proper acceptor dye is coupled.[57] Recently, researchers made a bimodal magnetic FND that is iron nanoparticles encapsulated in graphene structure on nanodiamonds by irradiation of microwave after mixing of FND and ferrocene. These magnetic FNDs underwent the uptake by HeLa cells through nonreceptor-mediated endocytosis, stayed in cytoplasm and exhibited no significant cytotoxicity.[58] It suggests the new particle can be utilized for magneto-optical imaging (MOI).

To elucidate the mechanism of FND uptake, FND were fed to HeLa cell and the degree of uptake shows exponential behavior with the half-life of 2.6 hours. Endocytosis of the FND did not occur in the presence of NaN_3 that blocks the production of ATP, the energy source of endocytosis. This result shows that endocytosis is the main mechanism of uptake. Further experiment was carried out to understand the mechanism of endocytosis. The fluorescence intensity was measured using two different conditions, one with sucrose which inhibits the formation of the clathrin-coated vesicle, and the other with filipin which inhibits the synthesis of cholesterol. The fluorescence signal became week upon the addition of sucrose, indicating that the clathrin-mediated endocytosis is a dominant process.[59]

Cell viability was tested using both A549 epithelial cells and HFL-1 normal fibroblasts together with 5 nm and 100 nm carboxylated FND. Most of the cells with the FNDs survived even after 48 hours whereas only 60% of the cells survived

in the presence of carbon nanotube. For the comparison of cytotoxicity of 100 nm FND and sodium arsenite ($NaAsO_2$) as a positive control, degree of apoptosis in A549 cells was measured by fluorescence microscope after injection of them. No significant change was observed in the case of 100 nm FND whereas the number of cells decreased dramatically in the case of $NaAsO_2$-treated cells and the shape of residual cells are severely deformed after 48 hours.[60] The comparison of cytotoxicity of FND with several other carbon particles was further assessed, and those were carbon black (CB), single-walled nanotube (SWNT), multi-walled nanotube (MWNT) and CdO (Figure A.3). The samples were introduced into neuroblastoma cell and macrophage. The most cytotoxic material was CdO, and the relative biocompatibility of carbon-based nanomaterial appeared to be FND>CB>MWNT>SWNT. When the generation of reactive oxygen species was compared, CB, SWNT and MWNT produced significant quantities of ROS, whereas FND produce a negligible quantity of ROS even in 100 μg/mL concentration.[61]

For a biological study, the surface of 140 nm FND was derivatized and coated with biocompatible polymer, polyethyleneglycol (PEG), and then a tumor targeting ligand, folic acid (FA), was conjugated to the complex. These modified FNDs were introduced into cancer cells. The transfection efficacy increased almost 20 times compared to the case in the absence of FA.[56] Another example is FNDs conjugated to actin-specific and mitochondria-specific antibodies. Those FNDs were delivered into the HeLa cell using 4th-generation dendrimer, cationic liposome and protamine

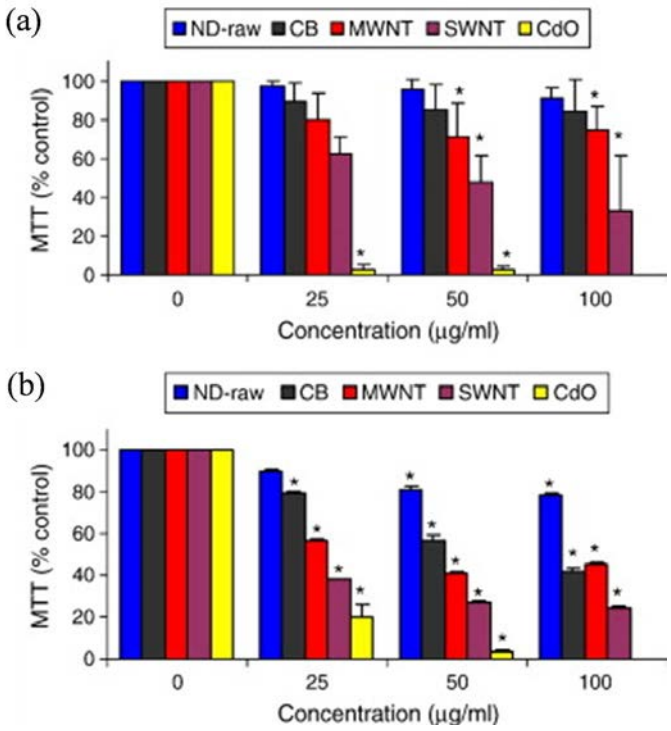

Figure A.3 Comparison of cytotoxicity by carbone-based nanomaterials and CdO after 24 hours of incubation in (a) neuroblastoma cells and (b) macrophages. The same trends were obtained from both cells (ND>CB>MWNT>SWNT>CdO). Macrophage cells are more prone to be effected by carbon-based nanomaterials. Copied from A. Schrand *et al*. 2007.

surface. It clearly showed that each FND was specifically targeted to actin and mitochondria.[62] Most FNDs distributed near the perinuclear region and the maximum number of FNDs in the cell was 100. Furthermore, three-dimensional single particle tracking in the cell can be achieved by using 35 nm FND.[56] The nanodiamonds introduced into cells are stably present in the hosts, and equally distributed when cells are divided (Figure A.4). They do not affect the level of both gene expression and protein expression.[63] All those results support the notion that FND can serves as biocompatible single-particle probes for various applications.

Although there have been many studies of evaluating the cytotoxicity and the biocompatibility of FND at the cell level, the investigation of organism-wide toxicity was recently carried out. N. Mohan. *et al*. introduced FND into living *Caenorhabditis elegans* (*C. elegans*) by two different methods, feeding and microinjection.[64] Upon feeding, bare FND stayed in the intestinal lumen whereas bioconjugated FND (with dextran or bovine serum albumin) were absorbed into the intestinal cells. The microinjected FNDs were stably present even in the next generation, and *C. elegans* did not release the orally administered FNDs. Any toxicity or stress was not detected and the next generations showed normal vitality, implicating the potential use of FND for organism-wide applications.

Recently, there has been an advent of the biomedical applications of FND using its facile surface modifications. Bio-imaging, bio-sensing and bio-detection using drug and antibody conjugations to FNDs are the main fields of the applications. One of the critical points to cure recurrent cancer is an effective delivery of the drug to

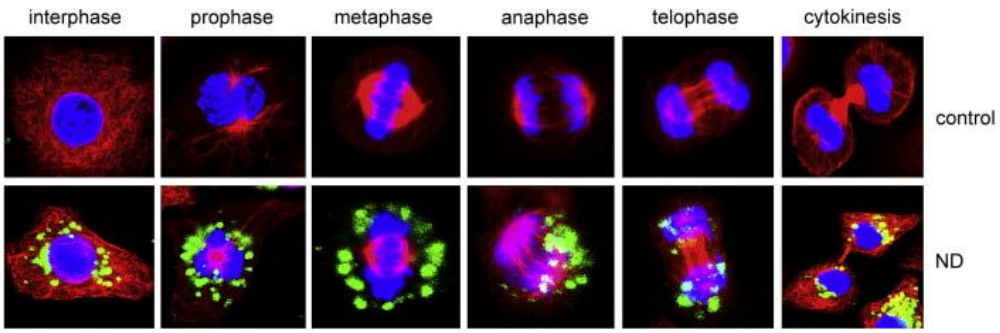

Figure A.4 The distribution of FND during mitosis. Intact A549 cells and FND (100 mg/mL) fed A549 cells were incubated for 48 hours followed by additional 24 hours of incubation with new, fresh culture medium. Microtubules were stained with anti-b-tubulin Cy3 (red in images), nuclei were stained with Hoechst 33258 (blue in images). Fluorescence from FND was encoded as green color in lower panel. The excitation wavelength is 488 nm, and fluorescence was collected at 510 nm ~ 530 nm. FND showed the division into two daughter cells during cytokinesis. Copied from K. K. Liu *et al*. 2009.

the site of interest. Doxorubicin (Dox)-conjugated FNDs were injected into the mouse, and the effect of these drugs on both liver and breast cancer was measured. The FND-based strategy was certainly advantageous not to dilute out the drug over the entire body and to target to the specific cancer tissue. Furthermore, it showed a superior ability to induce apoptosis of the cancer cells and to suppress the cancer growth while maintaining a low toxicity.[65,66] FND also can be used as a gene delivery vehicle potentially to treat genetic disorders or cancers. Dean Ho's group utilized 800 Da polyethyleneimine (PEI800) and amine ($-NH_2$) modification on the surface of FND. They found no evidence of cytotoxicity after injection of the modified FND intermingled with plasmid DNA into HeLa cell. A plasmid, pEGFPLuc encoding Green fluorescence protein (GFP), was introduced by the method into the HeLa cell and the fluorescence signal from the intracellular GFP was analyzed by confocal microscopy.[67] Other examples include the conjugation of alpha-bungarotoxin (α-BTX)[68] and paclitaxel[69], anti-cancer drugs, to FND. Each conjugated particle was injected and monitored in *Xenopus laevis* and mouse, respectively, and no toxic effect was found for both cases. Especially, there are many water-insoluble drugs for the treatment of cancer or inflammation and these drugs have difficulties in applying to the human body due to the reason. Those include purvalanol A, a drug for liver cancer, and 4-hydroxytamoxifen (4-OHT), a drug for breast cancer and dexamethasone, an anti-inflammatory drug. When they are conjugated to FND, the drugs can be more effectively utilized and monitored in a controllable fashion.[70]

Lastly, FNDs has been recognized as one of the most suitable nanoparticles to be coupled with super-resolution microscopy which overcomes the diffraction limit of optical microscopy. Ground state depletion (GSD) microscopy uses the photoswitching property of FND and the maximum spatial resolution is 7.6 nm in x and y axis. Three dimensional imaging is also possible by stimulated emission depletion (STED) microscopy.[5,71] The STED-based super-resolution fluorescence cell imaging of albumin-coated FND was reported.[72] Unlike bare FNDs, the bovine serum albumin (BSA)-coated FNDs were observed individually, a sign of their dispersive nature without having self-aggregation. The use of FND is extended to two photon microscopy to monitor freely diffusing lipid-encapsulated FNDs in cytoplasm and clear images were obtained by the microscopy.[41]

As describe in detail, FND is a fascinating nanoparticle because it does not show most-pervading multiple photophysical defects across organic and inorganic fluorophores. Those defects contain photobleaching and photoblinking upon strong and long-term irradiation. Together with easy schemes of conjugation to biological molecules, FND can be utilized as an important bioprobe. In addition, the excellent photophysical nature of the nanoparticle permits us to analyze biosystems using super-resolution microscopy as well as *in vivo* fluorescence microscopy.

A.2.3 Rare-earth upconversion nanoparticles (UCNP)

During last decade, a huge effort has been made to develop *in vivo* imaging systems for medical and diagnostic application. A main hurdle for this is that all the probes

excitable by visible wavelength light are nearly obsolete because the visible light cannot penetrate tissue deep enough and thus the probes in the body cannot be visualized easily. To solve this problem, probes excitable by near infrared (NIR) are employed because NIR can deeply penetrate a tissue to a depth of centimeters[11,73], and minimize the interference phenomena by the tissue autofluorescence.[74] As one of such probes, rare-earth upconversion nanoparticles (UCNPs) that emit high energy visible light when excited by the low energy NIR has become a new tool for *in vivo* imaging.[75]

Unlike general fluorescent materials, UCNPs have an anti-Stokes emission which emits higher energy than absorbed energy. This unusual luminescent phenomenon is explained by various mechanisms which are different from two-photon emission and second-harmonic generation process.[76-78] Upconversion process is necessary to have metastable intermediate state and is possible to absorb light sequentially. Energy Transfer Upconversion (ETU) is the common upconversion photoluminescence process. Two kinds of neighbouring ions, reservoirs, and emitters absorb same energy and live in metastable state. After non-radiative energy transfer from reservoirs to emitters, the highly excited emitters give out the light of higher energy. Thus, the emission efficiency of UCNPs depends on the distance between dopant ions. Other examples of the mechanisms are an excited state absorption (ESA) from sequential absorption of a single ion and photon avalanche (PA) having avalanche process started from non-resonant absorption.[79]

UCNPs have distinct advantages as bioprobes[80]. For example, UCNPs have large

Stokes shift between absorption and emission, long fluorescence lifetime, and relatively strong luminescence. The emission wavelength of UCNPs depends on controlling host matrix and the ratio of lanthanide dopants.[81,82] In other words, UCNPs of various colors can be synthesized. For that reason, it is possible to utilize them as multi-color imaging probes for simultaneous analysis of different types of biomolecules in a cell[83,84] because each type can be differently color-coded. Ga^{3+}, a material as a highly positive contrast agent for MRI due to high relaxivity, co-doped UCNP is developed for fluorescence and MR dual-modal imaging.[85,86]

The UCNP is superior to QD in several aspects including (i) mild irradiation condition (NIR irradiation vs. UV or short wavelength irradiation) not to damage bio-specimen[87], (ii) low toxicity necessary for *in vivo* imaging[88], (iii) negligible detection of autofluorescence caused by short wavelength excitation[89], and (iv) capability of selecting various light sources by the presence of 2-photon or 3-photon transition process. In comparison with organic fluorophores, UCNPs are much more photostable such that researchers can continuously monitor the particles in the body for a long period of time.

There are numerous reports of the use of UCNP for many different bioapplications. The UCNP can be chemically modified and coupled to biomolecules. X. F. Yu *et al*.[90] conjugated a neurotoxin to UCNP and injected to mouse to target and visualize the nanoprobe and found that the NCNPs were mainly present in the target glioma cancer (Figure A.5). This research suggests that the

NCNP can be a potential candidate for *in vivo* detection and diagnosis of cancer. Xu group synthesizes a low toxic and water-soluble β-$NAYF_4$:Yb, Er upconversion nanoparticles coated with polyethylenimine (PEI) molecules via electrostatic interactions.[91] As shown in Figure A.5, successful *in vivo* imaging data of *C. elegans* was obtained. Jiang *et al*. developed a FRET system consisting of dye-intercalated siRNA and UCNP to study the intracellular fate of siRNA such as the biostability of siRNA and the observation of siRNA release in native cell.[92] In addition, there are many other studies of the UCNPs. Those include brain blood vessel imaging of mouse, optical sectioning[93], whole-body imaging of mouse models,[94-96] and *in vivo* directly tracking of transplanted cell for studying cell dynamics.[97] Furthermore, an *in vitro* assay showed that UCNPs combined with meso-tetraphenyl porphyrine (TPP) photosensitizer exhibited cancer-killing activity when applied to HeLa cell[98], implying that the drug-nanoparticle complex can be utilized as therapeutic probes for cancer treatment. In addition, a multiplexed imaging system by UCNPS was developed by Stucky's group.[99] Each UCNP having a specific color code was conjugated to antigen-specific antibody and was served as a nanobarcode. When its cognate antigen was present, an optical encoding system was established by such multiplexed detection.[99] Babu *et al*. synthesize a new biocompatible cerium oxide nanoparticle combined with rare earth materials.[100]

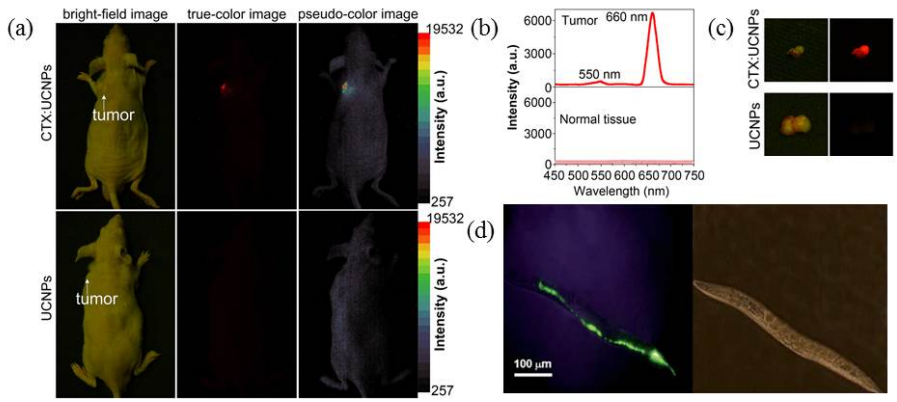

Figure A.5 (a) upconversion imaging of Balb-c nude mouse injected of CTX:UCNPs (top) and unlinked with UCNPs. (b) emission spectra detected from tumer (top) or normal tissue (bottom). (c) Imaging of tumor segregated form Balb-c nude mouse injected of CTX:UCNPs (top) and unlinked with UCNPs. Copied from X.-F. Yu *et al*. 2010. (d) Fluorescent image (left) and bright field image of *C. elegans* specifically targeted with NaYF4 : Yb,Er@OA nanoparticles. Copied from J. Chen *et al*. 2011.

A.2.4 Resveratrone

Recently, Yang *et al*. reported a new fluorescent probes from natural non-fluorescent molecule, *trans*-resveratrol.[101] Resveratrol is a polyphenol compound which can be found in grapes, berries, nuts and wines. Numerous reports show a lot of its positive effects to human such as anti-aging, anti-infection, lifespan-extending, anti-oxidant, and anti-carcinogenic.[102-106]

Trans-resveratrol undergoes photo-isomerization to form *cis*-resveratrol under illumination of UV light.[107,108] Many groups found and reported that fluorescence appeared after long-time irradiation of UV light.[109,110] The efforts to reveal the structure of fluorescent molecule, however, has not been successful yet. Yang *et al*. suggested the structure of new molecule by analyzing ESI-MS spectrum, ^{1}H NMR, ^{13}C NMR, DEPT NMR, 2D NMR, FT-IR, and IR spectrum. They revealed that the fluorescent molecule contains olefin and carbonyl group which cannot be formed by photo-isomerization. The IUPAC name of that molecule is (*E*)-4-(6,8-dihydroxynaphthalen-2-yl)but-3-en-2-one [dubbed resveratrone] (Figure A.6(a)). Theoretically the expected IR spectrum of resveratrone by *ab initio* calculation perfectly matched with experimentally obtained spectrum.

Photophysical and optical properties of the resveratrone were investigated. Its absolute fluorescence quantum yield is 0.49 and 0.31 in DMSO and isopropanol, respectively. These values are much higher than those of cyanine dyes. The fluorescence lifetime is found to be ~250 ps by time-correlated single photon

counting (TCSPC). Resveratrone has large Stokes shift (~150 nm) upon the absorption of 400 nm photons. In addition, two-photon emission was observed with intense 800 nm photons and two-photon cross-section is ~1.32 x 10^{-48} cm^4 s in ethanol (Figure A.6(b) and (c)). This light-induced organic fluorophores has multiple advantages to be utilized as an imaging probe. The size is relatively small (MW: 228.24 Da) and it can be prepared by facile one-step synthesis within relative short time (~90 sec). More importantly, like its natural precursor, resveratrol, we have found that it apparently shows an anticancer activity without any significant cytotoxicity to normal cells (unpublished data, Yang *et al.*). The optical properties of photochemically produced resveratrone in addition to other advantages make it well suited for an *in vivo* imaging agent.

A.3 Conclusion

Numerous fluorophores possessing excellent photophysical properties have been developed together with the advancement of optical imaging systems. To employ them at the *in vivo* or clinical levels, it is critical to assess their toxicity. Although semiconductor quantum dots have gained a great attention due to their brightness and other properties, the toxicological problems have hampered their uses as clinical technologies. In this review, we chose several promising fluorescence nanoparticles as well as an organic fluorophore derived from a natural compound, Resveratrol. There have been in-depth toxicity studies of the nanoparticles, silicon nanoparticles, FND and UCNPs, because multiple properties including their

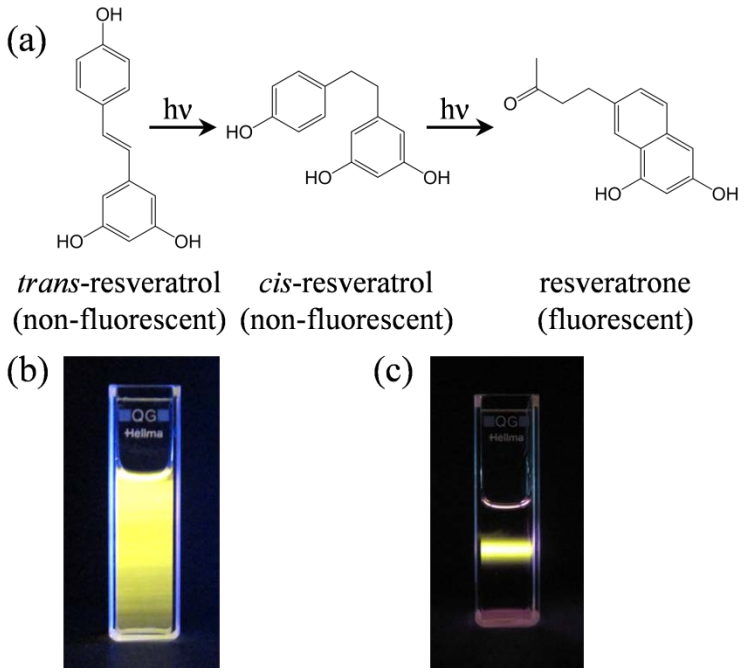

Figure A.6 (a) Proposed photochemical reaction pathway for the synthesis of the resveratrone. (b) Yellow photoluminescence of the resveratrolsolution under 305 nm UV irradiation. (c) Two-photon emission under strong 800 nm irradiation. Copied from I. Yang *et al*. 2012.

ingredients and sizes appear to be non-hazardous. As described in this review, they do not exhibit any significant potential toxicity and thus can be utilized as *in vivo* bioimaging probes. In addition, the photochemically produced resveratrone could be applied as a suitable organic fluorophore for *in vivo* applications because it does not induce any toxic effect as its natural precursor but shows excellent photophysical properties.

A.4 References

(1) Freudiger, C. W.; Min, W.; Saar, B. G.; Lu, S.; Holtom, G. R.; He, C.; Tsai, J. C.; Kang, J. X.; Xie, X. S. *Science* **2008**, *322*, 1857.

(2) Jones, S. A.; Shim, S.-H.; He, J.; Zhuang, X. *Nat. Methods* **2011**, *8*, 499.

(3) Westphal, V.; Rizzoli, S. O.; Lauterbach, M. A.; Kamin, D.; Jahn, R.; Hell, S. W. *Science* **2008**, *320*, 246.

(4) Rust, M. J.; Bates, M.; Zhuang, X. *Nat. Methods* **2006**, *3*, 793.

(5) Rittweger, E.; Han, K. Y.; Irvine, S. E.; Eggeling, C.; Hell, S. W. *Nat. Photonics* **2009**, *3*, 144.

(6) Chary, S. R.; Jain, R. K. *Proc. Natl. Acad. Sci*. **1989**, *86*, 5385.

(7) Zondervan, R.; Kulzer, F.; Orlinskii, S. B.; Orrit, M. *J. Phys. Chem. A* **2003**, *107*, 6770.

(8) Schuster, J.; Brabandt, J.; von Borczyskowski, C. *J. Lumin*. **2007**, *127*, 224.

(9) Medintz, I. L.; Uyeda, H. T.; Goldman, E. R.; Mattoussi, H. *Nat. Mater*. **2005**, *4*, 435.

(10) Resch-Genger, U.; Grabolle, M.; Cavaliere-Jaricot, S.; Nitschke, R.; Nann, T. *Nat. Methods* **2008**, *5*, 763.

(11) Gao, X.; Cui, Y.; Levenson, R. M.; Chung, L. W. K.; Nie, S. *Nat. Biotechnol*. **2004**, *22*, 969.

(12) Canham, L. T. *Appl. Phys. Lett*. **1990**, *57*, 1046.

(13) Cullis, A. G.; Canham, L. T.; Calcott, P. D. J. *J. Appl. Phys*. **1997**, *82*, 909.

(14) Bisi, O.; Ossicini, S.; Pavesi, L. *Surf. Sci. Rep*. **2000**, *38*, 1.

(15) Beard, M. C.; Knutsen, K. P.; Yu, P. R.; Luther, J. M.; Song, Q.; Metzger, W. K.; Ellingson, R. J.; Nozik, A. J. *Nano Lett*. **2007**, *7*, 2506.

(16) He, G. S.; Zheng, Q. D.; Yong, K. T.; Erogbogbo, F.; Swihart, M. T.; Prasad, P. N. *Nano Lett*. **2008**, *8*, 2688.

(17) Michalet, X.; Pinaud, F.; Lacoste, T. D.; Dahan, M.; Bruchez, M. P.; Alivisatos, A. P.; Weiss, S. *Single Mol*. **2001**, *2*, 261.

(18) Alsharif, N. H.; Berger, C. E.; Varanasi, S. S.; Chao, Y.; Horrocks, B. R.; Datta, H. K. *Small* **2009**, *5*, 221.

(19) Erogbogbo, F.; Yong, K. T.; Roy, I.; Hu, R.; Law, W. C.; Zhao, W. W.; Ding, H.; Wu, F.; Kumar, R.; Swihart, M. T.; Prasad, P. N. *Acs Nano* **2011**, *5*, 413.

(20) Erogbogbo, F.; Yong, K. T.; Hu, R.; Law, W. C.; Ding, H.; Chang, C. W.; Prasad, P. N.; Swihart, M. T. *Acs Nano* **2010**, *4*, 5131.

(21) De Angelis, F.; Pujia, A.; Falcone, C.; Iaccino, E.; Palmieri, C.; Liberale, C.; Mecarini, F.; Candeloro, P.; Luberto, L.; de Laurentiis, A.; Das, G.; Scala, G.; Di Fabrizio, E. *Nanoscale* **2010**, *2*, 2230.

(22) Sengupta, S.; Smitha, S. L.; Thomas, N. E.; Santhoshkumar, T. R.; Devi, S. K. C.; Sreejalekshmi, K. G.; Rajasekharan, K. N. *Brit. J. Pharmacol*. **2005**, *145*, 1076.

(23) Farokhzad, O. C.; Cheng, J. J.; Teply, B. A.; Sherifi, I.; Jon, S.; Kantoff, P. W.; Richie, J. P.; Langer, R. *Proc. Natl. Acad. Sci*. **2006**, *103*, 6315.

(24) He, Y.; Zhong, Y. L.; Peng, F.; Wei, X. P.; Su, Y. Y.; Lu, Y. M.; Su, S.; Gu, W.; Liao, L. S.; Lee, S. T. *J. Am. Chem. Soc*. **2011**, *133*, 14192.

(25) Wang, Q.; Ni, H. J.; Pietzsch, A.; Hennies, F.; Bao, Y. P.; Chao, Y. M. *J. Nanopart. Res*. **2011**, *13*, 405.

(26) Zong, C. H.; Ai, K. L.; Zhang, G.; Li, H. W.; Lu, L. H. *Anal. Chem*. **2011**, *83*, 3126.

(27) Low, S. P.; Williams, K. A.; Canham, L. T.; Voelcker, N. H. *J. Biomed. Mater. Res. A* **2010**, *93*, 1124.

(28) Slater, T. F.; Sawyer, B.; Strauli, U. *Biochimica. Et. Biophysica. Acta.* **1963**, *77*, 383.

(29) Bimbo, L. M.; Sarparanta, M.; Santos, H. A.; Airaksinen, A. J.; Makila, E.; Laaksonen, T.; Peltonen, L.; Lehto, V. P.; Hirvonen, J.; Salonen, J. *Acs Nano* **2010**, *4*, 3023.

(30) Choi, J.; Zhang, Q.; Reipa, V.; Wang, N. S.; Stratmeyer, M. E.; Hitchins, V. M.; Goering, P. L. *J. Appl. Toxicol.* **2009**, *29*, 52.

(31) Park, J. H.; Gu, L.; von Maltzahn, G.; Ruoslahti, E.; Bhatia, S. N.; Sailor, M. J. *Nat. Mater.* **2009**, *8*, 331.

(32) Lee, W. M.; Ha, S. W.; Yang, C. Y.; Lee, J. K.; An, Y. J. *Chemosphere* **2011**, *82*, 451.

(33) Kelm, E.; Korovin, S.; Pustovoy, V.; Surkov, A.; Vladimirov, A. *Appl. Phys. B* **2011**, *105*, 599.

(34) Wang, L.; Reipa, V.; Blasic, J. *Bioconjug. Chem.* **2004**, *15*, 409.

(35) Erogbogbo, F.; Tien, C. A.; Chang, C. W.; Yong, K. T.; Law, W. C.; Ding, H.; Roy, I.; Swihart, M. T.; Prasad, P. N. *Bioconjug. Chem.* **2011**, *22*, 1081.

(36) Li, Z. F.; Ruckenstein, E. *Nano Lett.* **2004**, *4*, 1463.

(37) Tilley, R. D.; Yamamoto, K. *Adv. Mater.* **2006**, *18*, 2053.

(38) Warner, J. H.; Hoshino, A.; Yamamoto, K.; Tilley, R. D. *Angew. Chem. Int. Ed.* **2005**, *44*, 4550.

(39) Fucikova, A.; Valenta, J.; Pelant, I.; Kusova, K.; Brezina, V. *physica. Status. Solidi. C* **2011**, *8*, 1093.

(40) Krueger, A. *Adv. Mater.* **2008**, *20*, 2445.

(41) Hui, Y. Y.; Cheng, C.-L.; Chang, H.-C. J. Phys. D: *Appl. Phys.* **2010**, *43*, 374021.

(42) Yu, S. J.; Kang, M. W.; Chang, H. C.; Chen, K. M.; Yu, Y. C. *J. Am. Chem.*

Soc. **2005**, *127*, 17604.

(43) Vaijayanthimala, V.; Tzeng, Y. K.; Chang, H. C.; Li, C. L. *Nanotechnology* **2009**, *20*, 425103.

(44) Kruger, A.; Liang, Y. J.; Jarre, G.; Stegk, J. *J. Mater. Chem*. **2006**, *16*, 2322.

(45) Krueger, A. *Chemistry **2008**, 14*, 1382.

(46) Fu, C. C.; Lee, H. Y.; Chen, K.; Lim, T. S.; Wu, H. Y.; Lin, P. K.; Wei, P. K.; Tsao, P. H.; Chang, H. C.; Fann, W. *Proc. Natl. Acad. Sci*. **2007**, *104*, 727.

(47) Seitz, F. *Rev. Mod. Phys*. **1946**, *18*, 384.

(48) Wee, T.-L.; Mau, Y.-W.; Fang, C.-Y.; Hsu, H.-L.; Han, C.-C.; Chang, H.-C. *Diam. Relat. Mater*. **2009**, *18*, 567.

(49) Davies, G.; Hamer, M. F. P. *Roy. Soc. Lond. A. Mat*. **1976**, *348*, 285.

(50) Chang, Y. R.; Lee, H. Y.; Chen, K.; Chang, C. C.; Tsai, D. S.; Fu, C. C.; Lim, T. S.; Tzeng, Y. K.; Fang, C. Y.; Han, C. C.; Chang, H. C.; Fann, W. *Nat. Nanotechnol*. **2008**, *3*, 284.

(51) Jelezko, F.; Wrachtrup, J. *Physica. Status. Solidi. A.* **2006**, *203*, 3207.

(52) Gruber, A.; Drabenstedt, A.; Tietz, C.; Fleury, L.; Wrachtrup, J.; vonBorczyskowski, C. *Science* **1997**, *276*, 2012.

(53) Collins, A. T.; Thomaz, M. F.; Jorge, M. I. B. *J. Phys. C* **1983**, *16*, 2177.

(54) Loubser, J.; Vanwyk, J. A. *Rep. Prog. Phys*. **1978**, *41*, 1201.

(55) Chao, J. I.; Perevedentseva, E.; Chung, P. H.; Liu, K. K.; Cheng, C. Y.; Chang, C. C.; Cheng, C. L. *Biophys. J*. **2007**, *93*, 2199.

(56) Zhang, B.; Li, Y.; Fang, C. Y.; Chang, C. C.; Chen, C. S.; Chen, Y. Y.; Chang, H. C. *Small* **2009**, *5*, 2716.

(57) Borsch, M.; Wrachtrup, J. *Chemphyschem* **2011**, *12*, 542.

(58) Chang, I. P.; Hwang, K. C.; Chiang, C. S. *J. Am. Chem. Soc*. **2008**, *130*, 15476.

(59) Faklaris, O.; Joshi, V.; Irinopoulou, T.; Tauc, P.; Sennour, M.; Girard, H.; Gesset, C.; Arnault, J. C.; Thorel, A.; Boudou, J. P.; Curmi, P. A.; Treussart, F. *Acs Nano* **2009**, *3*, 3955.

(60) Liu, K.-K.; Cheng, C.-L.; Chang, C.-C.; Chao, J.-I. *Nanotechnology* **2007**, *18*, 325102.

(61) Schrand, A.; Dai, L.; Schlager, J.; Hussain, S.; Osawa, E. *Diam. Relat. Mater*. **2007**, *16*, 2118.

(62) Mkandawire, M.; Pohl, A.; Gubarevich, T.; Lapina, V.; Appelhans, D.; Rodel, G.; Pompe, W.; Schreiber, J.; Opitz, J. J. Biophotonics 2009, 2, 596.

(63) Liu, K. K.; Wang, C. C.; Cheng, C. L.; Chao, J. I. *Biomaterials* **2009**, *30*, 4249.

(64) Mohan, N.; Chen, C. S.; Hsieh, H. H.; Wu, Y. C.; Chang, H. C. *Nano Lett.* **2010**, *10*, 3692.

(65) Chow, E. K.; Zhang, X. Q.; Chen, M.; Lam, R.; Robinson, E.; Huang, H. J.; Schaffer, D.; Osawa, E.; Goga, A.; Ho, D. *Sci. Transl. Med*. **2011**, *3*.

(66) Li, Y.; Zhou, X.; Wang, D.; Yang, B.; Yang, P. *J. Mater. Chem*. **2011**, *21*, 16406.

(67) Zhang, X. Q.; Chen, M.; Lam, R.; Xu, X. Y.; Osawa, E.; Ho, D. *Acs Nano* **2009**, *3*, 2609.

(68) Liu, K. K.; Chen, M. F.; Chen, P. Y.; Lee, T. J.; Cheng, C. L.; Chang, C. C.; Ho, Y. P.; Chao, J. I. *Nanotechnology* **2008**, *19*, 205102.

(69) Liu, K. K.; Zheng, W. W.; Wang, C. C.; Chiu, Y. C.; Cheng, C. L.; Lo, Y. S.; Chen, C.; Chao, J. I. *Nanotechnology* **2010**, *21*, 315106.

(70) Chen, M.; Pierstorff, E. D.; Lam, R.; Li, S. Y.; Huang, H.; Osawa, E.; Ho, D. *Acs Nano* **2009**, *3*, 2016.

(71) Han, K. Y.; Willig, K. I.; Rittweger, E.; Jelezko, F.; Eggeling, C.; Hell, S. W. *Nano Lett*. **2009**, *9*, 3323.

(72) Tzeng, Y. K.; Faklaris, O.; Chang, B. M.; Kuo, Y.; Hsu, J. H.; Chang, H. C. *Angew. Chem. Int. Ed*. **2011**, *50*, 2262.

(73) Smith, A. M.; Mancini, M. C.; Nie, S. M. *Nat. Nanotechnol*. **2009**, *4*, 710.

(74) Wang, F.; Liu, X. G. *Chem. Soc. Rev*. **2009**, *38*, 976.

(75) van de Rijke, F.; Zijlmans, H.; Li, S.; Vail, T.; Raap, A. K.; Niedbala, R. S.; Tanke, H. J. *Nat. Biotechnol* **2001**, *19*, 273.

(76) Auzel, F. *Chem. Rev*. **2004**, *104*, 139.

(77) Haase, M.; Schafer, H. *Angew. Chem. Int. Ed*. **2011**, *50*, 5808.

(78) Wang, F.; Liu, X. *Chem. Soc. Rev*. **2009**, *38*, 976.

(79) Chivian, J. S.; Case, W. E.; Eden, D. D. *Appl. Phys. Lett*. **1979**, *35*, 124.

(80) Chatterjee, D. K.; Gnanasammandhan, M. K.; Zhang, Y. *Small* **2010**, *6*, 2781.

(81) Wang, X.; Li, Y. *Chem. Comm*. **2007**, *27*, 2901.

(82) Heer, S.; Lehmann, O.; Haase, M.; Gudel, H. U. *Angew. Chem. Int. Ed*. **2003**, *42*, 3179.

(83) Wu, X.; Liu, H.; Liu, J.; Haley, K. N.; Treadway, J. A.; Larson, J. P.; Ge, N.; Peale, F.; Bruchez, M. P. *Nat. Biotechnol*. **2003**, *21*, 41.

(84) Han, M.; Gao, X.; Su, J. Z.; Nie, S. *Nat. Biotechnol*. **2001**, *19*, 631.

(85) Zhou, J.; Sun, Y.; Du, X. X.; Xiong, L. Q.; Hu, H.; Li, F. Y. *Biomaterials* **2010**, *31*, 3287.

(86) Johnson, N. J. J.; Oakden, W.; Stanisz, G. J.; Prosser, R. S.; van Veggel, F. C. J. M. *Chem. Mater*. **2011**, *23*, 4877.

(87) Yamazaki, Y.; Zinchenko, A. A.; Murata, S. *Nanoscale* **2011**, *3*, 2909.

(88) Derfus, A. M.; Chan, W. C. W.; Bhatia, S. N. *Nano Lett*. **2003**, *4*, 11.

(89) Lim, S. F.; Riehn, R.; Ryu, W. S.; Khanarian, N.; Tung, C.-k.; Tank, D.; Austin, R. H. *Nano Lett*. **2006**, *6*, 169.

(90) Yu, X.-F.; Sun, Z.; Li, M.; Xiang, Y.; Wang, Q.-Q.; Tang, F.; Wu, Y.; Cao, Z.; Li, W. *Biomaterials* **2010**, *31*, 8724.

(91) Chen, J.; Guo, C.; Wang, M.; Huang, L.; Wang, L.; Mi, C.; Li, J.; Fang, X.; Mao, C.; Xu, S. *J. Mater. Chem*. **2011**, *21*, 2632.

(92) Jiang, S.; Zhang, Y. *Langmuir* **2010**, *26*, 6689.

(93) Pichaandi, J.; Boyer, J.-C.; Delaney, K. R.; van Veggel, F. C. J. M. *J. Phys. Chem. C* **2011**, *115*, 19054.

(94) Nyk, M.; Kumar, R.; Ohulchanskyy, T. Y.; Bergey, E. J.; Prasad, P. N. *Nano Lett*. **2008**, *8*, 3834.

(95) Chatterjee, D. K.; Rufaihah, A. J.; Zhang, Y. *Biomaterials* **2008**, *29*, 937.

(96) Abdul Jalil, R.; Zhang, Y. *Biomaterials* **2008**, *29*, 4122.

(97) Idris, N. M.; Li, Z. Q.; Ye, L.; Sim, E. K. W.; Mahendran, R.; Ho, P. C. L.; Zhang, Y. *Biomaterials* **2009**, *30*, 5104.

(98) Shan, J.; Budijono, S. J.; Hu, G.; Yao, N.; Kang, Y.; Ju, Y.; Prud'homme, R. K. *Adv. Funct. Mater*. **2011**, *21*, 2488.

(99) Zhang, F.; Haushalter, R. C.; Haushalter, R. W.; Shi, Y.; Zhang, Y.; Ding, K.; Zhao, D.; Stucky, G. D. *Small* **2011**, *7*, 1972.

(100) Babu, S.; Cho, J. H.; Dowding, J. M.; Heckert, E.; Komanski, C.; Das, S.; Colon, J.; Baker, C. H.; Bass, M.; Self, W. T.; Seal, S. *Chem. Comm*. **2010**, *46*, 6915.

(101) Yang, I.; Kim, E.; Kang, J.; Han, H. S.; Sul, S.; Park, S. B.; Kim, S. K. *Chem. Comm*. **2012**, *48*, 3839.

(102) Quideau, S.; Deffieux, D.; Douat-Casassus, C.; Pouysegu, L. *Angew. Chem. Int. Ed*. **2011**, *50*, 586.

(103) Baur, J. A.; Sinclair, D. A. *Nat. Rev. Drug. Discov*. **2006**, *5*, 493.

(104) Bradamante, S.; Barenghi, L.; Villa, A. *Cardiovasc. Drug. Rev*. **2004**, *22*, 169.

(105) Jang, M. S.; Cai, E. N.; Udeani, G. O.; Slowing, K. V.; Thomas, C. F.; Beecher, C. W. W.; Fong, H. H. S.; Farnsworth, N. R.; Kinghorn, A. D.; Mehta, R. G.; Moon, R. C.; Pezzuto, J. M. *Science* **1997**, *275*, 218.

(106) Sinha, K.; Chaudhary, G.; Gupta, Y. K. *Life. Sci*. **2002**, *71*, 655.

(107) Martinez-Ortega, M. V.; Carcia-Parrilla, M. C.; Troncoso, A. M. *Nahrung* **2000**, *44*, 253.

(108) Roggero, J. P.; Archier, P. *Sci. Aliment*. **1994**, *14*, 99.

(109) Roggero, J. P.; Garciaparrilla, C. *Sci. Aliment*. **1995**, *15*, 411.

(110) Poutaraud, A.; Latouche, G.; Martins, S.; Meyer, S.; Merdinoglu, D.; Cerovic, Z. G. *J. Agr. Food. Chem*. **2007**, *55*, 4913.

Appendix B. Rapid and facile synthesis of a $(Zn_xAg_yIn_z)S_2$ nanocrystal library via sono-combichem method and its characterization including single nanocrystal analysis

This work was done by collaboration with KRICT.

B.1 Introduction

There has been remarkable achievement in the development of quantum dots (QDs), including II–VI compounds, for in the areas of sensors,[1] solar cells,[2] optical devices,[3] and imaging probes.[4–6] Especially, QDs as bio-imaging probes has gained a great attention because of their excellent and unique fluorescence properties such as brightness, photostability, size dependence in emission wavelength.[7,8] The use of QDs for industrial and biological applications, however, has been limited mainly due to the serious toxicity of their heavy metal components such as cadmium, selenium, and tellurium.[9] Thus far, many research groups have reported the synthesis of less-toxic luminescent nanocrystals that do not contain such heavy metals. They include InP, InP/ZnS, $CuInS_2$, $AgInS_2$, and ZnS–$AgInS_2$ (ZAIS).[10–15] Nevertheless, multiple drawbacks such as the lack of diverse emission colors, low fluorescence intensities, and delicate synthetic parameters have impeded the progress to replace QDs. To harness the unexplored potential of less-toxic luminescent nanocrystals (NCs), it will certainly be desirable to generate a library of such NCs exhibiting various distinct emission profiles and subsequently to screen a set of proper NCs by facile and rapid high throughput format synthesis and analysis.[16–18] Our critical factors for this task include combinatorial chemistry and simple reaction conditions to control the whole process. Here, we introduce a novel strategy for the fast synthesis of high quality $(Zn_xAg_yIn_z)S_2$ nanocrystals, the modified forms of ZAIS NCs, and the production of a ZAIS NC library according to

the ratio of the ingredients. The application of sonochemistry[19] together with a combinatorial chemistry allows us to assess the emission color tuning generated by a variety of different combinations among Zn, Ag, and In elements. To explore the feasibility of the ZAIS NC as a bio-imaging probe, several analyses were performed including agarose gel electrophoresis, cell imaging by confocal fluorescence microscopy, and single nanoparticle imaging at 488 nm laser light, which is a routinely used excitation wavelength for bio-imaging due to the reduction of damage to tissues.

ZAIS is composed of a group II alloyed with I–III–VI semiconductor nanocrystals ($ZnAgInS_2$) and their fluorescence properties can be determined simply by varying their composition without size-dependent band gap change. For a facile modulation of Zn, Ag, and In fractions to trace the effect of each component on fluorescence emission profiles, we construct the ternary forms of ZAIS (tZAIS) NCs $(Zn_xAg_yIn_z)S_2$, where $x + y + z = 1$ and their ratio can be changed within a defined total amount. Thus, the tZAIS combinatorial library was obtained by using a ternary-type composition array including 66 different combinations of three elements (Figure B.1 and B.2).

To establish a facile and rapid synthesis and screening procedure, we have developed and applied the sonochemical synthetic route[20] in parallel with combinatorial chemistry[21,22] that covers a variety of different combinations in the composition of Zn, Ag, and In. Subsequently, the resulting set of NCs was analyzed by visualizing their fluorescence properties upon UV irradiation (Figure B.1a) and

by measuring their emission profiles using a fluorometer (Figure B.1b). The sonochemistry utilizes ultrasound to introduce a rapid reaction time and milder operating conditions (e.g., relatively lower temperature and pressure) than other temperature-based systems,[14,18,23] and eliminates cumbersome synthesis steps of other methods. The effect of ultrasonic radiation on a reaction is attributed to the acoustic cavitations within collapsing bubbles which generate localized hot spots with extreme conditions (temperature = 5,000 K, pressure = 1,800 atm, and cooling rate = 10^{10} K s^{-1}).[19]

B.2 Experiment

B.2.1 Synthesis of precursor and $(Zn_xAg_yIn_z)S_2$ nanocrystals (NCs)

As a precursor, metal ion–diethyldithiocarbamate chelating complexes were prepared by slow drop-wise addition of 3 ml of aqueous solution including metal ions ($Zn(NO_3)_2 \cdot 6H_2O$, $AgNO_3$, $In(NO_3)_3 \cdot 3H_2O$) with various molar ratios [$(Zn_xAg_yIn_z)S_2$, x + y + z = 1 mole] into 30 mL of an aqueous solution containing an excess of sodium diethyldithiocarbamate for sufficient chelation between the metal ion and diethyldithiocarbamate. Resulting precursors were washed with distilled water several times and dried in an electric oven (ON-22GW, JEIO Tech, Korea). 100 mg of the precursor powder and 10 mL of dodecylamine were added into a 20 mL vial and ultrasonically treated (Sonic dismembrator Model 500, Fisher Scientific, USA) for 10 min (maximum temperature at about 160 °C) at 20 kHz

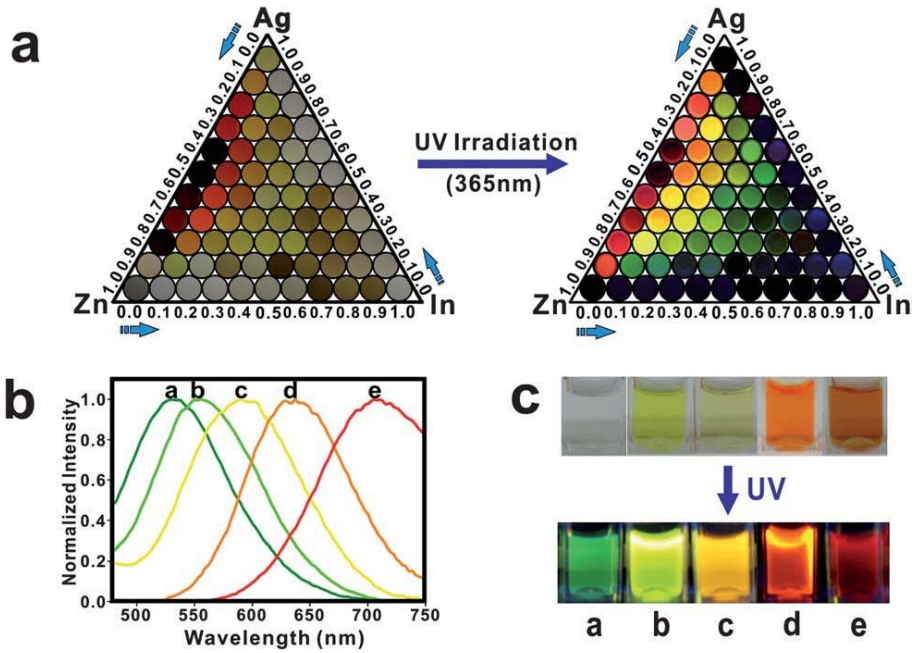

Figure B.1 Physical property of $(Zn_xAg_yIn_z)S_2$ nanocrystals (NCs) . a: A library of $(Zn_xAg_yIn_z)S_2$ NCs with 66 different combinations in composition. Their fluorescence and brightness are visualized by UV light illumination at 365 nm. b: Emission spectra of ternary forms of ZAIS (tZAIS) NCs with different color profiles. c: Picture of water-soluble MPA-coated $(Zn_xAg_yIn_z)S_2$ NCs (a: $(Zn_{0.4}Ag_{0.1}In_{0.5})S_2$ [tZAIS 50], b: $(Zn_{0.3}Ag_{0.2}In_{0.5})S_2$ [tZAIS 49], c: $(Zn_{0.2}Ag_{0.3}In_{0.5})S_2$ [tZAIS 48], d: $(Zn_{0.1}Ag_{0.4}In_{0.5})S_2$ [tZAIS 47], e: $(Zn_0Ag_{0.5}In_{0.5})S_2$ [tZAIS 46]).

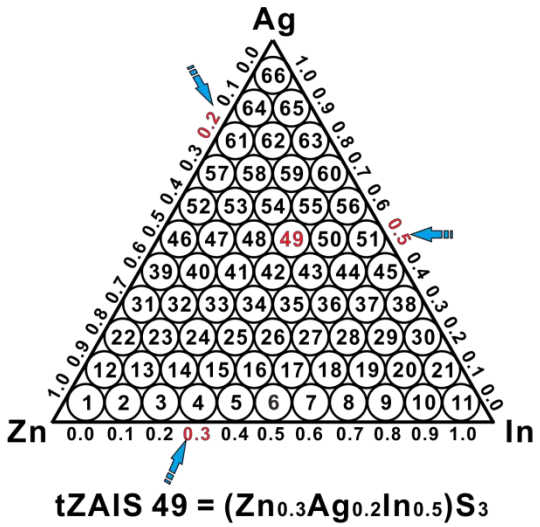

1	$(Zn_0Ag_1In_0)S_3$	23	$(Zn_{0.1}Ag_{0.7}In_{0.2})S_3$	45	$(Zn_{0.6}Ag_0In_{0.4})S_3$
2	$(Zn_{0.1}Ag_{0.9}In_0)S_3$	24	$(Zn_{0.2}Ag_{0.6}In_{0.2})S_3$	46	$(Zn_0Ag_{0.5}In_{0.5})S_3$
3	$(Zn_{0.2}Ag_{0.8}In_0)S_3$	25	$(Zn_{0.3}Ag_{0.5}In_{0.2})S_3$	47	$(Zn_{0.1}Ag_{0.4}In_{0.5})S_3$
4	$(Zn_{0.3}Ag_{0.7}In_0)S_3$	26	$(Zn_{0.4}Ag_{0.4}In_{0.2})S_3$	48	$(Zn_{0.2}Ag_{0.3}In_{0.5})S_3$
5	$(Zn_{0.4}Ag_{0.6}In_0)S_3$	27	$(Zn_{0.5}Ag_{0.3}In_{0.2})S_3$	49	$(Zn_{0.3}Ag_{0.2}In_{0.5})S_3$
6	$(Zn_{0.5}Ag_{0.5}In_0)S_3$	28	$(Zn_{0.6}Ag_{0.2}In_{0.2})S_3$	50	$(Zn_{0.4}Ag_{0.1}In_{0.5})S_3$
7	$(Zn_{0.6}Ag_{0.4}In_0)S_3$	29	$(Zn_{0.7}Ag_{0.1}In_{0.2})S_3$	51	$(Zn_{0.5}Ag_0In_{0.5})S_3$
8	$(Zn_{0.7}Ag_{0.3}In_0)S_3$	30	$(Zn_{0.8}Ag_0In_{0.2})S_3$	52	$(Zn_0Ag_{0.4}In_{0.6})S_3$
9	$(Zn_{0.8}Ag_{0.2}In_0)S_3$	31	$(Zn_0Ag_{0.7}In_{0.3})S_3$	53	$(Zn_{0.1}Ag_{0.3}In_{0.6})S_3$
10	$(Zn_{0.9}Ag_{0.1}In_0)S_3$	32	$(Zn_{0.1}Ag_{0.6}In_{0.3})S_3$	54	$(Zn_{0.2}Ag_{0.2}In_{0.6})S_3$
11	$(Zn_1Ag_0In_0)S_3$	33	$(Zn_{0.2}Ag_{0.5}In_{0.3})S_3$	55	$(Zn_{0.3}Ag_{0.1}In_{0.6})S_3$
12	$(Zn_0Ag_{0.9}In_{0.1})S_3$	34	$(Zn_{0.3}Ag_{0.4}In_{0.3})S_3$	56	$(Zn_{0.4}Ag_0In_{0.6})S_3$
13	$(Zn_{0.1}Ag_{0.8}In_{0.1})S_3$	35	$(Zn_{0.4}Ag_{0.3}In_{0.3})S_3$	57	$(Zn_0Ag_{0.3}In_{0.7})S_3$
14	$(Zn_{0.2}Ag_{0.7}In_{0.1})S_3$	36	$(Zn_{0.5}Ag_{0.2}In_{0.3})S_3$	58	$(Zn_{0.1}Ag_{0.2}In_{0.7})S_3$
15	$(Zn_{0.3}Ag_{0.6}In_{0.1})S_3$	37	$(Zn_{0.6}Ag_{0.1}In_{0.3})S_3$	59	$(Zn_{0.2}Ag_{0.1}In_{0.7})S_3$
16	$(Zn_{0.4}Ag_{0.5}In_{0.1})S_3$	38	$(Zn_{0.7}Ag_0In_{0.3})S_3$	60	$(Zn_{0.3}Ag_0In_{0.7})S_3$
17	$(Zn_{0.5}Ag_{0.4}In_{0.1})S_3$	39	$(Zn_0Ag_{0.6}In_{0.4})S_3$	61	$(Zn_0Ag_{0.2}In_{0.8})S_3$
18	$(Zn_{0.6}Ag_{0.3}In_{0.1})S_3$	40	$(Zn_{0.1}Ag_{0.5}In_{0.4})S_3$	62	$(Zn_{0.1}Ag_{0.1}In_{0.8})S_3$
19	$(Zn_{0.7}Ag_{0.2}In_{0.1})S_3$	41	$(Zn_{0.2}Ag_{0.4}In_{0.4})S_3$	63	$(Zn_{0.2}Ag_0In_{0.8})S_3$
20	$(Zn_{0.8}Ag_{0.1}In_{0.1})S_3$	42	$(Zn_{0.3}Ag_{0.3}In_{0.4})S_3$	64	$(Zn_0Ag_{0.1}In_{0.9})S_3$
21	$(Zn_{0.9}Ag_0In_{0.1})S_3$	43	$(Zn_{0.4}Ag_{0.2}In_{0.4})S_3$	65	$(Zn_{0.1}Ag_0In_{0.9})S_3$
22	$(Zn_0Ag_{0.8}In_{0.2})S_3$	44	$(Zn_{0.5}Ag_{0.1}In_{0.4})S_3$	66	$(Zn_0Ag_0In_1)S_3$

Figure B.2 Total compositional ternary library of $(Zn_xAg_yIn_z)S_2$ (tZAIS) NCs in terms of Zn, Ag, and In metal ratios. tZAIS 49 is an example of the numbering system.

power in air. The resulting suspension was centrifuged to remove by-products and washed with chloroform and methanol several times. The final products were re-dispersed in chloroform.

B.2.2 Synthesis of water soluble $(Zn_xAg_yIn_z)S_2$ NCs

$(Zn_xAg_yIn_z)S_2$ NCs were subjected to the ligand exchange method as mentioned in the main text. 400 mL 3-mercaptopropionic acid (MPA) was diluted in 10 mL methanol solution and subsequently 1 M KOH was added to bring the pH up over 13.0. The solution was combined with each $(Zn_xAg_yIn_z)S_2$ NC, and the mixture was vigorously stirred for 30 min. Then the sample was centrifuged and washed several times with methanol. The final product was re-dispersed in distilled water.

B.2.3 Characterization of $(Zn_xAg_yIn_z)S_2$ NCs

The resulting nanocrystals were analyzed using a Rigaku D/MAX-2200V X-ray diffractometer (Rigaku, Japan) with CuKa radiation (Ni filter). TEM and HRTEM images were obtained using a JEM-2100F field emission electron microscope (JEOL, Japan) at an accelerating voltage of 200 kV. Energy-dispersive X-ray spectroscopy (EDS) measurement was performed using Quantax 200 energy dispersive X-ray spectrometer (Bruker, Germany). Key parameters for the measurement are: (i) energy resolution was less than 127 V and peak shift (5~300 kcps) was less than 5 eV; (ii) Si Drift Detector (SDD) was utilized for data collection and the detected species were from Be (z = 4) to Am (z = 95).

B.2.4 Confocal imaging of single nanocrystals (ZAIS NCs and CdSe/ZnS QDs)

Confocal images of single NCs were collected using a home-built confocal laser scanning imaging system. The sample on the stage was illuminated by laser lights at both 488 nm (± 5 nm) and 455 nm (± 25 nm) with 12 μW powers. Mai Tai HP (Spectra-Physics, Santa Clara, CA) femto-second pulsed laser with 80 MHz repetition rates was used as a light source. Horizontally polarized light from the laser was depolarized after it passed through the supercontinuum generation fiber (FemtoWhite800, NKT Photonics, Birkerød, Denmark), and band-pass filters were utilized to optimize the condition. Samples were illuminated on a piezo stage (NanoMax-TS, Thorlabs, Newton, NJ) coupled with an objective (HCX PL APO 100X, 1.4 NA oil immersion, Leica). Emitted photons from single NCs were collected through 500 nm long-pass filter. Avalanche Photodiode (APD) was used as a detector (SPCM-AQR-14-FC, Perkin Elmer).

As a control, CdSe/ZnS QDs were purchased from QD Solution (Nanodot CS01-620, Korea). Diluted tZAIS 46, 47 and CdSe/ZnS (emission max. at 630 nm), CdSe (emission max. at 580 nm) QDs in chloroform were spotted on thin glass coverslips (Glaswarenfabrik Karl Hecht, GmbH & Co KG, 22 x 22 mm), and 15 μL of mounting medium (TDE; thiodiethanol) was added on another thin cover glass (Deckgläser, 24 x 60 mm) to match the difference of refractive indices. Subsequently, the samples were sandwiched by the cover glasses, followed by

sealing with nail polish. The scanned area of the images was 4 μm x 4 μm (pixel size: 256 x 256), and dwell time per pixel was 200 μs. Using *ImageJ* (http://rsbweb.nih.gov/ij/, NIH, USA), image analysis and quantification of signals were performed.

B.2.5 Time-resolved fluorescence measurement for tZAIS 46 NCs and CdSe/ZnS QDs

Fluorescence lifetime was measured by conventional time correlated single photon counting (TCSPC) method. TCSPC module was combined with Nanofinder 30 (Tokyo Instruments). A 40 MHz pulsed diode laser (LDH-P-C-405 with PDL 800-B driver, Picoquant) was used at 405 nm wavelength. The repetition rates were adjusted to 2.5 MHz according to the decay time window of each sample. The detection of single photon and determination of its arrival time in the signal period were performed using an avalanche photodiode (APD) (SPCM-AQD, Perkin Elmer, USA) and a Becker–Hickl PMS module (Becker & Hickl GmbH, Germany). tZAIS 46 NCs and CdSe/ZnS QDs were dissolved in chloroform for the measurement.

B.2.6 Cell culture of breast cancer cells (HCC 1954 and MCF-7) and cell viability assay

Breast cancer cell lines of MCF-7 and HCC 1954 were purchased from American Type Culture Collection (Manassas, VA) and Korean Cell Line Bank (Seoul, Korea), respectively. For confocal fluorescence imaging and cell viability assay, breast cancer cell lines were cultured according to conventional methods with slight

modifications. RPMI 1954 (HCC 1954) or DMEM with high glucose (MCF-7), 10 % fetal bovine serum (FBS), and Streptomycin-penicillin (Invitrogen, Carlsbad, CA) were used as growth media for these cells.

For confocal fluorescence imaging, HCC 1954 was grown in a cell culture slide with four chambers (BD Biosciences, MA) for about one day. Each 10 mL of MPA-coated tZAIS 46 and 47 NCs (1.5 mg/mL in distilled H_2O) was added to 1ml of RPMI 1954 media. Each 300 mL of the solution in RPMI 1954 was added into each chamber, and the sample was incubated for a day. After the ZAIS-containing media was removed, fresh RPMI 1954 media was supplied and the cells were further incubated for about 12~24 hours in RPMI 1954 media and fixed by 10% formalin solution (neutral buffered, Sigma-Aldrich). Fixed cells were washed and stored in cold Dulbecco phosphate buffered saline (DPBS) solution.

For the cell viability assay, cells were grown in 96-well plates. Cytotoxic effect was evaluated with MTT (3-[4,5-dimethylthiazol-2-yl]-2,5-diphenyltetrazolium bromide; thiazolyl blue) viability assay. MTT assay is a standard colorimetric assay that measures the activity of live-cell enzymes that reduce MTT to insoluble purple formazan crystals. Cells were seeded on 96-well plates at a density of about 1×10^4 cells per well and treated with nanocrystals at the indicated concentrations for 24 h. 1/10 volume of MTT stock (5 mg/mL in PBS) was added and further incubated for 1 h. The medium was aspirated and 100 ml of DMSO was added to each well. After 10 min of incubation, the absorbance at 570 nm was measured. All experiments were performed in triplicate.

B.2.7 Confocal fluorescence imaging of breast cancer cells containing ZAIS NCs

For confocal imaging of HCC 1954 cells containing ZAIS NCs, an upright type laser scanning microscope was used (LSM 5 Exciter, Zeiss, Germany). Two different wavelengths (458 nm and 488 nm) from an Ar laser were utilized to illuminate the ZAIS NCs in the fixed HCC 1954 cells. Emitted fluorescence photons were passed through a dichroic mirror and a 500 long-pass filter, and were detected. The fixed cells in a cell culture slide in four chambers were scanned under an objective with a 20X magnification after the chamber frame was removed according to manufacturer's manual. 100 ~ 200 mL PBS was added to prevent the drying of the samples. A single focal plane from the Z-stacks was selected and scanned to obtain the images showing organelles.

B.3 Results and discussion

A library of tZAIS nanocrystals was synthesized by the ultrasound decomposition of precursor powders with varying ratios of the metal fractions in solid solution. The precursor powders, metal ion–diethyldithiocarbamate chelating complexes of $(Zn_xAg_yIn_z)(S_2CN(C_2H_5)_2)_4$, were dissolved in dodecylamine and treated by ultrasound for 10 min (maximum temperature reached to about 160 °C, Figure B.3), and the products were washed and retrieved by centrifugation and the final products were re-dispersed in chloroform.

The metal ratio of Ag, In, and Zn for the synthesis plays a key role in

constructing the library of tZAIS for the outlook of the emission color tuning in the $(Zn_xAg_yIn_z)S_2$ NC solid solutions. Under UV irradiation at 365 nm wavelength, all the compositions of the ternary $(Zn_xAg_yIn_z)S_2$ solid solutions were directly compared according to fluorescence emission spectra as well as absorption spectra (Figure B.1, B.4 and B.5). The initial observation of fluorescence properties of the NC library is following. As the Ag concentration increases, the emission band at 602 nm [tZAIS 64] shifts to a longer wavelength of up to 726 nm [tZAIS 46] (Figure B.1a, B.2 and B.4). Various blue-shifted colors such as yellow and green are obtained as the Zn concentration increases. In the absence of Zn, different ratios between Ag and In produce mostly red fluorescent particles whereas there is no bright color when either of the Ag or In concentrations is zero. It should be noted that the Zn concentration plays an important role in tuning the emission color of the tZAIS NCs. Most of fluorescent compositions contain less than 50% Zn and the relative emission intensities of fluorescent tZAIS NCs from Figure B.5 are plotted as shown in Figure B.6. We further analyzed a set of NCs because some cases might have emissions below 450 nm and the obtained emission spectra in the Figure B.5 do not cover this range. Those NCs are tZAIS 11, 15, 16, 21, 38, and 45. The emission range of the NCs shown in Figure B.7 is blue except tZAIS 11, that is ZnS (known to emit a violet color).[24] In the case of the tZAIS 21 and 38, the emission ranges cover a large region (400 nm~600 nm) and neither spectra shows a single Gaussian curve, indicating that there are double or multiple emission ranges. The results obtained by a series of analyses show that the tZAIS NCs forming the library

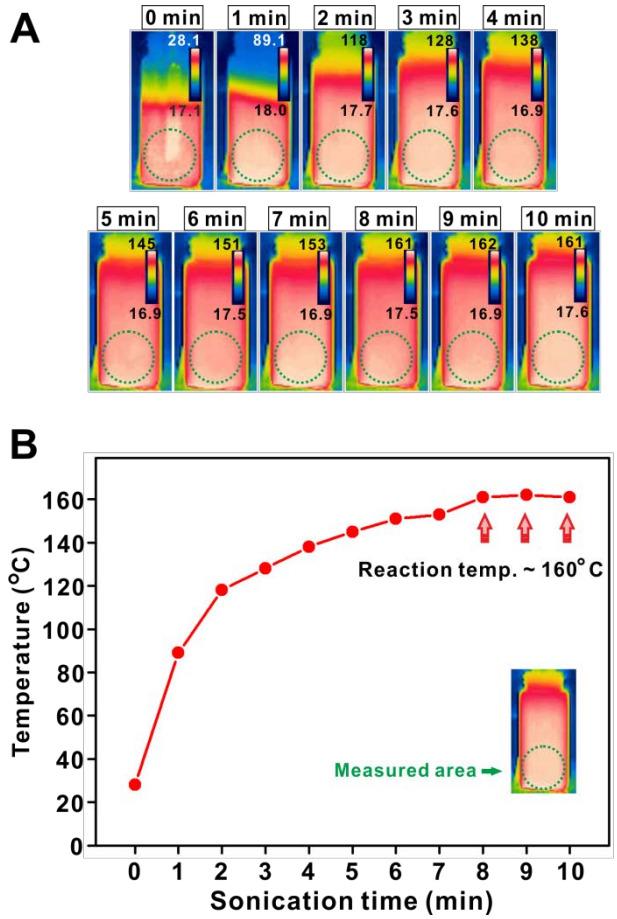

Figure B.3 Sonochemical synthesis of $(Zn_xAg_yIn_z)S_2$ NCs. A: Thermal images of the reaction vial taken by an infrared camera (FLIR T200, Sweden) for the synthesis of $(Zn_xAg_yIn_z)S_2$ NCs. Sonication in the vial increases temperature of the reaction solution up to about 160 °C. The ultrasonic irradiation time usually takes 10 min for the synthesis of $(Zn_xAg_yIn_z)S_2$ NCs. B: Temperatures of the local hot spot are plotted. Measured area (inset) is shown as a green circle. The temperature reaches 160 °C after 8 minutes of sonication (red arrows).

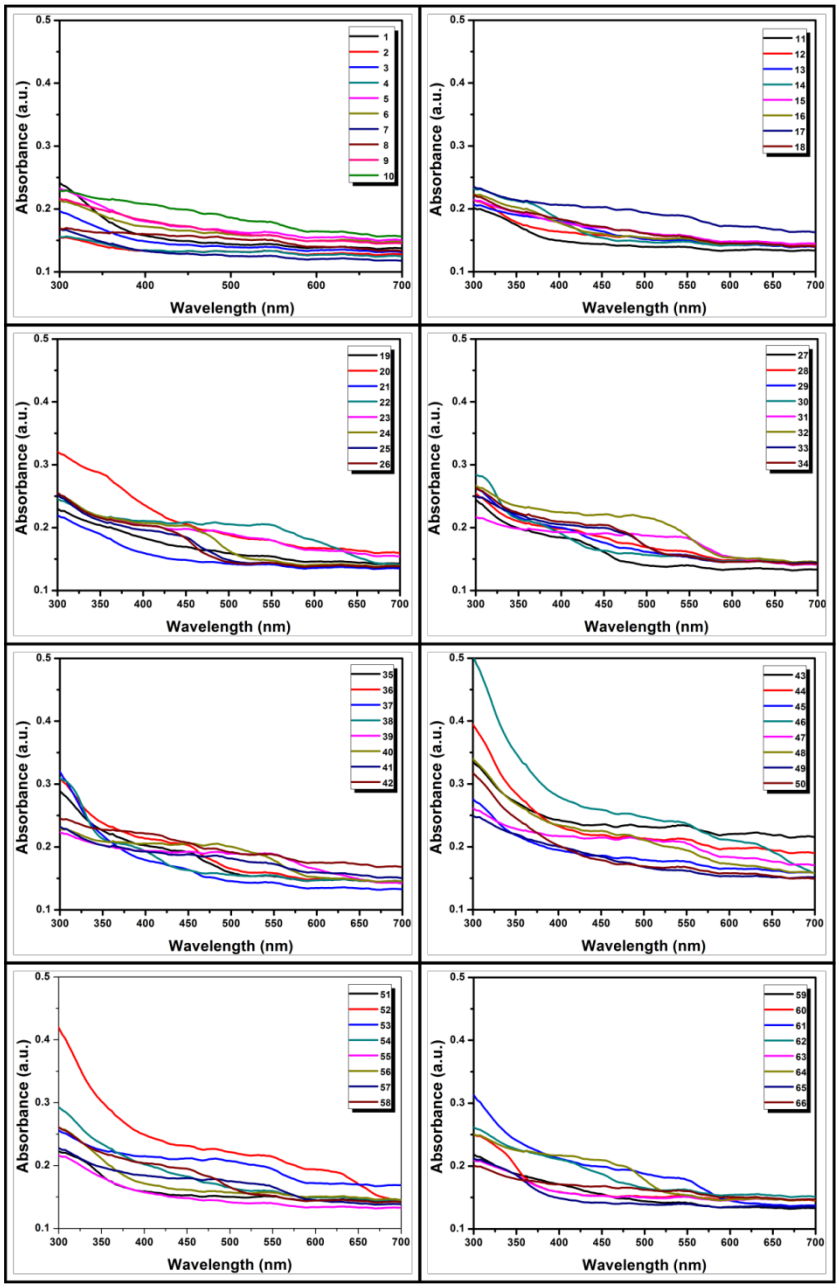

Figure B.4 UV-Vis absorption spectra of all $(Zn_xAg_yIn_z)S_2$ NCs.

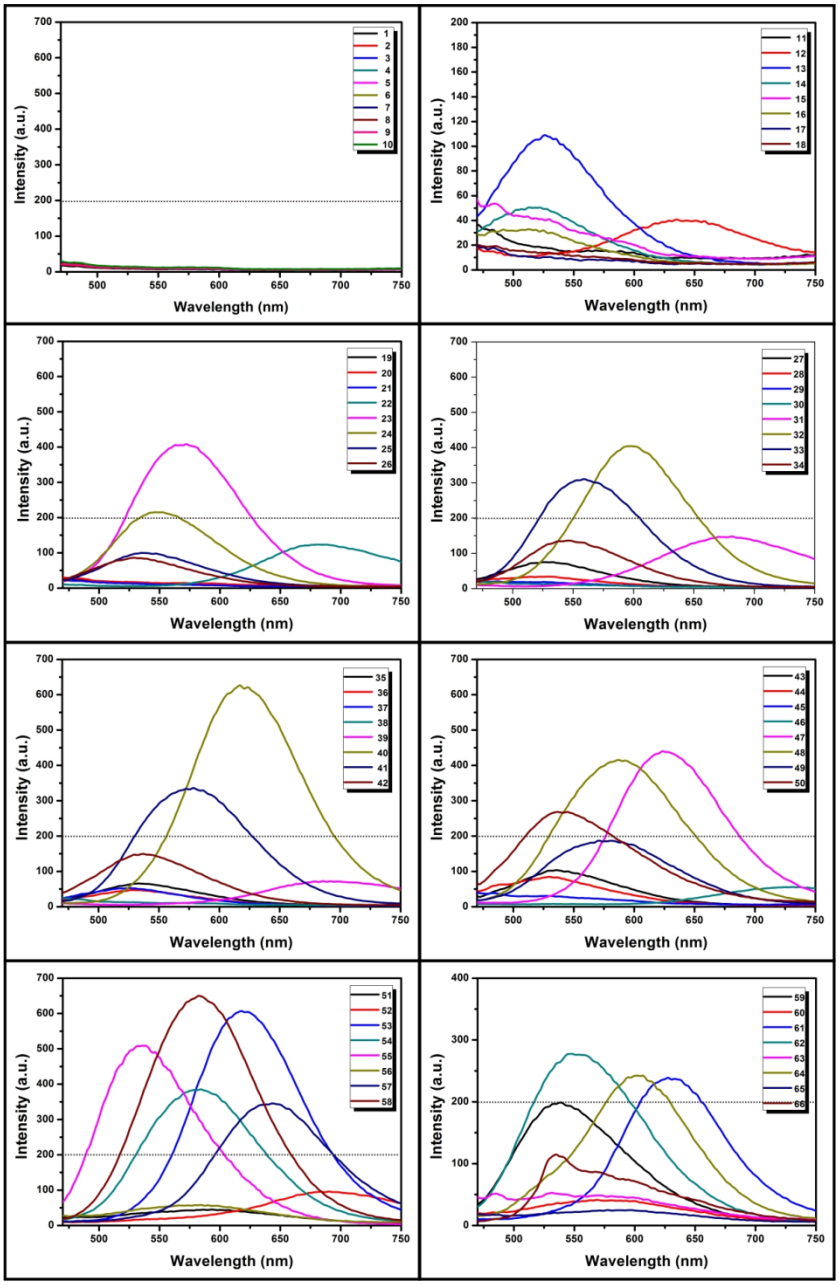

Figure B.5 Emission spectra of all $(Zn_xAg_yIn_z)S_2$ NCs by excitation at 365 nm.

can be categorized into blue, green, yellow, orange, and red fluorescent NPs, indicating that the fluorescence of the NCs covers the entire visible range. In the I–III–VI NCs system, the crystal defect by anion and cation off-stoichiometry was an important factor to determine PL emission. In the $(Zn_xAg_yIn_z)S_2$ systems, various ratios of Zn, Ag, and In composition result in an intrinsic off-stoichiometry effect which gives them the ability to induce different emission properties.[40]

Among all those fluorescent NCs, we chose two NCs, tZAIS 46 and tZAIS 47, for in-depth characterization of the tZAIS system. Transmission electron microscopy (TEM) images of tZAIS NCs clearly show their spherical shape with an average size of 3.9 nm and 4.1 nm, respectively (Figure B.8a). This suggests that changes in the composition of precursor powder do not greatly influence the size of $(Zn_xAg_yIn_z)S_2$ NCs. High-resolution TEM images show a clear lattice fringe (inset of the Figure B.8a).

The X-ray diffraction (XRD) peak positions and relative intensities of these $(Zn_xAg_yIn_z)S_2$ ($x + y + z = 1$) solid solutions show a good agreement with crystalline tetragonal $AgInS_2$. As shown in Figure B.8b, tZAIS NCs have three broad peaks at 26.4, 44.3, and 51.9, which can be assigned to the (112), (204), and (312) planes of the tetragonal $AgInS_2$ (Joint Committee on Powder Diffraction Standards (JCPDF) # 00-025-1330), and the synthesized samples did not contain any noticeable indication of other types of structures. When the Zn ion is added to change the composition from tZAIS 46 to 47, the diffraction peak positions are shifted to higher scattering angles and the main peak moves the position of the

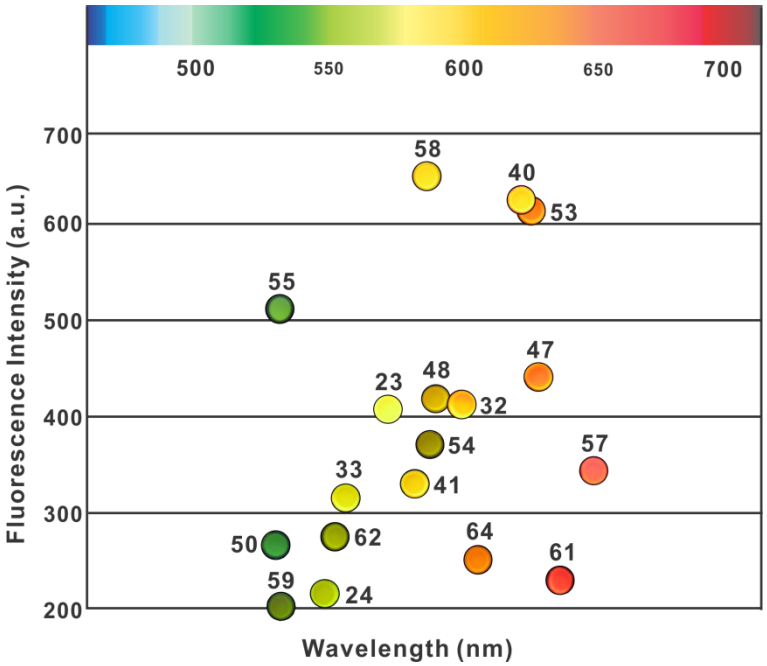

Figure B.6 Distribution of tZAIS NCs according to emission intensities and wavelengths.

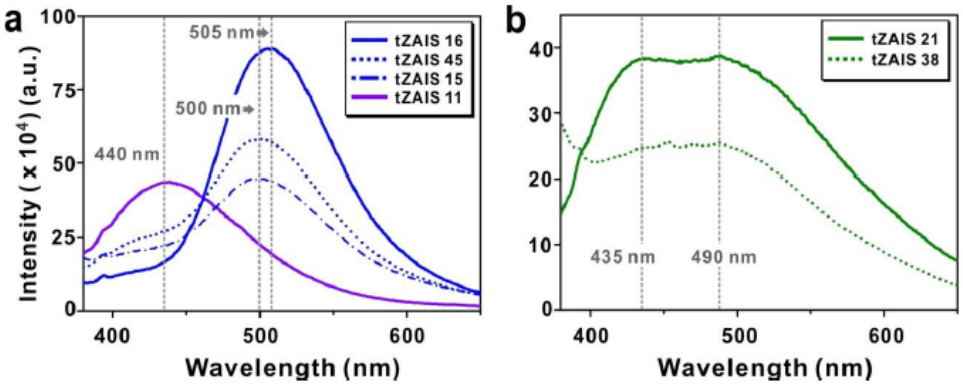

Figure B.7 tZAIS NCs with emission maxima at blue-shifted wavelength **a** and dual emission spectra **b**. Detail compositional information of blue-colored ZAIS NCs are as follows; $(Zn_1Ag_0In_0)S_2$ [tZAIS 11], $(Zn_{0.3}Ag_{0.6}In_{0.1})S_2$ [tZAIS 15], $(Zn_{0.4}Ag_{0.5}In_{0.1})S_2$ [tZAIS 16], $(Zn_{0.6}Ag_0In_{0.4})S_2$ [tZAIS 45]. ZAIS NCs with double or multiple emission maxima are $(Zn_{0.9}Ag_0In_{0.1})S_2$ [tZAIS 21], $(Zn_{0.7}Ag_0In_{0.3})S_2$ [tZAIS 38].

cubic ZnS phase (JCPDF; # 01-072-4841) peak.[18] For confirmation of the presence or absence of the Zn element, we used energy dispersive X-ray spectroscopy. As shown in Figure B.8c, tZAIS 46 NCs did not show the Zn element, whereas tZAIS 47 NCs do show the Zn element (inset figure in Figure B.8c). The PL quantum yields of tZAIS 46 and 47 were measured by comparing the integrated emission of NC samples with that of Rhodamine 6G. The PL quantum yields of the tZAIS 46 and 47 were found to be 11 and 20.9%, respectively.[40]

To evaluate ZAIS NCs as a bioimaging probe, we compared the photophysical properties of tZAIS 46 NCs with commercially available CdSe/ZnS QDs (Figure B.9). Single nanocrystals were imaged using a home-built confocal microscope system, and the feasibility of the NCs as bright, stable and trackable fluorophores was assessed to meet the current need in the bioimaging field.[25–27] According to our analysis, as shown in Figure B.10 and B.11, the fluorescence intensity of single tZAIS 46 NCs is higher than CdSe/ZnS QDs (emission maxima of both NCs are 630 nm) and apparently there are no typical phenomena of photoblinking, different from that of CdSe/ZnS QDs[28,29] (QDs in the blinking state are marked with white spotted circles, Figure B.10b). The fluorescence intensity-wise distribution of individual tZAIS 46 NCs and QDs at 488 nm excitation were plotted in Figure B.11 by particle-by-particle measurement. (Total intensity of each nanocrystal was calculated by multiplying area and mean intensity using *ImageJ*.) Distribution of the total 135 nanocrystals proves that tZAIS NCs were much brighter than CdSe/ZnS QDs at 488 nm excitation. We further evaluated the lifetime of these two NCs by

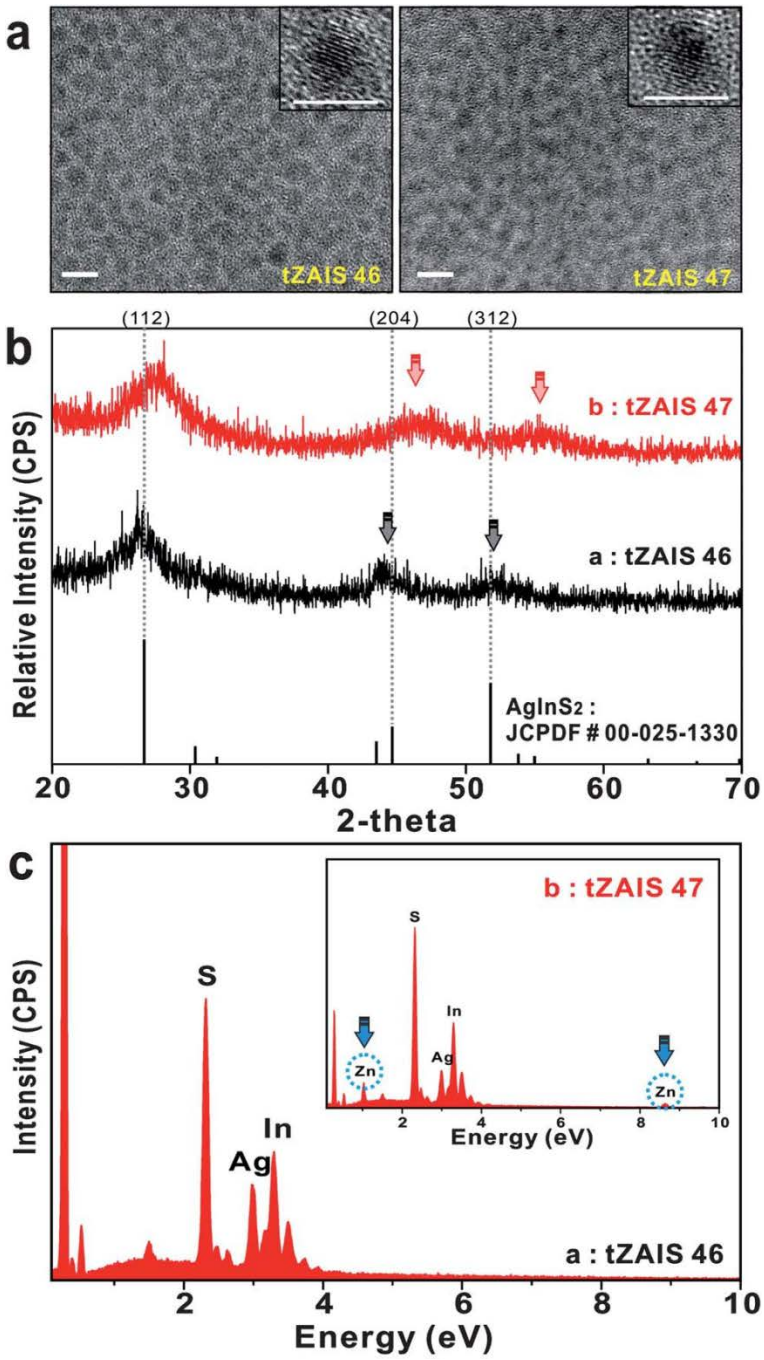
a
tZAIS 46
tZAIS 47
b
(112)
(204)
(312)
b : tZAIS 47
a : tZAIS 46
AgInS2 :
JCPDF # 00-025-1330
Relative Intensity (CPS)
20
30
40
50
60
70
2-theta
c
b : tZAIS 47
S
In
Ag
Zn
Zn
2
4
6
8
10
Energy (eV)
Intensity (CPS)
S
In
Ag
a : tZAIS 46
2
4
6
8
10
Energy (eV)

Figure B.8 Assessment of size and composition of tZAIS NCs (a) TEM images of $(Zn_xAg_yIn_z)S_2$ NCs for tZAIS 46(left) and tZAIS 47(right). Diameter of tZAIS 46 and 47 is about 3.9 nm and 4.1 nm, respectively (Scale bar: 10 nm). Size distributions of both NCs are apparently homogeneous. Both tZAIS NCs show high crystallinity (inset; scale bar = 5 nm). (b) X-ray diffraction patterns of tZAIS 46 and tZAIS 47 (46: $(Zn_0Ag_{0.5}In_{0.5})S_2$, 47: $(Zn_{0.1}Ag_{0.4}In_{0.5})S_2$). CPS stands for count per second, and tZAIS 47's peaks are shifted to higher scattering angle positions due to the increase of Zn component while tZAIS 46's peaks are exactly matched with reference peaks of $AgInS_2$. (c) Energy Dispersive X-ray Spectroscopy (EDS) data of tZAIS 46 and 47. The EDS data clearly show presence of Zn element for tZAIS 47.

time-correlated single photon counting (TCSPC).[30,31] Compared to lifetimes for CdSe/ZnS QDs (22.1 ns: 65.2%, 9.1 ns: 34.8%) as reported,[32] tZAIS 46 NCs show much longer decay times (290.5 ns: 91.1%, 9.1 ns: 8.9%) in Figure B.12. In addition, we analyzed the emitted photon trajectories from a single tZAIS NC and a CdSe/ZnS QD. tZAIS NC didn't show a dark state transition by blinking its intensity level, whereas CdSe/ZnS showed clear fluorescence intermittency from photophysical transitions between 'dark' states and 'bright' states (Figure B.13). Moreover, the amount of photons in a certain time unit (intensity) of single tZAIS 46 NC was 7~10 times higher than single CdSe/ZnS QD, which supports the analysis of the confocal images in Figure B.10. Overall, tZAIS NCs exhibit excellent properties suitable for single nanoparticle imaging, such as superior fluorescent intensity and strong stability without photoblinking. Furthermore, the longer lifetimes can be applied as a probe for fluorescence lifetime imaging[33] and characterization of detailed dynamic states.[34] Like QDs, the broad emission range is an intrinsic property of solid solution-based NCs (Figure B.9). Nevertheless, different NCs could be distinguished by the selection of proper band-pass filters to detect narrow emission ranges, thereby permitting multi-color imaging.[35,36]

We produced the water-soluble tZAIS nanocrystals by a ligand exchange method with 3-mercaptopropionic acid (MPA) (Figure B.14a)[37] because the water solubility is a prerequisite for biological applications. Figure B.1b and B.1c show the photoluminescence spectra and fluorescence images of the watersoluble MPA-tZAIS NCs ((a) $(Zn_{0.4}Ag_{0.1}In_{0.5})S_2$, (b) $(Zn_{0.3}Ag_{0.2}In_{0.5})S_2$, (c) $(Zn_{0.2}Ag_{0.3}In_{0.5})S_2$,

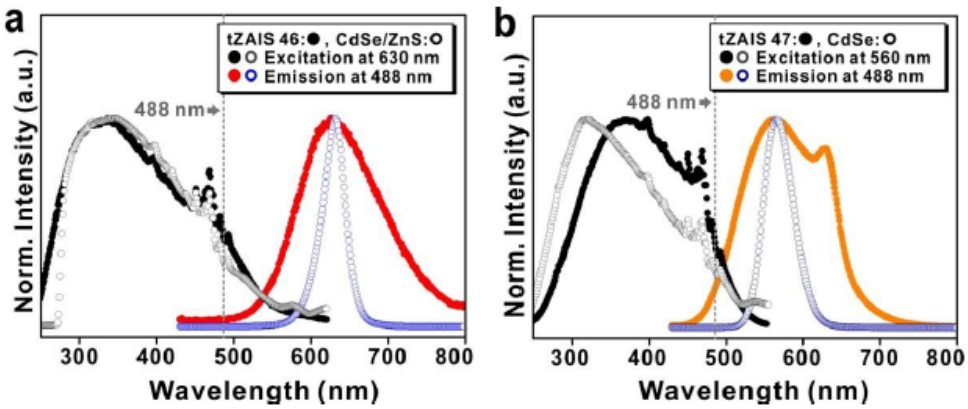

Figure B.9 Excitation and emission spectra of tZAIS 46 and CdSe/ZnS **a** and tZAIS 47 and CdSe **b**. Closed circles represent spectra of ZAIS NC and open circles show QD's spectra (CdSe/ZnS and CdSe). Excitation wavelengths (Black/white circles) were scanned at a fixed emission wavelength either at 630 nm **a** or at 560 nm **b.** All emission wavelength scans (the colored circles) were obtained at 488 nm excitation. All photoluminescence spectra were normalized.

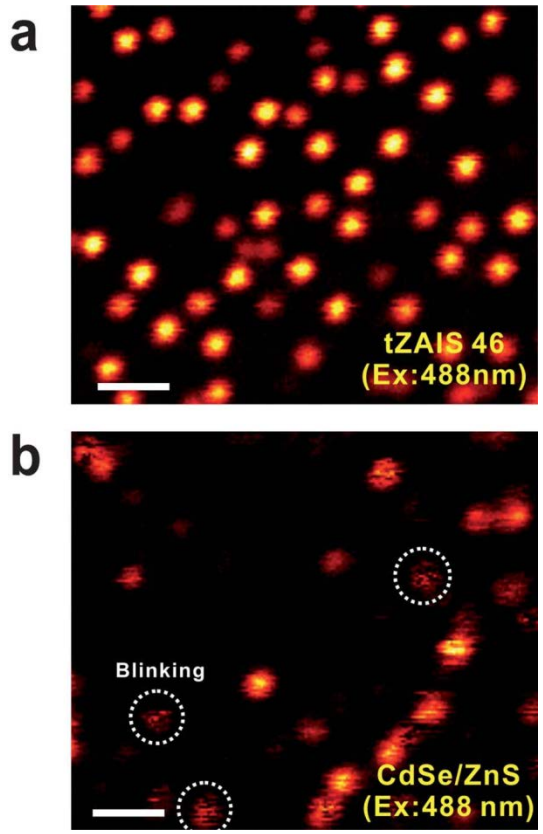

Figure B.10 Confocal images of single ZAIS nanocrystals (NC) (a) and single quantum dots (b). tZAIS 46 NCs exhibit much stronger intensity, compared to CdSe/ZnS QDs when these NCs were excited by laser light at 488 nm and emitted photons were collected through a 500 nm long-pass filter. Both ZAIS NCs and QDs have emission maxima at 630 nm. Scale bar: 500 nm.

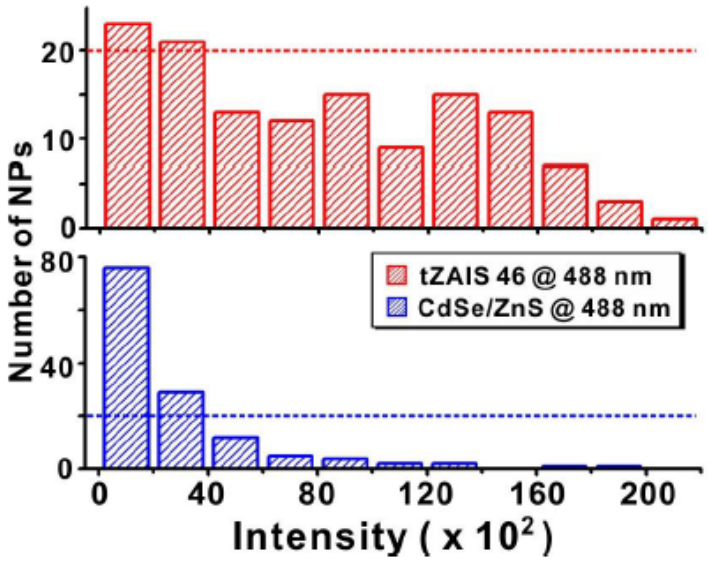

Figure B.11 Histogram of intensity distributions for single tZAIS 46 (top) and QD (bottom) at 488 nm excitation. Intensity of single NCs was calculated by multiplying mean intensity and defined area using *ImageJ*. The total numbers of analyzed particles were 135.

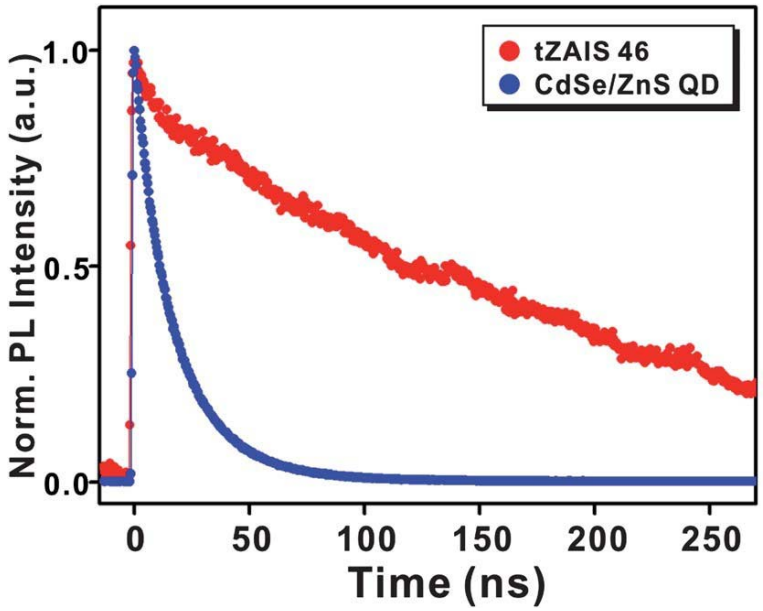

Figure B.12 Photoluminescence decay of tZAIS 46 NCs (red) and CdSe/ZnS QDs (blue). Lifetimes of tZAIS 46 NCs are 290.5 ns (91.1%) and 6.0 ns (8.9%). Lifetimes of CdSe/ZnS QDs are 22 ns (65.2%) and 9.1 ns (34.8%).

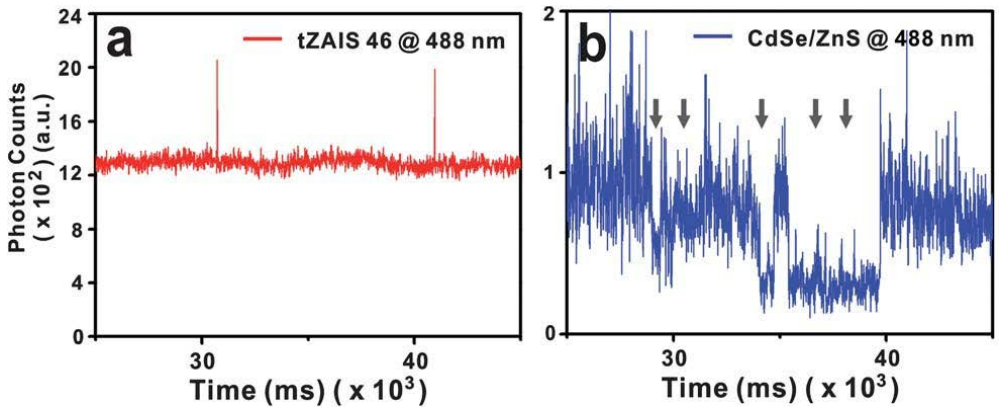

Figure B.13 Photon trajectories from (**a**) single tZAIS 46 NC and (**b**) CdSe/ZnS QD. The intensity of tZAIS 46 is 7~10 times higher than the one of QD. No photoblinking was seen from tZAIS 46 NC during 160 second acquisition time, different from CdSe/ZnS QD (gray arrows) .

(d) $(Zn_{0.1}Ag_{0.4}In_{0.5})S_2$, (e) $(Zn_0Ag_{0.5}In_{0.5})S_2$). Once the ligand exchange is carried out, the NCs become soluble in aqueous solution. We found that although most of the NCs are soluble, the solubility appears to be influenced by the presence of Zn in the NCs. For example, the MPA-coated tZAIS 47-50 are stable for months while tZAIS 46 shows a slow decay of the solubility. Perhaps, the interaction between Zn and thiol may play an important role for the ligand exchange and stability. The resulting NCs are analyzed by agarose gel electrophoresis. The negative charge in MPA on the NCs allows them to be run in the gel and UV illumination visualizes the NCs in the gel. Figure B.14b shows that NCs from tZAIS 46 to 49 are mobile in the electric field and are visualized simply by illumination at 365 nm by a handheld lamp.

To check the possibility of the NCs being applied to a cell-based assay system, the MPA-coated ZAIS NCs were introduced into breast cancer cells (HCC 1954) and confocal images with a single Z focal plane from Z-stack images were obtained (Figure B.15 and B.16). In some cases (Figure B.15a), ZAIS NPs were spread into the cytoplasm and nucleus. During the cell-fixation process, ZAIS NCs seemed to diffuse into the cytoplasm and nucleus. In the other cases (Figure B.15b), apparently the ZAIS NCs were trapped in vesicles such as endosomes, and located in the endoplasmic reticulum (ER) or Golgi organelles, indicating that the tZAIS NCs can be utilized as cell imaging fluorophores to clearly visualize detailed cellular organelles in a specific image plane of confocal microscope.

Fluorophores for biological applications have to meet multiple requirements such as excellent photophysical properties, a facile functionalization scheme for

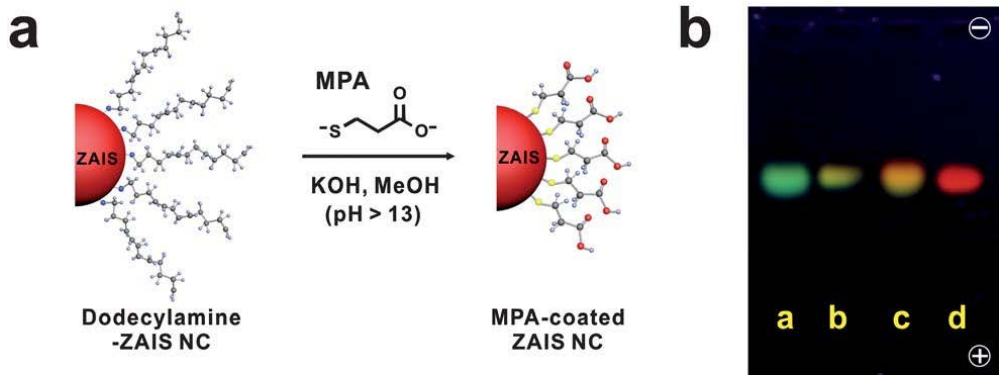

Figure B.14 (a) Preparation scheme of water-soluble tZAIS nanocrystal using 3-mercaptopropionic acid (MPA) (b) Electrophoretic analysis of water-soluble tZAIS nanocrystals on 0.8% agarose gel in Tris-borate-EDTA (TBE) buffer. lane a, tZAIS 49; lane b, tZAIS 48; lane c, tZAIS 47; lane d, tZAIS 46.

biomolecule attachment and biocompatibility without having any severe toxicity. The tZAIS NCs are photophysically suitable for in vitro assay and cell imaging, and can be applicable even to imaging in small animals.[35,38] Nevertheless, an additional concern regarding toxicity needs to be addressed. Thus, we evaluated the dosedependent cytotoxicity of the $(Zn_xAg_yIn_z)S_2$ NCs at a series of different concentrations of the NCs. To assess the cytotoxic effect of the water-soluble $(Zn_xAg_yIn_z)S_2$ NCs, we tested various concentrations (two-fold serial dilutions starting from 200 g/ml of tZAIS) of each sample for a cell viability 3-[4,5-dimethylthiazol-2-yl]-2,5-diphenyltetra zolium bromide (MTT) assay.[39] The result shows that the toxicity of each of the $(Zn_xAg_yIn_z)S_2$ NCs (tZAIS 46 and 47) was not found on two cell types (HCC 1954 and MCF-7) treated with the NCs after 24 hour post addition (Figure B.17 and B.18).

B.4 Conclusion

In conclusion, we have successfully constructed a library of $(Zn_xAg_yIn_z)S_2$ nanocrystals containing less-toxic elements (Zn, Ag, and In) by the sono-combichem method. The ultrasoundbased ZAIS nanocrystal synthesis can be utilized as a novel, simple and rapid method for creating a library of $(Zn_xAg_yIn_z)S_2$ NCs. The emission colors of the resulting NCs are tunable from blue to red, depending on their chemical composition. According to our characterization, the tZAIS NCs seem much brighter than QDs by up to about 10 times and more photostable due to their lack of photoblinking. Perhaps those are the most important

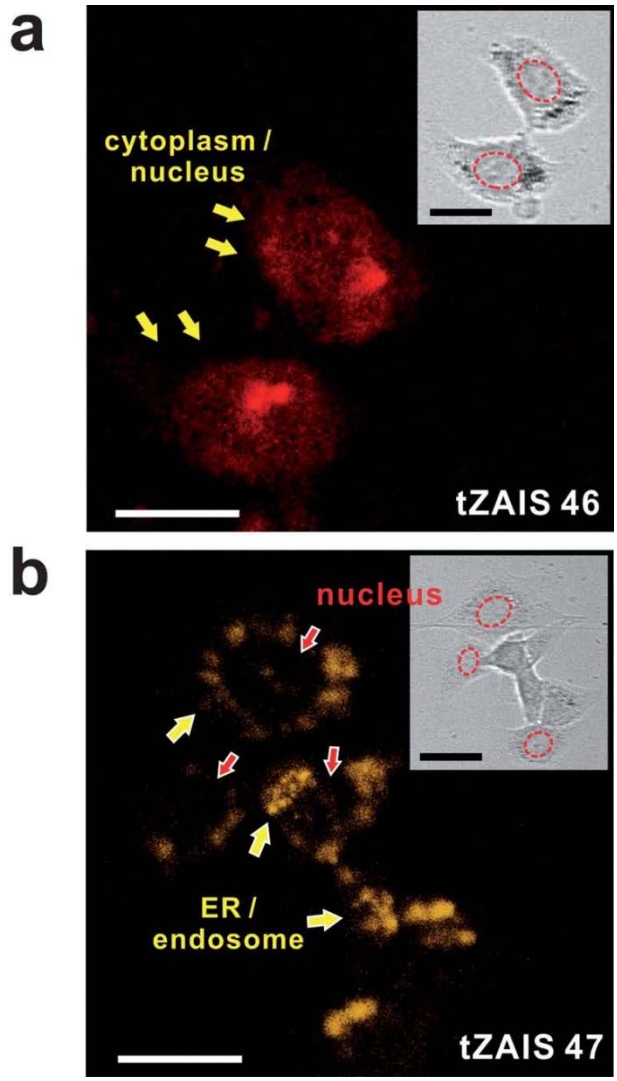

Figure B.15 Confocal images of breast cancer cells (HCC1954) containing (a) tZAIS 46 and (b) tZAIS 47. Internalized NCs into cells spread out in cytoplasm (a) or were confined in endosomes or ER (b). The insets show bright field images of the cells. The red-dotted circles denote nucleus. Scale bar: 50 μm

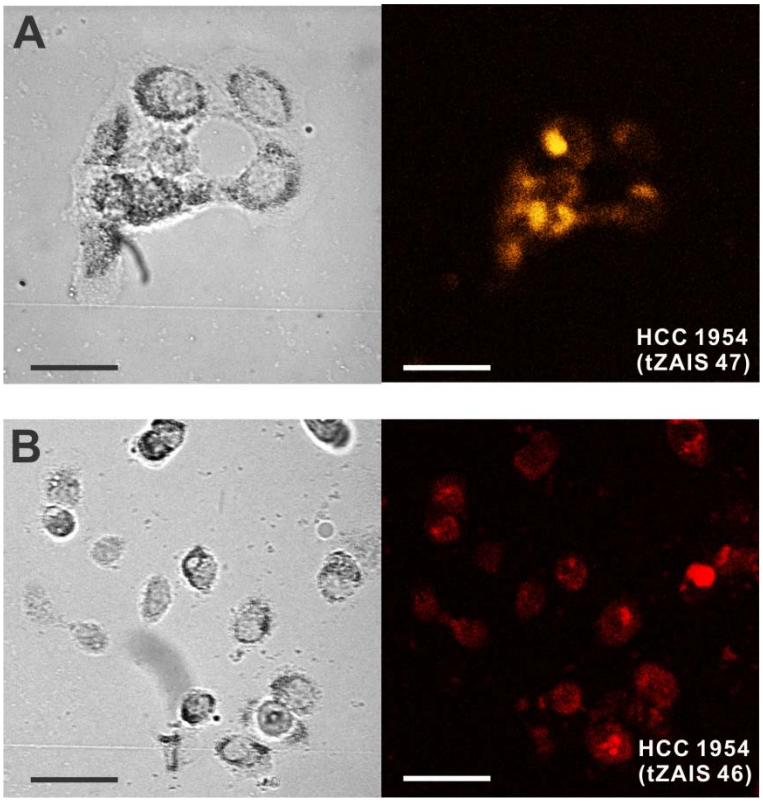

Figure B.16 Confocal fluorescence images of HCC 1954 cells containing (A) tZAIS 47 NCs and (B) tZAIS 46 NCs. Left panels show bright field images and right panels are confocal fluorescence images. Scale bar: 50 μm).

features of these NCs because they allow for more reliable fluorescence studies including single particle tracking. Their compact sizes of about 4 nm, regardless of the emission colors, can also be an added value as fluorescence probes. Moreover, tZAIS NCs are non-toxic to cells as evidenced using two cell types, HCC-1954 and MCF-7, thereby showing a feasibility of their use for bioimaging. In addition, the library of $(Zn_xAg_yIn_z)S_2$ NCs could assist in photocatalysts, quantum dot-like solar cells applications and other relevant areas.

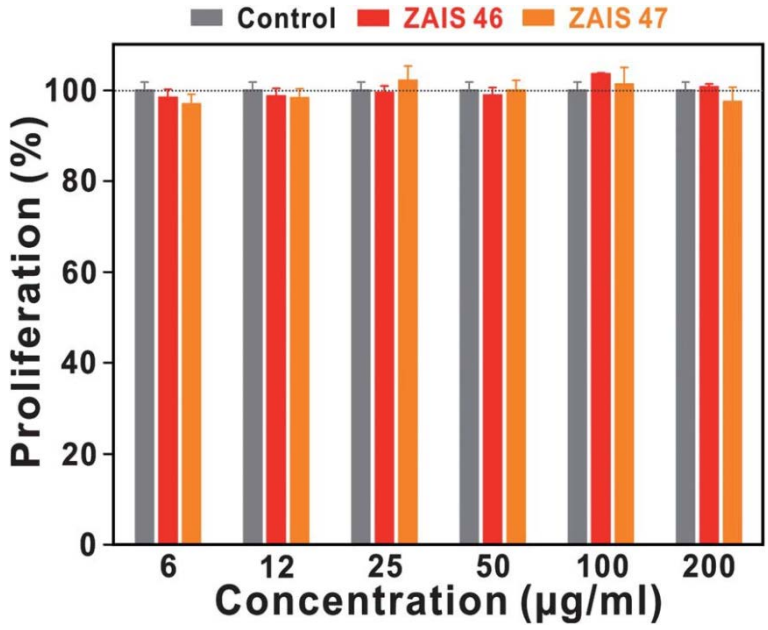

Figure B.17 MTT cell viability assay was performed to check the cell viability and cytotoxicity of tZAIS nanocrystals. There is no cytototoxic effect up to 200 µg/mL concentrations. All data are presented as mean SD. (tZAIS 46: $(Zn_0Ag_{0.5}In_{0.5})S_2$, tZAIS 48: $(Zn_{0.2}Ag_{0.3}In_{0.5})S_2$, tZAIS 50: $(Zn_{0.4}Ag_{0.1}In_{0.5})S_2$)

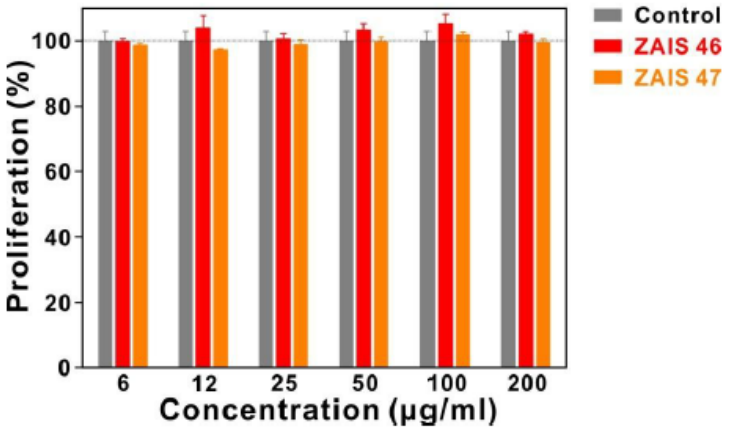

Figure B.18 MTT cell viability assay of breast cancer cells (MCF-7) in various concentration range of the $(Zn_xAg_yIn_z)S_2$ NCs. Cells are viable and there is no apparent cytotoxic effect up to 200 µg/mL of the NCs.

B.5 References

(1) Murphy, C. J. *Anal. Chem*. **2002**, *74*, 520 A.

(2) Kamat, P. V. *J. Phys. Chem*. C **2008**, *112*, 18737.

(3) Bhattacharya, P.; Ghosh, S.; Stiff-Roberts, A. *Annu. Rev. Mater. Res*. **2004**, *34*, 1.

(4) Klimov, V.; Mikhailovsky, A.; Xu, S.; Malko, A.; Hollingsworth, J.; Leatherdale, C.; Eisler, H.-J.; Bawendi, M. *Science* **2000**, *290*, 314.

(5) Bruchez, M.; Moronne, M.; Gin, P.; Weiss, S.; Alivisatos, A. P. *Science* **1998**, *281*, 2013.

(6) Bae, P. K.; Kim, K. N.; Lee, S. J.; Chang, H. J.; Lee, C. K.; Park, J. K. *Biomaterials* **2009**, *30*, 836.

(7) Michalet, X.; Pinaud, F.; Bentolila, L.; Tsay, J.; Doose, S.; Li, J.; Sundaresan, G.; Wu, A.; Gambhir, S.; Weiss, S. *Science* **2005**, *307*, 538.

(8) Medintz, I. L.; Uyeda, H. T.; Goldman, E. R.; Mattoussi, H. *Nat. Mater*. **2005**, *4*, 435.

(9) Hardman, R. Environ. *Health Perspectives* **2006**, *114*, 165.

(10) Li, L.; Reiss, P. *J. Am. Chem. Soc*. **2008**, *130*, 11588.

(11) Xu, S.; Kumar, S.; Nann, T. *J. Am. Chem. Soc*. **2006**, *128*, *1054*.

(12) Park, J.; Kim, S.-W. *J. Mater. Chem*. **2011**, *21*, 3745.

(13) Wang, X.; Pan, D.; Weng, D.; Low, C.-Y.; Rice, L.; Han, J.; Lu, Y. *J. Phys. Chem. C* **2010**, *114*, 17293.

(14) Zhong, H.; Zhou, Y.; Ye, M.; He, Y.; Ye, J.; He, C.; Yang, C.; Li, Y. *Chem. Mater*. **2008**, *20*, 6434.

(15) Hamanaka, Y.; Ogawa, T.; Tsuzuki, M.; Kuzuya, T. *J. Phys. Chem. C* **2011**, *115*, 1786.

(16) Torimoto, T.; Ogawa, S.; Adachi, T.; Kameyama, T.; Okazaki, K.-i.; Shibayama, T.; Kudo, A.; Kuwabata, S. *Chem. Comm*. **2010**, *46*, 2082.

(17) Uematsu, T.; Taniguchi, S.; Torimoto, T.; Kuwabata, S. *Chem. Comm.* **2009**, *48*, 7485.

(18) Torimoto, T.; Adachi, T.; Okazaki, K.-i.; Sakuraoka, M.; Shibayama, T.; Ohtani, B.; Kudo, A.; Kuwabata, S. *J. Am. Chem. Soc*. **2007**, *129*, 12388.

(19) Suslick, K. S. *Science* **1990**, *247*, 1439.

(20) Lee, S. J.; Kim, K. N.; Bae, P. K.; Chang, H. J; Kim, Y.-R.; Park, J. K. *Chem. Comm*. **2008**, *43*, 5574.

(21) Tian, L.; Vittal, J. J. *New J. Chem*. **2007**, *31*, 2083.

(22) Liu, G.; Liu, C.; Bard, A. J. *J. Phys. Chem. C* **2010**, *114*, 20997.

(23) Nairn, J. J.; Shapiro, P. J.; Twamley, B.; Pounds, T.; Von Wandruszka, R.; Fletcher, T. R.; Williams, M.; Wang, C.; Norton, M. G. *Nano Lett*. **2006**, *6*, 1218.

(24) Song, H.; Leem, Y.-M.; Kim, B.-G.; Yu, Y.-T. *J. Phys. Chem. Sol*. **2008**, *69*, 153.

(25) Pons, T.; Mattoussi, H. *Ann. Biomed. Eng*. **2009**, *37*, 1934.

(26) Ruthardt, N.; Lamb, D. C.; Bräuchle, C. *Mol. Ther*. **2011**, *19*, 1199.

(27) Pierobon, P.; Cappello, G. *Adv. Drug Deliver. Rev*. **2012**, *64*, 167.

(28) Mahler, B.; Spinicelli, P.; Buil, S.; Quelin, X.; Hermier, J.-P.; Dubertret, B. *Nat. Mater*. **2008**, *7*, 659.

(29) Wang, X.; Ren, X.; Kahen, K.; Hahn, M. A.; Rajeswaran, M.; Maccagnano-Zacher, S.; Silcox, J.; Cragg, G. E.; Efros, A. L.; Krauss, T. D. *Nature* **2009**, *459*, 686.

(30) Kuno, M.; Fromm, D.; Hamann, H.; Gallagher, A.; Nesbitt, D. *J. Chem. Phys*. **2001**, *115*, 1028.

(31) Becker, W.; Hickl, H.; Zander, C.; Drexhage, K.; Sauer, M.; Siebert, S.; Wolfrum, J. *Rev. Sci. Instrum*. **1999**, *70*, 1835.

(32) Fisher, B. R.; Eisler, H.-J.; Stott, N. E.; Bawendi, M. G. *J. Phys. Chem. B* **2004**, *108*, 143.

(33) Chang, C. W.; Sud, D.; Mycek, M. A. *Method.Cell Biol*. **2007**, *81*, 495.

(34) Talaga, D. S. *J. Phys. Chem. A* **2009**, *113*, 5251.

(35) Kosaka, N.; Ogawa, M.; Sato, N.; Choyke, P. L.; Kobayashi, H. *J. Invest. Dermatol*. **2009**, *129*, 2818.

(36) Han, M.; Gao, X.; Su, J. Z.; Nie, S. *Nat. Biotechnol*. **2001**, *19*, 631.

(37) Pong, B.-K.; Trout, B. L.; Lee, J.-Y. *Langmuir* **2008**, *24*, 5270.

(38) Gao, X.; Cui, Y.; Levenson, R. M.; Chung, L. W.; Nie, S. *Nat. Biotechnol*. **2004**, *22*, 969.

(39) Jung, J.; Solanki, A.; Memoli, K.; Kamei, K.; Kim, H. *Angew. Chem. Int. Ed*. **2010**, *49*, 103.

(40) Chen, B.; Zhong, H.; Zhang, W.; Tan, Z. A.; Li, Y.; Yu, C.; Zhai, T.; Bando, Y.; Yang, S.; Zou, B. *Adv. Funct. Mater*. **2012**, *22*, 2081.

Appendix C. Associative electron attachment to 2-aminopyridine-$(CO_2)_1$ complex: photoelectron spectroscopic and theoretical approach

C.1 Introduction

Carbon dioxide is a very inert molecule whose reactivity is low at room temperature. It does not make a stable anion in the gas phase since it has a negative adiabatic electron affinity (AEA).[1] Instead, it becomes a metastable anion with quite a long lifetime (< 100 μs) when it adopts a bent geometry which differs greatly from the geometry of the neutral species.[2,3] Clusters of carbon dioxide molecules have been extensively studied using photoelectron spectroscopy and theoretical calculations. DeLuca *et al*. and Tsukuda *et al*. found that core switching occurred in $(CO_2)_n^-$.[4,5] Clusters of CO_2 and H_2O, CO_2 and CH_3OH and CO_2 and atomic halide anions were also studied, and showed interesting properties.[6,7] Furthermore, the existence of $[O_2\text{-}CO_2]^-$ and $[Au\text{-}CO_2]^-$ were indirectly observed from IR spectrum that showed a red shift in asymmetric stretch and combination bands of asymmetric stretch with other vibrational frequencies.[8,9]

The most remarkable behavior observed, however, was the "associative electron attachment" to a neutral van der Waals complex, resulting in a new covalent bond being formed between the neutral molecule and CO_2 upon electron attachment. S. Y. Han *et al*. studied the associative electron attachment to $[(pyridine)_{1\text{-}6}\text{-}(CO_2)_{1\text{-}3}]$[10] and S. H. Lee *et al*. extended this study to whole azabenzene-$(CO_2)_n$ complexes.[11] Among the three diazine molecules (pyridazine, pyrimidine and pyrazine), pyridazine (Pd) formed only one covalent bond with two CO_2 molecules upon electron attachment due to the steric hindrance from the pre-existing CO_2 moiety

while the other two diazine molecules formed two stepwise formations of a covalent bond with the large electron binding energy shift (~2 eV). Here, we studied the 2-aminopyridine (2AP), which is analogous to [Pd-$(CO_2)_1$]. We compared the behavior of the [2AP-$(CO_2)_1$] van der Waal complex upon electron attachment to [Pd-$(CO_2)_2$]$^-$.

C.2 Experiment

The details of our experimental scheme have been described elsewhere.[12] A [2AP-$(CO_2)_1$]$^-$ complex anion was generated using a molecular beam apparatus with pulsed solenoid valve. The mixture of the evaporated 2AP and CO_2 (1.5 bar) gas was co-expanded with Ar carrier gas (4 bar) through the nozzle. The resulting van der Waals complex captured a low energy secondary electron which was generated by electron impact (400 eV, 200 μA). A Wiley-McLaren type time-of-flight mass spectrometer (TOF-MS) was used to separate the different anions by their masses. The mass-selected [2AP-$(CO_2)_1$]$^-$ anions were then irradiated by second harmonic output (532 nm, 2.33 eV) of a pulsed Nd:YAG laser in order to eject photoelectrons. The photoelectrons were collected using a magnetic-bottle type photoelectron spectrometer, and the electron kinetic energy was converted to electron binding energy by subtracting it from the photon energy.

C.3 Results and discussion

Figure C.1 shows the photoelectron spectrum of [2AP-$(CO_2)_1$]$^-$ obtained at 532 nm

with a single, broad featureless band which is evidence of the formation of a valence band anion. Surprisingly, $[2AP\text{-}(CO_2)_1]^-$ shows an exceedingly high vertical detachment energy (VDE) value (1.95 eV) as opposed to $2AP^-$ which has a negative VDE according to our calculations (~-1 eV, Table C.1).[13] This phenomenon is similar to that seen in azabenzene-$(CO_2)_n$ complexes where the neutral van der Waal complexes underwent associative electron attachment resulting in a covalent bond formation.[11] In contrast to the $[Pd\text{-}(CO_2)_2]^-$ complex, 2AP could form a covalent bond regardless of its structural similarity to $[Pd\text{-}(CO_2)_1]^-$. This might be due to the reduced steric hindrance of the CO_2 molecule during the approach process. The O-O distance in the CO_2 in $[Pd\text{-}(CO_2)_1]^-$ is 2.26 Å while H-H distance in the NH_2 in 2AP is only 1.71 Å. The relatively small size of the NH_2 made the approaching CO_2 molecule feel much less repulsion due to the steric hindrance. In addition to this, the approaching CO_2 molecule was acted upon by an attractive force in the case of $[2AP\text{-}(CO_2)_1]^-$ since the H atom in the NH_2 has a partial positive charge whereas the approaching CO_2 molecule was acted upon by a repulsive force in the case of $[Pd\text{-}(CO_2)_2]^-$ since the O atom in the CO_2 has a partial negative charge. Both the B3LYP and MP2 methods underestimated the VDE values by more than 0.5 eV; however, ΔVDE (~2.2 eV) is consistent with that seen in azabenzene-$(CO_2)_n$ complex anions.

Theoretical calculations revealed the structural changes that occurred upon electron attachment (Figure C.2). First of all, the distance between the N atom in 2AP and the C atom in the CO_2 decreased from 2.884 Å to 1.514 Å indicating the

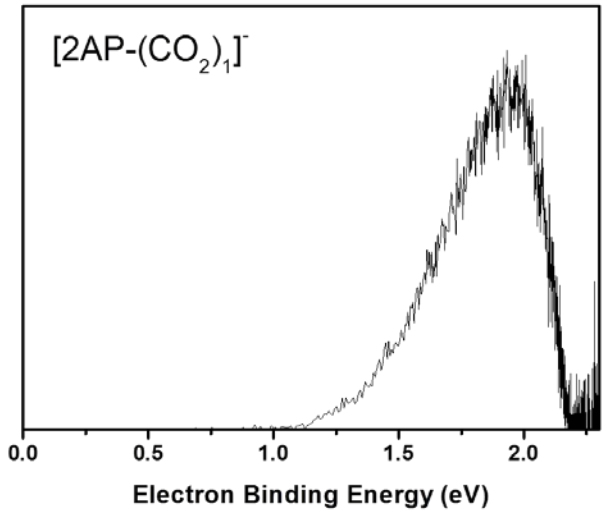

Figure C.1 Photoelectron spectrum of $[2AP\text{-}(CO_2)_1]^-$ obtained at 532 nm. Even 2AP molecule has negative VDE (~-1 eV), associative electron attachment shifts VDE more than 2 eV due to the extending of π–conjugation over the entire complexes via covalent bond formation.

	B3LYP	MP2	Experiment
n=0	-1.05 eV	-0.94 eV	N. A.
n=1	1.15 eV	1.35 eV	1.95 eV
ΔVDE	2.2 eV	2.29 eV	N. A.

Table C.1 VDE of $[2AP\text{-}(CO_2)_n]^-$, n=0 and 1 calculated at the B3LYP/6-311++G** and MP2/6-311++G** level

formation of the covalent bond. However, the C-O distance in the CO_2 increased from 1.164 Å to 1.254 Å indicating a decrease in the bond order due to the new covalent bond. Finally, the O-C-O angle decreased from 176.3° to 130.3° as was also seen in the [$(pyridine)_1$-$(CO_2)_1$] complexes.[10]

To elucidate the origin of the large VDE shift, we analyzed the charge distribution in both the neutral and anionic complexes (Figure C.2). In the neutral complex, both the 2AP and CO_2 molecules have a net charge of zero. However, the excess electron is totally delocalized to the entire anion complex to give -0.43e in 2AP and -0.57e in CO_2. This means that the π-conjugation in 2AP extended over the entire complex through a newly formed covalent bond, greatly stabilizing the anionic complex (~2 eV).

C.4 Conclusion

In conclusion, we investigated the associative electron attachment to the [2AP-$(CO_2)_1$] van der Waal complex using anion photoelectron spectroscopy and theoretical calculations. We found a covalent bond formation between 2AP and CO_2 opposite to that seen in $[Pd\text{-}(CO_2)_2]^-$ which could not form an additional covalent bond due to the steric hindrance. Excess negative charge is totally delocalized to the entire complex to give extended π–conjugation.

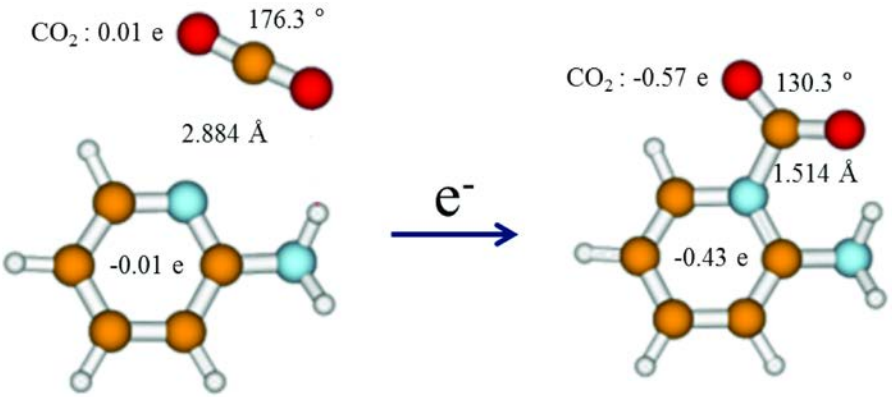

Figure C.2 Optimized geometries of neutral (left) and anionic (right) [2AP-$(CO_2)_1$] complex calculated at the B3LYP/6-311++G** level. A new covalent bond was formed between N in 2AP and C in CO_2 upon electron attachment. The distance between N and C decreased more than 1.3 Å. The O-C-O angle in CO_2 also decreased resulting in bent geometry. Note that the excess electron delocalized to the entire anion complex.

C.5 References

(1) Gutsev, G. L.; Bartlett, R. J.; Compton, R. N. *J. Chem. Phys*. **1998**, *108*, 6756.

(2) Cooper, C. D.; Compton, R. N. *Chem. Phys. Lett.* **1972**, *14*, 29.

(3) Compton, R. N.; Reinhardt, P. W.; Cooper, C. D. *J. Chem. Phys*. **1975**, *63*, 3821.

(4) DeLuca, M. J.; Niu, B.; Johnson, M. A. *J. Chem. Phys.* **1988**, *88*, 5857.

(5) Tsukuda, T.; Johnson, M. A.; Nagata, T. *Chem. Phys. Lett*. **1997**, *268*, 429.

(6) Tsukuda, T.; Saeki, M.; Kimura, R.; Nagata, T. *J. Chem. Phys*. **1999**, *110*, 7846.

(7) Arnold, D. W.; Bradforth, S. E.; Kim, E. H.; Neumark, D. M. *J. Chem. Phys*. **1995**, *102*, 3493.

(8) Schneider, H.; Boese, A. D.; Weber, J. M. *J. Chem. Phys*. **2005**, *123*, 074316.

(9) Boese, A. D.; Schneider, H.; Glöß, A. N.; Weber, J. M. *J. Chem. Phys*. **2005**, *122*, 154301.

(10) Han, S. Y.; Chu, I.; Kim, J. H.; Song, J. K.; Kim, S. K. *J. Chem. Phys*. **2000**, *113*, 596.

(11) Lee, S. H.; Kim, N.; Ha, D. G.; Kim, S. K. *J. Am. Chem. Soc*. **2008**, *130*, 16241.

(12) Song, J. K.; Lee, N. K.; Kim, J. H.; Han, S. Y.; Kim, S. K. *J. Chem. Phys*. **2003**, *119*, 3071.

(13) Frisch, M. J.; Trucks, G. W.; Schlegel, H. B.; G. E. Scuseria; Robb, M. A.; Cheeseman, J. R.; J. A. Montgomery, J.; T. Vreven; Kudin, K. N.; Burant, J. C.; Millam, J. M.; Iyengar, S. S.; Tomasi, J.; Barone, V.; Mennucci, B.; Cossi, M.; Scalmani, G.; Rega, N.; Petersson, G. A.; Nakatsuji, H.; Hada, M.; Ehara, M.; Toyota, K.; Fukuda, R.; Hasegawa, J.; Ishida, M.; Nakajima, T.; Honda, Y.; Kitao, O.; Nakai, H.; Klene, M.; Li, X.; Knox, J. E.; Hratchian, H. P.; Cross, J. B.; Adamo, C.; Jaramillo, J.; Gomperts, R.; Stratmann, R. E.; Yazyev, O.; Austin, A. J.;

Cammi, R.; Pomelli, C.; Ochterski, J. W.; Ayala, P. Y.; Morokuma, K.; Voth, G. A.; Salvador, P.; Dannenberg, J. J.; Zakrzewski, V. G.; Dapprich, S.; Daniels, A. D.; Strain, M. C.; Farkas, O.; Malick, D. K.; Rabuck, A. D.; Raghavachari, K.; Foresman, J. B.; Ortiz, J. V.; Cui, Q.; Baboul, A. G.; Clifford, S.; Cioslowski, J.; Stefanov, B. B.; Liu, G.; Liashenko, A.; Piskorz, P.; Komaromi, I.; Martin, R. L.; Fox, D. J.; Keith, T.; Al-Laham, M. A.; Peng, C. Y.; Nanayakkara, A.; Challacombe, M.; Gill, P. M. W.; Johnson, B.; Chen, W.; Wong, M. W.; Gonzalez, C.; Pople, J. A., Gaussian 03, Revision C.02; Gaussian, *Inc*: *Wallingford CT*, **2004** .

Appendix D. Photoelectron spectroscopy of 4-bromochlorobenzene dimer and trimer anions

D.1 Introduction

Clusters are the aggregates of molecules or ions which have intrinsic properties that are not found in their monomer unit.[1] Their structure and charge distribution greatly affect the properties of the clusters. Charge resonance is the key factor that determines the structure of the cation clusters of aromatic hydrocarbons.[2] T. Shida and S. Iwata also calculated the charge resonance band and observed it experimentally.[3] With advances in molecular beam apparatus and quantum calculations, anion clusters have been extensively studied.[4-6] Benzene does not form a stable dimer anion in the gas phase, and naphthalene forms a dimer anion which may have T-shaped geometry due to the strong repulsion from the π-electron.[7] Dimer anions larger than naphthalene all have parallel-displaced (PD) geometries with charge resonance.[8-10] Sometimes homocluster anions show ion core switching with the increase of the cluster size.[8]

For the heterodimer anions, the geometry is determined by the differences in electronegativity of the molecules. Dimer anions with a large electronegativity difference have T-shaped geometries and those with a small electronegativity difference have PD geometries.[11]

Bromochlorobenzene (BCB) is able to accept an extra electron even though benzene monomer cannot. We found that an excess electron entered the anti-bonding orbital formed between C and Br atoms in bromochlorobenzene monomer anion that has the character of atomic Br.[12] Thus, the electron binding energy (EBE)

is exceedingly large compared to that of other large aromatic hydrocarbon monomers. In this work, I report the photoelectron spectra and quantum calculation results for the dimer and trimer anions of 4-BCB, which are much different from those of the monomer anion.

D.2 Experiment

The details of our experimental scheme have been described elsewhere.[13] Briefly, thermally evaporated 4-BCB molecules were co-expanded with 5 bar of Ar carrier gas through a pulsed solenoid valve to generate molecular clusters. Low energy secondary electrons were generated from the ionization of Ar with high energy electron from an electron gun (400 eV, 200 μA), which attached to the neutral molecules and turned them into anions. A Wiley-McLaren type time-of-flight mass spectrometer with a mass gate was used to select anions by their mass. The anions then entered a magnetic-bottle-type photoelectron spectrometer and were irradiated by the second harmonic output (532 nm) of a pulsed Nd:YAG laser. The kinetic energy of the ejected photoelectron was measured to yield the photoelectron spectrum by subtracting it from the incident photon energy.

D.3 Results and discussion

In the mass spectrum of 4BCB cluster anions, the monomer anion has the largest peak intensity with the exception of the Br^- that comes from the dissociative

electron attachment. The dimer anion has a significant intensity while the trimer and larger clusters have a very low intensity under our experimental conditions.[12]

Figure D1 shows the photoelectron spectra (PES) of (a) $[4\text{-BCB}]_2^-$, and (b) $[4\text{-BCB}]_3^-$ obtained at 532 nm. The PES of $[4\text{-BCB}]_2^-$ is quite different from that of $[4\text{-BCB}]_1^-$ in our previous study. It seems that there is only one broad peak that stands for the new valence ion formation. The vibrational progression for the neutral dimer molecule appears in the PES with 0.05 eV energy gaps. Surprisingly, the vertical detachment energy (VDE) of the $[4\text{-BCB}]_2^-$ greatly decreased to 0.36 eV while that of the monomer anion was 2.40 eV (Table D1).[12] This drastic decrease in the VDE can be explained with the change of the ion core. In the case of the monomer anion, an electron cannot be delocalized to the benzene ring due to the strong repulsion between the approaching electron and the π–electron. Thus, the excess electron is mostly localized to the Br atom. The singly occupied molecular orbital (SOMO) is anti-bonding in nature where the atomic Br character is dominant. As a result, the VDE is quite large despite of the negative VDE of the benzene monomer anion (-1.12 eV).

In contrast, the excess electron can be delocalized over two 4-BCB molecules in $[4\text{-BCB}]_2^-$. A Mulliken charge analysis reveals that two 4-BCB molecules have -0.54e and -0.46e, respectively upon electron attachment.[14] The anion SOMO also verifies the delocalization of the excess electron throughout the entire cluster (Figure D2). The optimized geometries of the dimer are distorted PD (neutral) and T-shape (anion), respectively as seen in Figure D3.

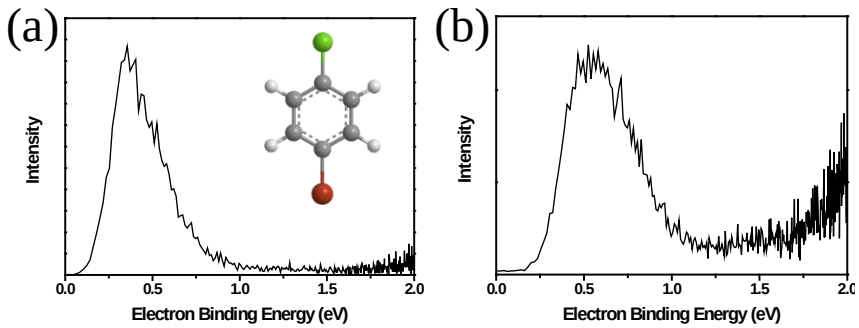

Figure D.1 Photoelectron spectra of (a) $[4\text{-BCB}]_2^-$, and (b) $[4\text{-BCB}]_3^-$ obtained at 532 nm (inset: molecular structure of the 4-BCB).

	VDE	AEA	Experiment
$[4\text{-BCB}]_2^-$	0.36 eV	0.14 eV	0.36 eV
$[4\text{-BCB}]_3^-$	0.44 eV	0.24 eV	0.53 eV

Table D.1 Vertical detachment energies (VDE) and adiabatic electron affinities (AEA) of $[4\text{-BCB}]_2^-$, and $[4\text{-BCB}]_3^-$ calculated at the B3LYP/6-31+G* level. These values were compared with the experimental VDE values.

The PES of $[4\text{-BCB}]_3^-$ is quite similar to that of $[4\text{-BCB}]_2^-$, thus allowing for the possibility that the trimer anion has a dimeric anion core. Furthermore, the VDE difference is 0.18 eV, which can be thought as the solvation effect of another 4-BCB molecule. However, the full-width at half maximum of the peak is larger than that of the dimer anion. In addition, the most stable geometry is totally different from that of the dimer anion. In both the neutral and anion states, $[4\text{-BCB}]_3$ has PD structures. Thus, the ion core of the trimer is not a dimeric core. However, delocalization of the excess electron is also expected by the Mulliken charge analysis and the SOMO of the anion. The moiety at the middle of the cluster has -0.58e and the remaining two moieties evenly share the residual negative charge (Figure D3). The SOMO is also extended to the entire cluster, thus verifying the delocalization of the excess charge (Figure D2). In addition, the nature of the electron delocalization is quite similar in the dimer and trimer anions. For both anions, most of the excess negative charge is delocalized over the benzene rings through the extended π-network (Table D2).

D.4 Conclusion

In conclusion, I investigated the electron attachment to 4-BCB dimer and trimer anions using anion photoelectron spectroscopy and theoretical calculations. I found that an excess electron can be delocalized to these clusters through extended π-network. However, the nature of the ion core is different for the dimer and trimer.

	neutral (HOMO)	anion (SOMO)
$[4\text{-BCB}]_2$	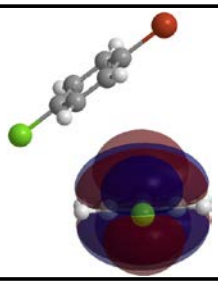	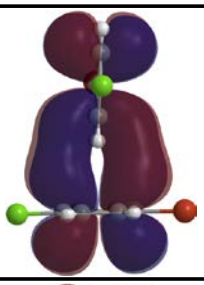
$[4\text{-BCB}]_3$	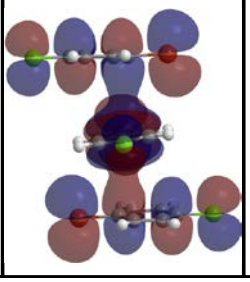	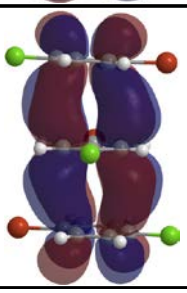

Figure D.2 HOMO (left column) and SOMO (right column) of 4-BCB clusters.

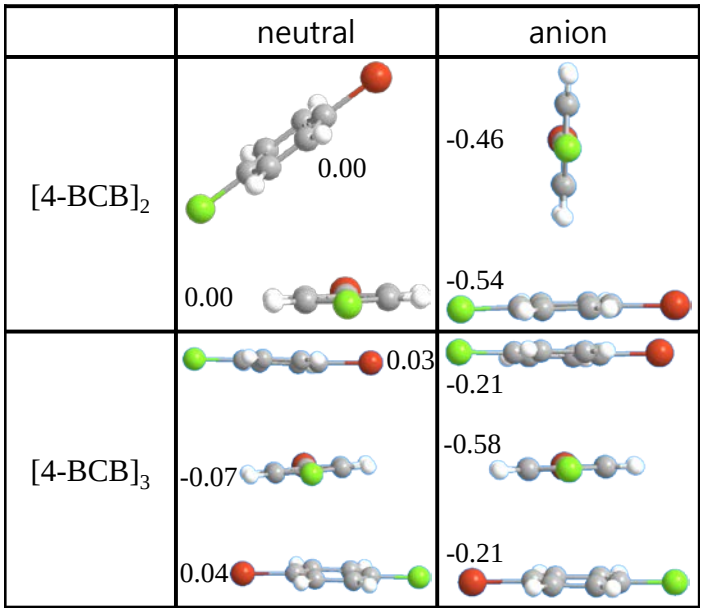

Figure D.3 Optimized geometries and Mulliken charge analysis of (a) $[4\text{-BCB}]_2^-$, and (b) $[4\text{-BCB}]_3^-$ obtained by the B3LYP/6-31+G* level of calculation.

		Cl	Ring	Br
$[4\text{-BCB}]_2^-$	neutral	0.27	0.05	-0.32
	anion	0.43	-0.97	-0.46
$[4\text{-BCB}]_3^-$	neutral	0.25	-0.31	0.06
	anion	-0.13	-0.87	0.00

Table D.2 Mulliken atomic charges for the dimer and trimer of 4-BCB calculated at the B3LYP/6-31+G* level.

D.5 References

(1) Mingos, D. M. P.; Wales, D. J. *Introduction to cluster chemistry*; Prentice Hall New York, **1990**.

(2) Bouvier, B.; Brenner, V.; Millie, P.; Soudan, J. M. *J. Phys. Chem. A* **2002**, *106*, 10326.

(3) Shida, T.; Iwata, S. *J. Am. Chem. Soc.* **1973**, *95*, 3473.

(4) Coe, J.; Lee, G.; Eaton, J.; Arnold, S.; Sarkas, H.; Bowen, K.; Ludewigt, C.; Haberland, H.; Worsnop, D. *J. Chem. Phys.* **1990**, *92*, 3980.

(5) Leopold, D. G.; Ho, J.; Lineberger, W. *J. Chem. Phys.* **1987**, *86*, 1715.

(6) von Helden, G.; Kemper, P. R.; Gotts, N. G.; Bowers, M. T. *Science* **1993**, *259*, 1300.

(7) Song, J. K.; Han, S. Y.; Chu, I.; Kim, J. H.; Kim, S. K.; Lyapustina, S. A.; Xu, S.; Nilles, J. M.; Bowen, K. H. *J. Chem. Phys.* **2002**, *116*, 4477.

(8) Song, J. K.; Lee, N. K.; Kim, S. K. *Angew. Chem. Int. Ed.* **2003**, *42*, 213.

(9) Ando, N.; Kokubo, S.; Mitsui, M.; Nakajima, A. *Chem. Phys. Lett.* **2004**, *389*, 279.

(10) Kim, J. H.; Lee, S. H.; Song, J. K. *J. Chem. Phys.* **2009**, *130*, 124321.

(11) Kim, N.; Lee, S. H. *Bull. Korean. Chem. Soc.* **2013**, *34*, 1441.

(12) Kim, N.; Sohn, T.; Lee, S. H.; Nandi, D.; Kim, S. K. *PCCP*. **2013**, *15*, 16503.

(13) Song, J. K.; Lee, N. K.; Kim, J. H.; Han, S. Y.; Kim, S. K. *J. Chem. Phys.* **2003**, *119*, 3071.(14) Frisch, M.; Trucks, G.; Schlegel, H. e. a.; Scuseria, G.; Robb, M.; Cheeseman, J.; Montgomery, J.; Vreven, T.; Kudin, K.; Burant, J. *Gaussian Inc., Wallingford, CT* **2008**.

국문초록

관찰 대상과의 상호 작용에 의하여 변하는 빛의 신호를 탐지하고 분석하여 대상을 연구하는 분광학과 대상을 직접 이미징하여 관찰하는 현미경 관찰학은 소립자 물리학에서부터 생명 현상 연구에 이르기까지 광범위하게 사용되고 있다. 이 두 기술은 보통 독립적으로 사용되는 기술이지만 많은 연구자들은 두 분야 접목하여 새로운 관찰 방법을 개발해왔다. 형광 현미경은 형광 분자를 표지함으로써 살아있는 개체를 훼손하지 않고 실시간으로 관찰할 수 있게 해 준다. 하지만 광학 현미경은 근본적으로 회절 한계에 의하여 그 분해능에 한계가 있다. 최근들어 분자의 흡수와 방출 등의 광물리적 성질을 이용하여 회절한계를 극복한 초고분해능 현미경들이 개발되었다. 그 결과로 관찰 대상은 세포 수준에서 세포 소기관, 단백질, 핵산 등의 매우 작은 크기를 갖는 생분자 수준까지 가능해졌다.

117 염기쌍에서 23,130 염기쌍에 이르는 다양한 종류의 핵산의 길이를 정확하고 정밀하게 측정하기 위하여 동적 분자 빗질 방법과 스테드 나노스코피를 결합하였다. 100 염기쌍 정도의 길이 차이까지 구별이 가능했으

며 이 기술을 복제 수 변이의 진단에 이용할 수 있을 것으로 전망된다.

스테드 나노스코피와 교차 레이저 여기 형광 공명 에너지 전달 단분자 분광학을 결합하여 광학 회절 한계보다 약 50 배 작은 부피에서 단분자를 관측할 수 있었다. 이중 가닥 핵산 분자에 (20 염기쌍) ATTO647N 과 DY-510XL 형광 분자를 표지하여 새로운 기술의 실행가능성을 테스트 하였다. 두 형광 분자 사이에 일어나는 형광 공명 에너지 전달을 공초점 상태와 스테드 상태에서 각각 측정하였다. 이 새로운 기술로 확산하는 핵산 단 분자를 기존 방법보다 100 배 진한 5 나노몰농도에서 관찰할 수 있었다.

커다란 단막 소포나 매달린 입식 지질막 같은 모델 지질막은 표면 상호작용 없이 막관통 단백질을 연구하는데 최적의 시스템이다. 하지만 그 기능을 유지하면서 막단백질을 커다란 단막 소포나 매달린 입식 지질막에 넣는 것이 어렵기 때문에 잘 연구되지 않고 있다. 이전의 핵산 중개 소포 융합에 힘입어 광합성 반응 중심 단백질을 포함하고 있는 소포로부터 커다란 단막 소포나, 핵산이 코팅되어 있는 유리 표면에 커다란 단막 소포의 붕괴로 생긴 입식 지질막으로 단백질 전달하는데 이 기술을 적용하였다. 전달된 단백질의 확산 행동이 연구되었고 이것을 유리에 고정된 이중 지질막에서의 확산과 비교해보았다. 또한 융합 전 후의 단백질의 기능과 방향성을 분석하였다.

브롬화염화벤젠, 브롬화요오드화벤젠, 염화요오드화벤젠에 대하여 분자빔 음이온 광전자 분광법을 사용하여 전자 부착을 연구하였다. 가장 주요한 생성물은 덜 전자친화적인 할로겐원소였다. 광전자 분광법과 이론 계산에서 접근하는 전자가 덜 전자친화적인 원자쪽을 공격하는 것으로 제시되었고 이는 질량 분석 결과와 일치한다. 요오드를 포함하고 있는 분자의 경우 분자로부터의 광전자와 요오드로부터의 광전자가 함께 관측되었으며 요오드로부터의 광전자는 분자가 광분해 반응에 의해 생긴 요오드로부터 나온 것으로 생각된다. 분자 오비탈 분석에서 전자가 접근함에 따라 오비탈 에너지의 재배열이 일어나는 것으로 나타났다. 이 현상들은 간단한 분자 오비탈 이론과 전자 친화도로 설명이 가능하다.

나프탈렌, 안트라센, 페난스렌, 파이렌의 이종이합체를 비행시간 질량분석법, 음이온 광전자 분광법, 이론 계산을 사용하여 연구하였다. 이들의 전자 친화도 차이에 따라 평행 구조와 T자 구조의 두 가지 구조가 가능하다. 평행 구조에서는 새로운 음이온 코어의 생성과 함께 분산력이 중요한 역할을 하며, T자 구조에서는 단량체 음이온 코어와 함께 파이-수소 상호작용이 중요한 역할을 한다. 이들의 안정된 구조와 전하 분포는 전자 친화도 차이에 의해 설명될 수 있다.

주요어: 초고분해능 스테드 나노스코피, 동적 분자 빗질, 단분자 분광학,

핵산 중개 소포 융합, 음이온 광전자 분광법, *Ab initio* 계산

학 번: 2006-20356

Acknowledgement

지구는 참 아름다운 곳이며 살아있는 모든 생명체는 너무나도 아름답습니다. 인간도 자연의 한 일부이지만 위대한 자연 앞에서 감히 자연을 이해하고 탐구하려 합니다. 화가와 피아니스트를 꿈꾸던 어린 아이가 천문학 서적을 읽고 과학자가 되기로 결심한지 20여년이 지났습니다. 과학에 대해 공부하면 할수록 우리가 자연에 대해 이해하고 있는 것이 거의 없다는 것을 깨닫게 됩니다. 하지만 작은 한 발자국을 나아가기 위하여 매 순간 실험하고 논문을 읽고 고민을 합니다.

저에게 화학으로의 길을 이끌어주신 노덕호 선생님께 진심으로 감사 드립니다. 고등학교 때 어떤 분야를 선택해야 할지 고민하는 저에게 화학으로의 입문을 먼저 제안해 주시고 열성적으로 지도해 주시며 화학의 즐거움에 눈뜨게 해 주셨습니다. 저의 고등학교 은사이신 김지현 선생님께도 감사 드립니다. 대학원 진학 후에 바쁘다는 핑계로 찾아 뵙지도 못했는데 항상 제자 걱정해 주시고 응원해 주시던 선생님께 죄송스러운 마음입니다. 2004년 서도 파출소에서 한 달간 근무한 인연으로 항상 저를 자식같이 여겨주시고 기도해주시는 김동화 소장님께도 감사 드립니다.

학부 3학년때부터 지금까지 항상 저를 믿어주시고 연구할 수 있도록 아낌없이 지원해 주신 김성근 교수님께 감사 드립니다. 부족한 저의 학위 논문을 기꺼이 심사해 주시고 많은 조언을 해 주신 민달희 교수님, 남좌민 교수님, 송재규 교수님, 김기현 교수님께도 감사의 말씀을 전합니다.

실험실에서 인연을 맺은 모든 선배님, 동기, 후배들에게도 감사하다는 말을 전하고 싶습니다. 이들과 함께 고민하고 토론하고 실험했던 경험들이 연구자로서의 자질을 키우는데 많은 도움이 되었습니다. 연구에 힘들고 지쳤을 때 Sinfonietta 에서의 연주 활동은 마음에 휴식과 위로를 가져다 주었습니다.

학생들을 좋아하셔서 밤 늦게까지 학생들과 직접 이야기도 하시고 같이 탁구도 쳐 주신 태신 바이오 사이언스 이태헌 사장님, 항상 투덜거리시지만 레이저에 문제 생기거나 어려운 일 생기면 항상 달려오셔서 도움을 주신 레이저 스펙트라 전길환 부장님께도 감사의 말씀을 드립니다.

I thank to Prof. Steven G. Boxer for giving me a wonderful research opportunity at Stanford University for six months. All group members in Boxer lab provided me a lot of help during my visiting. Especially, Brett Carter was a nice friend and a great advisor who taught me how to culture photosynthetic bacteria and how to extract and purify reaction center protein from them. Minsub Jung was a great mentor who taught me everything about vesicle fusion, membrane protein transfer and total internal reflection microscopy. Keun Bong Do, my junior colleague, helped me finding a monthly rental house, and he played tennis with me early in the morning. I got lots of advice on life in Palo Alto as well as on experiments from him. I really miss Madam Helen - a landlady, May and Sun who lived in the same house. I cannot forget the time in Palo Alto.

학위과정 중후반부에 생명의 아름다움과 고귀함을 깨닫게 해 준 나의 귀여운 거북들 탐이, 똑이, 잠이, 하늘이, 멍이, 청이에게도 진심으로 고맙고 사랑한다고 말하고 싶습니다. 이 아이들 때문에 항상 웃고 행복하고 감사한 하루하루를 보낼 수 있었습니다. 건강하게 오래오래 함께 하길 기원합니다.

지난 33 년간 자식을 위해서 모든 것을 희생하신 위대한 두 분의 부모님께 이 논문을 바칩니다. 제가 여기까지 올 수 있었던 것은 99% 이상 부모님의 공이라 말 할 수 있습니다. 집에 머무르는 짧은 시간마저 말도 안하고 무뚝뚝한 아들을 사랑으로 뒷바라지 해 주시느라 본인들의 인생이 거의 없다시피 하신 부모님을 생각할 때 마다 감사하고 죄송스럽고 안쓰러운 마음뿐입니다. 항상 건강하시고 앞으로 화목한 분위기에서 웃을 일이 많아지면 좋겠습니다. 늘 짜증만 내고 퉁명스러운 동생이 세상에서 제일 예쁘다고 하면서 아낌없이 주기만 하는 누나에게도 고맙고 따듯하게 대해 주지 못해서 미안하다는 말을 전합니다. 막내 손주

를 너무나도 예뻐해 주시고 세상을 떠나시는 날까지 제 이름을 부르시던 할아버지, 할머니, 외할아버지, 외할머니가 너무 그립습니다.

지난 5 년간 변함없이 제 곁에서 저에게 마음의 평안과 기쁨을 가져다 준 윤희에게 감사의 말을 전합니다. 바쁘고 힘들다고 웃는 모습도 많이 보여주지 못하고, 따뜻한 말 보다는 매정하고 차가운 말을 더 많이 했던 저를 항상 이해하고 사랑해준 너무나도 착한 마음씨에 고마움을 전합니다.

마지막으로 인류에게 음악이라는 와인을 선물해준 베토벤과, 인생의 희로애락과 우주의 사운드를 음악에 담은 말러에게도 존경과 감사의 뜻을 바칩니다.

2013.11.07

김 남 두